



UNIVERSITÀ
DI PAVIA

PhD IN BIOMEDICAL SCIENCES
DEPARTMENT OF MOLECULAR MEDICINE
UNIT OF BIOCHEMISTRY

**Generation and Characterization
of *In vitro* and *In vivo* Models of Osteogenesis Imperfecta**

PhD Tutor: Prof. Antonella Forlino

PhD dissertation of
Laura Leoni

XXXIII Cycle A.Y. 2019-2020

Contents

Introduction	5
Collagens	6
Collagen type I	6
Collagen type I biosynthesis	8
Osteogenesis imperfecta	13
OI classification	13
Bone fragility OI-like syndromes	22
TRIC-B role in the pathophysiology of OI type XIV	27
TRICs channels	27
Altered calcium homeostasis in OI type XIV	29
CRISPR/Cas system	33
Chapter I	
Generation and characterization of OI type XIV <i>in vitro</i> model	36
Introduction	37
Osteoblastic cell lines	37
Materials and methods	39
Human foetal osteoblast cell line	39
Knock-out <i>in vitro</i> model generation	39
hFOB 1.19 transfection	41
DNA extraction and genotyping	41
T7 endonuclease assay	42
Restriction enzymes	42
TA cloning	43
Protein lysates	43
Western blot	43
Calcium analysis	44
Collagen analysis	44
Cell proliferation	45
Alkaline Phosphatase assay	45
RNA extraction	46
Real time qPCR	46
Cell mineralization	46
Statistical analysis	47
Results	48
Generation of OI type XIV <i>in vitro</i> model	48
Impaired calcium flux in <i>TMEM38B</i> KO cells	53
Reduced collagen type I post translational modification in <i>TMEM38B</i> KO cells	55
Delay in <i>TMEM38B</i> KO cells differentiation	56

Reduced alkaline phosphatase activity in <i>TMEM38B</i> KO cells	58
Delay in <i>TMEM38B</i> KO cells mineralization	60
Impairment of <i>TMEM38B</i> KO cells proliferation	61
Discussion	63
Supplementary figures	67
Chapter II	
Generation and characterization of OI type XIV zebrafish model	68
Introduction	69
Zebrafish	69
Zebrafish skeleton	69
Vertebral column	70
Osteoblastogenic markers	71
Zebrafish collagen type I	72
Zebrafish models for osteogenesis imperfecta	73
Materials and methods	76
Zebrafish	76
<i>In silico</i> analysis	76
<i>In situ</i> hybridization	76
Generation of <i>tmem38b</i> zebrafish mutant	78
Microinjection	80
DNA extraction and genotyping	80
TOPO TA cloning	80
Genotyping	81
Screening of mutants	81
RNA extraction	82
Real time PCR (qPCR)	82
Collagen analysis	83
Amino acids analysis	83
Morphometric analysis	84
Alizarin red and alcian blue staining	85
X-ray	86
Micro-Computed Tomography	87
Whole mount immunohistochemistry	87
Histological analysis	88
Statistical analysis	89
Results	90
<i>In silico</i> analysis	90
<i>tmem38b</i> expression in zebrafish embryos	91
Generation of OI type XIV zebrafish models using CRISPR/Cas9 gene editing	93
Generation of two <i>tmem38b</i> mutants	93
Selection of F1 heterozygous and generation of F2 homozygous mutants	96

<i>tmem38b</i> expression in the two mutant zebrafish models	98
Skin and bone collagen type I analysis	99
Skeletal characterization of <i>tmem38b</i> ^{-/-} and <i>tmem38b</i> ^{Δ120-7/Δ120-7}	101
Morphometric analysis of <i>tmem38b</i> ^{-/-}	101
Swim bladder of <i>tmem38b</i> ^{-/-}	104
Mineralization analysis of <i>tmem38b</i> ^{-/-}	105
Vertebral dimensions of <i>tmem38b</i> ^{-/-}	106
Micro-computed tomography (μCT) of <i>tmem38b</i> ^{-/-}	109
Morphometric analysis of <i>tmem38b</i> ^{Δ120-7/Δ120-7} mutant	110
Swim bladder of <i>tmem38b</i> ^{Δ120-7/Δ120-7}	111
Vertebral dimensions of <i>tmem38b</i> ^{Δ120-7/Δ120-7}	111
Toluidine blue staining of <i>tmem38b</i> zebrafish mutants	112
Enlarged cisternae size and extracellular collagen fibers content in mutant fish	113
<i>Hspa5</i> expression	115
Hsp47 protein and transcript expression in <i>tmem38b</i> mutants	116
Discussion	119
Conclusion	124
Supplementary tables	125
Chapter III	
<i>Prolyl 3-hydroxylation complex: new insight from zebrafish OI models</i>	128
Prolyl 3-hydroxylation complex	129
Chapter IV	
<i>New pharmacological treatment for OI: an in vitro approach</i>	152
OI treatment	153
Chapter V	
<i>Early fracture healing is delayed in the <i>Coll1a2</i>^{+G610C} osteogenesis imperfecta murine model</i>	171
Chapter VI	
<i>Zebrafish: a resourceful vertebrate model to investigate skeletal disorders</i>	184
<i>Bibliography</i>	214

Introduction

Collagens

Collagens are the most abundant structural proteins in mammals, representing the major constituents of the extracellular matrix of connective tissues, such as tendon, cartilage, skin and bones. The large and heterogeneous collagens family comprises 28 members of proteins with similar function, involved in the formation of supra molecular networks that allow them to efficiently withstand traction and stretching (Mienaltowski and Birk 2014).

Collagens can be distinguished in different categories based on their structure: the classical fibrillar and network-forming collagens, FACITs (fibril-associated collagens with interrupted triple helices), MACITs (membrane associated collagens with interrupted triple helices) and MULTIPLEXINs (multiple triple helix domains and interruptions) (Shoulders and Raines 2009).

All collagens are characterized by a right-handed triple helix structure composed by three α -chains supercoiled around a central axis. This triple helix consists of three polypeptide chains, called α chains. Collagen molecules are distinguishable in homotrimers, like collagen type II, III, VII, VIII, X, if composed by three identical α chains, or heterotrimers like collagen type I, IV, V, VI, IX, and XI, when the helix is made up of three or at least two different polypeptides (Ricard-Blum 2011).

Collagen type I

Collagen type I is the most abundant protein in all vertebrates and it is present in several connective tissues such as bone, skin, tendon and cornea. It is a heterotrimeric protein composed by two $\alpha 1$ chains and one $\alpha 2$ chain, encoded by *COL1A1* and *COL1A2* genes, respectively (Ricard-Blum 2011; Gelse, Poschl, and Aigner 2003).

Collagen type I is synthesized as a procollagen precursor, characterized by an N-terminal propeptide, a central helical domain, where each α chain contains 338 uninterrupted Gly-Xaa-Yaa repeats, and a C-terminal propeptide. The presence of Glycine, which is the smallest amino acid, is necessary for the correct packaging of the α chains around the central axis, required for triple helix formation (Gelse, Poschl, and Aigner 2003; Nelson, Lehninger, and Cox 2008). The triple helix structure is then stabilized by intrachain hydrogen bonds

between the amino group (N-H) of each glycine and the carbonic group (COOH) of a nearby proline (Shoulders and Raines 2009).

The central collagen helix is connected to the propeptides by short and non-helical segments of approximately 15 to 20 amino acid residues, known as N- and C- telopeptides (Makareeva and Leikin 2014), respectively, necessary for collagen maturation and cross-links formation (Eyre, Paz, and Gallop 1984).

The N-propeptides avoid unexpected and earlier aggregation of newly synthesized chains (Mienaltowski and Birk 2014), facilitating the transport of procollagen molecules from the endoplasmic reticulum (ER) to the Golgi (Bächinger et al. 2010). C-propeptides, which are stabilized by intrachain disulphide bonds, guarantee the association between monomeric procollagen chains (Bulleid, Dalley, and Lees 1997) and determine chain selectivity (Lees, Tasab, and Bulleid 1997). Finally, C-terminal domains align and trigger the formation of the triple helix moving toward the N-terminus (Gelse, Poschl, and Aigner 2003) (**Figure 1**).

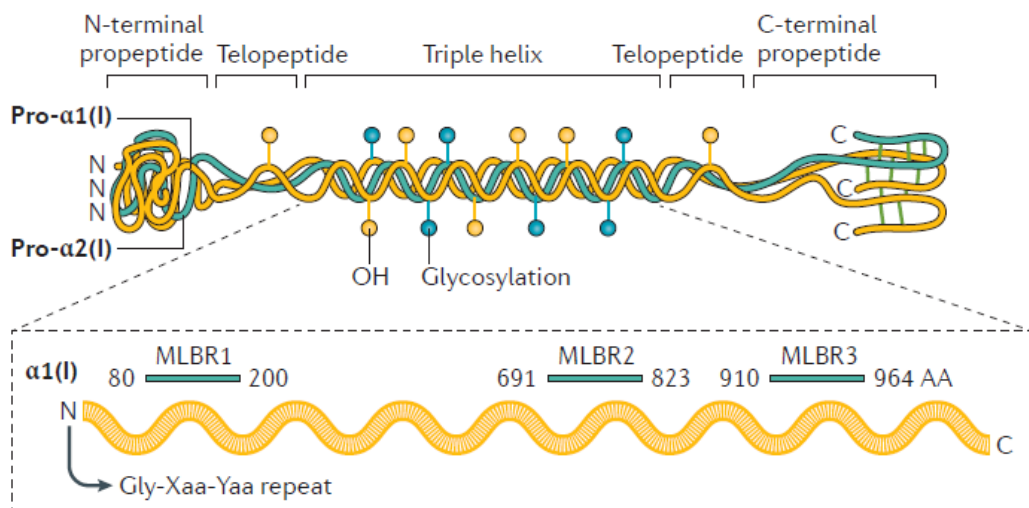


Figure 1. Structure of procollagen type I. Both amino-terminal and carboxyl-terminal propeptide sequences are proteolytically cleaved by specific proteases (a disintegrin and metalloproteinase with thrombospondin motifs 2 (ADAMTS2) and bone morphogenetic protein 1 (BMP1), respectively) that recognize a sequence in the telopeptides. The sequence of each collagen chain is characterized by Gly-Xaa-Yaa repeats (in which Xaa and Yaa are for about 30% proline and hydroxyproline). Along the $\alpha 1$ -chain, specific regions relevant for the interaction of collagen with other collagen molecules or with extracellular matrix proteins were identified, namely, major ligand-binding region (MLBR) (from Marini et al. 2017).

Collagen type I biosynthesis

Collagen type I biosynthesis starts with the transcription of *COL1A1* and *COL1A2* genes. The mRNA is then translated into pre-procollagen molecules which protrude into the lumen of the rough endoplasmic reticulum (ER), where thanks to the presence of a signal peptide, can be recognized by specific receptors (Gelse, Poschl, and Aigner 2003). Once the signal peptide is removed, the procollagen chains undergo to several different post translational modifications, such as proline and lysine hydroxylation (**Figure 2A**). Prolyl 3-hydroxylase, prolyl 4-hydroxylase and lysyl hydroxylase are the enzymes involved in C3-Proline, C4-Proline and Lysine hydroxylation, respectively (Gelse, Poschl, and Aigner 2003).

Hydroxyproline residues are necessary for intramolecular hydrogen bonds formation within the triple helix, which stabilize collagen triple helix structure, also leading to increase thermal stability (Bella and Hulmes 2017). The 4-hydroxyproline is essential for triple helix stability and indeed at least 90 prolyl residues have to be hydroxylated in Yaa position in order to guarantee the correct folding (Rossert and de Crombrughe 2002).

The hydroxylation of lysine residues is performed by Lysine Hydroxylase 1 (LH1), Lysine Hydroxylase 2 (LH2) and Lysine Hydroxylase 3 (LH3) encoded by *PLOD1*, *PLOD2* and *PLOD3*, respectively. LH1 and LH3 hydroxylate the Lys residues in the helical domain, while LH2 exclusively hydroxylates Lys residues in the telopeptides (Yamauchi and Sricholpech 2012; Gjaltema and Bank 2017).

The hydroxylysine (Hyl) residues are important for the formation of stable intermolecular cross-linking as well as for representing a site of attachment of carbohydrates, which are necessary to guarantee collagen fibril stabilization (Soroushanova et al. 2019). Collagen and proteins with collagenous sequences are subjected to the peculiar O-linked glycosylation of Hyl residues, while the more common N-linked glycosylation is restricted to propeptide regions (Clark 1979).

The O-glycosylation is catalysed by hydroxylysine-galactosyl-transferase and galactosyl hydroxylysine-glucosyl-transferase which attach either galactose unit or a disaccharide of galactose and glucose on collagen hydroxylysine residues (Hennet 2019).

The formation of Hyl residues and subsequent attachment of sugar components are essential to modulate fibrillogenesis (Hennet 2019).

Hydroxylation and glycosylation are necessary to stabilize the helical structure even if the efficiency of procollagen alpha chains formation and folding are also closely related to the presence of specific enzymes, such as peptidyl-prolyl *cis-trans*-isomerases, protein disulphide isomerase (PDI) and heat shock protein 47 (HSP47) (**Figure 2B**).

The peptidyl-prolyl *cis-trans*-isomerases Cyclophilin B (CyPB) thanks to its PPIase activity catalyses the *cis-trans* isomerization of proline imidic peptide bonds in the polypeptide, required for collagen folding kinetic (Steinmann, Bruckner, and Superti-Furga 1991; Bächinger et al. 1980).

Together with prolyl 3-hydroxylase 1 (P3H1) and cartilage associated protein (CRTAP), CyPB forms the ER resident prolyl 3 hydroxylation complex, involved in the hydroxylation of specific prolyl residues, such as the Pro986 on $\alpha 1$ chains of collagen type I, and also acting as molecular chaperone (Ishikawa et al. 2009) (**Figure 2C**).

Protein disulphide isomerase (PDI) was also implicated in procollagen folding, involved in intra and interchain disulphide bonds formation on procollagen molecules and in stabilizing procollagen structure (Koivu 1987).

Collagen folding and trafficking are also regulated by the specific collagen chaperone heat shock protein 47 (HSP47). The Heat shock protein 47 (HSP47) is a 47 kDa endoplasmic reticulum molecular chaperone able to bind pro-collagen α -chains as soon as they are assembled and prevent the association of collagen molecule and aggregates formation in the ER, thus facilitating the transport of procollagen from the ER to Golgi (Ishida and Nagata 2011). HSP47-procollagen interaction is pH-dependent, indeed the ER neutral-pH is required for HSP47 binding to procollagen molecules, while the lower pH (below 6.3) of the *cis*-Golgi is required for their dissociation (Nakai et al. 1992). HSP47 is then recycled back from Golgi to ER in a process mediated by KDEL (Lys-Asp-Glu-Leu) receptors (Satoh et al. 1996).

Once folded, procollagen molecules are packed into secretory vesicles, exported from the ER to the Golgi and then to the extracellular space (Makareeva and Leikin 2014). When collagen cannot be properly folded, the cell activates different alternative pathways, such as the ER associated degradation (ERAD) of misfolded chains by proteasomes in case of

impaired α chains assembly, or the autophagy pathway, usually activated when misfolded procollagen chains are due to structural defects (Fitzgerald, Lamandé, and Bateman 1999).

The trafficking between ER and Golgi is mediated by two transient Coat Protein complexes, COPI and COPII. The latter is involved in the export of protein from the ER, whereas COPI mediates the retrograde transport of ER-resident proteins and the later stages of ER-to-Golgi transport (Canty and Kadler 2005). In order to allow the transport of the rigid and very large folded procollagen molecules (around 300 nm in length) (Liu et al. 2017), the COP II coated vesicles cooperate with the transport and Golgi organization (TANGO) protein 1 to form “megacARRIER” vesicles (Malhotra and Erlmann 2015).

TANGO1, localized at the ER exit sites (ERES), is able to indirectly bind procollagen through its luminal Src homology 3 (SH3) domain and COPII components through its cytoplasmic proline rich domain (PRD), thus retarding the completion of the vesicle which grows to the point that it can contain the procollagen molecules (Saito et al. 2009). The SH3 domain of TANGO1 interacts with procollagen bounded HSP47 in the ER, directing procollagen molecules to COPII (Ishikawa et al. 2016), moving from the *cis* to the *trans* Golgi, where it is sorted for its final destination (Canty and Kadler 2005).

Once the procollagen molecules reach the extracellular space, two specific metalloproteinases, the A Disintegrin and Metalloproteinase with Thrombospondin Motifs 2 (ADAMTS2) and the Bone Morphogenic Protein 1 (BMP1), cleave the N- and C-propeptides, respectively (Yamauchi and Sricholpech 2012) (**Figure 2D**). The new secreted molecules spontaneously associate and form fibrils where collagen molecules are longitudinally staggered with respect to one another by a D-period motif of 67 nm (Yamauchi and Sricholpech 2012; Bella and Hulmes 2017).

The extracellular collagenous matrix is strengthened thanks to the formation of intra- and inter-molecular crosslinks within fibrils, as a result of the action of lysyl oxidase (LOX) (Eyre, Paz, and Gallop 1984). LOX enzymes perform oxidative deamination of the amino group of specific Lys and Hyl residues within the -C and -N terminal telopeptides and the triple helix domain, catalysing cross-link formation, the major collagen post-translational modification, which is involved in the determination of biomechanical properties of bone tissue (Piersma and Bank 2019).

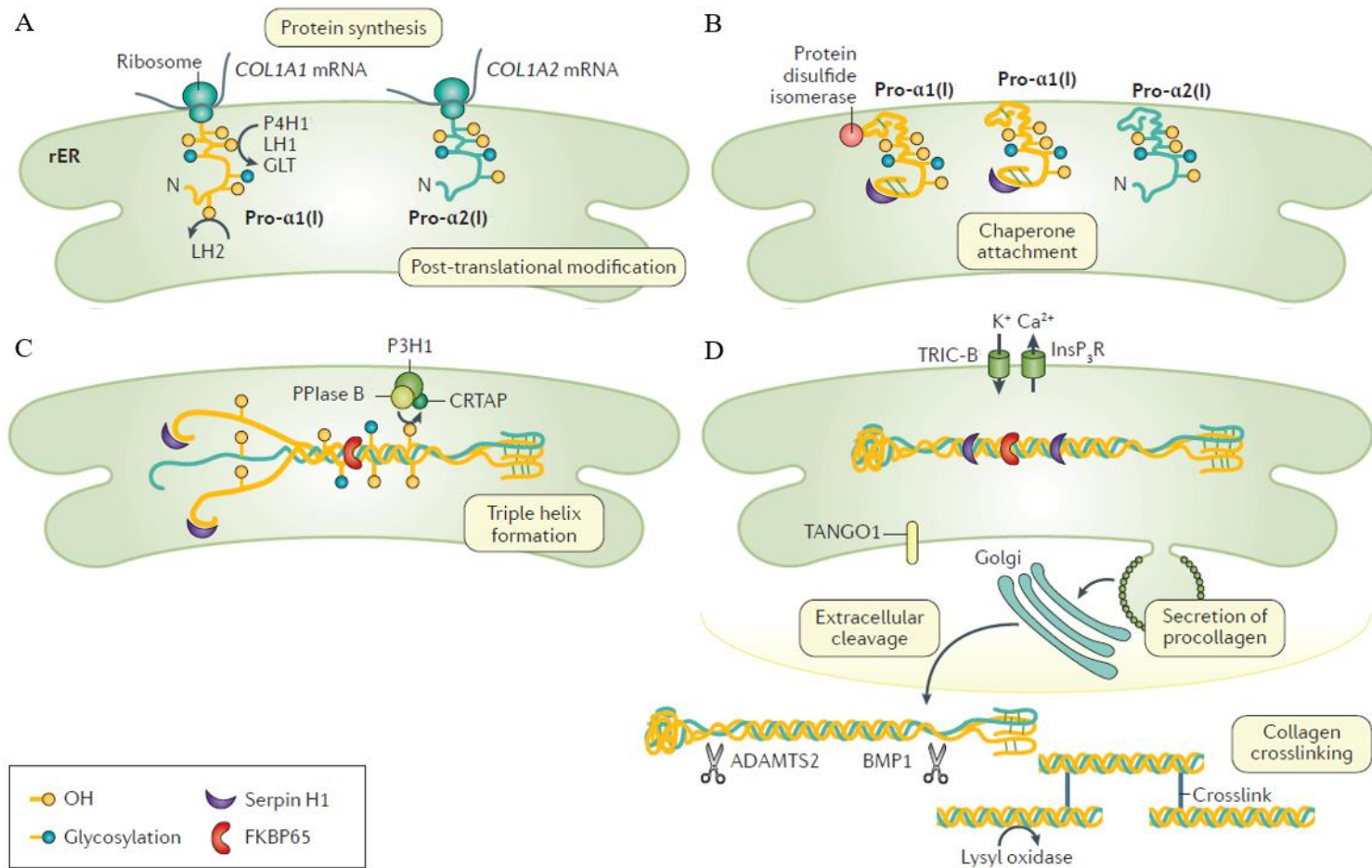


Figure 2. Collagen type I biosynthesis and processing. **A.** Translation of pro- α 1(I) and pro- α 2(I) and their post translational modification: Proline and Lysine hydroxylation and subsequently the glycosylation of hydroxylysine residues. **B.** Interactions with molecular chaperones to prevent premature triple helix formation, such as SERPINH1. **C.** Triple helix formation that comprises the association of two pro- α 1-chains and one pro- α 2-chain, thanks to the action of P3H1 complex and FKBP65 **D.** Collagen transport from ER to Golgi and then to the extracellular space, extracellular cleavage to collagen mediated by ADAMTS2 and BMP1 and crosslinking formation. ADAMTS2, a disintegrin and metalloproteinase with thrombospondin motifs 2; BMP1, bone morphogenetic protein 1; CRTAP, cartilage-associated protein; GLT, galactosyltransferase 1; InsP3R, inositol-1,4,5-triphosphate receptor; LH, lysyl hydroxylase; P3H1, prolyl 3-hydroxylase 1; P4H1, prolyl 4-hydroxylase 1; PPIase B, peptidyl-prolyl *cis-trans* isomerase B; rER, rough endoplasmic reticulum; TANGO1, transport and Golgi organization protein 1; TRIC-B, trimeric intracellular cation channel type B (from Marini et al. 2017).

Osteogenesis imperfecta

Osteogenesis Imperfecta (OI) is a connective tissue disorder with an incidence estimated around 1 in 10,000 births, mainly characterized by skeletal deformity, low bone mass and bone fragility. Patients can manifest also secondary features such as blue sclerae, hearing loss, dentinogenesis imperfecta, cardiac abnormalities and pulmonary dysfunction (Marini et al. 2017). It is caused for more than 85% by dominant mutations in either of the genes encoding collagen type I $\alpha 1$ and $\alpha 2$ chains, namely *COL1A1* and *COL1A2* (Marini, Forlino, et al. 2007). OI is also caused by recessive mutations in genes encoding for proteins involved in collagen type I post translational modifications, processing and extracellular fibril assembly (Kang, Aryal, and Marini 2017) and in genes involved in osteoblast differentiation and/or activity (Forlino and Marini 2016).

OI classification

In 1979 Sillence classification divided OI on the basis of clinical, radiographic and genetic features. Four different types of classical OI, from type I to IV, were identified and classified from mild to lethal. They were all caused by dominant mutations in *COL1A1* and *COL1A2* genes respectively (Sillence, Senn, and Danks 1979; Marini, Forlino, et al. 2007).

Starting from 2006 the discovery of mutations in different genes as causative of new forms of OI (Barnes et al. 2006) required a revision of the original classification (Marini et al. 2017) (**Figure 3, Table 1**).

1) Impairment of collagen synthesis and structure

This first group includes the four classical dominant OI forms (I-IV), due to mutations in *COL1A1* or *COL1A2* genes, leading to defects in collagen type I quantity or structure. Patients' phenotype varies depending on position of the mutations within the collagen chain, the nature of the substituted amino acid as well as the chain in which the substitution occurs. For instance, mutations in the 200 residues N-terminal region of the triple helix are generally associated with non-lethal phenotypes, whereas mutations in the C-terminal helical region, when collagen folding starts, may cause both lethal and moderate outcomes (Marini et al. 2017).

OI type I is the mildest dominant form and is mainly caused by null mutations in *COL1A1*, that induce premature termination codons in the coding sequence of one allele, leading to a reduced amount of normal collagen type I (Marini, Forlino, et al. 2007). OI type I patients present early osteoporosis with a series of fractures in the pre-pubertal years due to mild trauma. They are characterized by normal bone shape or mild bowing of long bones and minimal central vertebral compressions (Marini and Smith 2015). OI type I is divided into A and B subtypes based on the presence or absence of dentinogenesis imperfecta (Levin, Salinas, and Jorgenson 1978).

Structural collagen defects cause the full range of moderate and progressive deforming OI type IV and type III, respectively, as well as lethal type II (Sillence, Rimoin, and Danks 1979). Mutations responsible for collagen structural defects are usually the substitution of glycine within the Gly-Xaa-Yaa repeat with a bulkier or charged residue. Other 20/25% of mutations are in the 3' or 5' splice sites, leading to an exon skipping and 5% of mutations affects the 5' of C propeptide domain (Marini, Forlino, et al. 2007).

OI type II is the perinatal lethal form, characterized by *in utero* bone fractures. Radiologic features include absent or limited calvarial mineralization, flat vertebral bodies, short, broad femurs and ribs and evidence of bowing of long bones. Patients often die due to multiple pneumonias and respiratory insufficiency (Marini and Smith 2015).

OI type III, is the most severe form compatible with life. Patients have frequent fractures, short stature, scoliosis, vertebral compression and dentinogenesis imperfecta (Sinikumpu et al. 2015).

OI type IV is a moderate form, ranging from mild symptoms, like OI type I, to more severe manifestations. Patients present osteoporotic bones with several fractures and popcorn calcifications, while dentinogenesis imperfecta and hearing loss are rarely present (Van Dijk and Sillence 2014).

2) *Compromised bone mineralization*

The OI forms classified in this group are caused by defects in genes required for bone mineralization and osteoblasts differentiation (Marini et al. 2017).

OI type V is principally determined by a dominant point mutation in the 5'-UTR of *IFITM5*, encoding for the bone-restricted interferon-induced protein (BRIL), specifically expressed in the initial stages of osteoblast mineralization (Hanagata et al. 2011). As consequence of the substitution c-14C>T, BRIL is translated from a newly generated start codon with five extra residues at the N-terminus (MALEP). This mutation causes an increase in bone formation, leading to hyperplastic callus and ossification of membranes (Semler et al. 2012; Farber et al. 2014).

OI type V patients are characterized by an increased fracture incidence and impaired bone quality. In addition, patients are also subjected to hyperplastic callus formation during fracture healing, periosteal hyperplastic expansion and calcification of interosseus membrane (Rauch et al. 2013).

OI type VI is caused by mutations in *SERPINF1* gene, which encodes for the pigment epithelium derived factor (PEDF). PEDF is an anti-angiogenic factor involved in the interaction with the receptor activator of nuclear $\kappa\beta$ ligand (RANKL) pathway and in the increasing of osteoclasts activity (Becker et al. 2011). PEDF has a crucial role in maintaining bone homeostasis and regulating osteoid mineralization (Bogan et al. 2013). Recessive null mutations in *SERPINF1* and subsequently absence of PEDF lead to a delay in mineralization. OI type VI patients show a progressive severe degeneration of bone quality, with reduced bone mineral density, vertebral compression and long bone fractures (Trejo et al. 2017). The distinctive feature of this form is the coexistence of highly mineralized bone matrix with seeds of osteoid showing abnormally low mineral content, although overall mineral to-matrix content is increased (Fratzl-Zelman et al. 2015).

An heterozygous BRIL p.Ser40Leu mutation, which causes the retention of the mutant protein in the Golgi, was found in individuals that show the typical bone histology pattern described in OI type VI (Patoine et al. 2014). Fibroblasts and osteoblasts carrying BRIL p.Ser40Leu present impaired PEDF secretion, opposite to what observed in OI type V patients carrying the MALEP-BRIL production. These data reveal the role of BRIL in

regulating PEDF expression/secretion and further support the gain-of-function mechanism in OI type V carrying c.-14C>T mutation (Farber et al. 2014).

3) *Abnormal collagen post-translational modification*

This group is characterized by OI forms caused by recessive mutation in genes involved in procollagen type I folding and post translational modifications, in particular *CRTAP*, *P3H1* and *PPIB* (Marini et al. 2017).

In the endoplasmic reticulum, *P3H1*, *CRTAP* and *PPIB*, encoding for the prolyl 3-hydroxylase 1, the cartilage associated protein and cyclophilin B, respectively, are assembled in a 1:1:1 ratio to form the ER resident- prolyl 3-hydroxylation complex. This complex is involved in the hydroxylation of specific proline residues on collagen chains. P3H1 is the enzyme required to catalyse the hydroxylation on C-3 of $\alpha 1(I)$ -Pro986 and $\alpha 2(I)$ -Pro707. CRTAP is the helper protein which stabilizes the complex and CyPB is a peptidyl-prolyl *cis-trans* isomerase, which allows peptide bonds involving proline residues to reach the *trans* configuration required for proper protein folding (Ishikawa et al. 2009).

Null mutations in *CRTAP* and in *P3H1* cause OI type VII and OI type VIII, respectively. They are severe to lethal osteochondrodysplasias with rhizomelia, neonatal fractures, reduced mineral density, popcorn calcifications at the epiphyses and growth retardation. P3H1 and CRTAP are mutually supportive in the complex and the absence of one of them strongly affects the other, resulting in a similar clinical outcome (Forlino and Marini 2016).

From a biochemical point of view, defects in both *P3H1* and *CRTAP* lead to a delay in collagen folding, leaving the α chains more subjected to the post-translational modifier enzymes activity (Forlino et al. 2011).

OI type IX is caused by missense and non-sense mutations in *PPIB*, which lead to altered proper CyPB folding without impairing 3-prolyl hydroxylase complex activity (Marini, Cabral, and Barnes 2010). Despite CyPB belongs to the P3H1 complex, OI type IX individuals have a distinctive phenotype compared to types VII/VIII, showing moderate short stature, and the possibility to have vertebral compressions and lack of rhizomelia (Marini and Smith 2015).

4) *Compromised collagen processing and cross-linking*

This group includes OI forms caused by mutations in *SERPINHI* and *FKBP10* genes, encoding for HSP47 and FKBP65, and mutation in the bone morphogenic protein 1, BMP1 (Zeng et al. 1998; Nagata 2003; Ishikawa et al. 2008).

OI type X is a moderate to severe form caused by defects in *SERPINHI* gene, which encodes for HSP47, important for procollagen folding and trafficking between ER and *cis*-Golgi (Zeng et al. 1998).

Thirteen autosomal recessive mutations in *SERPINHI* were discovered and for c.233T>C missense mutation (p.Leu78Pro) a detailed biochemical analysis was described. This mutation results in the degradation of the endoplasmic reticulum resident HSP47 via the proteasome. This mutation slows down the transit time from inside the cell to the extracellular environment. Despite pro-collagen type I production rate is normal, the secreted collagen triple helical conformation is altered, making it more susceptible to protease degradation (Christiansen et al. 2010).

OI type X patients are characterized by reduced mineralization, deformity of long bones, blue sclerae and dentinogenesis imperfecta, skin bullae, pyloric stenosis and renal stones (Forlino and Marini 2016).

OI type XI is caused by mutations in *FKBP10*, that encodes for the peptidyl-prolyl *cis-trans* isomerase FKBP65, whose loss of activity results in incomplete stabilization of procollagen and lower hydroxylation of lysyl residues within the C-telopeptide, leading to a delayed secretion and to an impairment in proper cross-links formation. The hydroxylation of C-telopeptide lysyl residue is catalysed by lysyl hydroxylases 2 (LH2, encoded by *PLOD2*) suggesting that defects in FKBP65 may also alter LH2 activity (Schwarze et al. 2013). OI type XI is characterized by long bone fractures, platyspondyly and scoliosis. Interestingly, mutations in *FKBP10* are also responsible for Bruck syndrome, characterized by congenital contractures of joints, short stature and scoliosis and Kuskokwim syndrome, associated to congenital contractures with minimal skeletal involvement (Barnes et al. 2013; Schwarze et al. 2013).

OI type XIII is caused by mutations in BMP1 gene. *BMP1* encodes for the type I collagen C-propeptidase enzyme BMP1/mTLD, that plays a relevant role in extracellular matrix (ECM) formation. BMP1 removes the C-propeptides from the procollagen precursors of the major fibrillar collagen types and allows the assembly of mature collagen monomers into fibrils (Asharani et al. 2012). Homozygous substitution in the BMP1 signal peptide leads to a high bone mineral density phenotype (Asharani et al. 2012), while homozygous substitution (Phe249Leu) in the BMP1 protease domain result in osteoporotic phenotype, probably due to a residual BMP1 activity (Martínez-Glez et al. 2012).

5) *Altered osteoblast differentiation and function*

This group includes OI forms caused by mutations in genes involved in osteoblasts differentiation and function, such as *SP7*, *TMEM38B*, *WNT1*, *CREB3L1* and *MBTPS2*.

OI type XII is caused by loss of function mutations in *SP7*. *SP7* encodes for Osterix (OSX), a zinc finger specific transcription factor mainly expressed in osteoblasts, necessary for bone formation and homeostasis by promoting osteoblast differentiation and maturation (Lapunzina et al. 2010). A homozygous single base pair deletion has been reported in individuals with recurrent fractures, mild bone deformities, delayed tooth eruption, normal hearing, and white sclera (Lapunzina et al. 2010).

Recently a missense substitution in *SP7* (c.946C>T) has been found in patient with typical OI phenotypic features like short stature, joint hyperlaxity, general osteopenia, bone deformities and hearing loss (Fiscaletti et al. 2018).

OI type XIV is caused by mutations in *TMEM38B*, which encodes the ubiquitous voltage-dependent cation channel TRIC-B (Venturi et al. 2013). TRIC-B allows the transport of potassium ions across the ER membrane modulating calcium flux through the IP₃R channel (Cabral et al. 2016). Altered intracellular Ca²⁺ flux affects the activity of several Ca²⁺ dependent enzymes, including many enzymes and chaperones involved in post-traditional modifications and in the correct folding of collagen type I, such as proteins binding immunoglobulins (BIP), cyclophilin B (CyPB), the disulfide isomerase protein (PDI) and calreticulin (CRT) (Michalak et al. 2009).

Individuals with non-sense mutations and deletions show generalized osteopenia, long bone fractures from birth and overall severe bone deformity, but normal hearing, normal sclerae and dentinogenesis (Shaheen et al. 2012; Volodarsky et al. 2013).

OI type XV is determined by defects in *WNT1* (Wingless-related integration site), a glycoprotein involved in the activation of the β -catenin. *WNT1*, upon binding to the transmembrane receptors Frizzles and LRP5/6, leads to β -catenin nuclear translocation, thus activating the expression of several genes important for bone formation. Homozygous non-sense, frameshift, missense or splicing mutations in *WNT1* have been found in patients with severe OI type XV characterized by short stature, frequent fractures, vertebral compressions and in several cases also by brain malformations (Faqeih, Shaheen, and Alkuraya 2013). Interestingly, heterozygous mutations lead to early osteoporosis (Baron and Kneissel 2013).

OI type XVI is caused by non-sense, missense and frameshift mutations in *CREB3L1*, encoding for the endoplasmic reticulum stress-inducer Old Astrocyte Specifically Induced Substance (OASIS), a transcription factor largely expressed in osteoblasts. OASIS is usually proteolytically cleaved by membrane proteases, as consequence of mild ER stress during osteoblast differentiation. In the nucleus OASIS binds *COL1A1* promoter and stimulates its transcription.

Interestingly, it was demonstrated that OASIS regulates the expression of *SEC24D*, involved in COPII vesicles organization and in conferring directionality from ER to Golgi (Guillemyn et al. 2019). A patient with a homozygous c.911C> T lethal mutation (p.Ala304Val) in OASIS conserved nuclear localization sequence showed reduced *SEC24D* expression (Symoens et al. 2013; Guillemyn et al. 2019).

OI type XVII is caused by mutations in *SPARC*, which encodes for the secreted acid cysteine-rich protease, a glycoprotein that binds collagen type I in the extracellular matrix (Mendoza-Londono et al. 2015). In osteoid, *SPARC* binds collagen and hydroxyapatite crystals and releases calcium ions, enhancing mineralization of the bone collagen matrix (van Dijk et al. 2013). *SPARC* is composed by four domains: an N-terminal low-affinity calcium-binding domain that contains the mineral binding region, a Cysteine-rich domain, a hydrophilic region and an extracellular Ca^{2+} domain with an E-F hand motif at the C-

terminus that comprises the collagen binding domain (Rosset and Bradshaw 2016). Two nonsynonymous homozygous mutations in extracellular Ca^{2+} binding domain of SPARC were found; the c.497G>A (p.Arg166His) substitution in exon 7 and the c.787G>A (p.Glu263Lys) substitution in exon 9. The Arg166 and Glu263 are conserved in the extracellular Ca^{2+} binding domain of SPARC, which forms a salt bridge necessary for collagen binding. Mutations in these two amino acids significantly reduce SPARC affinity for collagen type I, leading a delay in collagen secretion and mild post translational overmodification (Rosset and Bradshaw 2016). OI type XVII patients have not evident skeletal abnormalities at birth, but frequent bone fractures, mild joint hyperlaxity and scoliosis emerge during development (Mendoza-Londono et al. 2015).

OI type XIX is the first described x-linked form caused by mutations in *MBTPS2* gene (Marini et al. 2017). *MBTPS2* is located on chromosome Xp22.11-p22.13 and encodes the membrane bound zinc site-2 metalloprotease (S2P). S2P is composed by 6 transmembrane domains and plays an important role in the regulation of intramembrane proteolysis (RIP) cascade of signal transduction among cellular compartments (Kang, Aryal, and Marini 2017).

Patients carrying *MBTPS2* mutation show an underhydroxylation of collagen type I lysine residues, which impairs cross-link formation, consequently leading to a reduced bone strength. Pre- and post-natal fractures of long bones and ribs are frequent as well as scoliosis and thoracic deformity, while teeth and sclerae are normal (Lindert et al. 2016).

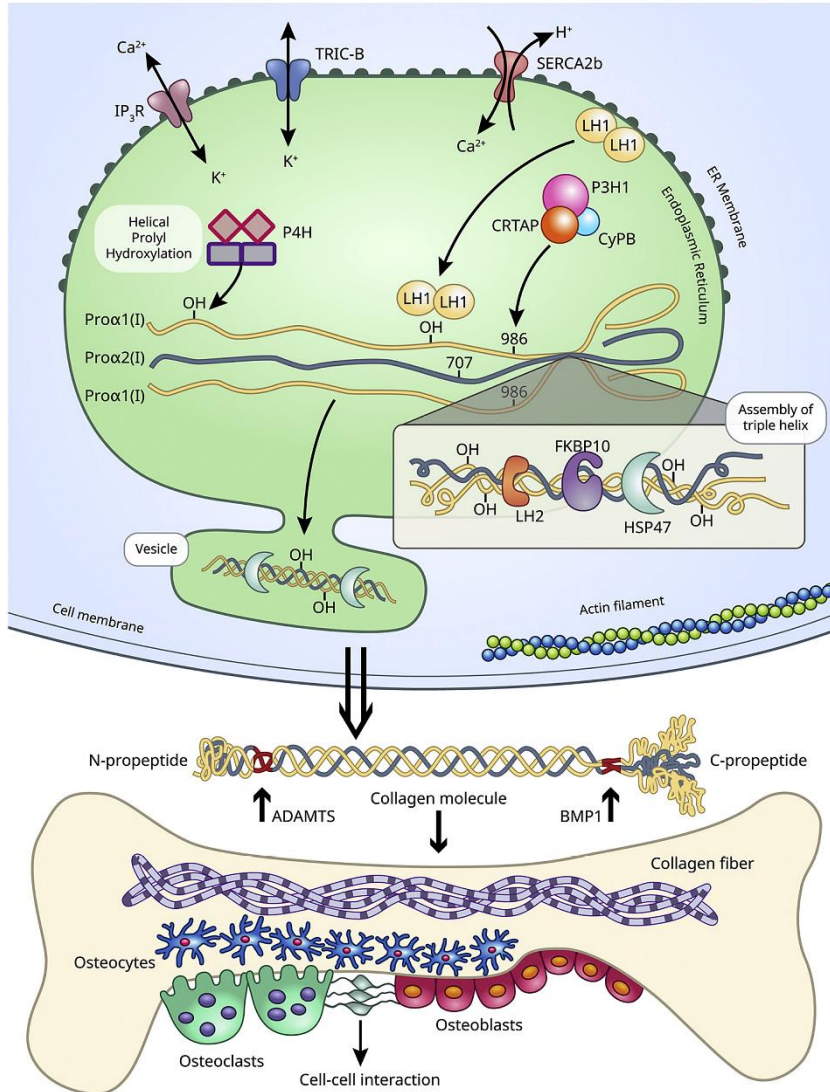


Figure 3. Proteins involved in collagen type I modification and folding. The collagen triple helical chains are modified post-translationally by LH1 and P4H1. P3H1 complex (P3H1, CRTAP, and CyPB) hydroxylates the Pro986 on $\alpha1(I)$ and Pro707 on $\alpha2(I)$. HSP47 interacts with FKBP10 stabilizing the triple helix and favouring its folding while LH2 hydroxylates prolyl residue in the C-telopeptide region. Calcium flux kinetic, which is indirectly controlled by TRIC channel, also affects functioning of multiple proteins involved in collagen synthesis and assembly. Secreted procollagen molecules are targeted by ADAMTS and BMP1 metalloproteases, resulting in the cleavage of N- and C-propeptides. Mature collagen will finally assemble into fibrils, that in bone will undergo mineralization (from Kang, Aryal et al. 2017).

Bone fragility OI-like syndromes

Recently, mutations in new genes associated to skeletal phenotypes have been discovered, suggesting the possibility to extend the OI classification.

Mutations in *PLS3* cause a bone fragility syndrome with either OI or early-onset osteoporosis features. *PLS3* is located on the X-chromosome (Xq23) and encodes plastin 3 protein (also known as Plastin T), an ubiquitous cytoskeletal protein involved in the formation of F-actin bundles and expressed in osteoblasts, osteocytes and osteoclasts (Fahiminiya et al. 2014).

In osteoclasts *PLS3* interacts in the cytosol with the NF- κ B repressing factor (NKRF), favouring its translocation into the nucleus. Here NKRF inhibits the transcription of Nuclear Factor of Activated T-cells Cytoplasmic 1 (NFATC1), a key regulator for osteoclastogenesis, thus supporting *PLS3* role in bone homeostasis. Patients with mutations in *PLS3* are characterized by reduced bone mineral density, vertebral compression and long bone fractures, but they have a normal collagen type I structure and synthesis (Balasubramanian et al. 2018; Costantini et al. 2018).

FAM46A belongs to the nucleotidyltransferases (NTase) fold superfamily, it is located on chromosome 6 and encodes a soluble protein, whose function is not yet known (Kuchta et al. 2016). Homozygous c.612_613 duplication in *FAM46A* gene, that causes a premature stop codon (p.Ser205Tyrfs*13) and subsequently the lack of the protein, was identified in a subject with clinical features that resemble the severe OI forms, now named OI type XVIII. This patient shows frequent fractures, bowing of long bones, wormian bones, blue sclerae and joint laxity (Doyard et al. 2018).

A mouse model, carrying a c.469G>T (p.Glu157*) mutation located in the highly conserved DUF1693 domain of *FAM46A* has been generated (Diener et al. 2016). Mutations in this domain are related to bone fragility in humans (Kuchta et al. 2016). Mutant mice have growth delay, multiple bone deformities and fractures, minimal trabecular bone and reduced cortical thickness (Lagali et al. 2002; Diener et al. 2016).

In addition, a functional proteomic study identified *FAM46A* as a binding partner for the TGF β effector SMADs (Colland et al. 2004), known to have a critical role in bone development and homeostasis (Wu, Chen, and Li 2016).

A loss of-function mutation (c.2T>C) in *CCDC134* gene is responsible for a new severe autosomal recessive form of OI. *CCDC134*, a coiled-coil domain containing protein 134, encodes a secreted protein that inhibits the phosphorylation of mitogen-activated protein kinase (MAPKs), such as extracellular signal-regulated kinase (ERK) or cJun N-terminal kinase (JNK) (Huang et al. 2008).

Both ERK and JNK are involved in bone remodelling by regulating osteoblasts and osteocytes responses to stress. Indeed, ERK is involved in the mechanical stress activation of osteoblasts (Katz, Boland, and Santillán 2006), whereas JNK in osteocyte apoptosis response to oxidative stress (Fontani et al. 2015).

A reduced expression of *COL1A1* and *OPN* (Osteopontin) was observed in patient' osteoblasts, as well as a mineralization defect, thus suggesting that the impairment of Erk1/2 phosphorylation is associated to an altered osteoblast function. *CCDC134* deficient patients are characterized by gracile and bowed long bones, pseudarthroses and pre- and postnatal growth retardation (Dubail et al. 2020).

Homozygous or frameshift mutations in Mesoderm Development LRP Chaperone (*MESD*) cause a new autosomal recessive progressively deforming type of OI (OI type XX). *MESD* encodes for an endoplasmic reticulum chaperone that binds the canonical Wntless-related integration site (WNT) signalling receptors LRP5 and LRP6. In absence of *MESD*, the LRP5 and LRP6 receptor cannot traffic to the cell surface causing a defect in WNT signalling (Hsieh et al. 2003).

In Moosa *et al.* five different individuals with homozygous mutations in the third and final exon of *MESD* were reported. These mutations are located downstream of the chaperone domain and upstream of the ER-retention domain, thus reducing the chaperoning role of the protein (Moosa et al. 2019).

Patients show general osteopenia, skeletal deformity, healed and newly acquired fractures. Disorganized dentition and/or oligodontia are sometimes present.

The relation between MESD mutations and OI could be supported by the well-known role of canonical WNT signaling pathway in skeletal development (Keupp et al. 2013; Hill et al. 2005; Gong et al. 2001). In addition, loss of function mutations in LRP5 are causative of Osteoporosis-Pseudoglioma syndrome and autosomal dominant juvenile osteoporosis and loss of function mutations in *WNT1* have been found in individual with autosomal recessive OI and early-onset dominant osteoporosis (Fahiminiya et al. 2014; Laine et al. 2013).

Table 1. Osteogenesis imperfecta forms. Modified from (Marini, Forlino et al. 2017)

Gene	Encoded protein	OI type	Inheritance	Clinical characteristics
<i>Impairment of collagen synthesis and structure</i>				
<i>COL1A1</i> or <i>COL1A2</i>	Collagen α 1 or collagen α 2 chain	I, II, III or IV	AD	Mild to very severe bone deformity; normal, grey to dark blue sclerae; absent to common hearing loss and dentinogenesis imperfecta.
<i>Compromised bone mineralization</i>				
<i>IFTM5</i>	Bone-restricted interferon-induced transmembrane protein-like protein (BRIL; also known as IFTM5)	V	AD	Normal to-severe skeletal deformity, intraosseous membrane ossifications, radiodense band and radial head dislocation, normal to blue sclerae and sometimes hearing loss
<i>SERPINF1</i>	Pigment epithelium-derived factor (PEDF)	VI	AR	Moderate to severe skeletal deformity, presence of osteoid, fish-scale appearance of lamellar bone pattern and childhood onset
<i>Abnormal collagen post translational modification</i>				
<i>CRTAP</i>	Cartilage associated protein (CRTAP)	VII	AR	Rhizomelia, bone fracture, reduced mineral density, popcorn calcification at the epiphyses, growth retardation and normal sclerae
<i>P3H1</i>	Prolyl 3-hydroxylase 1 (P3H1)	VIII	AR	
<i>PP1B</i>	Peptidyl-prolyl <i>cis-trans</i> isomerase B (CyPB)	IX	AR	Severe bone deformity with grey sclerae

<i>Compromised collagen processing and crosslinking</i>				
<i>SERPINH1</i>	Heat shock protein 47 kDa (HSP47)	X	AR	Severe skeletal deformity, blue sclerae, dentinogenesis imperfecta, skin abnormalities and inguinal hernia
<i>FKBP10</i>	65 kDa FK506-binding protein (FKBP65)	XI	AR	Mild to severe skeletal deformity, normal to grey sclerae and congenital contractures
<i>PLOD2</i>	Lysyl hydroxylase 2 (LH2)	No type	AR	Moderate to severe skeletal deformity and progressive joint contractures
<i>BMP1</i>	Bone morphogenic protein 1 (BMP1)	XIII	AR	Mild to severe skeletal deformity and umbilical hernia
<i>Altered osteoblast differentiation and function</i>				
<i>SP7</i>	Transcription factor SP7 (osterix)	XII	AR	Severe skeletal deformity with delayed tooth eruption and facial hypoplasia
<i>TMEM38B</i>	Trimeric intracellular cation channel B (TRIC-B)	XIV	AR	Moderate to severe bone deformity with normal-to-blue sclerae
<i>WNT1</i>	Proto-oncogene Wnt-1 (WNT1)	XV	AR	Severe skeletal abnormalities, white sclerae and possible neurological defects
<i>CREBL1</i>	Old astrocyte specifically induced substance (OASIS)	XVI	AR	Severe bone deformity
<i>SPARC</i>	Osteonectin (SPARC)	XVII	AR	Progressive severe bone fragility, mild joint hyperlaxity and scoliosis
<i>MBTPS2</i>	Membrane-bound transcription factor site-2 protease (S2P)	XIX	XR	Moderate to severe skeletal deformity, light blue sclerae, scoliosis and pectoral deformity
<i>New OI form</i>				
<i>FAM46A</i>	FAM46A protein	XVIII	AR	Frequent fractures, bowing of long bones, wormian bones, blue sclerae and joint hyperlaxity.
<i>MESD</i>	LRP chaperone (MESD)	XX	AR	Osteopenia, skeletal deformity, healed and newly acquired fractures, disorganized dentition and/or oligodontia

<i>Unclassified OI forms</i>				
<i>PLS3</i>	Plastin 3 (PLS3)	Unclassified	XR	Reduced bone mineral density, vertebral compression and long bone fractures
<i>CCDC134</i>	Coiled-coil domain-containing protein 134 (CCDC134)	Unclassified	AR	Gracile and bowed long bones, pseudarthroses, pre- and postnatal growth retardation

TRIC-B role in the pathophysiology of OI type XIV

TRICs channels

The trimeric cation channels, TRICs, are responsible for the transport of K^+ ions across the endoplasmic or sarcoplasmic reticulum (ER or SR) membranes.

The mammalian family of TRICs is composed by TRIC-A and TRIC-B subtypes, which are encoded by two different genes: *TMEM38A* and *TMEM38B*. TRIC-A couples with ryanodine receptors (RyRs) to mediate Ca^{2+} release in excitable cells, especially within striated muscle cells and brain (Yazawa et al. 2007), while TRIC-B synchronizes with inositol trisphosphate receptors (IP₃Rs) to mediate Ca^{2+} release in all cell types (Zhou et al. 2014).

Due to the high percentage of identity among vertebrates, a TRICs subtypes conformational model can be represented by the crystal structure of *Gallus gallus* GgTRIC-A and *Xenopus laevis* XITRIC-B, respectively (Wang et al. 2019).

They are both symmetric trimers of 7 transmembrane (TM) subunits and each protomer is composed of inverted quasi-repeats of triple-helix bundles (THBs) plus an additional transmembrane domain 7 (TM₇). While TM₁₋₃ and TM₄₋₆ domains are similar, the TM₇ stands on the lateral side of the trimer, making contact with the pre-TM helix, TM₀ (**Figure 4**). Each protomer has a N-terminal end located in the ER/SR lumen, a C-terminal end in the cytoplasm (**Figure 4**) and a central hourglass-shaped pore, characterized by hydrophobic and positive highly conserved residues that crosses the ER/SR membrane (Wang et al. 2019). The positively charged KEV motif, highly conserved among species and required for pore formation, confers the sensitivity to voltage at the TM₄ helix allowing the regulation of the channel activity (Wang et al. 2019).

Interestingly, it was recently discovered that high concentrations of Ca^{2+} inhibit channel activity and vice versa. Indeed, Ca^{2+} binding causes a rotameric shift in the channel conformation stabilizing the interactions between TM₂ and TM₄. This stabilization extends through the lengths of these helices with consequent strengthening of the interactions that lead to the blockage of the pore and preventing the passage of the potassium ion (Wang et al. 2019).

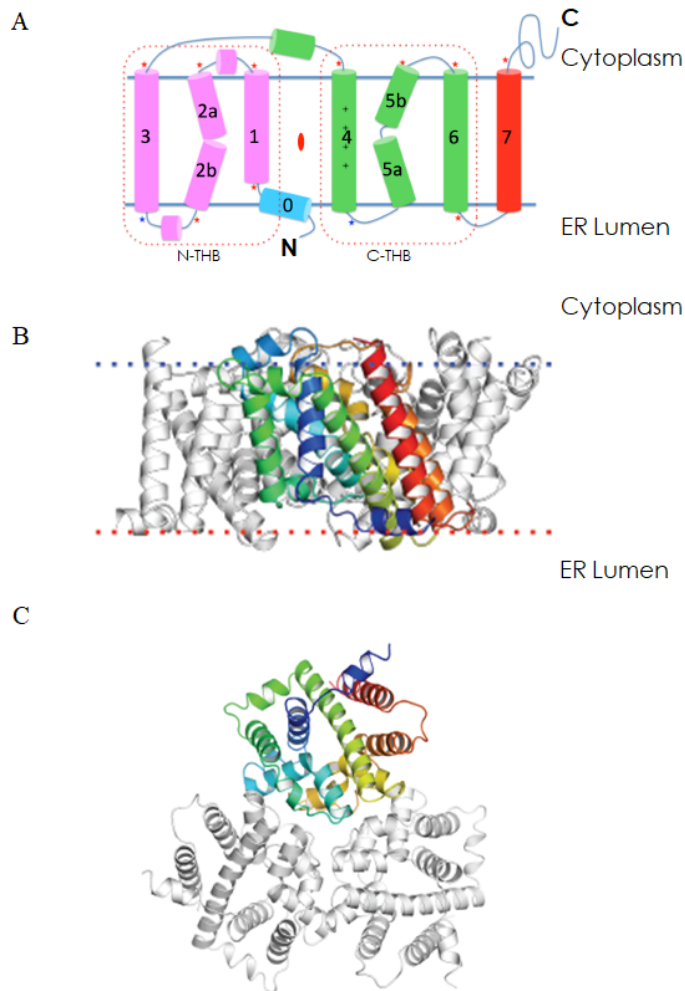


Figure 4. Structure of TRIC-B channel. **A.** Membrane topology diagram for TRIC channels. TM₁₋₃ constitutes N-triple-helix bundles (N-THB), and TM₄₋₆ constitutes C-triple-helix bundles (C-THB), coloured in purple and green, respectively. The additional TM₀ is in light-blue and TM₇ is in red. **B.** Ribbon drawing of the TRIC trimer, as viewed from the membrane, and from the intracellular side. **C.** One protomer is coloured spectrally from dark blue at its N-terminus to red at its C-terminus (from Wang et al. 2019).

Altered calcium homeostasis in OI type XIV

Calcium homeostasis has an important effect on several cell functions, such as secretion, contraction–relaxation, motility, metabolism, protein synthesis, modification and folding, gene expression, cell-cycle progression and apoptosis (Corbett and Michalak 2000). A relevant role of calcium in modulating the activity of chaperones and enzymes involved in collagen type I synthesis, such as the Lysyl Hydroxylase 1 (LH1), which is required for its lysine hydroxylation, was reported (Michalak et al. 2009).

In addition, collagen type I has a Ca^{2+} binding site at the C-terminal domain, necessary for interchain hydrogen, disulfide bonds stabilization and for the correct procollagen trimerization and folding (Bourhis et al. 2012; Cabral et al. 2016).

For these reasons, the impairment in calcium homeostasis was hypothesized to be responsible for collagen type I related diseases, such as osteogenesis imperfecta (Cabral et al. 2016).

The intracellular calcium homeostasis is regulated by continuous flow through the endoplasmic reticulum (ER) or sarcoplasmic reticulum (SR) membrane, the main stores of intracellular calcium, and the cytoplasm. The intracellular calcium bidirectional flux involves specific receptors on the ER membrane. The inositol-1,4,5-triphosphate (IP_3R) receptor and the ryanodine receptor (RyRs) mediate the ER Ca^{2+} release following concentration gradient toward the cytoplasm, while the ATPase (SERCA) channel allows active Ca^{2+} recycle back to the ER (Corbett and Michalak 2000).

Ca^{2+} flux is also regulated by opposite K^+ or Na^+ currents, which can cross the ER membrane throughout specific channels. Among them, TRICs act as K^+ counter-ion channels balancing the charge potential during Ca^{2+} release/uptake from the ER/SR lumen (Yamazaki et al. 2009; Pitt et al. 2010; Venturi et al. 2013).

An impairment in RyR- and IP_3R - mediated Ca^{2+} release was observed in Tric-a and Tric-b knock-out mouse models, respectively, thus indicating a shared role in calcium signalling. In addition, Tric-a knock-out mice exhibit reduced or irregular muscle contractile responses and develop hypertension (Yamazaki et al. 2011; Tao et al. 2013; Zhao et al. 2010). On the other hand, Tric-b knock-out mice are subjected to pulmonary dysfunction and they die immediately after birth due to an insufficient surfactant production at the level of alveoli

(Yamazaki et al. 2009). Additional post mortem analysis showed skeletal tissue abnormalities in *Tric-b* knock-out mice, such as reduced body size and an impaired ossification associated with insufficient collagen matrix production (Zhao et al. 2016).

The skeletal phenotype of the murine model is somehow in line with what observed in patients with loss of function mutations in *TMEM38B*, which are affected by a recessive form of osteogenesis imperfecta, referred in OMIM as OI type XIV (**Table 2**). This OI form is not lethal, likely being *TRIC-B* not essential for surfactant production in human pneumocytes. OI type XIV patients are characterized by a high degree of phenotypical variability with mild bone deformities, low bone mass, mild recurrent fractures, growth retardation and short stature (Lv et al. 2016). Dentinogenesis imperfecta, grey-blue sclerae, hearing loss and development of scoliosis have extremely variable incidence (Webb et al. 2017), while the cardiac abnormalities and muscular hypotonia are poorly observed.

The absence of *TRIC-B* causes in patients' cells an alteration of the ER Ca^{2+} homeostasis, as demonstrated by the decrease of both cytoplasmic $[\text{Ca}^{2+}]$ and IP_3R -mediated Ca^{2+} flux in Ca^{2+} free media obtained from proband primary fibroblasts and osteoblasts. These findings validated the role of *TRIC-B* in maintaining intracellular Ca^{2+} levels (Cabral et al. 2016). Disruption of ER-calcium flux kinetics in *TMEM38B*-null cells is associated with altered activity of several collagen modifying enzymes and chaperones, resulting in abnormal folding and post translational modifications of collagen type I (Cabral et al. 2016).

OI is often characterized by excessive post translational modification and intracellular collagen type I retention in the ER (Besio et al. 2018; Besio et al. 2019). On the contrary, OI type XIV patients present an under-modified collagen type I, likely due to a 20-30% decrease in hydroxylysines content (Cabral et al. 2016). The reduced lysine hydroxylation and thus the consequent lower level of glycosylation, could be due to an impairment of *LH1* activity. Furthermore, *LH1* works in complex with *CyPB*, which modulates the collagen type I cross-linking by differentially affecting lysine hydroxylation in a site-specific manner (Ishikawa et al. 2012). Interestingly, even if *LH1* patients' levels are normal, an impaired protein activity could compromise its interaction with *CyPB*, which was demonstrated being Ca^{2+} mediated (Cabral et al. 2016).

In addition, a delayed procollagen chain assembly was found in OI type XIV patients' cells, since an impaired Ca^{2+} flux kinetics seems affect the activity of PDI, which normally is implicated in procollagen folding, in intra and interchain disulphide bonds formation on procollagen molecules and in stabilizing procollagen structure (Koivu 1987). To regulate the altered Ca^{2+} homeostasis PDI can be sequestered by calreticulin, thus compromising its role in collagen folding (Cabral et al. 2016). The resulting under-modified collagen type I is then susceptible to cell retention and proteasomal degradation (Cabral et al. 2016).

Recently, it has been proved that the accumulation of mutant proteins in the ER plays an important role in modulating the severity of phenotype in several diseases including skeletal collagen-related disorders (Boot-Handford and Briggs 2010; Gawron 2016). The collagen type I intracellular retention and consequent ER stress activation were described as key players in modulating the phenotype of dominant and recessive forms of OI (Besio et al. 2018; Besio et al. 2019).

In *Tricb*^{-/-} osteoblasts it was shown that the intracellular collagen retention induces ER stress, as demonstrated by the enlarged ER cisternae (Zhao et al. 2016).

Moreover, in OI type XIV patients the activation of the unfolded protein response (UPR) was detected and an increased expression of ATF4, the transcription factor activated by the PERK pathway, was observed (Liang et al. 2006).

Contrarily to classical OI forms, characterized by high bone turnover, with lower matrix production, resulting in a typical hypermineralized matrix, in TRIC-B deficient bone the number of osteoblasts, as well as the mineral apposition rate, are low to normal. OI type XIV patients are also characterized by low bone volume and low bone turnover that allow bone packets to mineralize longer (Roschger et al. 2014).

OI type XIV patients are characterized by a reduced osteoblasts number, as consequence of a lower expression of the early osteoblastogenic markers *RUNX2* and *SP7*. Moreover, the reduced *COL1A1* expression suggested an impairment in collagen synthesis (Cabral et al. 2016).

Although bone tissue mineralization appears normal in OI type XIV patients, the expression of ALP (Alkaline Phosphatase), a marker of mature osteoblasts, as well as Osteocalcin (*BGLAP*) and Osteopontin (*OPN*), which inhibit crystal growth, are increased (Fujisawa and

Tamura 2012; de Bruyn et al. 2013). Moreover, the expression of *SOST*, encoding for sclerostin, expressed by osteocytes and important to inhibit osteoblastic bone formation (Lewiecki 2014), is delayed, suggesting an impairment in osteocyte differentiation and in bone remodelling.

Interestingly, a reduced expression of the osteoclast markers *Cathepsin K (Ctsk)* and *Atp6vd02* gene, was observed in *Tricb^{-/-}* mice, thus confirming that an impaired Ca^{2+} flux leads to a reduction in osteoclasts number (OCs) and in bone resorption (Webb et al. 2017).

Table 2. *TMEM38B* mutations found in OI type XIV patients.

Position in the gene	Mutations		References
	DNA	Protein	
Exon 4	c.455_542del	p.Gly152Alafs*5	(Shaheen et al. 2012)
Intron 3	g.32476_53457delins ATTAAGGTATA	p.Gly152Alafs*5	(Volodarsky et al. 2013; Cabral et al. 2016; Caparros-Martin et al. 2017)
Exon 1-2	chr9: g.105,682,311__ 105,716,202del	-	(Rubinato et al. 2014; Cabral et al. 2016)
Intron 3	c.455-7 T>G	p.Arg151_Gly152insValLeu	(Lv et al. 2016)
Exon 4	c.507 G>A	p.Trp169*	(Lv et al. 2016; Cabral et al. 2016; Webb et al. 2017; Caparros-Martin et al. 2017)
Exon 1	c.63dupT	p.Asp22*	(Webb et al. 2017; Cabral et al. 2016)

TMEM38B sequence: ENSG00000095209, TRIC protein: Q9NVV0.

CRISPR/Cas system

In the last decades, several gene modification approaches, such as physical, chemical and transposon-mediated insertional mutagenesis have been tested in order to study the phenotypic and genetic correlation in a certain pathological condition (Lawson and Wolfe 2011). Nevertheless, these techniques were not sequence specific. In the 1970s, the endogenous mechanisms of DNA double strand break repair (DSB) was discovered and methods for generating precise breaks at specific DNA sites have been introduced as a valuable strategy for targeted genomic engineering.

In this scenario, one of the most successful genome editing tool was represented by the Clustered Regularly Interspaced Short Palindromic Repeats (CRISPR/Cas) system.

CRISPR/Cas is a bacterial and archaea adaptive immune system used to protect against foreign RNA or DNA, such as viruses or plasmids (Khadempour et al. 2019). The bacterial CRISPR locus is characterized by a DNA repeated sequence (21 to 48 bp in length) that includes 26 to 72 bp foreign nucleic acids sequence (Godde and Bickerton 2006). In the bacterial genome there are also loci containing genes encoding for Cas protein, the nucleases required to cleave the foreign nucleic acids (van der Ploeg 2009).

The CRISPR/Cas immune defence process is composed by three steps: adaptation, expression and interference.

During adaptation the foreign DNA sequence, called protospacer, is recognized and integrated in the CRISPR locus by different enzymes, such as Cas1, Cas2 and Cas3. Each integration event generates a new spacer motif and the duplication of the repeat unit (Barrangou et al. 2007; Garneau et al. 2010). The recognition of exogenous nucleic acids and the selection of spacer precursors are guaranteed by the presence of short conserved regions (2 to 5 nt long) called protospacer adjacent motives (PAMs).

The second step is characterized by the expression of pre CRISPR RNA (pre-crRNA) which are then cleaved by endonucleases complexes into small mature non-coding CRISPR RNAs (crRNAs). crRNAs generally contain a single spacer and a partial repeat that allow the formation of hairpin structures. The mature crRNAs are associated with specific Cas proteins in a complex called CASCADE (CRISPR-associated complex for antiviral defence) (Makarova et al. 2011). Finally, during the interference the CASCADE complex plays an

important role in specific base pairing recognition of the target, thanks to the crRNAs that works as guide for protospacer recognition and cleavage (Brouns et al. 2008).

CRISPR/Cas systems have been classified into three distinct types (I, II, and III) based on the Cas proteins involved.

Type I CRISPR/Cas system is characterized by the presence of a large multidomain protein, Cas3, with distinct DNA helicase and nuclease activity (Sinkunas et al. 2011). The crRNA is processed by Cas6 (a subunit of the CASCADE complex) and the interference process is mediated by both Cas3 and CASCADE (Makarova et al. 2011).

Type II CRISPR/Cas system is characterized by a single multifunctional protein, Cas9, which drives the processing of pre crRNA and the degradation of phage and plasmid DNA (Garneau et al. 2010). Moreover, in type II systems an additional trans activating crRNA (tracrRNA) is transcribed from the CRISPR locus. The tracrRNA is complementary to the precrRNA so they first hybridize and then hybrids are digested by the RNase III (Jinek et al. 2012). The α -helical domain of Cas9 recognizes and binds crRNA:tracrRNA duplexes, while its nuclease domains, RuvC and HNH, recognize PAM sequences and catalyse exogenous DNA cleavage (Nishimasu et al. 2014).

Type III CRISPR/Cas systems use Cas6 to process the crRNA (Bhaya, Davison, and Barrangou 2011). The interference is mediated by two different protein complexes, Csm and Cmr, composed by both Cas proteins and Repeat Associated Mysterious Proteins (RAMP). They resemble the type I CASCADE complex and they can selectively recognize exogenous DNA (Csm) or RNA (Cmr) (Burmistrz and Pyré 2015).

In 2012 Jinek and colleagues engineered the CRISPR/Cas type II system by creating a single strand RNA guide which contains all the essential components of crRNA and tracrRNA, necessary to guide Cas9 at the cleavage site (Jinek et al. 2012). The most used targeted endonuclease exploited for genome editing is the bacterial Cas 9 enzyme, which is extracted from *Streptococcus Pyogenes* (Deveau et al. 2008).

The guide RNA is composed by a 20-nucleotide sequence complementary to the target DNA at the 5' end, while the 3' terminal comprises a stem loop structure required for Cas9 binding. The recognition of the target DNA by Cas9 is allowed thanks to the presence of the PAM

motif. Since PAM sequence is usually NGG, it limits the availability of Cas9 target sites in the human genome to an average of one target site every eight base pairs (Hsu, Lander, and Zhang 2014). Therefore, directed evolution approaches generated variants with altered PAM specificities (Kleinstiver et al. 2015).

Once the guide RNA pairs with the target sequence, the HNH and RuvC nuclease domains of Cas9 cleave both target DNA strands (Jinek et al. 2012).

Nuclease-induced DNA DSBs can be repaired by one of the two major mechanisms that occur in all cell types and organisms: nonhomologous end-joining (NHEJ) and homology-directed repair (HDR). The NHEJ repair mechanism results in the small insertions or deletions (*indels*) at the site of the break. This is the efficient mechanism that leads to the generation of knock-out (KO) models. On the other hand, the HDR repair mechanism facilitates precise copying of the template at a specific site of the genome, leading to a creation of knock-in (KI) models (Gupta and Shukla 2017).

Recently, the CRISPR/Cas9 system has been successfully used to generate both *in vitro* and *in vivo* models for several diseases. Model organisms are an indispensable tool to better understand disease pathophysiology and to develop novel therapies.

Therefore, my PhD project has been focused on the generation and further characterization of both an *in vitro* and an *in vivo* models for OI type XIV, using CRISPR/Cas9 system, in order to better elucidate the role of TRIC-B in the pathophysiology of osteogenesis imperfecta.

Chapter I
Generation and characterization of OI type XIV
in vitro model

Introduction

Osteoblastic cell lines

In vitro cultures represent one of the most consolidated models to study cell behaviour in normal or pathological conditions, independently from the external context, which can be the tissue, organ or the entire organism. Nevertheless, the absence of biokinetics may cause a misinterpretation of data, thus leading to retain *in vivo* models necessary to fill this gap (Saeidnia, Manayi, and Abdollahi 2015).

However, *in vivo* studies are usually preceded by or combined with less ethically demanding *in vitro* studies, in order to obtain a first overview on the topic, thus reducing direct side effects on animals or humans. In the bone field, several osteoblastic cell lines have been developed in order to elucidate molecular mechanisms of skeletal diseases (Czekanska et al. 2012).

Among the available osteoblastic cell lines, primary human osteoblasts can be used both preclinically and clinically and avoiding interspecies differences. However, these cells represent a heterogeneous population and therefore present phenotypic differences related to the skeletal position from which they were isolated (Kasperk et al. 1995; Martínez et al. 1999). In addition, the extraction from long bones, jaw and iliac crest is difficult and painful (Czekanska et al. 2012).

To overcome these limits, *in vitro* models usually applied in bone research are the immortalized osteoblasts, which do not need isolation from fresh biopsy, are easy to maintain and are characterized by relative phenotypic stability (Grigoriadis et al. 1985; Leis et al. 1997).

The immortalization of cells could be achieved by different approaches, including ectopic expression of telomerase or telomerase reverse transcriptase (TERT), by mutating the tumor protein (*P53*) and retinoblastoma (*RB*) genes, or introducing the oncogenes (Maqsood et al. 2013). Moreover, immortalized cells can be obtained through malignant bone or bone marrow tumors, even if increasing the risk of altering molecular and cellular phenotypes (Hicok et al. 1998).

The first part of my PhD has been focused on the generation and validation of OI type XIV *in vitro* model by using the human foetal osteoblasts hFOB1.19 immortalized cell line. This commercially available cell line was conditionally immortalized by transfection with a gene coding for a temperature-sensitive mutant (*tsA58*) of SV40 large T antigen (T Ag) and a gene coding for neomycin (G418) resistance. The T antigen expression in human cells and its subsequent interaction with the *RB* gene lead to an increased cell proliferation (Chou 1989; Ludlow et al. 1989).

At 34 °C, when SV40 is active, the hFOB line promotes proliferation and reduces differentiation. At 39.5 °C, when SV40 is no longer active, cell proliferation is reduced and osteoblastic differentiation is induced (Hicok et al. 1998). In this way, osteoblast differentiation can be easily studied by changing temperature, without the need for other differentiation factors.

A primary characterization of hFOB1.19 line was performed on individual neomycin resistant colonies. Clones with high alkaline phosphatase (ALP) levels were further analysed to evaluate the expression of phenotypic markers of osteoblasts, such as osteopontin, osteonectin, osteocalcin, bone sialoprotein and collagen type I. All of these markers were highly expressed in post confluent hFOB cells, indicating that at this step the cells differentiate towards mature osteoblasts.

Furthermore, hFOB cells in postconfluent cultures formed mineralized nodules, a typical feature of the late stage osteoblasts (Harris et al. 1995).

Therefore, hFOBs relatively undifferentiated cells programmed to differentiate in osteoblasts upon reaching confluence, and provide a good model system for studying osteoblast differentiation in both normal and pathological conditions (Harris et al. 1995).

Materials and methods

Human foetal osteoblast cell line

The immortalized human foetal osteoblast (hFOB) 1.19 (ATCC) cell line was used to generate the *TMEM38B* knock-out model. Cells were grown at 34 °C in humidified atmosphere containing 5% CO₂ in Dulbecco's Modified Eagle's Medium/Nutrient Mixture F-12 Ham (DMEM:F12) containing 2.5 mM L-glutamine and 15 mM 2-[4-(2-hydroxyethyl)piperazin-1-yl]ethanesulfonic acid (HEPES) (Sigma 2906) and added with 1.2 g/L NaHCO₃, 10% bovine serum (Euroclone) and 0.3 mg/ml geneticin (G418).

For the differentiation experiments, cells were kept in DMEM media (Euroclone) added with 100 nM dexamethasone (Sigma D-4902), 50 µg/ml ascorbic acid 2-phosphate (Fluka 49752) and 10 mM beta-glycerophosphate (Sigma G-9891). The cells were maintained in this medium at 37 °C for 4, 8, 12 or 15 days (based on the type of experiment).

Knock-out in vitro model generation

The knock-out *in vitro* model was generated by CRISPR/Cas9 gene editing. The target sequences in human *TMEM38B* were selected using the online available softwares CHOP CHOP and CRISPRscan. Three RNA guides (gRNA) were selected, one on exon 2 (gRNA2) and two on exon 3 (gRNA3.1 and gRNA3.2). They were synthesized by annealing the two synthetic oligonucleotides shown in **Table 1**. The two complementary oligonucleotides were mixed in equimolar quantity (100 µM), and annealed with the following cycle: 3 min at 95 °C followed by 1 min at 25 °C.

Table 1. Target sequence and oligonucleotides used for the synthesis of the gRNAs. The PAM (NGG) sequence is underlined; the nucleotides inserted to ensure the cloning into the plasmids are in red. In bold, the G inserted, when necessary, to start the sequence of the gRNAs with a G, as required by the U6 RNA polymerase.

Gene	Exon	Target sequence	Synthetic oligonucleotides
<i>TMEM38B</i> (<i>gRNA2</i>)	2	5'-GCTATGCTCCACTGTTTTGG <u>TGG</u> -3' (nt 16120-16142)	5'- CACCG GCTATGCTCCACTGTTTTGG-3'
			5'- AAAC CCAAAACAGTGGAGCATAGC-3'
<i>TMEM38B</i> (<i>gRNA3.1</i>)	3	5'-AGAACTTGGAAAATAGT <u>AGG</u> -3' (nt 32107-32126)	5'- CACCG GAACTTGGAAAATAGTAGG-3'
			5'- AAAC CTACTATTTTCCAAGTCC-3'
<i>TMEM38B</i> (<i>gRNA3.2</i>)	3	5'- <u>TGG</u> ATAGTCATGATAGCTAT-3' (nt 32165-32186)	5'- CACCG GGGATAGTCATGATAGCTAT-3'
			5'- AAAC ATAGCTATCATGACTATCCC-3'

TMEM38B genomic sequence NG_032971.1, chromosome 9

The expression plasmid pSpCas9(BB)-2A-PURO (Addgene PX459), which contains the Cas9 sequence under control of β -actin promoter, was linearized with BbsI enzyme (new England Biolabs). Linearized plasmid was purified with Nucleospin Gel and PCR Clean-up kit (Machinery-Nagel) and the ligation with double strand fragment of RNA guide was performed using T4 DNA ligase (Thermo Scientific) o/n at room temperature (RT). Transformation of competent DH5 α cells was performed using 0.1 μ g of pSpCas9(BB)-2A-PURO ligation. A colony PCR screening was performed using one primer on the plasmid and the other on the insert, in order to verify its presence (**Table 2**). The thermal cycle comprised 10 min at 95 °C, 3 min at 95 °C, 40 cycles of 1 min at 95 °C, 1 min at 64 °C, 1 min at 72 °C, and 10 min of elongation at 72 °C.

Table 2. Primers used for colony PCR.

Plasmid-guide	Primer localization	Primer sequence
pSpCas9(BB)-2A-PURO-gRNA2	Insert	5'-CACCGCTATGCTCCACTGTTTTGG-3'
	Plasmid	5'-CCATTTGTCTGCAGAATTGGCGCAC-3'
pSpCas9(BB)-2A-PURO-gRNA3.1	Insert	5'-CACCGGAACTTGGAAAATAGTAGG-3'
	Plasmid	5'-CCATTTGTCTGCAGAATTGGCGCAC-3'
pSpCas9(BB)-2A-PURO-gRNA3.2	Insert	5'-AAACATAGCTATCATGACTATCCC-3'
	Plasmid	5'-CCATTTGTCTGCAGAATTGGCGCAC-3'

To further confirm the presence of the insert, samples were sequenced (GATC Biotech AG). To obtain the gRNA, the construct was first linearized using BamHI (Promega) and purified with Nucleospin Gel and PCR Clean-up Kit (Machinery-Nagel). Then, *in vitro* transcription was performed using the MEGAscript T7 Kit (Invitrogen). After DNA digestion with Turbo DNA-free Kit (Ambion), the gRNA was purified using mirVana miRNA Isolation Kit (Invitrogen) and its quality and size were checked by electrophoresis on 10% (v/v) polyacrylamide-urea-SDS gel.

hFOB 1.19 transfection

For hFOB 1.19 cells transfection 1×10^6 cells/well were plated into 6 well/plate and cultured for 24 hours in DMEM:F12 media. The transfection with pSpCas9(BB)-2A-PURO, pSpCas9(BB)-2A-PURO-gRNA2, pSpCas9(BB)-2A-PURO-gRNA3.1 and pSpCas9(BB)-2A-PURO-gRNA3.2 was performed using LTX DNA transfection reagent (Invitrogen 15338-100) following manufacturer's indication. 0.5 μ g of plasmid was used for each well. Selection of transfected cells was carried out by adding puromycin (2 μ g/ml) to the media for 48 hours. The DNA was extracted, and the target efficiency was evaluated using T7 endonuclease assay or by digestion with different specific restriction enzymes. To obtain the single clonal lines transfected cells were plated in 96 well plate at 2-8 cells/well density.

The not transfected hFOB cells were used as control for all experiments.

DNA extraction and genotyping

For DNA extraction from clone, cells were incubated with 500 μ L of lysis buffer (100 mM Tris HCl pH 8.5, 5 mM EDTA, 0.2% SDS (w/v), 200 mM NaCl) added with 12 μ L of 15 mg/mL proteinase K (Sigma Aldrich) and incubated at 37 °C overnight. The DNA was precipitated with equal volume of isopropanol and then centrifuged at 14000 g for 30 minutes. Following an 70% ethanol wash, the pellet was resuspended in Tris-EDTA (20 mM Tris-HCl, 1 mM EDTA pH 8.0).

The genotype was determined through amplification of human *TMEM38B* sequence (NC_000009) using specific primer (**Table 3**).

Table 3. Sense and reverse primers used for clone genotyping

Gene	Primers for genotyping		Amplicon (bp)
<i>TMEM38B</i> (Exon 2)	Sense	5'- ACTTTACCATTTTCAGGAGCAGC-3' (16058-16079 nt)	200 bp
	Reverse	5'-TCACATAGGTCACCATACTGGC-3' (16237-16258 nt)	
<i>TMEM38B</i> (Exon 3)	Sense	5'-TGTGTTTTGCCAAATTGTTGTT-3' (31917-31938 nt)	428 bp
	Reverse	5'-CAGCCAACAGAAACAAGGTTTT-3' (32323-32344 nt)	

The PCR cycle included 3 min denaturation at 94 °C, followed by 40 cycles at 94 °C for 30 seconds, 30 seconds at specific annealing temperature (64 °C for exon 2 and 54 °C for exon 3), 1 min at 72 °C and ended with 10 min at 72 °C. The amplicon was checked through electrophoresis on 1% (w/v) agarose gel in TAE buffer (40 mM TRIS-HCl, 1 mM EDTA, 20 mM CH₃COOH, pH 8.2).

T7 endonuclease assay

10 µL of amplified DNA were denatured and renatured following this cycle: 5 min at 94 °C, then decrease to 85 °C at -0.2 °C/sec and at the end from 85 °C to 25 °C at -0.1 °C/sec. After this cycle, the samples were digested by T7 endonuclease I (0.2U/µL) at 37 °C for 1 hour. Reaction products were then checked on 8% (v/v) polyacrylamide gel.

Restriction enzymes

In order to genotype the clonal lines specific restriction enzymes were used after PCR amplification of the targeting region. The selected enzymes were able to cut only the WT sequence (**Table 4**). The digestion products were checked on 8% (v/v) polyacrylamide gel.

Table 4. Restriction enzymes used for clone genotyping

Gene	Restriction enzymes	Restriction site	Fragment length
<i>TMEM38B</i> exon 2	BstXI	CCANNNNN/NTGG	WT: 78 bp and 122 bp Mutant clone: 200 bp
	XcmI	CCANNNNN/NNNTGG	
<i>TMEM38B</i> exon 3	BspHI	T/CATGA	WT: 262 bp and 166 bp Mutant clone: 428 bp
	BclI	CCATCNNNN/	

TA cloning

In order to determine the specific mutations of the clonal lines generated by CRISPR/Cas9 gene editing, the TOPO TA cloning kit (Invitrogen) was used following manufacturer's recommendation. The PCR amplicons of target sequence were gel purified with Nucleospin Gel and PCR Clean-up kit and cloned in pCR II-TOPO vector. Then the *E. Coli* DH5 α cells were transformed with the vector containing the PCR amplicon. The plasmid DNA was extracted from single colony using EuroGOLD Plasmid Miniprep I kit (Euroclone) and the specific region was sequenced (GATC Biotech AG).

Protein lysates

Cells were plated in 6 well/plate or 25 cm² flask in DMEM:F12 media at 34 °C. Following phosphate buffered saline (PBS) (Sigma-Aldrich) wash, cells were lysed and sonicated in RIPA buffer (150 mM NaCl, 1% IGEPALR CA-630, 0.5% sodiumdeoxycholate, 0.1% SDS, and 50 mM Tris, pH 8) supplemented with protease inhibitors (13 mM benzamidine, 2 mM N-ethylmaleimide, 5 mM ethylenediaminetetraacetic acid, 1 mM phenylmethylsulfonyl fluoride and 2 mM NaVO₃).

Proteins were quantified by RC DC Protein Assay (Bio- Rad). Bovine serum albumin (BSA) (Sigma-Aldrich) was used as standard.

Western blot

Proteins extracted from WT and mutant clones were separated on 12% (v/v) SDS-PAGE acrylamide and the gel was electrotransferred to a PVDF membrane (GE Healthcare) at 100 V for 2 h in 19 mM Tris-HCl, 192 mM glycine and 20% (v/v) methanol. Membranes were then blocked with 5% (w/v) milk in TBS-Tween (20 mM Tris-HCl, 500 mM NaCl, pH 7.5 (TBS), 0.05% (v/v) Tween-20 (Sigma-Aldrich)) at RT for 1 h. After washing with TBS-T, they were incubated with 1:500 primary antibody against TRIC-B (Invitrogen) in 2.5% milk in TBS-T o/n at 4 °C. The anti-rabbit secondary antibody (Cell Signaling) was added (1:10000 in 2% milk in TBS-T) for 1 h at RT. The signal was detected by ECL western blotting detection reagents (GE Healthcare) and images were acquired with Image Quant LAS 4000 (GE Healthcare).

Calcium analysis

The calcium flux was evaluated in WT and mutant clones with FURA-2 dye using a fluorescence microscope. 2×10^5 cells were plated on cover slip (9 mm diameter) (Marienfeld, 0111520) in a 6 well plate. The cells were incubated with 4 mM FURA-2AM in 150 mM NaCl, 6 mM KCl, 1.5 mM CaCl₂, 1 mM MgCl₂, 10 mM glucose and 10 mM Hepes (PSS) for 20 min at 37 °C in the dark. Cells were washed in PSS solution and analysed with a fluorescence microscope with Zeiss Achroplan 40X lens.

The cells were excited at 340 and 380 nm and the light emitted was revealed at 510 nm. The calibration of intracellular calcium was done using Grynkiewicz (Grynkiewicz, Poenie, and Tsien 1985). The UTP (100 µM) was added for 5 minutes, in absence of external calcium, to stimulate calcium release from ER through the IP₃R channel.

Collagen analysis

Labelling of collagen with L-[2,3,4,5-³H]-proline (PerkinElmer) was used to evaluate collagen overmodification in WT and mutant clones. A total of 2.5×10^4 cells was plated in 6-well plates and grown for 24 h. Cells were then incubated for 2 h with serum-free DMEM containing 4 mM glutamine, 100 µg/ml penicillin and streptomycin, and 100 µg/ml (+)-sodium L-ascorbate (Sigma-Aldrich) to stimulate collagen production. The labelling was performed for 18 h in the same media using 28.57 µCi of 3H-Pro/ml. Protease inhibitors (1.52 mg/mL EDTA, 1.57 mg/mL benzamidine, 0.25 mg/mL N-ethylmaleimide) were added to both media and cell layer fractions and 20 µg of bovine collagen was used as carrier for the collagen precipitation.

The collagen was precipitated with half volume of 96% ethanol for 1 hour at 4 °C and centrifuge at 13000 g for 20 minutes. The supernatant was discarded, and pellet was resuspended in 0.5 M acetic acid. Subsequently, samples were digested o/n with 100 ng/ml of pepsin in 0.5 M acetic acid at 4 °C. Collagen was then precipitated using 2 M NaCl, 0.5 M acetic acid. Collagen was resuspended in Laemmli buffer (62 mM Tris-HCl pH 6.8, 10% glycerol, 2% sodium dodecyl sulfate, 0.02% bromophenol blue) and the radioactivity [counts per minute (CPM)] was measured using a liquid scintillation analyzer (PerkinElmer TRI-CARB 2300 TR).

Equal amounts of ^3H -labeled collagen from WT and mutant clones were loaded on 6% urea-SDS gels in a non-reducing condition. The gels were fixed in 45% methanol, 10% glacial acetic acid, incubated for 1 h with enhancer (PerkinElmer, 6NE9701), washed in deionized water and dried. ^3H gel radiographs were obtained by direct exposure of dried gels to hyperfilm (Amersham) at $-80\text{ }^\circ\text{C}$. The radiography films were digitalized by VersaDoc 3000 (Bio-Rad).

Cell proliferation

The solution Cell Titer 96 AQueous Cell proliferation Assay that contains MTS [3-(4,5-dimethylthiazol-2-yl)-5-(3-carboxymethoxyphenyl)-2-(4-sulfophenyl)-2H-tetrazolium salt] was used to perform the proliferation assay. To this purpose 5×10^3 cells were plated in 96 well/plate in complete DMEM:F12 medium at $34\text{ }^\circ\text{C}$ and $37\text{ }^\circ\text{C}$. After 24, 48, 72 e 96 hours of culture the medium was replaced with $100\text{ }\mu\text{L}$ of fresh medium. After 1 hour the MTS reagent was added and incubated at $34\text{ }^\circ\text{C}$ and $37\text{ }^\circ\text{C}$ for 4 hours. The absorbance was measured at 490 nm with a plate reader Clario star (BMG labtech). Technical triplicates were performed for all clones. The values were normalized to day 1 of proliferation and then to the control cells.

Alkaline Phosphatase assay

The commercial kit for Alkaline phosphatase (Abnova KA1642) was used to analyse the activity of this marker in WT and mutant clone at 0, 4, 8, 12 and 15 days of differentiation, following the manufacturer's recommendation. Briefly, 2×10^5 cells were plated in 33 mm petri dish in DMEM media. The day after, the differentiation factors (100 nM dexamethasone, $50\text{ }\mu\text{g/ml}$ ascorbic acid 2-phosphate and 10 mM beta-glycerophosphate) were added to the media and the cells were moved to the $37\text{ }^\circ\text{C}$ incubator. At 0, 4, 8, 12 and 15 days of differentiation the cell layer was washed with PBS, then 0.2% Triton-X-100 was added to lysate the cells. The lysate was collected and quantified with Quantum Protein kit (Euro Clone). The absorbance (405 nm) was measured using Clario star reader and the results were normalized to day 0.

RNA extraction

RNA was extracted from cells at different differentiation time: 0, 4, 8, 12 and 15 days. 2×10^5 cells were plated in 35 mm petri dish in DMEM complete media at 34 °C. The day after, the differentiation factors (100 nM dexamethasone, 50 µg/ml ascorbic acid 2-phosphate and 10 mM beta-glycerophosphate) were added to the media and the cells were moved to 37 °C. After 0, 4, 8, 12 and 15 days of differentiation, the media was discarded, and the cells were lysed in 1 ml QIAzol Lysis Reagent (QIAGEN) and RNA was extracted following manufacturer's recommendation. Genomic DNA was removed upon treatment with Turbo DNA Free Kit (Ambion). Finally, RNA concentration was evaluated by measuring the absorbance at 260 nm using Nanodrop (Cellbio ND-1000), while its quality was check by electrophoresis on 1% (w/v) agarose gel in TBE in Diethyl pyrocarbonate (DEPC) water.

Real time qPCR

The High Capacity cDNA Reverse Transcription kit (Applied Biosystems) was used to retrotranscribe 500 ng of RNA in 20 µL final volume. qPCR was performed in triplicate in a 25 µL final volume using Taqman Universal PCR Master mix (Applied Biosystems) and commercial TaqMan probes: Hs01047973_m1, *RUNX2*; Hs01866874_s1, *OSTERIX/SP7*; Hs01587814_g1, *BGLAP*; Hs00164004_m1, *COL1A1*, Hs99999905_m1, *GAPDH* which was used as a housekeeping gene. qPCR was performed using a Mx3000P (Stratagene) thermocycler following this programme: 10 min at 95 °C for Taq enzyme activation, 40 cycles at 95 °C for 15 sec for denaturation and 1 min at 60 °C for the annealing and extension reaction. The relative expression level of each gene was calculated using the $\Delta\Delta C_t$ method.

Cell mineralization

2×10^4 cells were plated in 24 well/plate in DMEM:F12 media and grew at 34 °C. Two days after the media was changed and substituted with DMEM supplemented with differentiation factors (100 nM dexamethasone, 50 µg/ml ascorbic acid 2-phosphate and 10 mmol/L beta-glycerophosphate). The media was changed every two days for 15 days. After 15 days of differentiation, cells were fixed in 10% (v/v) formaldehyde (Sigma–Aldrich) at RT for 30 min. Cells were then washed with dH₂O and stained with 58 mM alizarin red s (Sigma) pH 4.1-4.3 for 45 min at RT in the dark. For quantification 200 µL of 10% (v/v) acetic acid

were added to each well, and the plate was incubated at room temperature for 30 min with shaking. Cells were scraped and transferred to a 1.5-mL tube. After vortexing for 30 s, the sample was heated at 85 °C for 10 min, incubated on ice for 5 min, centrifuged at 20000g for 15 min and 200 µL of the supernatant were moved in a new tube. Then 75 µL of 10% (v/v) ammonium hydroxide was added to neutralize the acid. Aliquots of the supernatant were read at 405 nm using the UVIDEC-340 double beam spectrophotometer (Jasco).

Statistical analysis

All values were expressed as mean \pm standard deviation (SD) or standard error (ER). Technical triplicates were performed for all experiments, except for ALP and alizarin red staining assay where technical duplicates were performed. Statistical comparisons were based on Student's T-test considering statistically significant a p value < 0.05 .

Results

Generation of OI type XIV *in vitro* model

CRISPR Cas9 genome editing was used to generate OI type XIV model in immortalized hFOB1.19 cell line (ATCC). By CHOPCHOP and CRISPRscan software three RNA guides (gRNAs) were selected on *TMEM38B* gene, one on exon 2 (gRNA2) and two on exon 3 (gRNA3.1 and gRNA3.2) (**Table 1**). Each guide was subcloned in the pSpCas9(BB)-2A-PURO plasmid and constructs were transfected in hFOB (**Figure 1A**). The targeting efficiency was evaluated by T7 endonuclease I (T7EI) assay. Briefly, the DNA was extracted from transfected and untransfected control cells and amplified using specific primers flanking the guide targeting locus. After denaturation and renaturation, the amplicon underwent T7 endonuclease I digestion, which cuts only heteroduplex generated in presence of mismatches caused by Cas9 cleavage followed by non-homologous end joining (NHEJ) repair system activation. The presence of the amplicon digested bands, proving the successful targeting, was obtained with two of the three guides, gRNA2 and gRNA3.2, which were chosen for further experiments (**Figure 1B**).

Serial dilutions of the cells transfected with gRNA2 or gRNA3.2 separately or with a mix of the two guides were performed to obtain single clonal lines. The DNA from expanded single clonal lines was extracted and the presence of successful targeting evaluated both by T7 endonuclease I assay and by restriction nuclease digestion using enzymes expected to only cut WT DNA. Based on CHOPCHOP suggestion, BstXI and XcmI enzymes were selected for mutation in exon 2 while BspHI and BccI were chosen for mutations in exon 3. DNA digestion with the selected restriction enzymes allowed to distinguish whether the different clonal lines had none, one or two targeted alleles (**Figure 1C-D**).

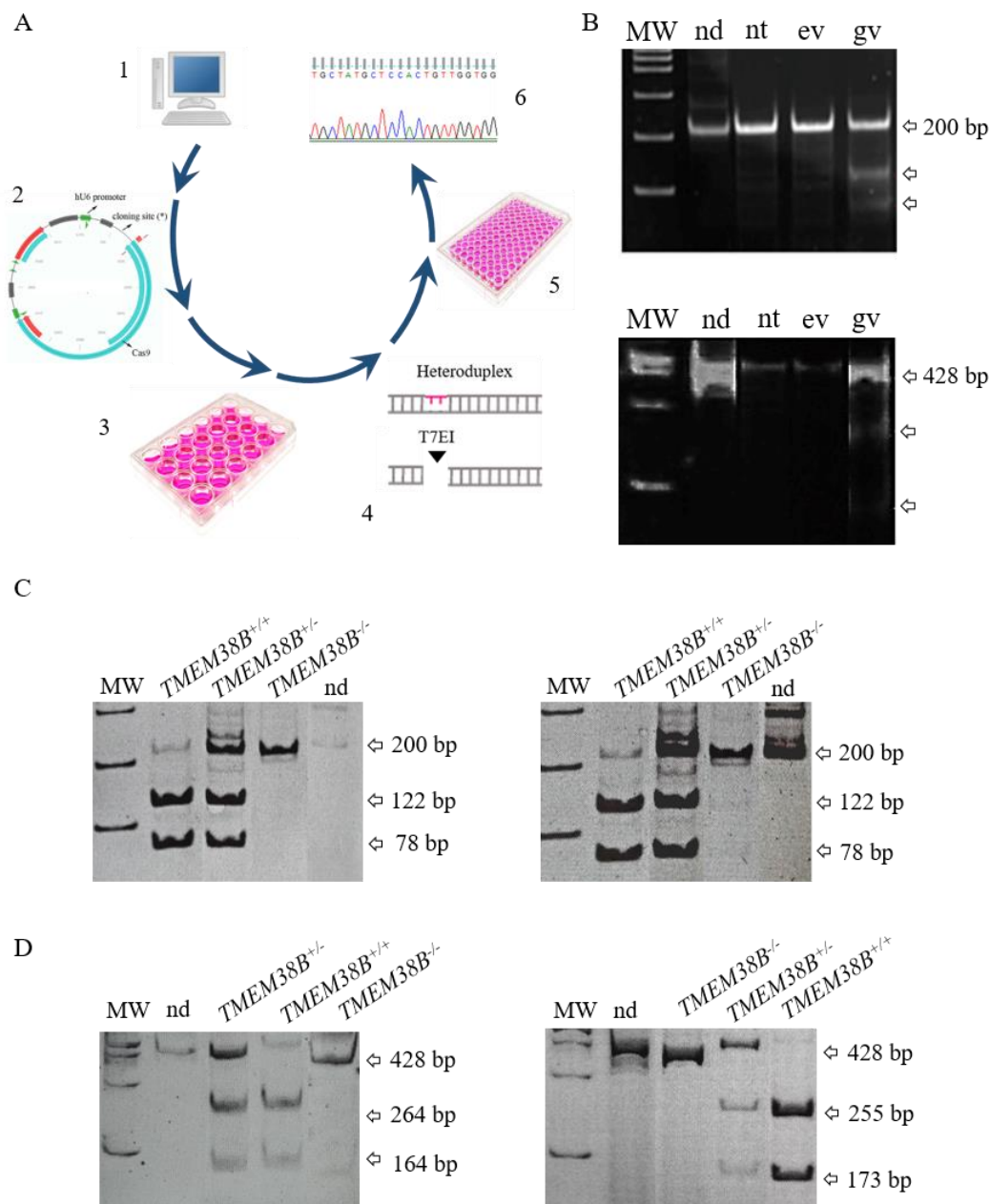


Figure 1. OI type XIV *in vitro* model generation. **A.** Strategy used to generate *in vitro* *TMEM38B* models by CRISPR/Cas9 genome editing. *In silico* target sequence identification (1), cloning of gRNA in the eukaryotic expressing vector (2), hFOB cells transfection (3), evaluation of targeting efficiency by T7 endonuclease I assay (4), single cell clonal lines obtained by serial dilution of the transfected cells (5) and clones genotyping by sequencing (6) are the foreseen necessary steps. **B.** Screening of hFOB using T7 endonuclease assay. Representative gel indicating in targeted cells the presence of the amplicon fragments after T7 endonuclease digestion. **C.** Mutant clonal lines screening using the restriction enzymes BstXI (left) and XcmI (right) that specifically recognize the wild type sequence. Representative gel images indicating the expected bands after restriction enzyme digestion of amplicon obtained from gRNA2 transfected clones. **D.** Mutant clonal lines screening using the

restriction enzymes BclI (left) and BspHI (right) that specifically recognize the wild type sequence. Representative gel images indicating the expected bands after restriction enzyme digestion of amplicon obtained from gRNA3.2 transfected clones. Arrows indicate the bands upon enzyme cleavage. MW: molecular weight; nd: not digested amplicon, nt: digested amplicon from not transfected cells, ev: digested amplicon from cells transfected with empty vector; gv: digested amplicon from cells transfected with gRNA containing construct.

The DNA extracted from 14 clonal lines was sequenced around the targeting region to identify the specific mutations introduced by genome editing. In the majority of cases mutations were small insertions or deletions (*indels*), resulting in frameshifts responsible for premature stop codon formation at the protein level (**Table 5, 6 and 7**). As expected, based on the activation of the endogenous NHEJ repair, different mutations were detected in different clones, some in homozygosity, some in heterozygosity or compound heterozygosity. Interestingly, in some clones more than two different mutations were identified.

Table 5. Mutations identified in gRNA2 transfected clones.

Clone	Digestion		DNA mutations	Protein mutations
	BstXI	XcmI		
A3	Not digested	Not digested	c.176_177ins132	p.F59L; p.F59_G60ins44
			c.173_176delGTTT	<i>p.C58Lfs*72</i>
			c.174delT	<i>p.F59Lfs*73</i>
A4	Digested	Digested		
A6	Not digested	Not digested	c.171_181del11ins636	<i>p.H57Efs*113</i>
			c.174delT	<i>p.F59Lfs*73</i>
			c.171_187del17	<i>p.C58Ffs*75</i>
A7	Not digested	Not digested	c.176_177insG	<i>p.F59Lfs*81</i>
			c.174delT	<i>p.F59Lfs*73</i>
A12	Not digested	Not digested	c.176_177ins219	<i>p.F59Lfs*61</i>
			c.180_196del17insG>A	<i>p.G61Sfs*75</i>
			c.174_175delTT	<i>p.F59Wfs*80</i>
A13	50% Digested	50% Digested	Ns	Ns
A17	Not digested	Not digested	c.177_178ins228	p.F59_G60ins76
			c.177_182delTGGTGG	p.F59_G60del; p.G61L
			c.173_188del16	<i>p.F59Yfs*68</i>

Ns: Not sequenced

Table 6. Mutations identified in gRNA 3.2 transfected clones.

Clone	Digestion		DNA mutations	Protein mutations
	BspHI	BccI		
B11	50% Digested	50% Digested	c.414_454del41	<i>p.N139Cfs*147</i>
			c.399_449del51	p.N134_A159del
			c.426_454del29	<i>p.I142Mfs*151</i>
B14	50% Digested	50% Digested	c.435_437delAGC	p.A146del
			c.426_437del12	p.V143_A144del
B17	50% Digested	50% Digested	c.431_434delTGAT	<i>p.M144Kfs*156</i>
			c.427_447del21insG>A	p.V143_W149del; p.A150T
			c.435_441del7	<i>p.I145Mfs*155</i>
B19	50% Digested	50% Digested	c.432_438del7	<i>p.M144Ifs*155</i>
			c.438_443delTATTGG	p.I147_G148del
			c.433_437delATAGC	<i>p.I145Yfs*159</i>
			c.437_438insT	<i>p.I147Yfs*162</i>
B28	Digested	Digested	Ns	Ns

Ns: Not sequenced

Table 7. Mutations identified in gRNA 2 and gRNA 3.2 transfected clones.

Clone	Digestion		DNA mutations	Protein mutations
	BstXI/XcmI	BspHI/BccI		
C5	Not digested/Not digested	50% Digested/Nd	gRNA 2	
			c.172_182delTGGTGG	p.F59_G60del;p.G61L
			c.177delT	p.F59Lfs*73
			c.159_209del51	p.A54_A70del
			gRNA3.2	
			c.408_444del38	<i>p.Y136Lfs*148</i>
			c.437_443del7	<i>p.A146Dfs*155</i>
			c.436_446del9	p.A146_G148del
			c.429_438del10	<i>p.M144Lfs*154</i>
			c.432_437delGATAGC	p.M144_I145del; p.A146I
C10	Not digested/Not digested	Nd/Not digested	gRNA2	
			c.177delT	<i>p.F59Lfs*73</i>
			gRNA 3.2	
			c.439_440delATins3549	<i>p.I147Afs*156</i>
			c.438_443delTATTGG	p.I147_G148del

Ns: Not sequenced; Nd: not determined.

To confirm the successful generation of *TMEM38B* knock-out (KO) clones, the absence of protein expression was assessed by western blotting using a specific antibody against human TRIC-B (**Figure 2**). Some of the mutant clones lacking TRIC-B were selected for further characterization.

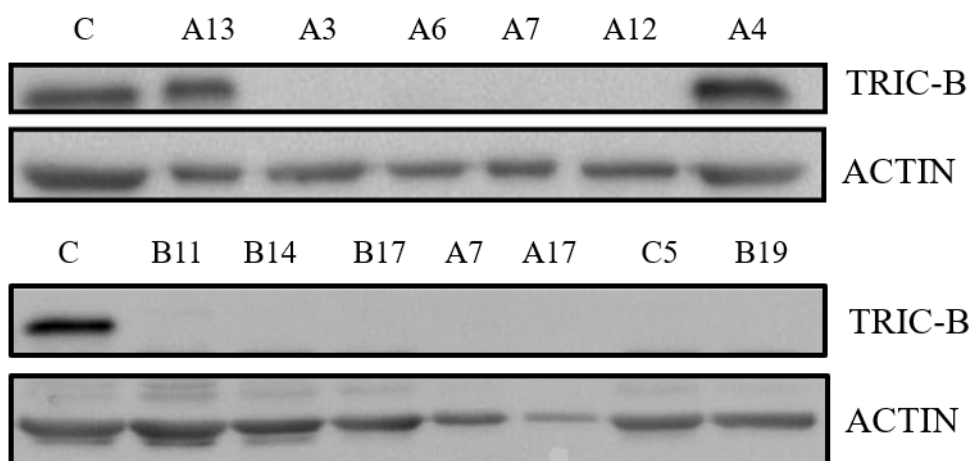


Figure 2. Western blot to confirm the absence of TRIC-B in mutant clones. The absence of protein expression is evident in mutant clones obtained from gRNA2 transfection: A6, A7, A12, A4, A17; from gRNA3.2 transfection: B19; and from transfection with both guides: C5. Clone identified as WT (A4) or heterozygous (A13) from restriction enzyme digestion analysis expressed the protein similarly to not-transfected control cells (C).

Impaired calcium flux in TMEM38B KO cells

In OI type XIV patients' cells the absence of the endoplasmic reticulum (ER) potassium channel TRIC-B is associated to an impaired ER Ca²⁺ release, due to the lack of the K⁺ counter-flux necessary to prevent ER membrane polarization (Cabral et al. 2016).

In order to validate the *TMEM38B* KO clones as *in vitro* model for OI type XIV, the Ca²⁺-sensitive fluorophore FURA-2 was used. Resting [Ca²⁺]_i was significantly decreased in A3, A6 and A12 KO clones with respect to control cells (**Figure 3A**). TRIC-B has been shown to regulate ER Ca²⁺ mobilization through IP₃Rs (Cabral et al. 2016; Zhao et al. 2016), which are the main ER Ca²⁺ releasing channels in non-excitable cells (Berridge, Bootman, and Roderick 2003). Preliminary experiments confirmed that endogenous Ca²⁺ release induced by the IP₃-producing autacoid UTP (100 μM) was abrogated by depletion of the ER Ca²⁺ store with cyclopiazonic acid (CPA; 20 μM) (**Supplementary Figure 1A**) and by blocking IP₃Rs with 2-aminoethoxydiphenyl borate (2-APB; 50 μM) (**Supplementary Figure 1B**) (Lodola et al. 2017; Cabral et al. 2016). When the IP₃Rs-mediated release of Ca²⁺ stores was stimulated with UTP (100 μM), release of Ca²⁺ from the ER was significantly reduced in *TMEM38B* KO clones compared to control cells, confirming in mutant clones the impairment of Ca²⁺ flux from the ER (**Figure 3B**).

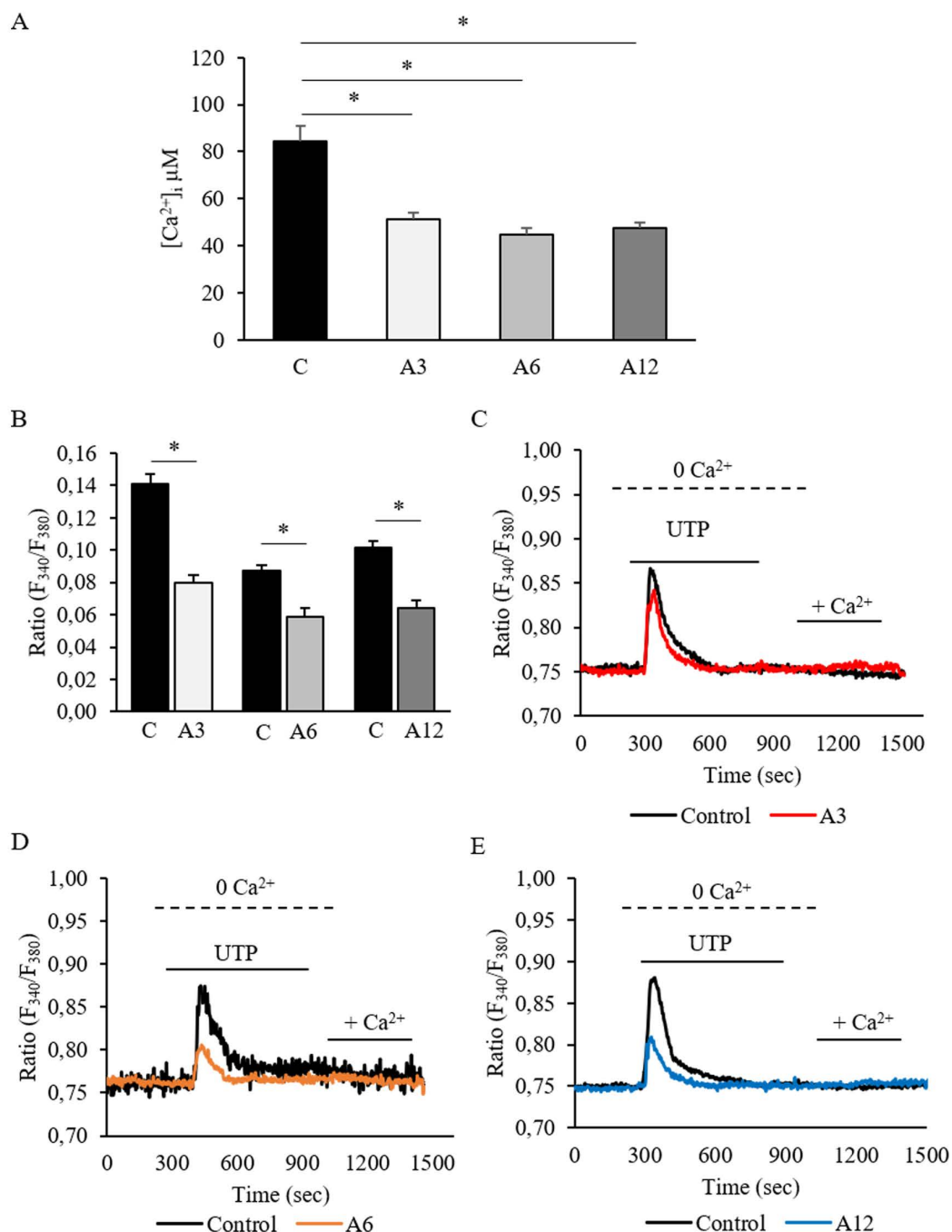


Figure 3. Intracellular Ca^{2+} concentration and ER calcium flux. **A.** Resting $[Ca^{2+}]_i$ was reduced in KO clones (A3, A6 and A12) with respect to control cells. **B.** UTP (100 μ M) was used to stimulate the IP_3R channel in the absence of extracellular Ca^{2+} ($0Ca^{2+}$). The calcium flux through IP_3R is significantly less in mutant cells (A3, A6 and A12) compared to control cells. The values were expressed as mean \pm standard error (ER). **C-D-E.** Traces of ER calcium release in A3, A6 and A12 compared to control cells. The re-addition of extracellular Ca^{2+} after recovery of the intracellular Ca^{2+} transient did not result in a detectable increase in $[Ca^{2+}]_i$, which suggests that store-operated Ca^{2+} entry is not operative in the hFOB1.19 cell line ($*P < 0.05$).

Reduced collagen type I post translational modification in TMEM38B KO cells

Collagen obtained from OI type XIV patients' fibroblasts and osteoblasts has been previously proved to show a faster electrophoretic mobility explained by a reduction of triple helical lysine hydroxylation, likely affecting the glycosylation level (Cabral et al. 2016). Interestingly, ^3H -proline labelled collagen type I, extracted from medium and cell layer fractions from KO clones, showed a SDS-PAGE faster migration respect to control (**Figure 4**). Surprisingly, the collagen electrophoretic pattern was not comparable for all tested clones. In the KO clones A3, A6 and C5 collagen α bands migrate faster than not transfected control cells, but in A12 the $\alpha 2(\text{I})$ was missing.

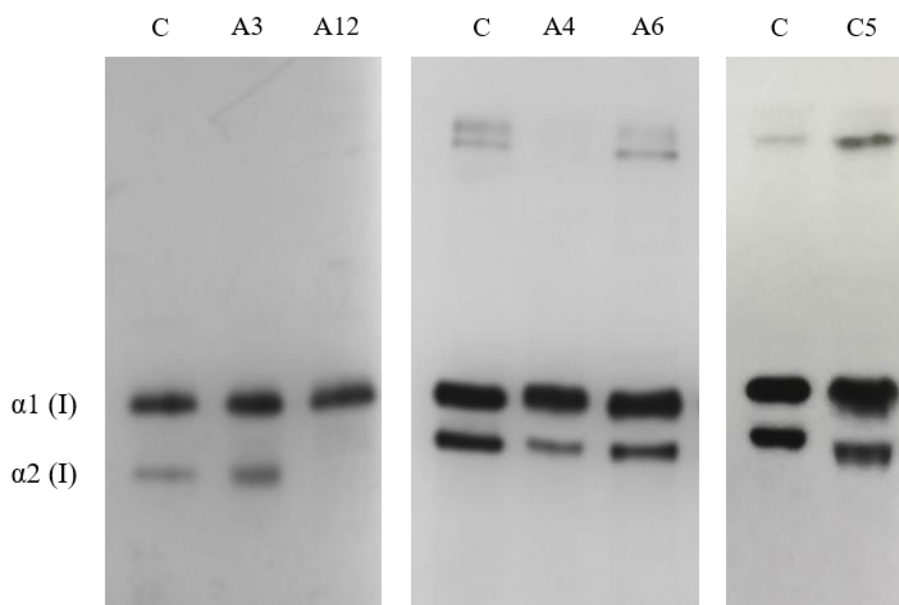


Figure 4. Collagen type I analysis. Representative image of SDS-PAGE analysis of ^3H -collagen type I extracted from media of control hFOB cells (C), KO clones (A3, A12, A6 and C5) and a WT clone (A4). Collagen type I α bands show a faster electrophoretic migration compared to control and WT clone.

Delay in TMEM38B KO cells differentiation

Impaired expression of early and late osteoblastic genes was reported in human OI type XIV osteoblasts (Webb et al. 2017). Both early and late osteoblastogenic markers expression was analysed after 0, 4, 8, 12 and 15 days of culture in differentiation medium of control and A3 and B17 *TMEM38B* KO clones. The early differentiation markers (*RUNX2*, *SP7*) and *COL1A1* were significantly reduced at all time points in A3 with respect to control, as in patients' osteoblasts (**Figure 5A-B-C**). The expression of the late marker *BGLAP* was also reduced resembling what previously reported for human cells and KO mice bone (Webb et al. 2017; Zhao et al. 2016). On the contrary, in B17 KO clone the expression of *RUNX2* was significantly higher with respect to control cells at day 0 and 4 of differentiation, while was significantly reduced starting from day 8 (**Figure 5E**). The expression of all the other markers was higher in B17 with respect to control cells (**Figure 5F-G-H**).

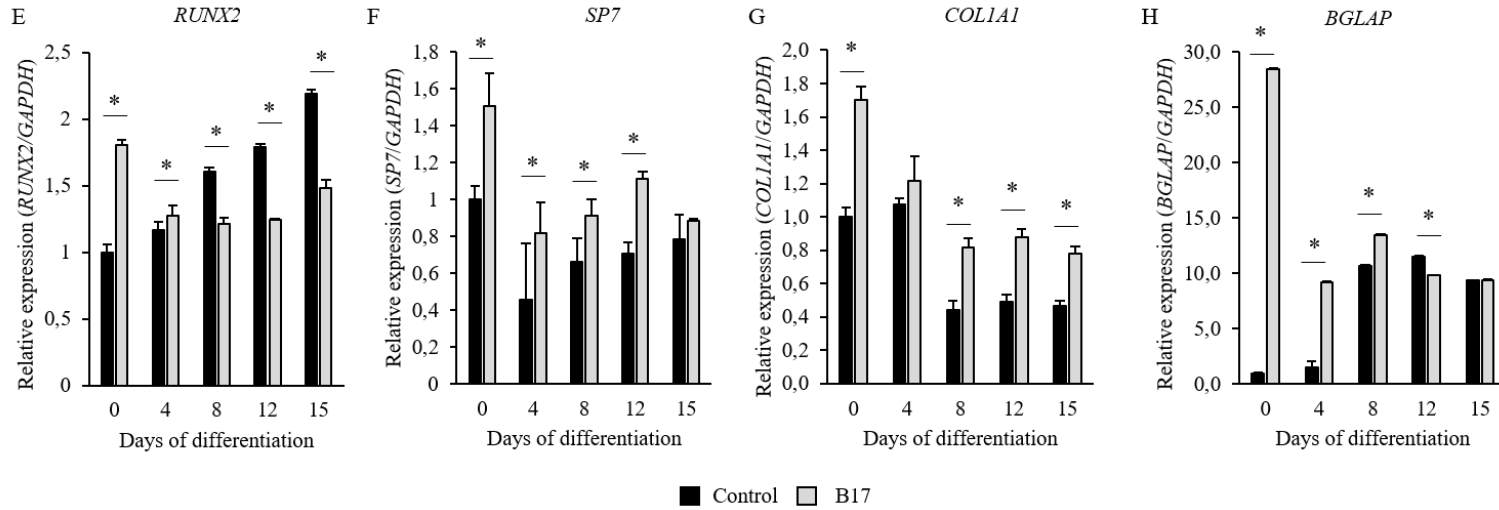
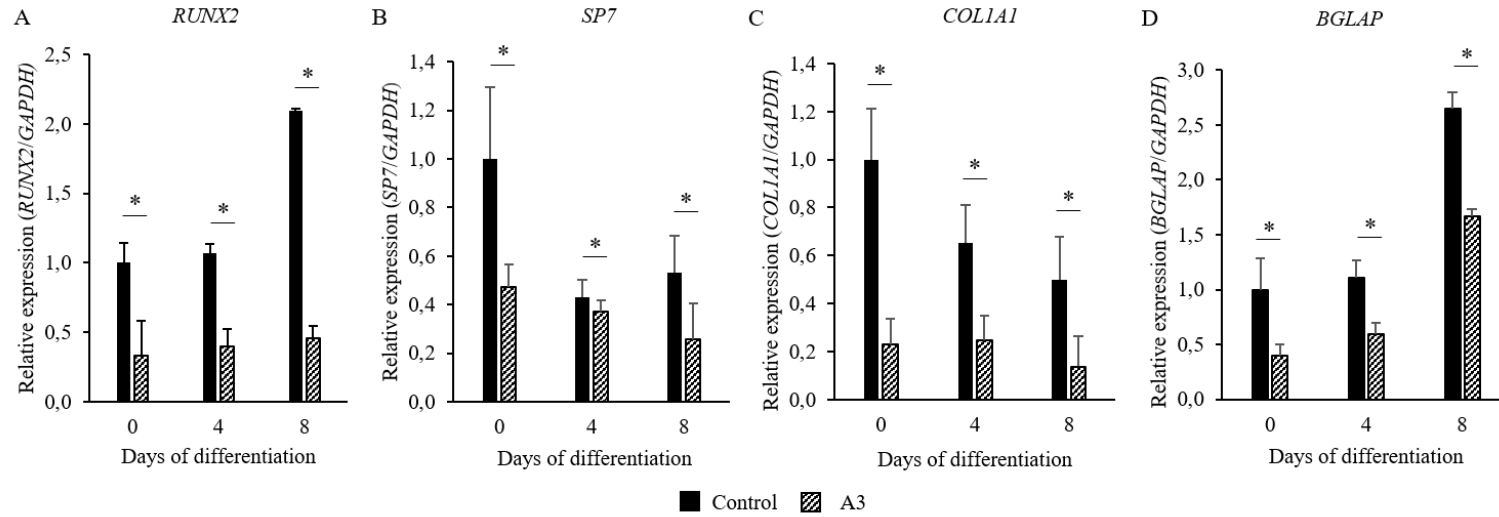


Figure 5. Early and late osteoblastogenic markers expression analysis of WT and KO mutant clones. In A3 mutant clone *RUNX2* (A), *SP7* (B) *COL1A1* (C) and *BGLAP* (D) expression were reduced with respect to control cells. In B17 clone *RUNX2* expression (E) was reduced starting from day 8 of differentiation; on the contrary *SP7* expression (F) was increased compared to control. In B17 *COL1A1* (G) and *BGLAP* (H) expression was increased for the first 8 days of differentiation compared to control at all time points (*P<0.05).

Reduced alkaline phosphatase activity in TMEM38B KO cells

To evaluate mineralization, the alkaline phosphatase (ALP) activity was measured in cell lysates of KO clones and control cells, cultured at 37 °C in differentiation media. The enzymatic activity was tested at 0, 4, 8, 12 and 15 days of culture. The KO mutant clones showed a reduced ALP activity with respect to control cells supporting an impairment in mineralization (**Figure 6**).

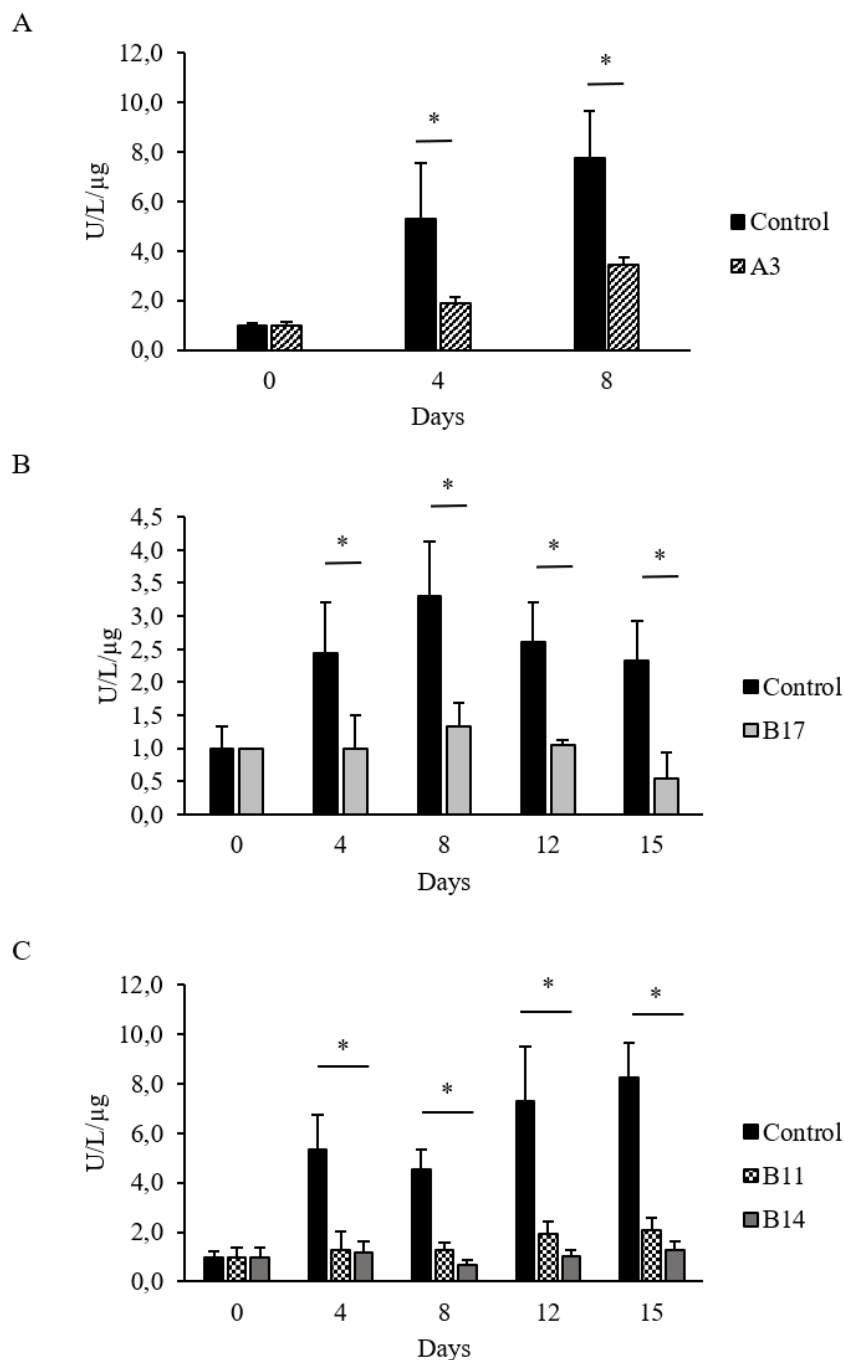


Figure 6. Alkaline phosphatase (ALP) activity analysis. **A.** The activity of ALP was significantly reduced in A3 mutant clone compared to WT at 4 and 8 days of differentiation. **B.** The activity of ALP was significantly reduced in B17 mutant clone compared to WT at 4, 8, 12 and 15 days of differentiation. **C.** The activity of ALP was significantly reduced in B11 and B14 mutant clones compared to WT at 4, 8, 12 and 15 days of differentiation. All data were normalized on day 0 (KO clone: A3, B11, B14, B17) (* $P < 0.05$).

Delay in TMEM38B KO cells mineralization

The delay in matrix mineralization was further confirmed in A3 *TMEM38B* KO clone, following 15 days of *in vitro* culture in mineralized medium, by quantitation of alizarin red S (ARS) staining.

Even if the amount of minerals increased during differentiation in both control and mutants, KO cells revealed a significant reduction in mineral deposition with respect to controls (**Figure 7**).

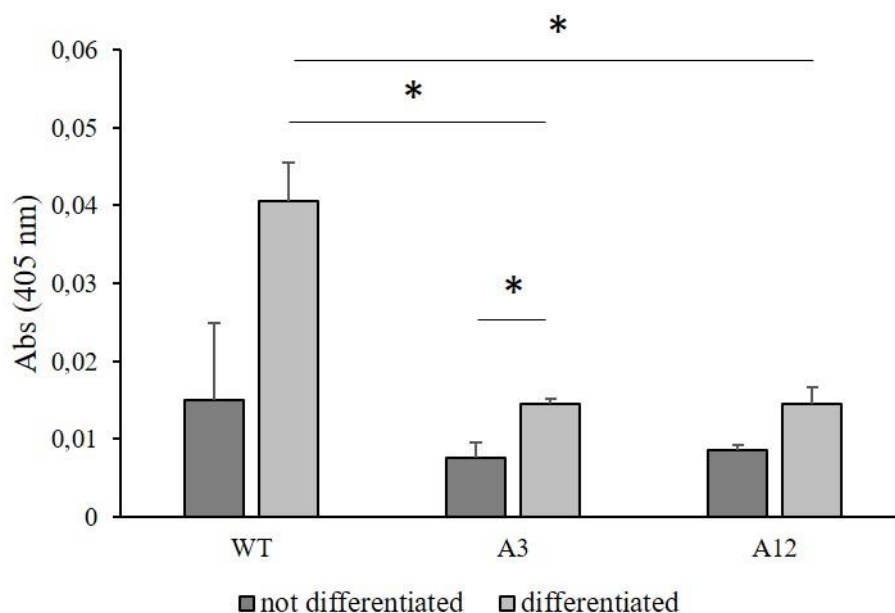


Figure 7. Mineralization level analysis by ARS staining. The mineral amount was significantly reduced in differentiated KO clones with respect to WT (* $P < 0.05$).

Impairment of TMEM38B KO cells proliferation

Intracellular calcium levels are important for different cellular processes including cellular proliferation. To this reason the proliferation assay was performed both at 34 °C, which is the normal temperature required for optimal hFOB proliferation and at 37 °C, the normal growth temperature of human osteoblasts.

After 4 days all KO clones analysed showed a reduced proliferation with respect to control cells at both temperatures, with the exception of A12, which at 34 °C proliferated at the same rate of control cells (**Figure 8C-F**). The WT clones A4 and B28 showed proliferation rate comparable to control cells at both temperatures tested (**Figure 8C-F**).

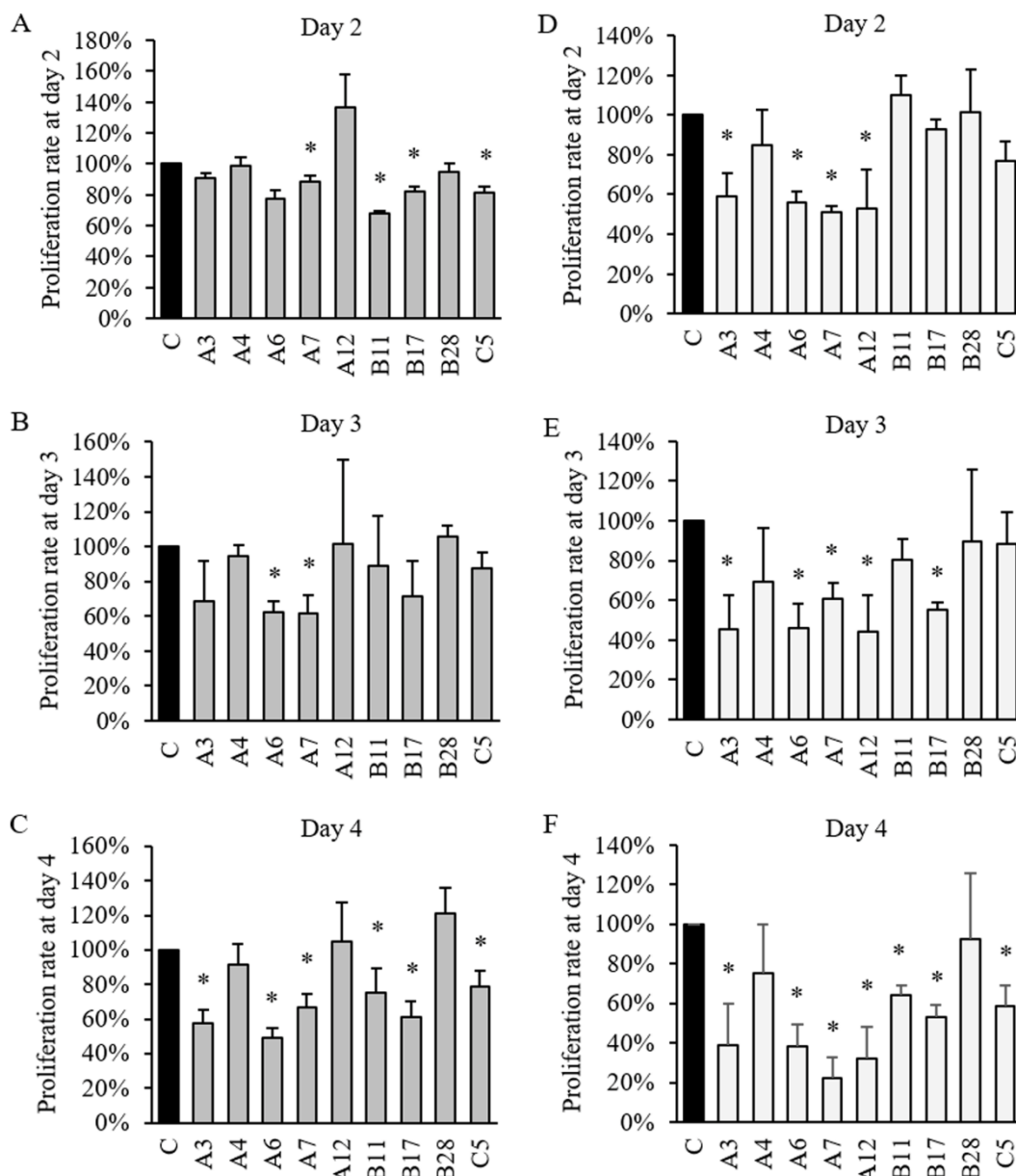


Figure 8. Cellular proliferation analysis. Day 2 (A), day 3 (B) and day 4 (C) of proliferation at 34 °C. Proliferation at 34 °C was reduced for all mutant clones compared to control cells, with the exception of A12 showing a proliferation similar to control. The proliferation of WT clones at 34 °C was similar to control cells. Day 2 (D), day 3 (E) and day 4 (F) of proliferation at 37 °C. Proliferation at 37 °C was reduced in all mutant clones compared to control cells. The proliferation of WT clones at 37 °C was similar to control cells (*P<0.05).

Discussion

CRISPR/Cas9 gene editing was used to generate an *in vitro* model for the osteogenesis imperfecta type XIV, characterized by mutations in *TMEM38B* gene. This OI form is extremely rare and only 6 different mutant alleles have been identified so far (<https://www.le.ac.uk/genetics/collagen/>), three of which consisting of deletion causing protein loss-of-function. Thus, considering that CRISPR/Cas9 system is based on a nuclease cleavage followed by the activation of the endogenous error prone non-homologous DNA repair system (NHEJ), it looks the quickest and more efficient way to obtain *in vitro* model of the disease. Indeed, the NHEJ repair is often responsible for *indels* mutations associated to premature stop codon and loss-of-function of the targeted protein.

Being OI type XIV a brittle bone heritable disorder, the best cellular type to generate an *in vitro* model is represented by the osteoblasts, the bone forming cells of the skeletal system.

Unfortunately, primary osteoblasts are not easy to obtain from OI patients due to the invasive procedure required to isolate bone tissue, furthermore this cell type is stable in culture only for one/two passages and after that it trans-differentiates to fibroblasts like-cells (Czekanska et al. 2012; Kartsogiannis and Ng 2004). Moreover, primary cells are often difficult to transfect, and the generation of stable transfected cells was indeed necessary for our purpose (Gresch and Altrogge 2012). To overcome this limitation, we chose the immortalized human foetal osteoblast cell line hFOB 1.19, widely used in the bone field thanks to its easy growth, high transfection efficacy and possibility to behave both as immature and mature osteoblasts based on culture condition.

60 Crispr/Cas9 targeted clones were obtained following hFOB 1.19 transfection with two of the three different RNA guides selected and tested. Interestingly, the Sanger sequence of 14 clones pointed out in most of them the presence of more of the two expected mutations in the *TMEM38B* alleles (**Table 5-6-7**). This suggested either a limit in the cell dilution methods used for single cell isolation or, likely, a prolonged activity of the Cas9 enzyme following the first cell divisions.

Nevertheless, the absence of the TRIC-B protein evaluated by western blotting using specific antibody (**Figure 2**) confirmed in 30 clones the correct targeting. A deep molecular and biochemical analysis was performed in few of them.

Impairment of K^+ flux across the ER membrane was reported to compromise the release of Ca^{2+} ions through IP_3R channels from the intracellular storage in human and mice OI type XIV (Cabral et al. 2016; Zhao et al. 2016). A dysregulation of calcium flow through the ER membrane was proved in the analyzed mutant clones by electrophysiology analysis. Resting $[Ca^{2+}]_i$ was significantly decreased in A3, A6 and A12 KO clones with respect to control cells (**Figure 3A**), as observed in OI type XIV patients, and the release of Ca^{2+} from the ER was significantly reduced in *TMEM38B* KO clones compared to control cells (**Figure 3B-C-D-E**), as reported for both *Tric-b^{-/-}* murine and patients' cells.

The alteration of the intracellular calcium flux could compromise the activity of different Ca^{2+} dependent enzymes including many enzymes and chaperones involved in post-traditional modifications and in the correct folding of collagen type I (Michalak et al. 2009), but this hypothesis need still confirmation and the availability of an *in vitro* cellular model can indeed shed a new light.

The main feature that distinguishes OI type XIV from other forms of the disease is the synthesis of undermodified collagen type I, identified by slower electrophoretic migration of the α bands in SDS-PAGE. Cabral et al. proved that OI type XIV collagen shows reduced triple helical hydroxylysine level and this may indeed impair the protein glycosylation (Cabral et al. 2016). The electrophoretic analysis of the pepsinized collagen type I extracted from medium and cell layer of A3 and A6 hFOB 1.19 KO clones revealed a faster migration of the α bands compared to WT cells, suggesting a reduced protein glycosylation. The faster migration was detectable also in the C5 mutant clone. Surprisingly, in the A12 clone the $\alpha 2(I)$ was missing (**Figure 4**), supporting the presence of *in vitro* off target sites, even if the *in silico* analysis was excluding their presence.

The impaired Ca^{2+} flux is known to influence osteoblast differentiation and proliferation (Shaheen et al. 2012). Indeed, in OI type XIV patients a reduced expression of the early osteoblast markers *RUNX2* and *SP7* was described, associated to the reduced *COL1A1* expression, suggesting an impairment in cell differentiation (Cabral et al. 2016).

Interestingly, only *Col1a1* and *Col1a2* expression was reduced in mRNA extracted from KO mice bone, whereas the expression level of *Runx2* and *Sp7* match WT values. No clear explanation for such difference was hypothesized, but it should be considered that in humans the expression was evaluated on RNA extracted from cultured cells and in mice on RNA extracted from bone tissue.

The mutant *TMEM38B*^{-/-} A3 clone revealed a significant reduction with respect to control in the expression of the early differentiation markers *RUNX2* and *SP7*, as well as of *COL1A1*, reproducing the human cells findings (**Figure 5A-B-C**) (Webb et al. 2017). We could not perform the same analysis on the A6 clone since the cells after few freezing and thawing cycles stop to grow. Thus, in order to evaluate the effect on gene expression on a different clone we selected B17. Surprisingly in B17 KO clone the expression of *RUNX2* was significantly higher with respect to control cells for the first days of differentiation, while was significantly reduced starting from day 8 (**Figure 5E**). The expression of *SP7* and *COL1A1* was higher in B17 at all time points with respect to control cells (**Figure 5F-G**).

In both patients and mice osteoblasts the expression of the late osteoblast marker *BGLAP* was reduced compared to control up to 15 days of *in vitro* differentiation, when the mutant and WT values were similar. An increased expression of *BGLAP* was detected at later stages in KO cells compared to control (Webb et al. 2017). In the bone of KO mice *Bglap* resulted significantly reduced (Zhao et al. 2016).

In A3 the expression of the late marker *BGLAP* was reduced resembling what previously reported for patients' cells and KO mice bone (**Figure 5D**), while in B17 the expression of *BGLAP* was higher compared to control cells (**Figure 5H**).

Alkaline Phosphatase is an enzyme that hydrolyses the inorganic pyrophosphate (PPi) in inorganic phosphate, which is necessary for hydroxyapatite formation, favouring bone matrix mineralization (Halling Linder et al. 2017). Although bone tissue mineralization appears normal in OI type XIV patients, the expression of ALP was found increased (Webb et al. 2017), but no data were reported on its activity. In the analysed KO mutant clone ALP activity was reduced in analysed mutant clones with respect to control cells, supporting a possible delay in mineralization (**Figure 6**).

Interestingly, alizarin red staining revealed in A3 a reduced amount of mineral deposition after 15 days of differentiation matching murine KO data (Zhao et al. 2016) (**Figure 7**).

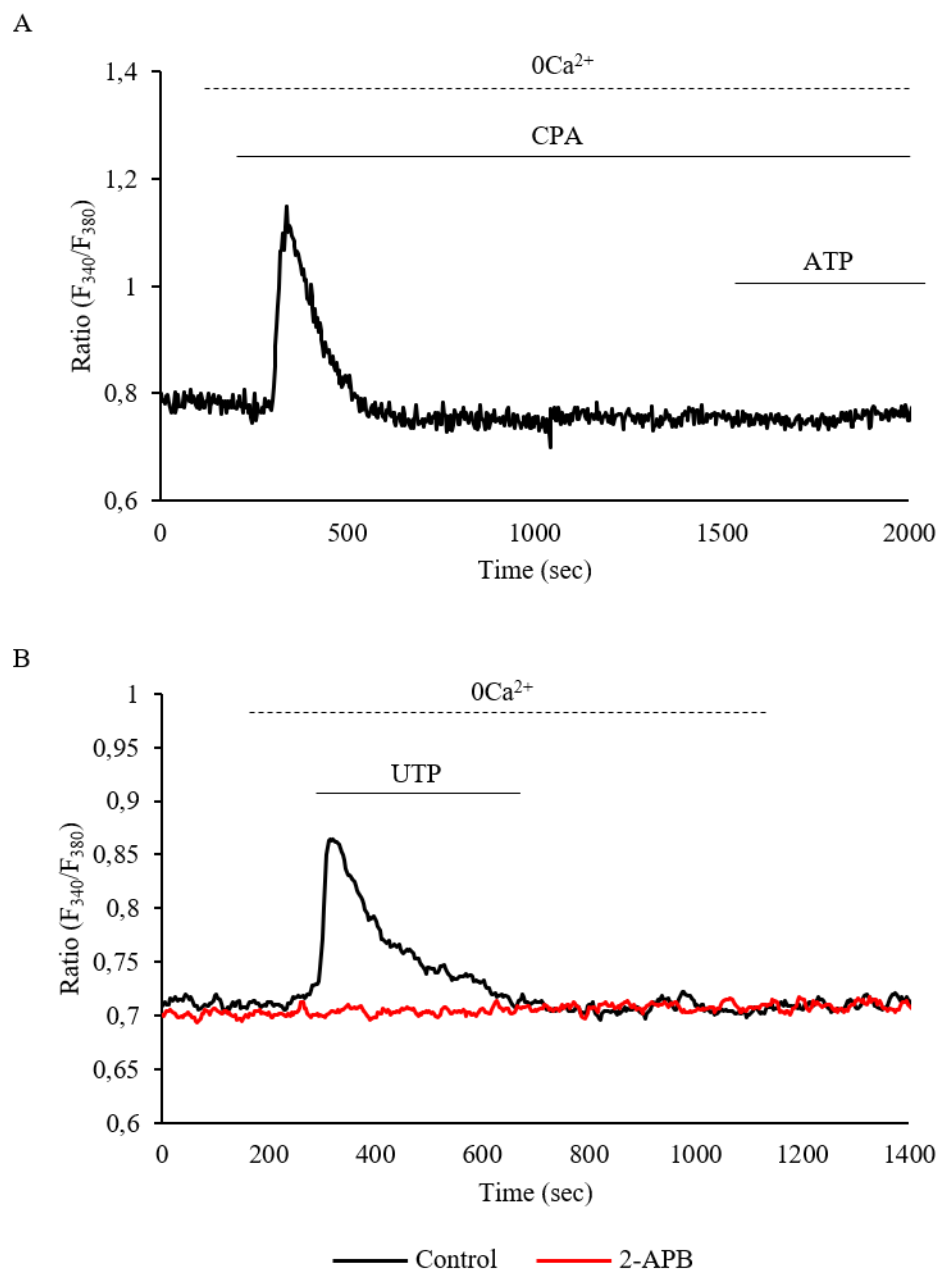
Osteoblast proliferation was not evaluated in OI type XIV human and murine osteoblasts, but Ca^{2+} is a relevant second messenger in signal transduction and it is required at various key regulatory points of the cell cycle, thus playing an essential role in the regulation of cell proliferation. The proliferation was evaluated in several KO clones both at 34 °C, the temperature allowing rapid cell division of hFOB, and at 37 °C, the osteoblasts physiological growth temperature. *TMEM38B* knock-out hFOB clones proliferated significantly less than control cells at both temperatures, supporting the importance of intracellular calcium homeostasis for this process in osteoblasts. A12 clone proliferation was the only one similar to control cells (**Figure 8**).

In our hands the CRISPR proved to be a friendly and powerful tool to create an *in vitro* osteoblast model for OI type XIV, but some technical limitations emerged. The accuracy and reliability of the CRISPR technology was clearly hampered by the already described off-target effects due to Cas9 endonuclease cleavage at loci different that the gRNA target site (Wang and Wang 2019). Even in clones showing the proper *TMEM38B* target both at DNA and protein level, differences in molecular and biochemical properties were identified. For instance, in A12 clone impaired calcium flux and mineralization was flanked by a loss of $\alpha 2(\text{I})$ expression and normal proliferation and in B17 clone an increased expression of early osteoblast markers was detected, likely suggesting a CRISPR/Cas9 off-target activity either in *COL1A2* gene or in transcription factors regulating osteoblast differentiation.

These data pointed out the necessity to characterize several CRISPR clones focusing on the validation of a panel of well-known peculiar characteristic of the model to be created.

Overall, we successfully generated one mutant clone, resembling all the molecular and biochemical hallmarks of human OI type XIV osteoblasts, and this cell line will be used for further investigation of the molecular bases of the disease. Indeed, A3 clone shows the main characteristics found in OI osteoblasts, confirming that the lack of the TRIC-B channel leads to an alteration in the calcium flow released by the ER and that this alteration affects differentiation and mineralization. Furthermore, an impairment in cell proliferation was for the first time demonstrated in OI type XIV cells.

Supplementary figures



Supplementary Figure 1. A. UTP-induced endogenous release of Ca²⁺ by IP₃R was abrogated by depletion of ER Ca²⁺ deposit with cyclopiazonic acid (CPA; 20 μM). B. Calcium flux was inhibited when 2-APB (2-aminoethoxydiphenyl borate) (50 μM) was used, which blocked IP₃R, confirming that the calcium release signal was mediated by IP₃R.

Chapter II
Generation and characterization of OI type XIV
zebrafish model

Introduction

Zebrafish

Zebrafish is a fresh water bony fish belonged to the cyprinid family of teleost, originated from the river of Gange (Rob et al. 2010) in the Himalayan region of South Asia (Khan and Alhewairini 2018).

Zebrafish was initially considered the model of choice for developmental studies thanks to embryos transparency, which allow to directly follow the rapid organs growth. Moreover, the zebrafish genome was fully sequenced and 70% of its genes have a human orthologue (Howe et al. 2013). The high level of genes conservation, as well as comparable cellular processes, made zebrafish a valid model to investigate human pathologies (Rob et al. 2010).

Several are the advantages in using zebrafish as model organism, such as the external fertilization and the large number of offspring from a single mating, the rapid development and the reduced dimensions, 3-4 cm at adult stage (Laize, Gavaia, and Cancela 2014). In addition, zebrafish has been recently discovered as good vertebrate model to study organ regeneration, since it is able to regenerate fins, heart, central nervous system structures, jaw, hair cells, pancreas, liver, and kidney (Wang et al. 2012).

Zebrafish skeleton

Zebrafish can be exploited as a valid model for study human skeletal diseases since it shares the basic skeletal components and the osteoblastogenic pathways of differentiation with mammals (Apschner, Schulte-Merker, and Witten 2011). Zebrafish and mammalian skeleton have in common the major categories of skeletal tissues, such as cartilage, bone, dentine and all cells types: chondroblasts, chondrocytes, osteoblasts, osteocytes and osteoclasts (Witten et al. 2017).

Three types of ossification processes can be distinguished in zebrafish: intramembranous, endochondral and perichondral ossification.

The teleost intramembranous ossification is typical of the skull, vertebral column, scales and fin rays (Hall 2015), while in mammals it is mostly restricted to the bones of the cranial vault and the dentary (Hirasawa and Kuratani 2015). Intramembranous ossification starts with the

aggregation of the mesenchymal stem cells, which then differentiate into pre-osteoblasts, and then become mature osteoblasts, starting to lay down a mineralized bone matrix (Hall 2015).

Endochondral ossification, the main ossification in mammals, is uncommon in teleosts. This type of ossification is characterized by the mesenchymal cells' condensation and differentiation in chondroblasts and chondrocytes, which then secrete an extracellular cartilage matrix as a template, finally replaced by bone matrix. Unlike mammals, in teleost endochondral ossification is divided in two types. Endochondral ossification type I is characterized by the presence of a resting zone and a proliferation zone with columnar cartilage, followed by a hypertrophic zone and then a region in which cartilage matrix calcifies (calcification zone) (Weigele and Franz-Odenaal 2016). There is also a degradation zone where chondroclasts degrade the cartilaginous matrix, thus allowing osteoblasts to lay down the bone matrix. This ossification type is typical of few bones, such as the ceratohyal and the radials in the pectoral fin.

In the endochondral type II ossification the calcification and ossification zones are missing, but adipose cells replace the cartilage template (Weigele and Franz-Odenaal 2016). This type of ossification is typical of a tubular concave bones filled with adipose tissue, such as branchial arches, ethmoid and hypuralia (Weigele and Franz-Odenaal 2016).

The third type of teleost ossification is not present in mammals and it is the perichondral ossification. It is an intramembranous ossification starting from the surface of a cartilage template, where the osteoblasts aggregate and deposit bone matrix in perichondrium (Hall 2015), and it is typical of Meckel's cartilage and hyomandibular bone.

Vertebral column

The notochord has an essential role during development and once ossified it gives rise to vertebral column (Stemple 2005). The notochord is composed by large and vacuolated chordocytes, covered by an epithelial layer of chordoblasts which secrete the notochord sheath. This sheath is a stratified structure composed of a thin external membrane containing elastin that covers a thicker layer of mainly collagen type II (Stemple 2005).

In zebrafish, the vertebrae form by direct mineralization of the notochord sheath, called the chordacentrum (Bensimon-Brito et al. 2012; Arratia and Schultze 1992), unlike mammals where the vertebrae ossify from the cartilaginous template, by endochondral ossification.

Zebrafish vertebra is built by intramembranous ossification outside the notochord onto the chordacentrum, which consists of a compact autocentrum and trabecular arcocentrum (Arratia and Schultze 1992). Osteoblasts produce collagen type I and start to ossify the autocentrum at the level of the intervertebral disc, then, also the ossification of both neural and haemal arches takes place (Inohaya, Takano, and Kudo 2007).

The vertebral column is regionalized in a precaudal region, closer to the skull, and in a caudal region. The more anterior precaudal vertebrae constitute the Weberian apparatus, in which the vertebrae are fused. The vertebrae are composed by the centra, neural arches and spines, and haemal arches and spines; In addition, the precaudal vertebrae present also parapophysis and ribs. Finally, the last three caudal vertebrae are modified to support the caudal fin. The vertebral column ossifies in a specific order: vertebrae 3 and 4 are the first to ossify, followed by the bi-directional ossification of the others (Bird and Mabee 2003).

Osteoblastogenic markers

Zebrafish and mammals share also the osteoblastogenic markers. For instance, the runt-related transcription factor 2 (*runx2*) is present in also in zebrafish as the two isoforms *runx2a* and *runx2b*, expressed during the early stage of osteoblastic differentiation (Li et al. 2009). In addition, intermediate and late bone cells differentiation stages are characterized in tetrapods, as in mammals by the expression of osterix (*osx*) and osteonectin/sparc (*osn*) (Li et al. 2009).

However, there are some differentially expressed genes between human and zebrafish, such as *coll10a1* and *sox9*, which encode for collagen type X and SRY-Box Transcription Factor 9, respectively (Eames et al. 2010; Li et al. 2009; Yan et al. 2005). In tetrapods, *COL10A1* is expressed only during chondrocytes development and it is associated with hypertrophic chondrocytes. Zebrafish *coll10a1* expression overlaps with *osx* expression, suggesting that collagen type X plays an important role during both the intermediate and mature stages of osteoblast differentiation (Li et al. 2009).

In mammals the transcription factor SOX9 is required for mesenchymal condensation, leading to the formation of the cartilaginous template (Komori 2010), while in zebrafish it is involved in both cartilage and bone development. In particular, *sox9a* is mainly expressed in the mesenchyme and perichondrium of branchial arches, while *sox9b* in the epithelium that surrounds each arch and is required for the differentiation of these cartilages into bone (Yan et al. 2005).

Zebrafish collagen type I

In mammals, collagen type I, is an heterotrimer composed of two identical $\alpha 1$ chains and one $\alpha 2$ chain, encoded by *COL1A1* and *COL1A2*, respectively (Uitto 1979). In many teleosts, including zebrafish, collagen type I is composed by three different chains $\alpha 1$, $\alpha 2$ and $\alpha 3$, encoding by *coll1a1*, *coll1a2* and *coll1a3* respectively (Morvan-Dubois et al. 2003), assembled in a heterotrimeric protein with 1:1:1 stoichiometry (Gistelink, Gioia, et al. 2016).

Synten analysis of human, mouse and zebrafish type I collagen encoding genes revealed a high level of conservation among these different species. Moreover, zebrafish pro $\alpha 1$ (I) shows 77% and 76% conserved amino acids with human and murine pro $\alpha 1$ (I) chains respectively, while pro $\alpha 3$ (I) has 75% identity with both of them.

Interestingly, pro $\alpha 1$ and pro $\alpha 3$ share a 78% of homology, the same theoretical molecular weight (137 kDa) as well as the same isoelectric point (5.4) (Gistelink, Gioia, et al. 2016). These similarities are due to the fact that they originated from the duplication of a common ancestor α (I) coding gene likely duplicated during the whole genome duplication event occurred in the teleost more than 340 million years ago (Christoffels et al. 2004).

The expression analysis of collagen genes in zebrafish revealed their expression at 3-4 days post fertilization (dpf), coinciding with the formation of the first bony structures in the head of the zebrafish embryo and thus emphasizing their relevance for bone formation during early development. In addition, collagen genes are maternally expressed thus, indicating the important role of the protein since the earliest stages of development. Moreover, in zebrafish the collagen type I genes are mainly expressed in the ectoderm, which develops in bony elements, in ligaments and tendons. Thus, the collagen type I genes are expressed in the same tissues as in humans, including bone and skin (Gistelink, Gioia, et al. 2016).

Zebrafish models for osteogenesis imperfecta

In the last years, thanks to the easy genetic manipulation as well as the optimization of several genome editing techniques, several zebrafish models for skeletal human disorders, such as osteogenesis imperfecta, osteoporosis, osteopenia, craniosynostosis, craniofacial defects and spinal deformities have been generated (Laize, Gavaia, and Cancela 2014). Among these, several zebrafish mutants, carrying defects in genes associated with both dominant and recessive OI forms, are available, proving the goodness of the model in reproducing the disease outcome.

Chihuahua (*Chi*^{+/-}) is a zebrafish model for dominant OI and carries a glycine substitution (G574D, p.G736D) in the triple helical domain of the α 1 chain of collagen type I. *Chi*^{+/-} has been generated by N-ethyl-N-nitrosourea (ENU)-mutagenesis technique and resembles the severe OI type III form. X-ray and μ CT revealed the severe *Chi*^{+/-} phenotype characterized by skeletal malformation, including shorter vertebral bodies, kyphoscoliosis, and evidence of fractures (Fisher, Jagadeeswaran, and Halpern 2003; Gioia et al. 2017). Moreover, in *Chi*^{+/-} model it was demonstrated that the overmodified collagen type I is retained in the endoplasmic reticulum of mutant cells, causing an enlargement of ER cisternae and likely ER stress (Gioia et al. 2017).

Microwaved (*med*^{+/-}) carries a G>A (p.Glu888Lys) recessive mutation in *coll1a1*, which causes reduced bone ossification, thickness of vertebral bodies and undulation of the larval fin (Asharani et al. 2012).

Recently, other zebrafish carrying mutations in collagen encoding genes have been described. The double knock-out mutant for *coll1a1* and *coll1a2* (*coll1a1*^{+/-}; *coll1a2*^{+/-}) shows a reduced level of α 1 and α 2 of collagen type I, resulting in a mild skeletal phenotype with increased bone fragility typical of OI type I (Gistelink et al. 2018).

The *coll1a1*^{dmh13/+}, *coll1a1*^{dmh14/+}, *coll1a2*^{dmh29/+} and *coll1a2*^{dmh15/+} which carry mutations in *coll1a1*, *coll1a2* and *coll1a2*, respectively, have been generated in a forward genetics screen (Henke et al. 2017). The mutant alleles result in dominant transmitted aminoacidic substitutions in zebrafish α 1 (p.Gly1093Arg, p.Gly1144Glu), α 2 (p.Gly1123Asp) and α 2 (p.Gly882Asp) chains, respectively. These mutations are all clustered in an important region

for collagen-non collagenous protein interaction (major ligand binding region 3) and they are associated with variable phenotypic outcomes, ranging from moderate OI type IV to perinatal lethal OI type II (Marini et al. 2017; Sweeney et al. 2008). Moreover, the variability of the excessive post translational modification throughout this set of mutants has been related to the position of the mutation in the collagen type I helix (Sweeney et al. 2008; Gioia et al. 2017; Cabral et al. 2006; Gistelinc et al. 2018).

Frially fins (*frf*^{-/-}) has been generated by ENU mutagenesis and carries missense or nonsense mutation in *bpm1*, responsible in human for the recessive OI type XIII (Asharani et al. 2012). Its phenotype is characterized by ruffled larval fin, shortened body axis, malformed craniofacial structures and generalized osteopenia (Asharani et al. 2012). Bmp1 plays a role in generating mature collagen type I through the cleavage of the C-terminal propeptide. This processing is essential for the self-assembly of mature collagen monomers into fibrils. In *frf*^{-/-} collagen type I the c-propeptide is not been removed, confirming the impairment of Bmp1 activity (Asharani et al. 2012).

plod2^{-/-} mutant carries the c.2037T>A substitution in *plod2* gene, resulting in a premature stop codon at position 679. PLOD2 mutations in human are responsible for recessive OI/Bruck syndrome (Gistelinc, Witten, et al. 2016). The *plod2*^{-/-} mutation is in the highly conserved catalytic domain of lysyl hydroxylase 2 (LH2), the enzyme involved in the hydroxylation of lysine residues of fibrillar collagen telopeptides and required for cross-links formation within collagen fibrils in the extracellular matrix. *plod2*^{-/-} mutants are short, show severe skeletal abnormalities, bone fragility, fractures and increased mineral density in vertebrae (Gistelinc, Witten, et al. 2016). Moreover, the *plod2*^{-/-} model presents an impaired degree of organization of type I collagen, which is especially evident in the mature collagen adjoining the notochord (Gistelinc, Witten, et al. 2016).

Mutant for *sp7* was generated using N-ethyl-N-nitrosourea (ENU)-mutagenesis technique. The mutation isolated was p.Leu145*, which causes the introduction of a stop codon at position 145, truncating the protein before the three zinc finger domains. This mutant shows scoliosis, poor bone growth, ribs fractures, and specific craniofacial, as seen in patients with the absence of all three zinc fingers domains, proving to be an accurate model for this recessive form of OI (Kague et al. 2016).

Recently, two novel OI type VII and VIII zebrafish mutants have been generated by CRISPR/Cas9 system. They carry mutations in *crtap*, which encodes for the cartilage associated protein and in *p3h1*, which encode for the prolyl-3-hydroxylase, two members of the prolyl 3-hydroxylation complex. Both *crtap*^{-/-} and *p3h1*^{-/-} show the typical OI patients' features, such as a reduced size, severe skeletal deformities, body disproportion and altered mineralization. The overmodified and intracellularly retained collagen type I results in an ER cisternae enlargement, a typical condition observed also in OI patients and murine models (Tonelli, Cotti, et al. 2020).

Table 1. Zebrafish models for osteogenesis imperfecta.

Model	Transmission	Gene	Affected protein	Human OI type	References
<i>chihuahua</i>	AD	<i>coll1a1</i>	Type I collagen, α 1	II-IV	Fisher et al. 2003
<i>microwaved</i>	AR	<i>coll1a1</i>	Type I collagen, α 1	II-IV	Asharani et al. 2012
<i>frilly fin</i>	AR	<i>bmp1</i>	Bone morphogenetic protein 1	XIII	Asharani et al. 2012
<i>dmh13</i>	AD	<i>coll1a1</i>	Type I collagen, α 1	II-IV	Henke et al. 2017
<i>dmh14</i>	AD	<i>coll1a1</i>	Type I collagen, α 1	II-IV	Henke et al. 2017
<i>dmh29</i>	AD	<i>coll1a1b</i>	Type I collagen, α 3	II-IV	Henke et al. 2017
<i>dmh15</i>	AD	<i>coll1a2</i>	Type I collagen, α 2	II-IV	Henke et al. 2017
<i>plod2</i>	AR	<i>plod2</i>	Lysyl hydroxylase 2	No type	Gistelinck et al. 2016
<i>sp7</i>	AR	<i>sp7</i>	Transcription factor sp7	XII	Kague et al. 2016
<i>p3h1</i> ^{-/-}	AR	<i>p3h1</i>	Prolyl 3-hydroxylase 1	VII	Tonelli et al. 2020
<i>crtap</i> ^{-/-}	AR	<i>crtap</i>	Cartilage associated protein	VIII	Tonelli et al. 2020

Materials and methods

Zebrafish

Zebrafish (AB) were kept into the ZebTec (Tecniplast) semi closed recirculation housing system at 28 °C, conductivity 500 µS, pH 7.5, and 14:10 hours light:dark cycle. The system is located in the centralized animal facility of the University of Pavia. Zebrafish embryos were collected into petri dishes containing fish water (1.2 mM NaHCO₃, 0.1 g/L instant ocean, 1.4 mM CaSO₄, 0.00002% (w/v) Methylene blue) and kept at 28 °C into an incubator. At 7 days post fertilization (dpf) larvae were introduced into the ZebTec (Tecniplast) system. During experimental procedures both adult and larvae were anesthetized with a 0.016% (w/v) 3-Aminobenzoic acid ethyl ester methanesulfonate salt solution (Tricaine, Sigma Aldrich) in fish water and euthanized with an overdose of the same solution (0.03% (w/v) tricaine). All experiments were performed in accordance with the approved guidelines, in agreement with EU Directive 2010/63/EU for animals. The experimental protocol was approved by the Italian Ministry of Health (Approval Animal Protocol No. 1191/2016).

In silico analysis

The synteny analysis of the chromosomic regions surrounding *tmem38b* in zebrafish (*D. rerio*, ENSDARG00000100549), chicken (*G. gallus*, ENSGALG00000027472), mouse (*M. musculus*, ENSMUSG00000028420), human (*H. sapiens*, ENSG00000095209) and frog (*X. tropicalis*, ENSXETG00000000907) was performed using the genome browser Genomicus v93.01 (www.genomicus.biologie.ens.fr).

Protein homology between zebrafish and human TRIC-B was analysed using UniProt Blast software (<http://www.uniprot.org/blast/>).

In situ hybridization

In situ hybridization was performed to localize the *tmem38b* transcript in WT embryos. An 841 bp amplicon was obtained by RT-PCR amplification of wild type zebrafish *tmem38b* mRNA (ENSDART00000168983) using primers on exon 1 (5'-TCAATCTGAACGAGCTCGCATTT-3', 20-42 nt) and on exon 10 (5'-AAGAAGCAGAAGCCAGCAAAAAG-3', 839-861 nt). The amplicon was subcloned in

pGEM-T-Easy vector (Promega) and ligation was performed using T4 DNA ligase o/n at RT. DH5 α *E.Coli* competent cells were transformed and plated on agar plates containing 100 μ g/mL ampicillin. A colony PCR, performed with the primers indicated above, allowed to select positive colonies. Plasmid DNA was extracted using the Qiagen Plasmid Maxi Kit (Qiagen), linearized by enzymatic digestion with SacII (New England BioLabs) for the antisense RNA probe, and with SpeI (Promega) for the sense probe *in vitro* synthesis and finally gel purified using Nucleospin Gel and PCR Clean-up Kit (Machinery-Nagel). RNA probes were synthesized with the Maxiscript SP6/T7 Kit (Ambion) using 1 μ g of plasmid as template. DNA was eliminated by DNase digestion using the Turbo DNA-free Kit (Ambion).

Embryos at 24, 48, 72, 96 and 120 hours post fertilization (hpf) were fixed in 4% (w/v) paraformaldehyde (PFA) o/n at 4 °C, washed in phosphate buffered saline (PBS), dehydrated with a decreasing PBS/increasing methanol series (75%/25%, 50%/50%, 25%/75%) and stored in 100% methanol at -20 °C until use. Samples were re-hydrated with an increasing PBS/decreasing methanol series (25%/75%, 50%/50%, 75%/25%), washed with PBS-T (PBS, 0.1% Tween) and then digested with 10 μ g/mL proteinase K for a time depending on embryos' developmental stage. 24 hpf embryos were digested for 10 min, while starting from 48 hpf the digestion time was prolonged to 30 min. After several washes with PBS-T (PBS, 0.05% Tween), samples were fixed in 4% (w/v) PFA for 20 min and washed again in PBS-T to eliminate residue of PFA. A blocking solution 50%/50% PBS-T/hybridization buffer (50% formamide, Fluka 47670), SSC 20X (3 M NaCl, 0.3 M sodium citrate pH 5.0), 5 mM EDTA pH 8, 0.2% Tween-20, 0.5% CHAPS) was added together with 50 μ g/mL yeast RNA (Yeast RNA Sigma R-6625) and 100 μ g/mL heparin (Sigma H-7005) and samples were incubated at 64 °C for at least 1 hour. Embryos were incubated o/n at 64 °C with a new hybridization buffer added with specific sense or antisense 2 ng/ μ L probe, previously denatured at 90 °C for 10 min. Washes with decreasing hybridization buffer (Hyb)/increasing SSC (Hyb/SSC 2x 75/25, Hyb/SSC 2x 50/50, Hyb/SSC 2x 25/75) at 64°C were then performed, until samples were incubated with 2x SSC for 10 min and 0.2 x SSC for 30 min at 64 °C. After 10 min wash with piperazine-N,N'-bis (ethanesulfonic acid), 0.5 M 1,4-piperazinediethanesulfonic acid (PIPES, Sigma Aldrich) NaCl samples were treated with 200 U/mL T1 RNase and 10 μ g/mL RNaseA in 0.5 M PIPES NaCl for 10 min at 37

°C and for 5 min at RT. Blocking with MAB (0.15 M C₄H₄O₄, 0.15 M NaCl pH 7.5) and 2% blocking Boheringer reagent (Roche) was performed for 1 hour at RT. Samples were then incubated with anti-digoxigenin AP anti-DIG (11093274901, Roche) 1:5000 in MAB blocking o/n at 4 °C. Samples were first washed in MAB, then in MABT (MAB, 1% Tween-20) and in 0.1 M Tris-HCl pH 9.5/ 0.1 % Tween. Finally, NTMT solution (0.1 M NaCl, 0.1 M Tris HCl pH 9.5, 50 mM MgCl₂ and 1% Tween-20) was added for 30 min. Samples were then incubated in the dark with NTMT, NBT (nitro blue tetrazolium) (Promega) and BCIP (5-bromo-4-chloro-3-indolyl-phosphate) (Promega), until the appearance of a violet signal. Finally, images were acquired using a Leica M165 FC microscope connected to a Leica DFC425 C digital camera.

Generation of *tmem38b* zebrafish mutant

In order to generate the zebrafish mutant for *tmem38b* through CRISPR/Cas9 system, a target sequence was selected using the free online software CHOP CHOP (<https://chopchop.cbu.uib.no/>). The RNA guide (gRNA), complementary to the target sequence localized on exon 7, was synthesized by annealing the two synthetic oligonucleotides shown in **Table 2**. The two oligonucleotides were mixed in equimolar amount (100 μM), and annealed with the following cycle: 3 min at 95 °C followed by 1 min at 25 °C. gRNA fragment concentration was determined by absorbance at 260 nm and double stranded fragments were cloned in pT7-gRNA vector (Addgene plasmid #46759), previously linearized with BsmBI 10 U/μL (New England BioLabs)

Table 2. Target sequence and oligonucleotides used for the synthesis of the gRNA. The PAM (NGG) sequence is underlined; the nucleotides inserted to ensure the cloning into the plasmids are in red.

Gene	Target sequence	Synthetic oligonucleotides
<i>tmem38b</i> (gRNA)	5'-GGTTCGTCACCTTCCTTCATGG-3' (11391-11413)	5'-TAGGTTCTCGTCACCTTCCTTCA-3' (11394-11414)
		5'-AAACTGAAGGAAGTGACGAGAA-3' (11394-11411)

The linearized plasmid was purified with Nucleospin Gel and PCR Clean-up kit (Machinery-Nagel) and ligation was performed using T4 DNA ligase (Thermo Scientific) o/n at RT. DH5 α *E. coli* cells were transformed using 0.105 μ g of T7-gRNA ligation and incubating cells in ice for 30 min, followed by 90 seconds at 42 °C and 2 min in ice. Cells were grown in 900 μ L of Luria Bertani Broth (LB) at 37 °C for 1 hour, then plated on agar plate containing 100 μ g/mL ampicillin and let grow o/n. A colony PCR was performed using one primer on the plasmid and the other on the insert to verify the subcloning success (**Table 3**). The PCR thermal cycle was: 10 min at 95 °C, 3 min at 95 °C, 40 cycles of 1 min at 95 °C, 1 min at 64 °C, 1 min at 72 °C, and 10 min of elongation at 72 °C. Positive colonies were picked and grown o/n in LB with 100 μ g/mL ampicillin.

Table 3. Primers used for colony PCR.

Primer localization	Primer sequence
gRNA Ex7 (Insert)	5'-TAGGTTCTCGTCACTTCCTTCA-3'
T7gRNA (Plasmid)	5'- TACCGCACAGATGCGTAAGG-3'

Plasmid DNA was extracted using the Qiagen Plasmid Maxi kit (Qiagen) and the presence of the insert was confirmed by Sanger sequencing (GATC Biotech AG).

The plasmid was then linearized by BamHI (Promega), purified using Nucleospin Gel and PCR Clean-up Kit (Machinery-Nagel) and used as template for *in vitro* transcription that was performed using the MEGAshortscript T7 Kit (Invitrogen). The gRNA was then purified using mirVana miRNA Isolation Kit (Invitrogen) and quality and size were checked by electrophoresis on 10% (v/v) polyacrylamide SDS gel.

For Cas9 endonuclease the pT3TS-nCas9n vector (Addgene plasmid #46757), which contains the Cas9 sequence, was linearized with XbaI (New England BioLabs) and purified with Nucleospin Gel and PCR Clean-up kit (Machinery-Nagel). Plasmidic DNA was transcribed with mMessage mMachine T3 Kit (Thermo Fisher) and DNA template was removed using Turbo DNA-free Kit (Ambion). The polyadenylation, necessary for expression in animal cells was performed using the Poly (A) Tailing Kit (Ambion). The transcript was purified with RNasy Mini Kit (Qiagen) and checked by electrophoresis on 1% (w/v) formaldehyde agarose gel.

Microinjection

Embryo microinjections were performed through an InjectMan (Eppendorf) micromanipulator assembled on a Leica M165 FC stereomicroscope. *tmem38b*-gRNA_{exon7} RNA (12.5 ng/ μ L), Cas9 (300 ng/ μ L), Danieau (58 mM NaCl, 0.7 mM KCl, 0.4 mM MgSO₄, 0.6 mM Ca(NO₃)₂, 5 mM Hepes pH 7.6) and a 10x fluorescent dye (dextran tetramethylrhodamine conjugated, Molecular Probes) were mixed in a 5 μ L final volume and denatured at 60 °C for 10 min before being loaded on a borosilicate capillary through a Eppendorf 930001007 tip (Eppendorf). Pressure and injection time were modulated in order to inject between 2 and 4 nL of mixture in each embryo. The day after injection surviving embryos were screened under fluorescence microscope and the ones showing consistent fluorescent signal were considered positively injected and grown for further experiments.

DNA extraction and genotyping

DNA was extracted from embryos or caudal fin from adult fish. Samples were digested in 100 μ L of lysis buffer (100 mM Tris HCl pH 8.5, 5 mM EDTA, 0.2% SDS (w/v), 200 mM NaCl) and 20 μ L of 15 mg/mL proteinase K (Sigma Aldrich) o/n at 55 °C. A centrifugation step at 14000g at room temperature (RT) was performed to remove residual tissues. The supernatant was then transferred in a new tube and DNA precipitated with equal volume of isopropanol. Following centrifugation at 14000g at RT the supernatant was discarded, and the pellet washed with 400 μ L of 70% ethanol. After centrifugation at 14000 g at RT, the supernatant was discarded and the pellet dried and resuspend in 30 μ L of Tris-EDTA buffer (20 mM Tris-HCl, 1 mM EDTA pH 8.0) o/n at 55 °C.

TOPO TA cloning

To determine single mutations obtained in F0 mosaics and F1 fish, TOPO TA cloning kit (Invitrogen) was used. PCR reaction was set up using 2 μ L of genomic DNA as template, mixed with buffer Taq polymerase 1x (GenScript), 0.2 mM dNTPs, 0.04 U/ μ L Taq polymerase (GenScript) and 0.3 μ M primers in a final volume of 50 μ L. Primers used are listed in **Table 4**. The PCR cycle started with 3 min denaturation at 94 °C, followed by 40 cycles at 94 °C for 30 sec, 30 sec at 56 °C annealing temperature, 1 min at 72 °C and it ended with 10 min at 72 °C.

PCR products were gel-purified using Nucleospin Gel and PCR Clean-up kit (Machinery-Nagel) and cloned into the pCR II-TOPO vector following the kit instructions. The recombinant vector was used to transform DH5 α competent *E. coli* cells and plasmid DNA was isolated from single colonies with EuroGOLD Plasmid Miniprep I kit (Euroclone) and sequenced by Sanger sequencing (GATC Biotech AG).

Table 4. Sense and reverse primers designed on *tmem38b* exon 7 sequence.

	Gene	Primers for genotyping		Amplicon
		Sense	Antisense	
1	<i>tmem38b</i> (exon 7)	5'-ATCTGGTGTCTTACTGTCCGCT-3' (11316-11337)	5'-GTTGATAATTAATCCCCTGGCG-3' (11504-11528)	212 bp
2	<i>tmem38b</i> (exon 7)	5'-TTACTGTCCGCTGGATGTGG-3' (11326-11345)	5'-CAGAGCGTCGCTGTATTTGC-3' (11448-11467)	142 bp

Genotyping

The genotype was determined through amplification of the *tmem38b* sequence (NC_007132) using primers indicated in **Table 4**. 1 μ L genomic DNA was mixed with buffer Taq polymerase 1x (GenScript), 0.2 mM dNTPs, 0.04 U/ μ L Taq polymerase (GenScript) and 0.3 μ M primers in a final volume of 25 μ L. The amplification cycle was: 3 min denaturation at 94 $^{\circ}$ C, followed by 40 cycles at 94 $^{\circ}$ C for 30 sec, 56 $^{\circ}$ C for 30 sec, 72 $^{\circ}$ C for 1 min and it ended with 10 min at 72 $^{\circ}$ C. For *tmem38b*^{A120-7/120-7} mutant the amplicon was checked by electrophoresis on 10% acrylamide gel (v/v) while for *tmem38b*^{-/-} mutant was checked on 12% (v/v) acrylamide gel in TBE buffer (0.1M TRIS-HCl, 0.1M H₃BO₃, 2mM EDTA, pH 8.2), in order to determine the genotype. For WT fish the amplicon was 142 bp, while for the *tmem38b*^{A120-7/120-7} and *tmem38b*^{-/-} the amplicons were 118 and 135 bp, respectively.

Screening of mutants

T7 endonuclease assay

10 μ L of PCR product, obtained using the primers listed in **Table 4**, were denatured and renatured for 5 min at 94 $^{\circ}$ C, then cooled to 85 $^{\circ}$ C at -0.2 $^{\circ}$ C/sec and further cooled to 25 $^{\circ}$ C at -0.1 $^{\circ}$ C/sec. Samples were then digested with T7 endonuclease I (0.2 U/ μ L) in 1x Buffer 2 (New England BioLabs) at 37 $^{\circ}$ C for 1 hour. T7 endonuclease specifically recognizes and cuts DNA heteroduplex, thus the assay was used to discriminate WT and mosaic fish.

Products were checked on 8% (v/v) polyacrylamide gel and digitally acquired after ethidium bromide staining through VersaDoc 3000 (BioRad). A 212 bp amplicon was expected for the WT, while two more bands at 130 and 80 bp were expected for mosaic fish.

RNA extraction

RNA was extracted from skin and caudal fin of adult WT and mutant fish and from embryos at different developmental stages: 2-4 cells, 16-32 cells, 64-128 cells, high, sphere, 30% epiboly, 50% epiboly, 80% epiboly, 5-10 somites, 15-20 somites, 24 hours post fertilization (hpf) 48 hpf, 72 hpf and 96 hpf using Qiazol (QIAGEN), following the manufacturer's suggestion. The genomic DNA was removed upon treatment with Turbo DNA Free Kit (Ambion). Finally, RNA concentration was evaluated by measuring the absorbance at 260 nm using the nanodrop, while its quality was check by electrophoresis on 1% (w/v) agarose gel in TBE 1x in DEPC water.

Real time PCR (qPCR)

The High Capacity cDNA Reverse Transcription kit (Applied Biosystems) was used to retrotranscribe different quantity of RNA (300 ng to 1 µg) in 20µL final volume. qPCR was performed in triplicate in a 25 µL final volume using Taqman Universal PCR Master mix (Applied Biosystems) and commercial TaqMan probes for *tmem38b*, *β-actin1*, *rpl13a*, *serpinh1a*, *serpinh1b* and *hspa5* (probe Dr03434781_m1, Dr03432610_m1 and Dr03119260_g1, Dr03137916_m1, Dr03150230_g1, Dr03107861_m1 Applied Biosystems). The Mx3000P (Stratagene) thermocycler, and the Quant Studio 3 Real-Time PCR System (Applied Biosystems) were used for qPCR on embryos and on adult, respectively. In both cases the following programme was applied: 10 min of Taq enzyme activation at 95 °C, 40 cycles of 15 sec of denaturation at 95 °C and 1 min annealing and extension at 60 °C. The relative expression levels of each gene were calculated using the $\Delta\Delta C_t$ method. Statistical analysis has been performed taking into account technical triplicates.

Collagen analysis

Collagen was extracted from bone and skin of adult WT and mutant fish. Samples were defatted in 0.1N NaOH o/n at 4 °C, washed in water, and bone samples were decalcified in 0.5 M EDTA pH 7.4 for 48 hours at 4 °C. Tissues were then digested for 48 hours at 4 °C with 0.1 mg/mL pepsin in 0.5 M CH₃COOH. After digestion, samples were centrifuged at 14000 rpm at 4 °C for 40 min. Both the supernatant (Pepsin Soluble Fraction I, PSCI) and the pellet (Pepsin Soluble Fraction II, PSCII) were kept. PSCI was precipitated o/n with 0.9 mM NaCl in 0.5 M CH₃COOH, centrifuged for 40 min at 14000 rpm at 4 °C. The pellet was resuspended in 0.5 M CH₃COOH and precipitated a second time with 0.9 mM NaCl in 0.5 M CH₃COOH o/n at 4 °C and the same protocol was repeated the day after. After the second precipitation, PSCI was centrifuged at 14000 rpm at 4 °C for 40 min and the supernatant was discarded. The pellet was washed twice with 70% ethanol in ice, centrifuged at 14000 rpm at 4 °C for 30 min and the pellet was dried and resuspended in 0.5 M CH₃COOH o/n at 4 °C on head-over-head. PSCII was instead further digested with 0.1 mg/mL pepsin in 0.5 M CH₃COOH shaking for 48 hours at 4 °C and then the same protocol as for PSCI was applied. Samples were quantified using Sircol Soluble Collagen Assay Kit (Biocolor), following the manufacturer's protocol.

Purified collagen was analysed on a 6% polyacrylamide gel electrophoresis (SDS-PAGE) containing 0.5 M urea. Gels were fixed in 45% (v/v) methanol, 10% (v/v) acetic acid and stained o/n with 0.08M picric acid, 0.04% (w/v) Coomassie Brilliant Blue R250 (Sigma Aldrich), destained in tap water and acquired with Versadoc3000 (Biorad).

Amino acids analysis

Collagen type I, extracted from skin and bone of WT and *tmem38b* fish (30 µg) as described above, was hydrolyzed in 6M HCl at 110 °C under nitrogen and hydrolysates were derivatized with orthophthalaldelyde (OPA) and 9-fluorenyl-methyl-chloroformate (FMOC). OPA and FMOC derivatives were analyzed by Jasco X-LC Amino Acid Analyzer with a fluorescence detector (excitation/emission at 340/446 nm for OPA-amino acids an excitation/emission at 268/308 nm for FMOC-amino acids). The results are means of three independent analyses on three WT and three *tmem38b*^{-/-} and one *tmem38b*^{Δ120-7/Δ120-7} fish.

Morphometric analysis

Zebrafish were anesthetized with 0.016% (w/v) tricaine and images of fish in lateral position were acquired with a Leica M165 FC microscope (Leica) connected to a Leica DFC425 C digital camera (Leica). Measurements were performed using the Leica LAS v4.5 software (Leica). The Standard Length (SL) was measured as the distance from the upper part of the snout to the caudal peduncle, or to the posterior tip of the notochord in larvae. The Height of Anterior of Anal fin (HAA) was measured immediately anteriorly to the anal fin and perpendicularly to the axis defined by the SL as the distance from ventral to dorsal. The Snout-Operculum Length (SOL) is the distance from the snout to the operculum. The Height at Eye (HE) is the distance from ventral to dorsal, measured posteriorly to the eye and perpendicularly to the axis defined by the SL (Parichy et al. 2009) (**Figure 1B**).

The level of the swim bladder insufflation was evaluated by counting the number of lobes on lateral light images of larvae at 5, 7, 14, 21 dpf (**Figure 1A**).



Figure 1. Representative lateral images of larvae and adult fish. **A.** Lateral view of 21 dpf larva. The Standard length is indicated in red and the arrowheads indicate the first and the second lobe of the swim bladder. Scale bar: 2 mm. **B.** Lateral images of adult fish. In red the standard length, in yellow the Height at Eye (HE), in light blue the Snout-Operculum Length (SOL) and in green the Height of Anterior of Anal fin (HAA). Scale bar: 5 mm.

Alizarin red and alcian blue staining

Cartilage and bone were stained with alcian blue and alizarin red S in order to evaluate the mineralization level of mutant and WT. Fish were euthanized with an overdose of 0.03% (w/v) tricaine and fixed o/n in 4% (w/v) PFA in PBS with 0.9 mM CaCl₂ and 0.49 mM MgCl₂, pH 7.4 at 4 °C. The day after, samples were washed and stored in PBS with 0.9 mM CaCl₂ and 0.49 mM MgCl₂, pH 7.4.

Upon fixation in 4% (w/v) PFA, 7, 14 and 21 dpf fish were bleached in 3% (v/v) H₂O₂, 0.5% (w/v) KOH at RT. After few washes in 25% (v/v) glycerol, 0.1% (w/v) KOH samples were stained for 2 hours with 0.01% (w/v) alizarin Red S (Sigma Aldrich), 25% (v/v) glycerol, 100 mM Tris–HCl, pH 7.5 at RT. Soft tissues were digested with 1 mg/mL trypsin (Trypsin from bovine pancreas, Sigma Aldrich) in 30% (w/v) solution of saturated B₄Na₂O₇. Few washes in saturated (w/v) B₄Na₂O₇ were performed to stop tissue digestion and then samples were stained for 2 more hours with 0.01% (w/v) alizarin Red S (Sigma Aldrich), 25% (v/v) glycerol, 100 mM Tris–HCl, pH 7.5 solution at RT. Finally, fish were washed in increasing glycerol series (25, 50, 80%), 0.1% KOH and stored at 4 °C in 100% glycerol, 0.1% KOH. For 1 and 2 mpf fish a double staining with alcian blue and alizarin red was performed. Fish were first put o/n at RT with a solution of 0.02% (w/v) alcian Blue 8GX (Sigma Aldrich), 70% (v/v) ethanol, 80 mM MgCl₂ and then hydrated in a series of ethanol (80, 50, 25%), in 100 mM Tris–HCl, pH 7.5, 10 mM MgCl₂. To eliminate the pigmentation a bleaching step was performed with 3% (v/v) H₂O₂, 0.5% (w/v) KOH at RT, followed by two washes in 25% (v/v) glycerol, 0.1% (w/v) KOH. Soft tissues were digested with 1 mg/mL trypsin (Trypsin from bovine pancreas, Sigma Aldrich) in 30% (w/v) solution of B₄Na₂O₇. Few washes in 100% (w/v) B₄Na₂O₇ were performed to stop tissue digestion. Then samples were stained with 0.01% (w/v) alizarin Red S (Sigma Aldrich), 25% (v/v) glycerol, 100 mM Tris–HCl, pH 7.5 solution at RT for 2 hours. Finally, samples were washed in increasing glycerol, 0.1% KOH series (25, 50, 80%) and stored at 4 °C in 100% glycerol, 0.1% KOH. Images were acquired using a Leica M165 FC microscope connected to a Leica DFC425 C digital camera. The level of ossification of notochord (NC), 5th ceratobranchial (5CB), cleithrum (CL), palatoquadrate (PQ), hyomandibular bone (HM), ceratohyal bone (CHB) and brachioistegal ray 3 (BS3) was qualitatively described from beginning/incomplete to

complete ossification based on the intensity of the staining (**Figure 2**). Two independent investigators unaware of the genotype performed the analysis. At 1 and 2 mpf the vertebral dimensions were evaluated by measuring from the second centrum articulated with the ribs, while at 21 dpf counting 10 vertebrae starting from the first ossified centrum (**Figure 3A**)

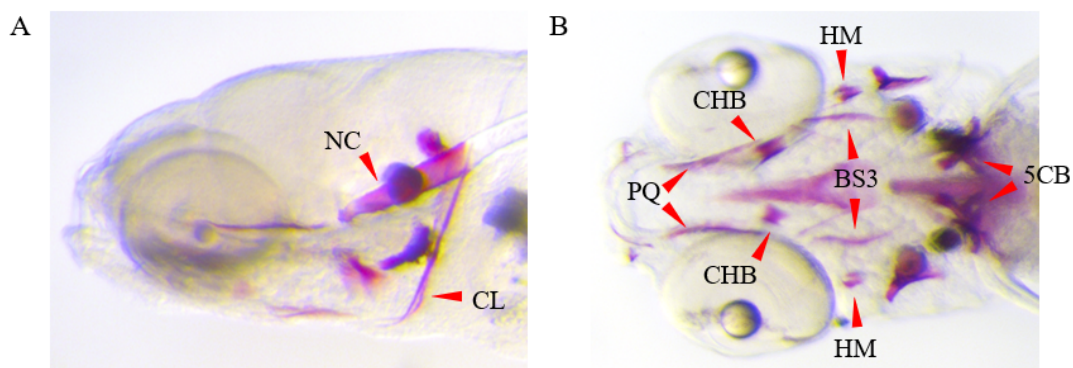


Figure 2. Alizarin red staining. **A.** Representative lateral image of alizarin red stained fish to evaluate the mineralization of notochord (NC) and cleithrum (CL). **B.** Representative ventral image of fish stained with alizarin red to evaluate the mineralization of 5th ceratobranchial (5CB), ceratohyal bones (CHB), palatoquadrate (PQ), hyomandibular bone (HM) and brachioistegal ray 3 (BS3).

X-ray

X-Ray of 4 and 6 mpf fish were performed using Faxitron Mx-20 (Faxitron), 25 kV for 10 seconds. Images were acquired by Kodak Direct View Elite CR System and k-Pacs software (Kodak) and vertebrae length and height were measured as shown in **Figure 3C**.

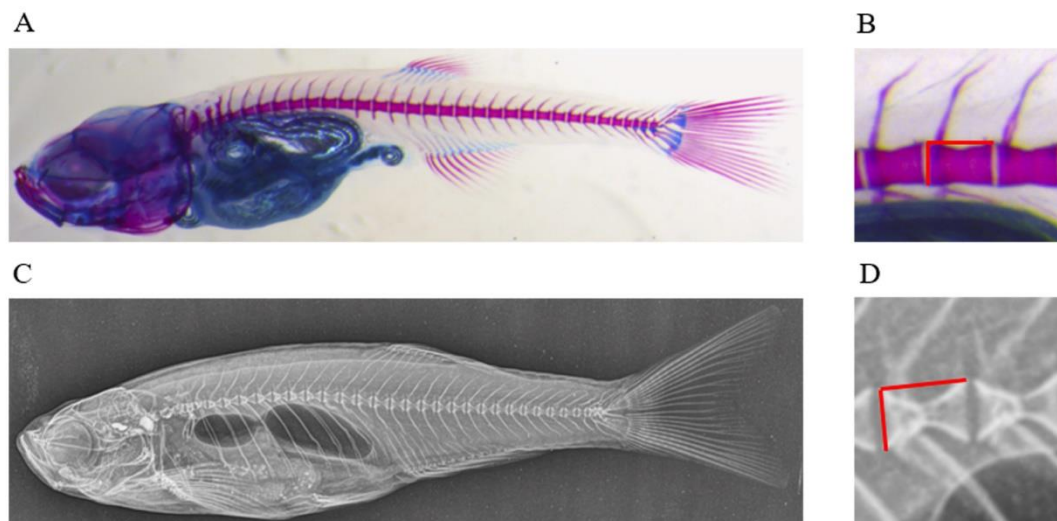


Figure 3. **A.** Representative lateral image of alizarin red and alcian blue double stained adult fish. **B.** Magnification of vertebral centra. Red lines show measured centrum length and height. **C.** Representative lateral image of x-ray performed on adult fish. **D.** Magnification of vertebral centra. Red lines show measured centrum length and height.

Micro-Computed Tomography

Micro-Computed Tomography (μ CT) at a resolution of 2 μ m (Skyscan 1272, Bruker, Kontich, Belgium) was used to evaluate skeletal morphology and bone microstructures. Adult fish were fixed in 4 % (w/v) PFA for 24 hours and placed in a moist chamber during scanning. Whole body scans were acquired at 40 kV and 230 μ A. Ring artifact and beam hardening correction was kept constant for all samples during reconstruction with NRecon (Bruker, Kontich, Belgium).

The vertebral body length (VBL), ratio of bone volume and total volume (BV/TV), bone volume (BV), thickness of the vertebral bone (V. Th), eccentricity, moment of inertia, cortical thickness (C. Th) and bone perimeter (B. Pm) were evaluated.

Whole mount immunohistochemistry

WT and mutant zebrafish embryos were collected at 5 dpf and fixed o/n in 4% (w/v) PFA in PBS. After being washed in PBS, samples were permeabilized in increasing methanol series (0%, 25%, 50%, 75%, 100%) and stored at -20 °C until use. Samples were then hydrated

with decreasing ethanol scale (100%, 80%, 70%, 50%, 0%) in PBS and digested with 0.1% (w/v) proteinase K in PBS at 25 °C for 15 min and 2% (w/v) hyaluronidase in PBS at 25 °C for 20 min. After 30 min in 4% (w/v) PFA embryos were washed in 50 mM NH₄Cl in PBS, for 1 h at RT. Embryos were incubated with 0.5% (w/v) bovine serum albumin (BSA, Sigma Aldrich) and 0.5% (v/v) H₂O₂, for 30 min at RT to block the activity of endogenous peroxidase. After a 5 min wash with PBS, 0.05% (v/v) Tween-20 (Sigma Aldrich) (PBS-T) samples were incubated in 5% (w/v) BSA in PBS-T as blocking solution for 2 h at RT. Hsp47b or Hsp47a purified antibody (1:100 in 5% BSA in PBS-T) (kindly provided by Prof Wegener, Cologne) and anti-rabbit secondary antibody (1:200 in 1% BSA in PBS-T) were used. DAB substrate (Thermo Scientific) was added until appearance of the staining. Fish were then incubated in increasing glycerol series (25%, 50%, 80%) and stored at 4 °C in 100% glycerol. Images were acquired using a Leica M165 FC microscope connected to a Leica DFC425 C digital camera. The purple dots in the skin were considered a positive signal and the intensity was evaluated from zero to high (0, +, ++). Two independent investigators unaware of the genotype performed the analysis.

Histological analysis

For histological analysis WT and mutant fish at 1 mpf were fixed o/n at 4 °C in 1.5% (v/v) PFA (Sigma Aldrich), 1.5% (v/v) glutaraldehyde (Sigma Aldrich), 0.1 M sodium cacodylate buffer (pH 7.4) and 0.001% (w/v) CaCl₂. The samples were decalcified in 0.1M EDTA for 5 days at 4 °C. Samples were rinsed in 0.1 M sodium cacodylate buffer containing 10% sucrose and post fixed for 36 h using 1% (w/v) OsO₄ in 0.1M sodium cacodylate buffer at pH 7.4 containing 0.825% (w/v) K₃Fe (CN)₆. After rinsing with demineralized water, specimens were dehydrated in presence of CuSO₄ bars. Subsequently, zebrafish were infiltrated with low-viscosity epoxid embedding medium (Spurr 1969).

Parasagittal 1 mm semi-thin sections of the sites of interest were mounted on superfrost slides stained for 1 min with toluidine blue (0.2% toluidine blue, 2% Na₂CO₃), rinsed with demineralized water, air-dried and mounted with DPX (Fluka, Buchs).

A Leitz DL22 microscope (Leica) equipped with a PL APO 63/1.40 Oil lens and a 5MP CCD camera was used for analysis and documentation.

Ultra-thin (50-90 nm) sections were cut using a Reichert UltracutS ultramicrotome (Leica) with a diamond knife (Diatome Ltd.) and mounted on formvar-coated single slot copper grids (Agar Scientific). The sections were stained with uranyl acetate and lead citrate (EM stain, Leica) and viewed with a Jeol JEM-1010 (Jeol Ltd) TEM operating at 60 kV.

Images were digitalized using the DITABIS drum scan system (Ditabis AG) (Dewit, Witten, and Huysseune 2011).

Transmission electron microscopy (TEM) images were used to measure the area of collagen type I fibers in osteoblast and fibroblasts' extracellular matrix. The empty space between collagen type I fibers in extracellular matrix was measured by Leica LAS v4.5 software (Leica), and then the collagen type I fibers area was calculated.

Statistical analysis

All values were expressed as mean \pm standard deviation (SD). Unpaired parametric t-test or the analogous non-parametric test (Kruskal Wallis or Dunn's test) was applied to assess differences in quantitative parameters between each mutants and their respective WT group. A p-value level less than 0.05 was considered significant. Statistical analyses were performed using Excel or SigmaPlot.

Results

In silico analysis

Despite the genome duplication occurred in teleosts over 340 million years ago (Meyer and Schartl 1999), only one copy of *tmem38b* is present in zebrafish. *tmem38b* maps on chromosome 21, is composed by 10 exons and encodes for the 289 amino acids protein Tric-b. The *in silico* analysis, performed using the genome browser Genomicus (v 93.01) to investigate the conservation of the chromosomal region surrounding *tmem38b* among zebrafish and other vertebrates, revealed a synteny block including, in all the analysed species, two conserved *tmem38b* flanking genes (*rad23B* and *klf4*) (**Figure 4A**).

The conservation of tric-b between humans and zebrafish was evaluated by Blastp analysis. The amino acids alignment revealed that the zebrafish Tric-b protein has 45% homology and 66% similarity with the human protein. Moreover, the seven transmembrane domains and the KEV tripeptide, which is important to guarantee the correct formation and regulation of pore channel, are conserved (**Figure 4B**).

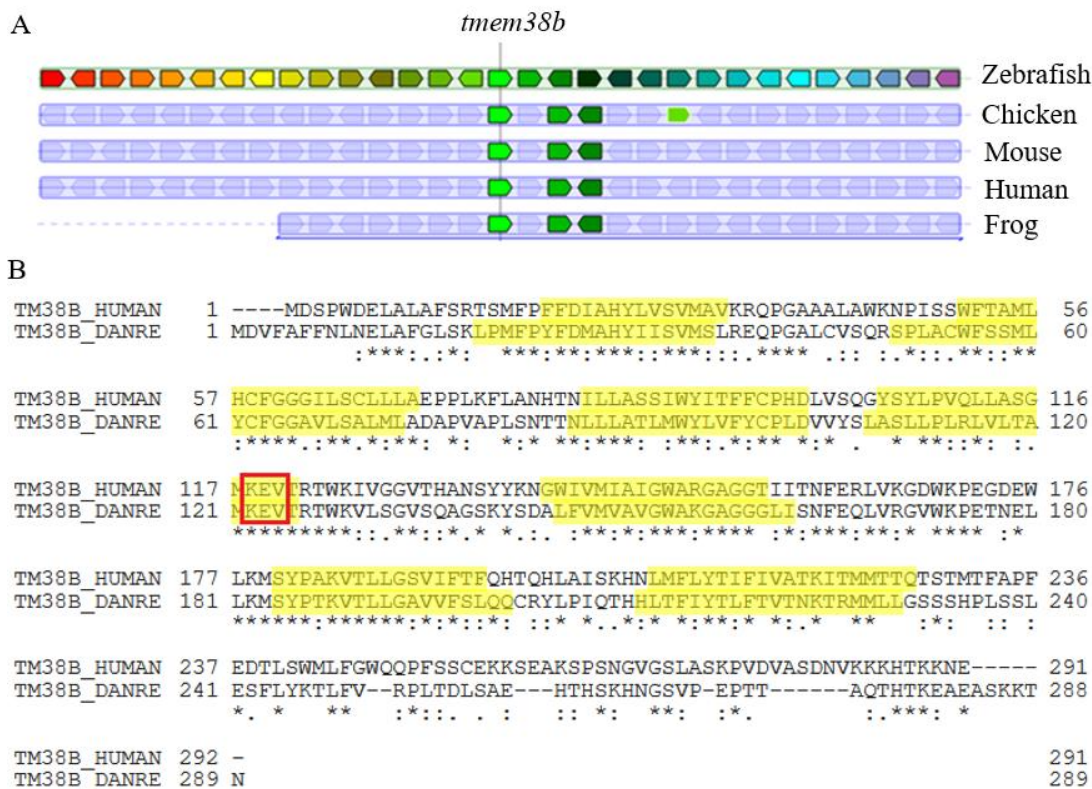


Figure 4. In silico analysis of *tmem38b*. A. Synteny map comparing the genes flanking *tmem38b* locus among zebrafish (*D. rerio*), chicken (*G. gallus*), humans (*H. sapiens*), mouse (*M. musculus*) and frog (*X. tropicalis*). B. Alignment of the *H. sapiens* and *D. rerio* *Tric-b*. The seven transmembrane domains are highlighted in yellow and the red box indicates the KEV motif. Asterisks indicate positions with fully conserved residue, colons indicate the conservation of amino acids with strongly similar property and dots indicate conservation between amino acids sharing weak similar property.

tmem38b expression in zebrafish embryos

tmem38b temporal and spatial expression were evaluated on WT embryos. The real-time qPCR performed on RNA extracted from pools of embryos at different stages of development (from 2-4 cells to 96 hours post fertilization (hpf)) revealed 2 peaks of expression. A maternal *tmem38b* transcript was present at 16-32 cells stage, suggesting a relevant role of the gene during the very first stages of development. In addition, a second peak of expression was detectable during the somitogenesis, confirming also a *tmem38b* role during the zygotic period (**Figure 5A**). *In situ* hybridization was performed on WT embryos

at 72 and 120 hpf to determine the spatial localization of *tmem38b*, which was detected at the level of the head bones and of the swim bladder (**Figure 5B**).

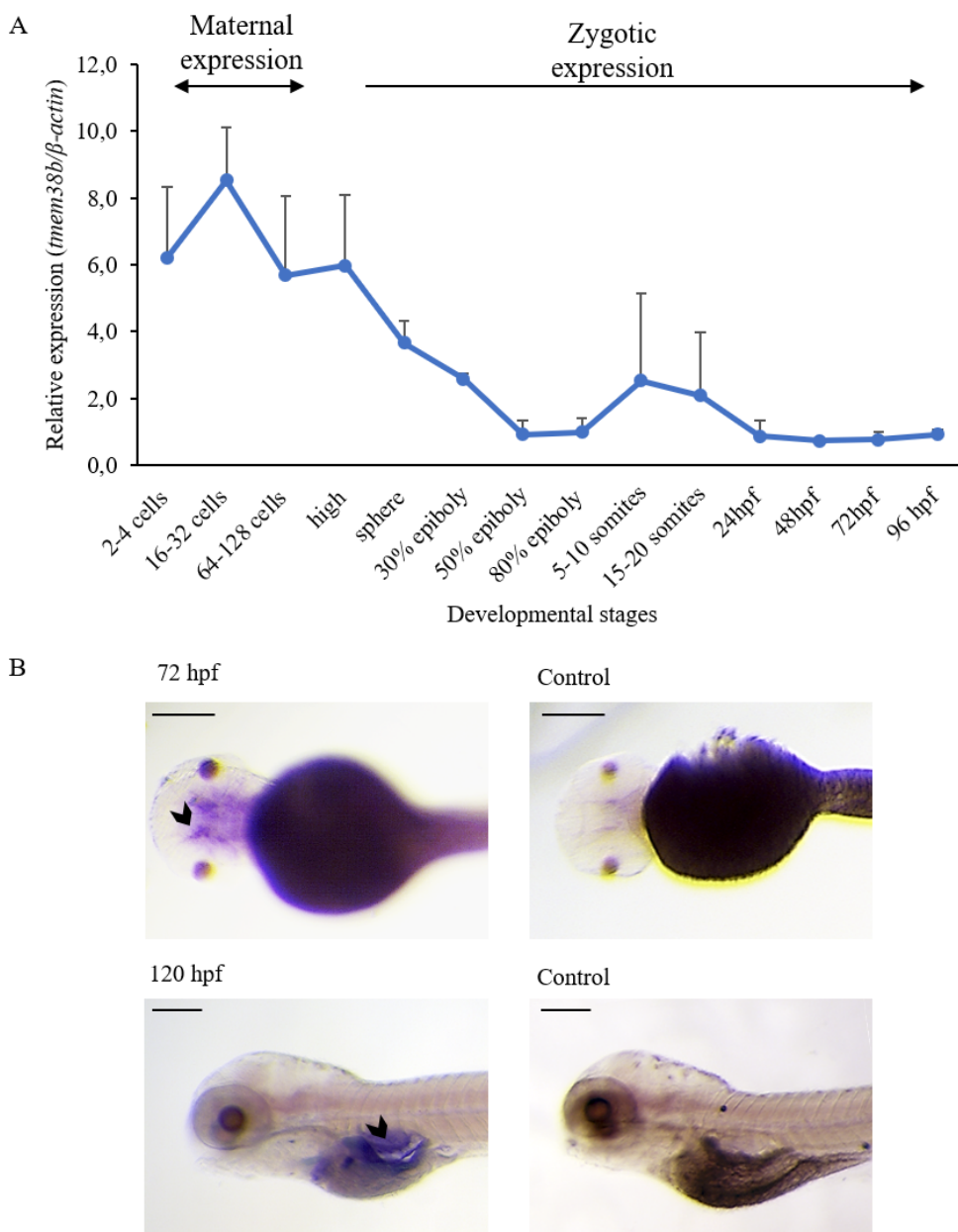


Figure 5. Temporal and spatial analysis of *tmem38b* expression. **A.** *tmem38b* temporal expression at different embryonic stages, from 2-4 cell stage to 96 hours post fertilization (hpf). **B.** Whole mount in situ hybridization on WT embryos at 72 and 120 hpf. The violet signal (black arrowhead) indicates the presence of *tmem38b* transcript in the head bones and in the swim bladder. For control the sense probe was used. Scale bar: 200 μ m.

Generation of OI type XIV zebrafish models using CRISPR/Cas9 gene editing

OI type XIV zebrafish models were obtained by CRISPR/Cas9 gene editing. The selection of the genomic target sequence in *tmem38b* gene was performed using the online available software CHOPCHOP (<https://chopchop.rc.fas.harvard.edu>) (**Figure 6A**). Among several potential targets, which are 20 bp stretches with a 5'-GG dinucleotide necessary for optimal T7 promoter transcription efficiency, a sequence on exon 7 of *tmem38b* was chosen (11391-11416 nt, NC_007132.7) based on the absence of potential off targets and on the optimal GC-content (52%) (Gagnon et al. 2014).

Two commercially available plasmids were used to synthesize the gRNA and Cas9 mRNA, respectively. The first contains the cloning site for the gRNA sequence under the control of T7 promoter and the second the Cas9 endonuclease coding sequence with nuclear localization signals (nls) at both amino and carboxyl end and codons optimized for zebrafish expression (nls-zCas9-nls) (Jao, Wentz, and Chen 2013). The cloning experiment was performed as described in Methods and both gRNA and Cas9 mRNA were synthesized, after plasmid linearization, by *in vitro* transcription.

Generation of two *tmem38b* mutants

The *tmem38b* gRNA and Cas9 mRNA were mixed with the red tracer rodhamine and co-injected into one/two-cell-stage embryos. A successful injection was determined at 1 day post fertilization (dpf) by the visualization of the tracer inside the embryo under a fluorescent microscope. The targeting efficiency was verified using the T7 endonuclease I (T7EI) assay. To this purpose 10 embryos were selected, DNA extracted and amplified in the region of the selected target sequence. After denaturation and renaturation, the DNA amplicons were digested by T7 endonuclease and only in presence of mutations the amplicon (212 bp), containing heteroduplex, was cut by the enzyme into two fragments (~ 80 and ~130 bp) (**Figure 6B**).

The F0 mosaic zebrafish obtained by CRISPR/Cas9 were screened by T7EI assay, as described above, and by Sanger sequencing. Since the double-stranded breaks catalysed by the Cas9 endonuclease lead to the activation of the error-prone non-homologous end joining (NHEJ) repair system, successfully targeted embryos were mosaic, carrying different mutations. Indeed, the sequence electropherograms obtained from mosaic fish appeared

disturbed and the signal decreased in the target region, due to the presence of more than one mutation in the same locus. The overall mutagenesis rate was 63%.

In order to identify the specific mutations, the amplified region containing the targeted sequence of F0 mosaic fish was subcloned in the TA cloning vector and sequenced. The majority of mutations were insertion/deletion (*indels*), which lead to the introduction of premature stop codon at the protein level (**Table 5**).

The F0 mosaic zebrafish were crossed with wild type to identify fish with mutation in the germ line. To this purpose, several pools of embryos from the various mating were collected at 1 dpf and screened by T7EI assay.

Table 5. Mutations identified in *tmem38b* F0 fish.

DNA mutation	Protein defect	Frequency
c.529_532delGAAG	p.Glu123*	6% (1/16)
c.523_529delATGAAGG	p. <i>Met121Lysfs*122</i>	6% (1/16)
c.525_538delAAGGAAGTGACGA	p. <i>Lys122Asnfs*150</i>	6 % (1/16)
c.524_540delTGAAGGAAGTGACGAGA	p. <i>Met121Asnfs*149</i>	6 % (1/16)
c.528_529insTGACGA	p.Glu123*	6 % (1/16)
c.524_527delTGAA	p. <i>Met121Arg*123</i>	13% (2/16)
c.527_538delAAGGAAGTGACGAinsGTGACGAGTGACGT	p.Lys122Ser; Glu123Asp; <i>Val124Glufs*125</i>	6 % (1/16)
c.526_540delAAGGAAGTGACGAGA	p.Lys122_Arg126del	6 % (1/16)
c.523_532delATGAAGGAAG	p.Met121*	6 % (1/16)
c.527_528delAGinsTATGAAGCCAT	p. <i>Lys122Ilefs*123</i>	6 % (1/16)
c.526_528delAAGinsCACCT	p.Lys122His; Glu123Leu; <i>Val124Lysfs*125</i>	6 % (1/16)
c.524_532delTGAAGGAAG	p.Lys122_Val124del	6 % (1/16)
c.524_530delTGAAGGA	p. <i>Met121Lysfs*122</i>	6 % (1/16)
c.526_527insCGAGAACC	p.Lys122Thr; Glu123Arg; Val124Thr; Thr125Arg; <i>R126Kfs*127</i>	6 % (1/16)
c.523_527delATGAA_insT	p.Met121Trp; Glu123*	6 % (1/16)
c.526_532delAAGGAAG	p.Lys122*	6 % (1/16)
c.528_531delGGAA	p.Glu123*	13% (2/16)
c.529delG	p. <i>Glu123Lysfs*124</i>	6 % (1/16)
c.525_533delGAAGGAAinsTAGGCT	p.Met121Ile; Lys122Arg; <i>Glu123Leufs*124</i>	6 % (1/16)
c.527_533delAGGAAGTinsCGA	p.Lys123Thr; Glu123Arg; Val124Arg; Thr125Glu; Arg126Pro; Thr127Gly; Trp128Arg; <i>Lys129Phefs*130</i>	6 % (1/16)

Selection of F1 heterozygous and generation of F2 homozygous mutants

Two zebrafish F1 mutant lines were selected and used to generate and characterize the F2 homozygous *tmem38b* knock-out fish. The first mutant line was characterized by a 7 nucleotides deletion, which caused frameshift and led to the introduction of a premature stop codon at amino acid 122 (c.524_530delTGAAGGA, p.*Met121del*122*, *tmem38b*^{-/-}) (**Figure 6C**). The second mutant carried a 24 nucleotides *in frame* deletion, resulting in the deletion of the KEV motif (c.517_540del24nt, p.*Ala120_Thr127*, *tmem38b* ^{Δ 120-7/ Δ 120-7}) (**Figure 6C**).

Heterozygous fish for the same mutation were crossed to obtain the homozygous F2 mutants. To genotype both *tmem38b*^{-/-} and *tmem38b* ^{Δ 120-7/ Δ 120-7} different size of PCR products were evaluated; the expected amplicons were 142 bp for the WT and 135 bp and 118 bp amplicons for *tmem38b*^{-/-} and *tmem38b* ^{Δ 120-7/ Δ 120-7}, respectively (**Figure 6D-E**).

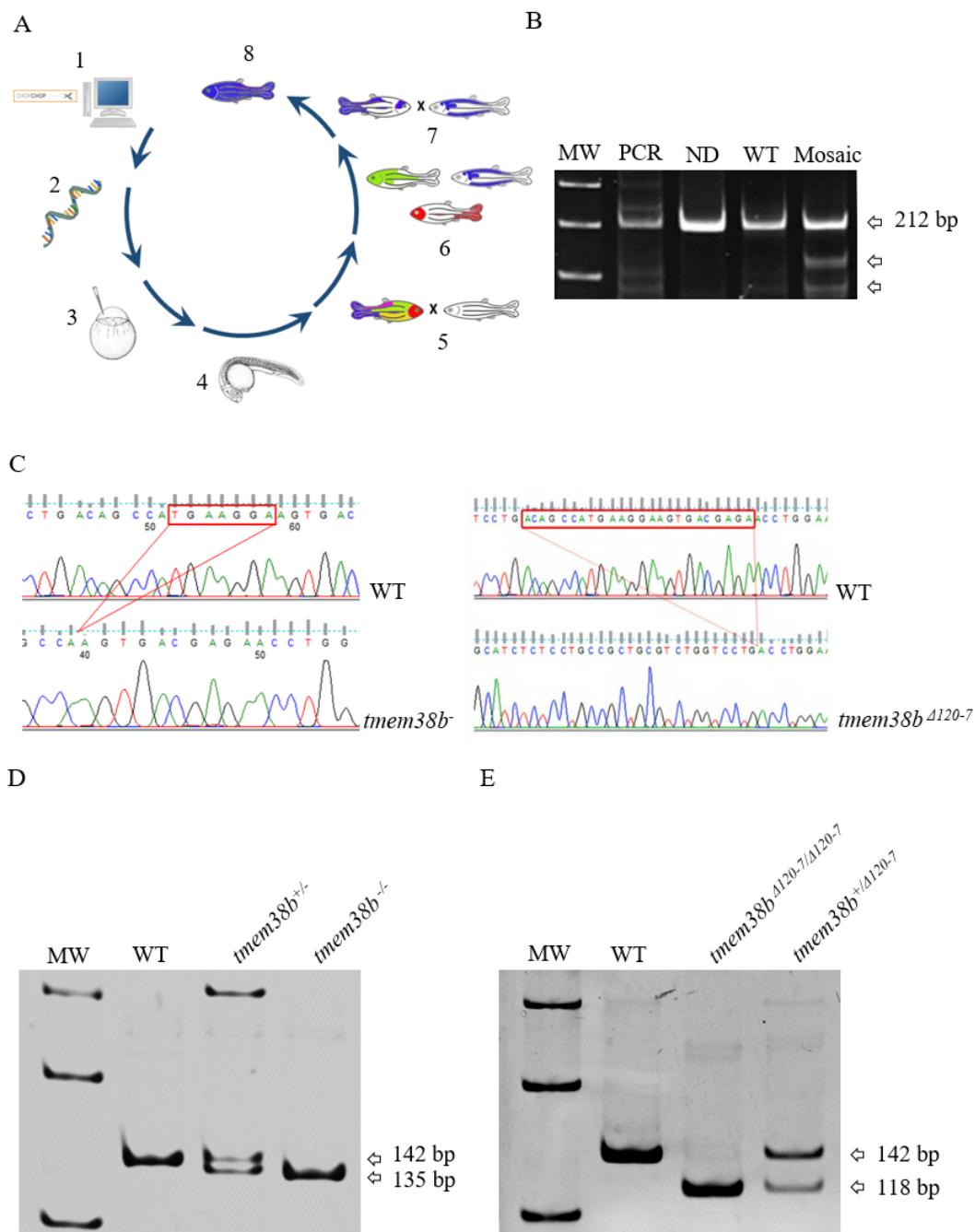


Figure 6. *In vivo* OI type XIV model generation using CRISPR/Cas9 system. **A.** Schematic view of the strategy adopted to create OI type XIV zebrafish models. **A.** (1) *In silico* target sequence identification; (2) generation of gRNA and Cas9 mRNA; (3) injection of the RNAs in zebrafish fertilized embryos; (4) evaluation of targeting efficiency by T7 endonuclease assay; (5) generation of mosaic germ line fish; (6) crossing mosaic with WT fish to obtain the F1 heterozygous animals; (7-8) crossing heterozygous fish with identical mutations to obtain the F2 homozygous. **B.**

Representative gel, which indicates the expected bands after T7EI assay. Arrows indicate the cleaved bands. ND = not digested **C.** Mutations found in selected heterozygous F1 fish. On the left panel, the *tmem38b*^{-/-} mutant allele carrying 7 bp deletion; on the right panel, the *tmem38b*^{Δ120-7} mutant allele carrying 24 bp deletion. **D.** Representative gel indicating the expected PCR products for *tmem38b*^{-/-} genotype. **E.** Representative gel indicating the expected PCR products for *tmem38b*^{Δ120-7/Δ120-7}. MW: molecular weight; bp: base pair.

tmem38b expression in the two mutant zebrafish models

To analyse *tmem38b* transcript level, qPCR on RNA extracted from skin of adult fish was performed. In *tmem38b*^{-/-} the expression was strongly reduced compared to WT (WT: 0.74 ± 0.23, *tmem38b*^{-/-}: 0.08 ± 0.01; p<0.01), suggesting the activation of non-sense mediated mRNA decay (NMD). Only 50% of the transcript was expressed in heterozygous fish respect to WT, as expected (*tmem38b*^{+/-}: 0.26 ± 0.03) (**Figure 7A**). On the contrary, the *tmem38b* expression in *tmem38b*^{Δ120-7/Δ120-7} homozygous and heterozygous was comparable to WT (WT: 1.59 ± 0.78; *tmem38b*^{+/Δ120-7}: 1.27 ± 0.4; *tmem38b*^{Δ120-7/Δ120-7}: 2.00 ± 0.8) (**Figure 7B**).

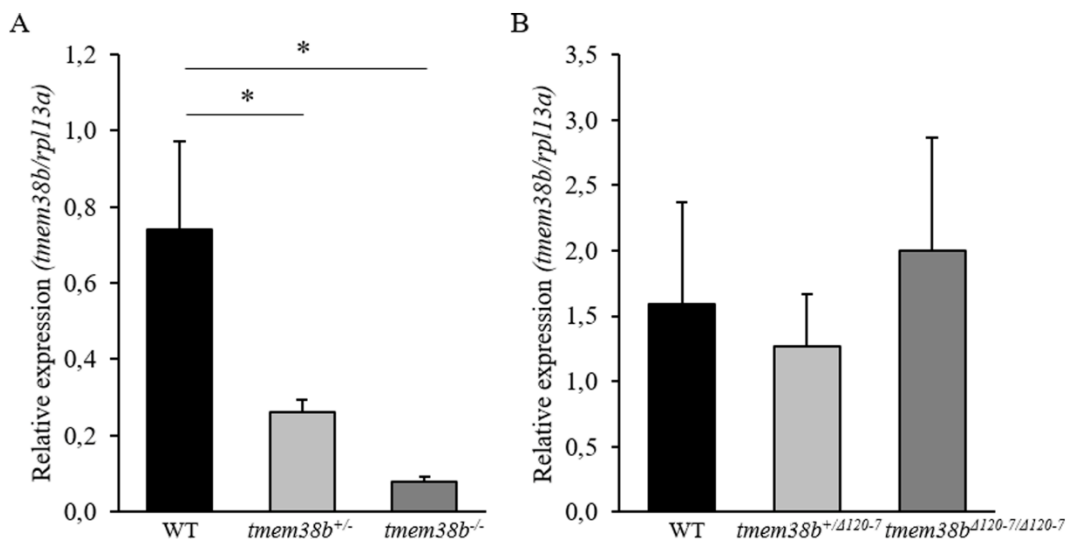


Figure 7. *tmem38b* expression analysis. **A.** A 90% reduction of *tmem38b* transcript was found in *tmem38b*^{-/-} compared to WT (WT n=2, *tmem38b*^{+/-} n=2; *tmem38b*^{-/-} n=2). **B.** Normal level of transcript was observed in *tmem38b*^{Δ120-7} heterozygous and homozygous mutants compared to WT. (WT n=2, *tmem38b*^{Δ120-7/-} n=2; *tmem38b*^{Δ120-7/Δ120-7} n=2) (*P<0.05).

Skin and bone collagen type I analysis

OI type XIV patients are characterized by reduced collagen type I post translational modification due to decreased hydroxyl-lysine level, as revealed by a faster α (I) bands migration on SDS-PAGE of type I collagen extracted from patients' fibroblasts and osteoblasts (Cabral et al. 2016). Collagen type I was extracted from skin and bone of adult WT, *tmem38b*^{-/-} and *tmem38b* ^{Δ 120-7/ Δ 120-7} fish and analysed by SDS-Urea-PAGE. No difference in electrophoretic mobility was detectable by Coomassie blue gel staining (**Figure 8**).

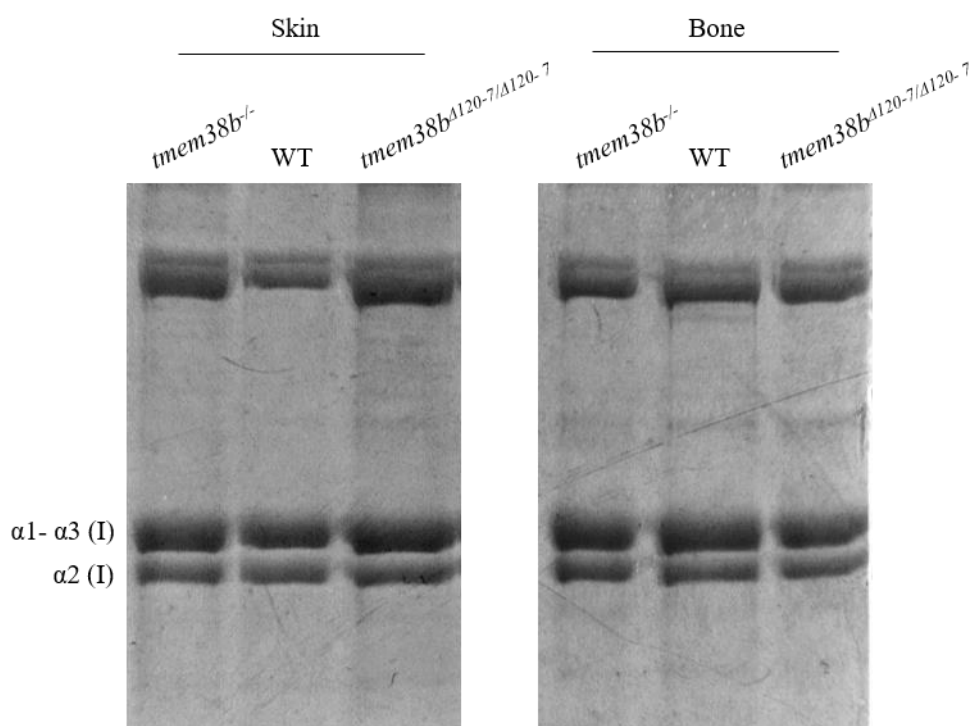


Figure 8. Representative type I collagen SDS-Urea-PAGE. The α bands of collagen type I extracted from skin and bone of both *tmem38b* mutants showed a migration comparable to WT fish.

Amino acid analysis was performed to investigate the level of lysine and proline hydroxylation in collagen samples extracted from bone and skin of WT and homozygous mutant. In *tmem38b*^{-/-} the Hyl percentage (Hyl/Hyl+Lys) was similar to WT, both in bone and in skin (**Table 6**). In *tmem38b* ^{Δ 120-7/ Δ 120-7} a significant reduction of Hyl content was detectable in collagen extracted from bone (**Table 6**).

Table 6. Collagen type I lysine/hydroxylysine and proline/hydroxyproline ratio of *tmem38b* mutant fish compared to WT. In bold the p value <0.05.

		Hyl/Hyl+Lys (%) Mean \pm SD	p value	Hyp/Hyp+Pro (%) Mean \pm SD	p value
Bone	WT	38.6 \pm 1.3		45.3 \pm 0.5	
	<i>tmem38b</i> ^{-/-}	38.0 \pm 0.8	0.52	45.4 \pm 0.2	0.97
	<i>tmem38b</i> ^{Δ120-7/Δ120-7}	33.1 \pm 3.1	0.004	45.1 \pm 0.4	0.51
Skin	WT	32.6 \pm 1.7		45.2 \pm 0.4	
	<i>tmem38b</i> ^{-/-}	31.3 \pm 0.8	0.28	44.5 \pm 0.4	0.09
	<i>tmem38b</i> ^{Δ120-7/Δ120-7}	31.7 \pm 0.5	0.47	44.9 \pm 0.3	0.45

Skeletal characterization of $tmem38b^{-/-}$ and $tmem38b^{\Delta 120-7/\Delta 120-7}$

A deep morphometric and skeletal analysis was undertaken to characterize the phenotype of both mutants. The $tmem38b^{-/-}$ was evaluated first and, based on the collected data, the other model was analysed.

Morphometric analysis of $tmem38b^{-/-}$

The standard length (SL) of WT and $tmem38b^{-/-}$ was measured from 5 dpf to 6 months post fertilization (mpf). At 21 dpf and 1 mpf $tmem38b^{-/-}$ fish were significantly shorter than WT (21 dpf: WT: 5.80 ± 0.39 mm, $tmem38b^{-/-}$: 5.53 ± 0.59 mm, $p < 0.05$; 1 mpf: WT: 7.18 ± 1.05 mm, $tmem38b^{-/-}$: 6.4 ± 1.35 mm, $p < 0.05$) (**Figure 9**). At all the other time points no differences were detectable (**Supplementary Table 1**). The heterozygous fish length was always similar to WT, thus they were not further considered for the characterization.

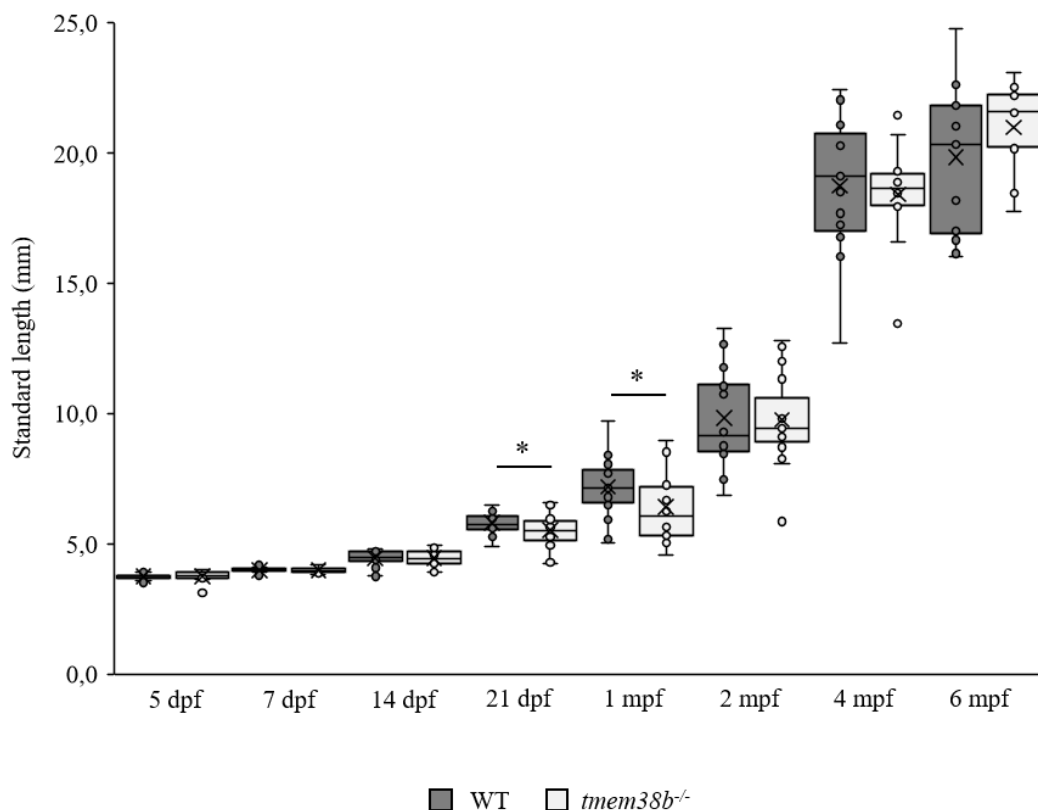


Figure 9. Growth curve of WT and *mem38b*^{-/-} fish. *mem38b*^{-/-} fish showed a reduced standard length compared to WT at 21 dpf and 1 mpf. (number of fish: 5dpf WT: 13, *mem38b*^{-/-}:12; 7 dpf: WT: 19, *mem38b*^{-/-}: 8; 14 dpf WT: 33, *mem38b*^{-/-}: 20; 21 dpf WT: 32, *mem38b*^{-/-}: 27; 1 mpf WT: 27, *mem38b*^{-/-}: 19, 2 mpf WT: 18, *mem38b*^{-/-}: 19; 4 mpf WT: 15, *mem38b*^{-/-}: 11; 6 mpf WT: 15, *mem38b*^{-/-}: 10). Data were expressed as mean \pm SD (*P<0.05).

The other morphometric measurements evaluated at 1, 2, 4 and 6 mpf, described in Methods, were the Height at Eye (HE), the Height of Anterior of Anal fin (HAA), the Snout-Operculum Length (SOL) (**Supplementary Table 2**).

At 1 mpf the HE was significantly reduced in *mem38b*^{-/-} compared to WT (WT: 1.23 ± 0.22 mm, *mem38b*^{-/-}: 1.08 ± 0.28 mm, $p=0.05$). The HAA and the SOL showed a reduced trend in homozygous fish, without reaching significant difference (HAA WT: 0.85 ± 0.22 mm, *mem38b*^{-/-}: 0.71 ± 0.27 mm, $p=0.08$; SOL WT: 1.91 ± 0.29 mm, *mem38b*^{-/-}: 1.67 ± 0.44 mm, $p=0.06$). Body disproportion was also analysed, the SL/HAA ratio was significantly higher in homozygous *mem38b*^{-/-} compared to WT (WT: 8.98 ± 1.33 mm, *mem38b*^{-/-}: 10.07

± 1.85 mm, $p=0.03$) suggesting a reduced body thickness in mutant fish, while the SOL/HE ratio was similar between WT and mutant (WT: 1.56 ± 0.07 , $tmem38b^{-/-}$: 1.52 ± 0.08 , $p=0.22$) (**Figure 10, Supplementary Table 2-3**). At 2, 4 and 6 mpf the parameters mentioned above were similar between WT and mutant fish (**Supplementary Table 2-3**).

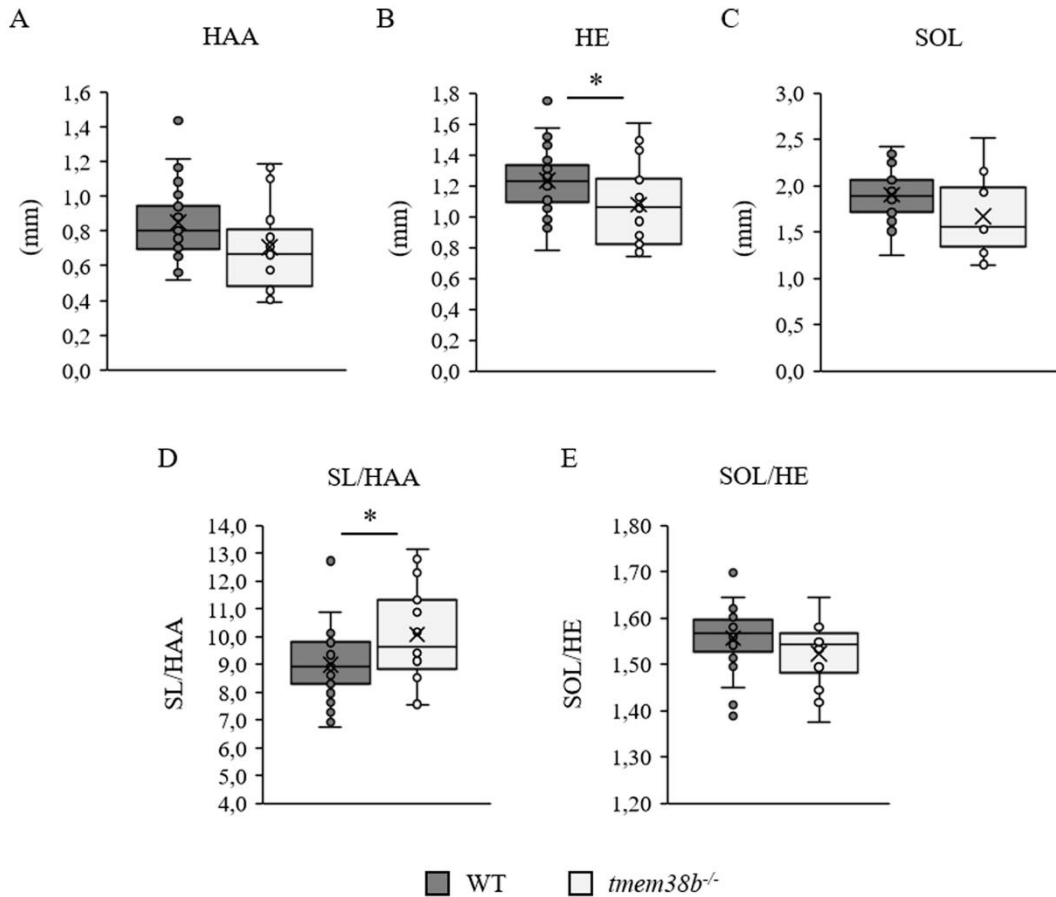


Figure 10. Morphometric parameters evaluated at 1 mpf in WT and *tmem38b*^{-/-} fish. **A.** A reduced trend in Height of Anterior of Anal fin (HAA) was evident in mutant fish compared to controls (WT n=25, *tmem38b*^{-/-} n=15). **B.** The *tmem38b*^{-/-} fish showed a significant reduced length of Height at Eye (HE) compared to WT (WT n=26, *tmem38b*^{-/-} n=15). **C.** The Snout-Operculum Length (SOL) was reduced in mutant fish compared to controls (WT n=23, *tmem38b*^{-/-} n=13). **D.** *tmem38b*^{-/-} showed a significant increase of SL/HAA ratio with compared to WT, suggesting a decrease of body thickness (WT n=25, *tmem38b*^{-/-} n=15). **E.** The ratio SOL/HE, an indicator of the size of the head, was similar in mutant and WT fish (WT n=23, *tmem38b*^{-/-} n=12). Data were expressed as mean \pm SD (* $P < 0.05$).

Swim bladder of *tmem38b*^{-/-}

tmem38b knock-out mice die immediately after birth for pulmonary insufficiency (Zhao et al. 2016). Since the fish swim bladder has the same evolutionary origin of the mammals' lungs (Graham 1997), the level of its inflation was evaluated from 5 dpf, when the first lobe develops, to 21 dpf, when both lobes are completely formed (Winata et al. 2009). No differences were detected at 5, 7 and 14 dpf between WT and *tmem38b*^{-/-} mutant (**Figure 11A-B-C**). Interestingly, at 21 dpf a significant decreased level of insufflation was detected in *tmem38b*^{-/-} fish with only 52% mutants which properly inflated both lobes (**Figure 11D**).

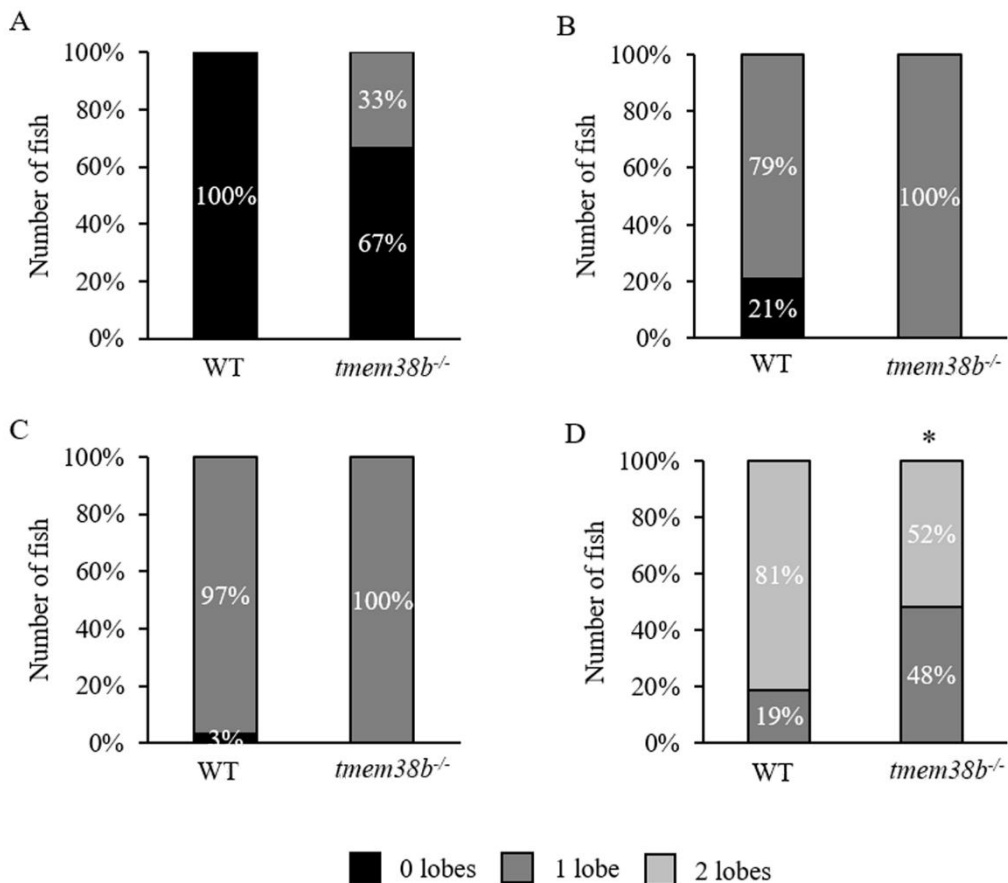


Figure 11. Inflation of swim bladder lobes in WT and *tmem38b*^{-/-} fish. A. Percentage of WT and *tmem38b*^{-/-} fish with inflated swim bladder at 5 dpf (WT n= 13, *tmem38b*^{-/-} n=12). B. Percentage of WT and *tmem38b*^{-/-} fish with inflated swim bladder at 7 dpf (WT n= 19, *tmem38b*^{-/-} n=8). C. Percentage of WT and *tmem38b*^{-/-} fish with inflated swim bladder at 14 dpf (WT n= 33, *tmem38b*^{-/-} n=20). D. Percentage of WT and *tmem38b*^{-/-} fish with inflated swim bladder at 21 dpf (WT n= 32, *tmem38b*^{-/-} n=27). 0, 1 and 2 in the legend refer to swim bladder inflated lobes (*P<0.05).

Mineralization analysis of *tmem38b*^{-/-}

Osteogenesis imperfecta is a bone related disorder characterized by reduced mineral density. Alizarin red staining was performed at 7, 14, 21 dpf and 1 and 2 mpf in order to evaluate the mineralization level of *tmem38b* mutants compared to controls.

The mineralization level of notochord (NC), 5th ceratobranchial (5 CB), cleithrum (CL), palatoquadrate (PQ), hyomandibular bone (HM), ceratohyal bone (CHB) and brachioistegal ray 3 (BS3) was evaluated, as described in Methods.

At 7 dpf no differences were detectable between WT and mutants in all cranial bones analysed (**Figure 12A**). At 14 dpf only 53% of *tmem38b*^{-/-} fish showed a complete level of mineralization of the NC in comparison with WT (82%) (**Figure 12B**). Moreover, at this stage the number of mineralized vertebrae was slightly reduced in mutant with respect to WT (WT: 11.26 ± 6.13 , *tmem38b*^{-/-}: 9.16 ± 5.07).

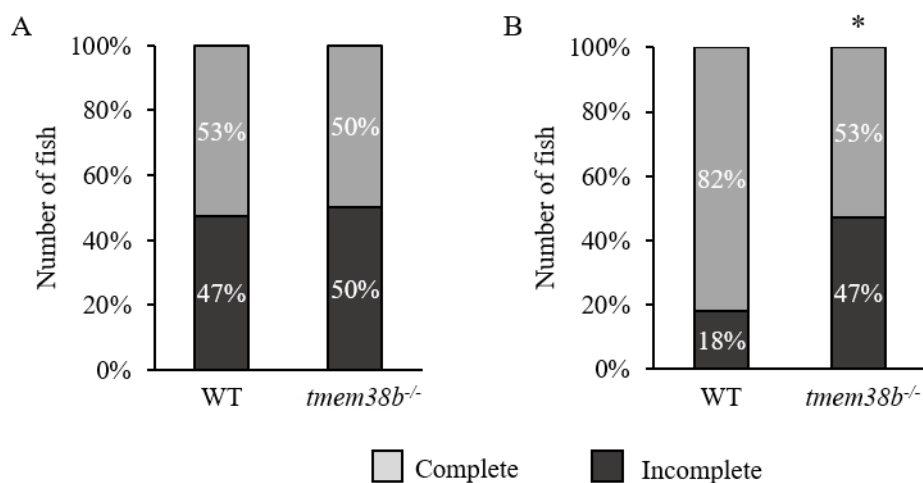


Figure 12. Analysis of notochord mineralization level. A. At 7 dpf the percentage of mutant fish with reduced notochord mineralization was similar to WT. B. At 14 dpf the percentage of mutant fish with reduced mineralization level was significantly less than WT (7 dpf, WT n= 19, *tmem38b*^{-/-} n=8; 14 dpf, WT n= 28, *tmem38b*^{-/-} n=17) (*P<0.05).

Vertebral dimensions of *tmem38b*^{-/-}

Alcian blue and alizarin red staining were performed at 21 dpf, 1 and 2 mpf, in order to analyse vertebral mineralization and size (**Figure 13A**). At 21 dpf and 1 mpf *tmem38b*^{-/-} vertebrae were characterized by a significant reduced length and height compared to WT (21 dpf, length: WT: 0.123 ± 0.019 mm, *tmem38b*^{-/-}: 0.113 ± 0.022 mm, $p < 0.01$; height: WT: 0.104 ± 0.027 mm, *tmem38b*^{-/-}: 0.098 ± 0.012 mm, $p = 0.01$; 1 mpf length: WT: 0.153 ± 0.021 mm, *tmem38b*^{-/-}: 0.135 ± 0.030 mm, $p < 0.01$, height: WT: 0.114 ± 0.011 mm, *tmem38b*^{-/-}: 0.108 ± 0.013 mm, $p < 0.01$).

At 2 mpf *tmem38b*^{-/-} showed reduced vertebral height compared to controls, but no changes in vertebral length (length: WT: 0.225 ± 0.051 mm, *tmem38b*^{-/-}: 0.223 ± 0.041 mm, $p = 0.73$; height: WT: 0.153 ± 0.026 mm, *tmem38b*^{-/-}: 0.144 ± 0.015 mm, $p < 0.01$) (**Figure 13B-C**).

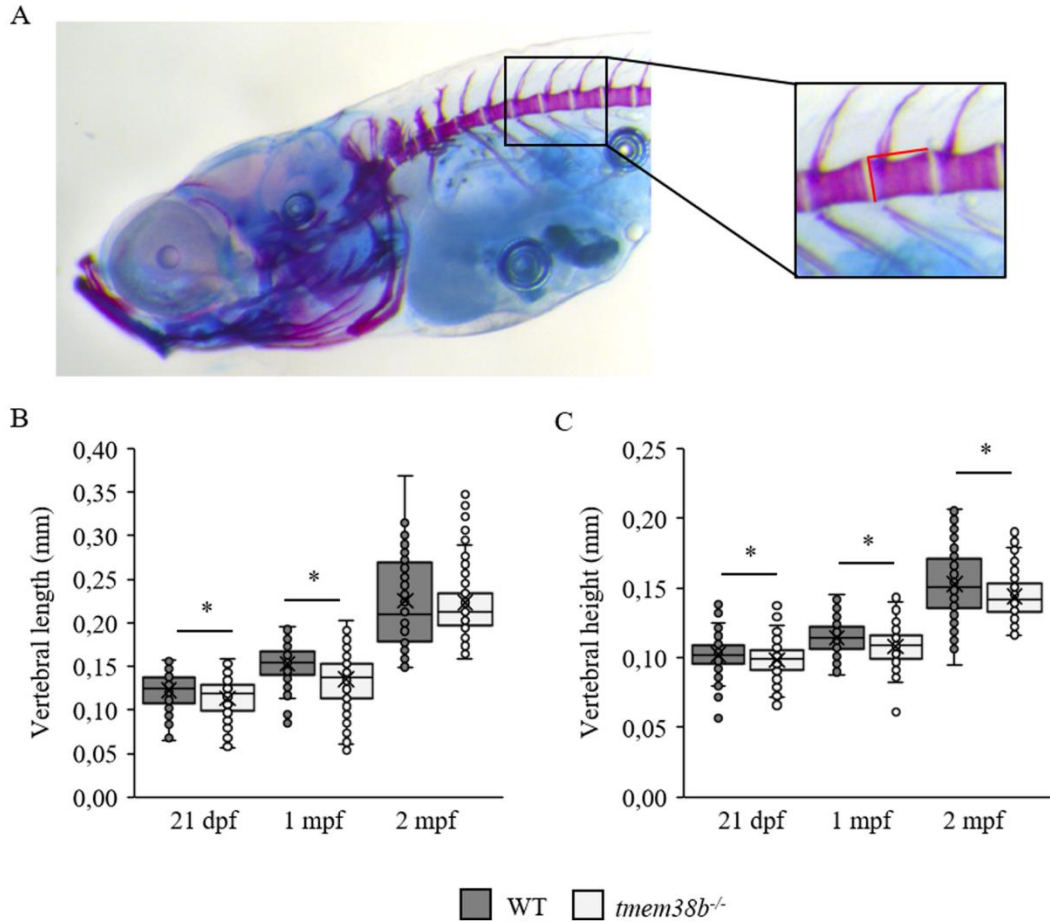
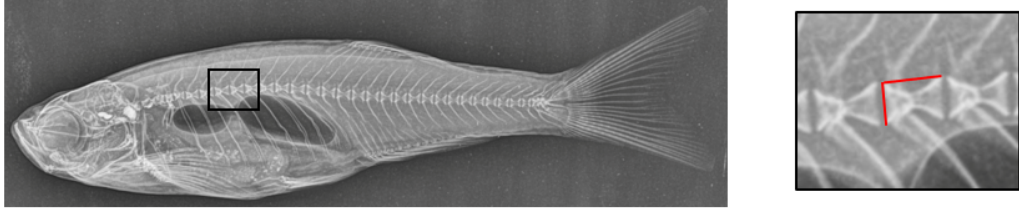


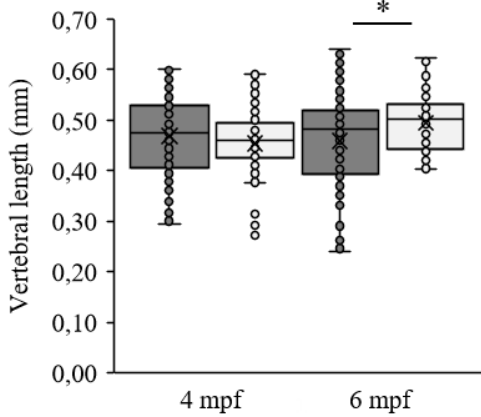
Figure 13. Analysis of vertebral dimension at juvenile stage (21 dpf, 1 mpf and 2 mpf). **A.** Representative image of alcian blue/alizarin red staining. In the enlarged panel red lines indicate vertebral length and height. **B.** Vertebral length was significantly smaller in *mem38b*^{-/-} fish compared to WT at 21 dpf and 1 mpf. **C.** Vertebral height was significantly smaller in *mem38b*^{-/-} fish compared to WT at 21 dpf, 1 and 2 mpf. 21 dpf: WT n=29, *mem38b*^{-/-} n= 25; 1 mpf: WT n= 24, *mem38b*^{-/-} n= 18; 2 mpf: WT n= 13, *mem38b*^{-/-} n= 14). Data were expressed as mean \pm SD (*P<0.05)

X-rays analysis on 4 mpf WT and *mem38b*^{-/-} (**Figure 14A**) showed no differences in vertebral length between WT and *mem38b*^{-/-} (WT: 0.468 ± 0.07 mm; *mem38b*^{-/-}: 0.454 ± 0.07 mm), but significantly reduced vertebral height (WT: 0.312 ± 0.058 mm, *mem38b*^{-/-}: 0.293 ± 0.038 mm; $p < 0.01$). Interestingly, at 6 mpf *mem38b*^{-/-} showed both increased vertebrae length and height compared to WT (length: WT: 0.458 ± 0.096 mm, *mem38b*^{-/-}: 0.495 ± 0.053 mm, $p < 0.01$; height WT: 0.315 ± 0.058 , *mem38b*^{-/-}: 0.329 ± 0.028 mm, $p < 0.05$) (**Figure 14B-C**).

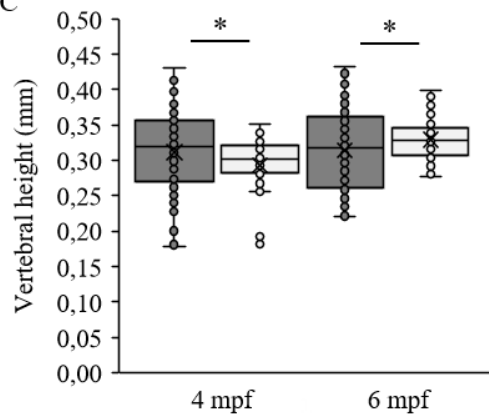
A



B



C



■ WT □ *mem38b*^{-/-}

Figure 14. Analysis of vertebral dimension at adult stage (4 mpf and 6 mpf). A. Representative x-ray image used to measure vertebral length and height at 4 and 6 mpf. In the enlarged panel red lines indicate vertebral length and vertebral height. B. Vertebral length was significantly higher in *mem38b*^{-/-} fish compared to WT at 6 mpf. C. Vertebral height was significantly smaller in *mem38b*^{-/-} fish compared to WT at 4 mpf, but significantly increased in *mem38b*^{-/-} at 6 mpf (4 mpf: WT n= 15, *mem38b*^{-/-} n= 11; 6 mpf: WT n= 12, *mem38b*^{-/-} n= 9) Data were expressed as mean ± SD. (*P<0.05)

Micro-computed tomography (μ CT) of *tnem38b*^{-/-}

Micro-computed tomography scan was performed on WT and *tnem38b*^{-/-} fish at 9 months post fertilization on the second and third precaudal vertebral bodies (**Figure 15**). No differences were detectable in any of the analysed parameters: bone volume (BV), vertebral body thickness (VTh), vertebral body length (VBL), moment of inertia, vertebral eccentricity and bone perimeter (BPm) (**Table 7**).

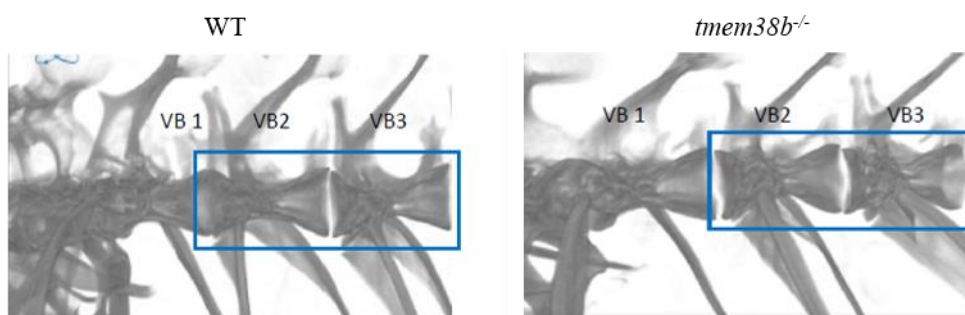


Figure 15. Vertebral region of WT and *tnem38b*^{-/-} analysed by microCT. In the blue boxed the second (VB2) and third (VB3) precaudal vertebral bodies analysed by microCT.

Table 7. Bone parameters evaluated in adult WT and *tnem38b*^{-/-} zebrafish using μ CT scan.

Parameters	WT	<i>tnem38b</i> ^{-/-}	P value
VBL (μ m)	616.13 \pm 33.5	590.25 \pm 62.7	0.49
BV/TV (%)	43.400 \pm 1.37	45.275 \pm 2.08	0.18
BV (mm ³)	0.012 \pm 0.002	0.012 \pm 0.003	0.89
Moment of inertia (mm ⁴)	0.0003 \pm 0.0001	0.0004 \pm 0.0001	0.53
Eccentricity	0.473 \pm 0.021	0.475 \pm 0.013	0.84
CTh (mm)	0.028 \pm 0.002	0.029 \pm 0.002	0.42
BPm (mm)	0.853 \pm 0.04	0.870 \pm 0.08	0.71

VBL = vertebral body length, BV/TV = ratio of bone volume and TV, BV = bone volume, VTh = thickness of the vertebral bone, eccentricity, moment of inertia, and BPm = bone perimeter. WT and *tnem38b*^{-/-} (WT n=4 and *tnem38b*^{-/-} n=4).

Morphometric analysis of *tmem38b*^{Δ120-7/Δ120-7} mutant

Based on the differences detected in *tmem38b*^{-/-} mutant, the morphometric analysis of *tmem38b*^{Δ120-7/Δ120-7} was performed at 21 dpf and 1 mpf. At both stages no differences were detected for any of the analysed parameters in *tmem38b*^{Δ120-7/Δ120-7} fish compared to WT (Figure 16, Supplementary Table 4-5-6). Also, heterozygous fish, evaluated at both ages, were similar to WT.

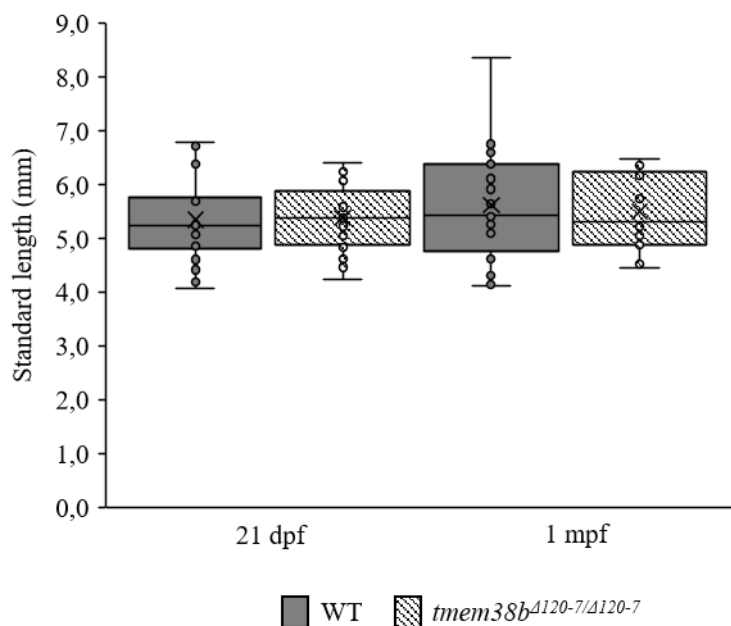


Figure 16. Growth curve of WT and *tmem38b*^{Δ120-7/Δ120-7} fish at 21 dpf and 1 mpf. *tmem38b*^{Δ120-7/Δ120-7} fish had a standard length similar to WT at both 21 dpf and 1 mpf. Data were expressed as mean ± SD (dpf= days post fertilization; mpf = months post fertilization; 21 dpf WT n=28, *tmem38b*^{Δ120-7/Δ120-7} n=23; 1 mpf WT n=21, *tmem38b*^{Δ120-7/Δ120-7} n=13).

Swim bladder of *tmem38b*^{A120-7/Δ120-7}

Since the *tmem38b*^{-/-} mutant fish showed a delay in swim bladder insufflation at 21 dpf, the analysis was performed also in *tmem38b*^{A120-7/Δ120-7}. No difference was detectable between mutant and WT, which present the same level of inflation (**Figure 17**).

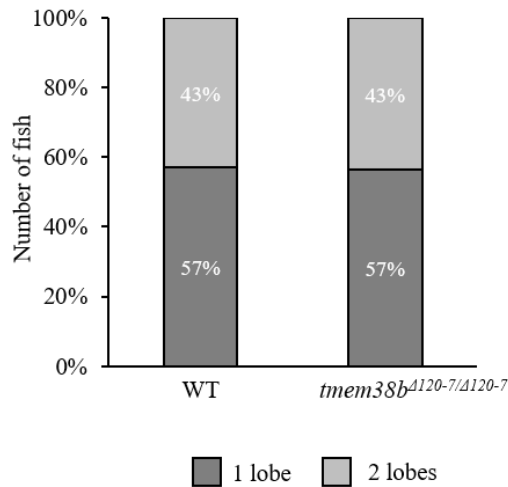


Figure 17. Inflation of swim bladder lobes in WT and *tmem38b*^{A120-7/Δ120-7} fish. The percentage of mutant fish with inflated swim bladder was identical between WT and mutant (WT n=28, *tmem38b*^{A120-7/Δ120-7} n=23).

Vertebral dimensions of *tmem38b*^{A120-7/Δ120-7}

Alcian blue and alizarin red staining were performed in *tmem38b*^{A120-7/Δ120-7} at 21 dpf and 1 mpf, in order to analyse vertebral mineralization and dimensions, as performed for *tmem38b*^{-/-} mutant (**Figure 18**).

At 21 dpf *tmem38b*^{A120-7/Δ120-7} vertebrae were characterized by a significant reduced length and height compared to WT (length: WT 0.116 ± 0.039 mm, *tmem38b*^{A120-7/Δ120-7}: 0.107 ± 0.015 mm, $p < 0.05$; height: WT: 0.102 ± 0.016 mm, *tmem38b*^{A120-7/Δ120-7}: 0.097 ± 0.007 mm, $p < 0.01$).

At 1 mpf *tmem38b*^{A120-7/Δ120-7} vertebrae were characterized by a significant reduced height in comparison to WT (WT: 0.097 ± 0.014 mm, *tmem38b*^{A120-7/Δ120-7}: 0.092 ± 0.014 mm, $p < 0.05$), but no difference was detected in vertebral length (WT: 0.108 ± 0.034 mm, *tmem38b*^{A120-7/Δ120-7}: 0.109 ± 0.036 mm).

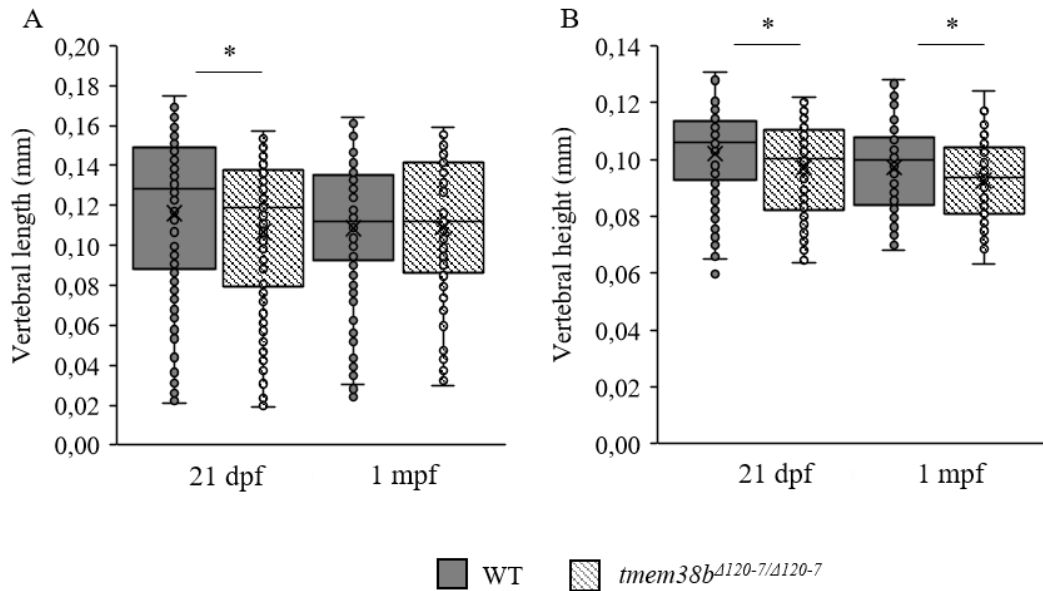


Figure 18. Analysis of vertebral dimensions at juvenile stage (21 dpf and 1 mpf). **A.** Vertebral length was significantly shorter in *mem38b*^{A120-7/A120-7} fish compared to WT at 21 dpf. **B.** Vertebral height was significantly shorter in *mem38b*^{A120-7/A120-7} fish compared to WT at both stages, 21 dpf and 1 mpf (21 dpf: WT n= 22, *mem38b*^{A120-7/A120-7} n= 20; 1 mpf: WT n= 12, *mem38b*^{A120-7/A120-7} n= 9). Data were expressed as mean \pm SD (*P<0.05).

Toluidine blue staining of mem38b zebrafish mutants

Toluidine blue histological analysis on 1 mpf WT, *mem38b*^{-/-} and *mem38b*^{A120-7/A120-7} mutants was performed to dissect the morphometric differences identified by whole mount staining. Interestingly, *mem38b*^{A120-7/A120-7} mutant revealed a reduced medial vertebral height in notochord with respect to WT (**Figure 19**). This result was confirmed in 1 mpf by measurements in whole mounted alizarin red stained fish (WT: 0.087 ± 0.015 mm, *mem38b*^{A120-7/A120-7}: 0.083 ± 0.013 mm; $p=0.06$). Interestingly, also in *mem38b*^{-/-} fish the medial vertebral height was reduced compared to control (WT: 0.091 ± 0.011 mm, *mem38b*^{-/-}: 0.086 ± 0.013 mm; $p<0.01$).

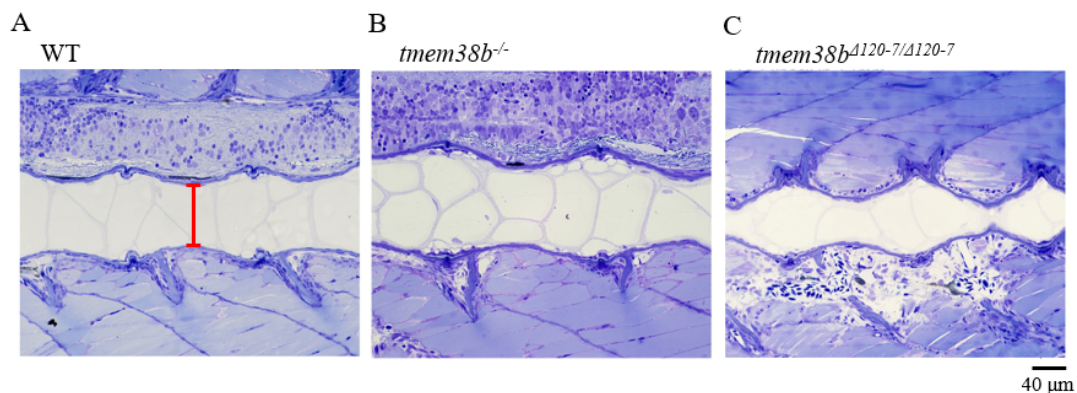


Figure 19. Toluidine blue stained semi-thin sections of WT and mutant fish at 1 mpf. A. WT semi thin section. **B.** Semi thin section of *tmem38b*^{-/-} stained with toluidine blue. **C.** Semi thin section of *tmem38b*^{A120-7/A120-7} stained with toluidine blue revealed a reduced notochord height with compared to WT. The red line indicates the notochord height. Magnification 250 x, scale bar: 40 µm (WT n=1; *tmem38b*^{-/-} n= 1, *tmem38b*^{A120-7/A120-7} n= 2).

Enlarged cisternae size and extracellular collagen fibers content in mutant fish

In OI type XIV patients the altered Ca²⁺ flux causes ER stress, the activation of the unfolded protein response (UPR) and a reduced amount of collagen in the extracellular matrix (Cabral et al. 2016). In *Tmem38b* knock-out mice osteoblasts have enlarged ER cisternae, likely due to mutant collagen retention (Zhao et al. 2016).

Based on these observations, WT, *tmem38b*^{-/-} and *tmem38b*^{A120-7/A120-7} were analysed by transmission electron microscopy (TEM) at 1 mpf. In both mutant osteoblasts showed an increased number of cisternae slightly enlarged, whereas in fibroblasts their size was clearly wider than WT (**Figure 20**).

The analysis of collagen fibers area was performed on TEM images of WT and both *tmem38b* mutant fish at 1 mpf. *tmem38b*^{A120-7/A120-7} osteoblasts extracellular matrix presents a significantly reduced amount of collagen type I fibers compared to WT, suggesting a reduced collagen secretion and/or mutant collagen assembly (WT: 0.69 ± 0.02 , *tmem38b*^{-/-}: 0.72 ± 0.02 , $p=0.15$; *tmem38b*^{A120-7/A120-7}: 0.62 ± 0.05 , $p<0.05$); the same trend was found in fibroblasts without reaching significant difference (WT: 0.67 ± 0.03 , *tmem38b*^{-/-}: 0.74 ± 0.01 , *tmem38b*^{A120-7/A120-7}: 0.65 ± 0.06 , $p=0.58$) (**Table 8**). On the contrary, in *tmem38b*^{-/-} mutant the amount of collagen type I fibers in osteoblasts' and fibroblast' matrix was similar to WT (**Table 8**).

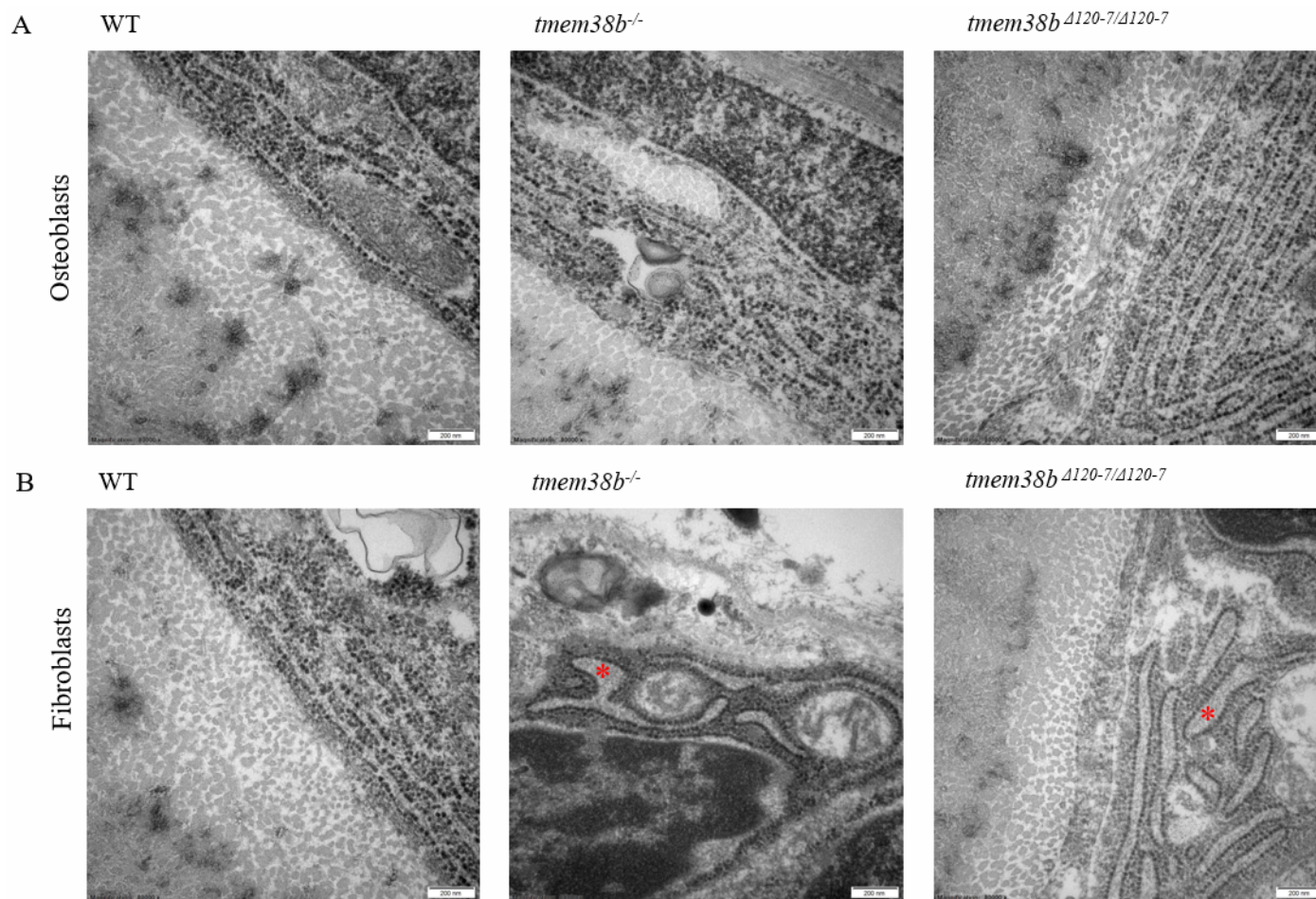


Figure 20. Transmission electron microscopy of osteoblasts and fibroblasts. **A.** Transmission electron microscopy images of 1 mpf WT, *tmem38b*^{-/-} and *tmem38b*^{Δ120-7/Δ120-7} osteoblasts at the level of the notochord sheath. An abundant ER was evident in both mutants with respect to WT. **B.** Transmission electron microscopy images of 1 mpf WT, *tmem38b*^{-/-} and *tmem38b*^{Δ120-7/Δ120-7} fibroblasts at the level of the notochord sheath. Enlarged ER cisternae (asterisk) was evident in mutant with respect to WT. Magnification 80000x. Scale bar: 200 nm.

Table 8. Area of collagen type I fibers in extracellular matrix of WT and *tmem38b* mutant osteoblasts and fibroblasts. The values were normalized on the total area of extracellular matrix considered. In bold the p value <0.05.

	Osteoblasts		Fibroblasts	
	Mean ± SD	p value	Mean ± SD	p value
WT	0.69 ± 0.02		0.67 ± 0.03	
<i>tmem38b</i> ^{-/-}	0.72 ± 0.02	0.15	0.74 ± 0.01	Nd
<i>tmem38b</i> ^{Δ120-7/Δ120-7}	0.62 ± 0.05	0.02	0.65 ± 0.06	0.58

Nd: not determined due to low number of images available.

Hspa5 expression

The enlargement of ER cisternae, evaluated by TEM, suggested the activation of the unfolded protein response (UPR) pathway in mutant cells. For this reason, the expression of the master UPR regulator *Hspa5*, encoding for BIP, was evaluated on RNA extracted from a pool of 5 WT, *tmem38b*^{-/-} and *tmem38b*^{Δ120-7/Δ120-7} caudal fins. An overexpression of *hspa5* was detected in *tmem38b*^{Δ120-7/Δ120-7} compared to WT (WT: 0.95 ± 0.18, *tmem38b*^{Δ120-7/Δ120-7}: 2.18 ± 0.2, p<0.01) (**Figure 21B**), while in the *tmem38b*^{-/-} mutant the expression of *hspa5* was decreased (WT: 0.97 ± 0.19, *tmem38b*^{-/-}: 0.69 ± 0.24, p<0.05) (**Figure 21A**).

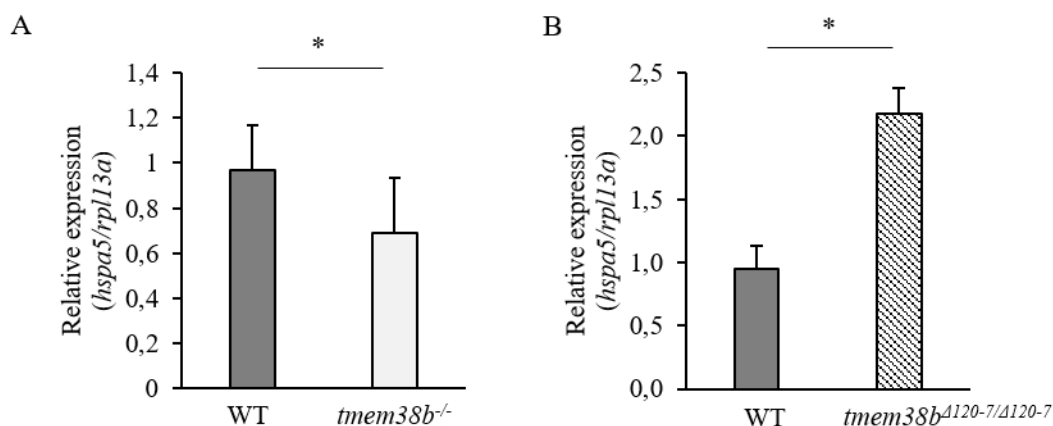


Figure 21. Analysis of *hspa5* expression in *tmem38b* zebrafish mutants. **A.** *hspa5* was less expressed in *tmem38b*^{-/-} fish with respect to WT (WT n= 3, *tmem38b*^{-/-}n=3). **B.** *hspa5* expression was significantly increased in *tmem38b*^{Δ120-7/Δ120-7} fish compared to WT (WT n= 2, *tmem38b*^{Δ120-7/Δ120-7} n= 2) Data were expressed as mean ± SD (*P<0.05).

Hsp47 protein and transcript expression in *tmem38b* mutants

The Heat shock protein 47 (Hsp47) is the collagen type I specific chaperone, which binds to collagen α -chains as soon as they are assembled and prevents the association of procollagen molecule and formation of aggregates in the ER, thus facilitating their transport from the ER to Golgi (Ishida and Nagata 2011). For this reason, the expression of Hsp47 was investigated in *tmem38b* zebrafish mutants. To detect the level of expression of Hsp47, whole mount immunohistochemistry on 5 dpf WT and both mutants was performed by using two antibodies against the two *D. rerio* Hsp47 isoforms (anti-Hsp47a and anti-Hsp47b), and the intensity of the signal was evaluated.

Both isoforms were expressed at the level of skin and of intersomites in WT and mutant fish (**Figure 22-23**). Interestingly, a significant higher expression of Hsp47a (**Figure 22**) and Hsp47b (**Figure 23**) was detected in both *tmem38b*^{-/-} and *tmem38b*^{*A120-7/A120-7*} compared to WT.

The RNA expression level of *serpinh1a* and *serpinh1b*, encoding for Hsp47a and Hsp47b, respectively, was analyzed by qPCR. The expression of both isoforms in *tmem38b*^{-/-} was similar to WT (**Figure 22D-23D**) (*serpinh1a*: WT: 0.82 ± 0.34 , *tmem38b*^{-/-}: 1.05 ± 0.33 , $p=0.17$; *serpinh1b*: WT: 0.66 ± 0.43 , *tmem38b*^{-/-}: 0.47 ± 0.18 , $p=0.24$). In *tmem38b*^{*A120-7/A120-7*} mutant both transcripts were significantly increased compared to WT fish (*serpinh1a*: WT: 0.80 ± 0.17 , *tmem38b*^{*A120-7/A120-7*}: 1.03 ± 0.09 , $p<0.05$; *serpinh1b*: WT: 0.87 ± 0.13 , *tmem38b*^{*A120-7/A120-7*}: 2.35 ± 0.45 , $p<0.01$) (**Figure 22E-23F**).

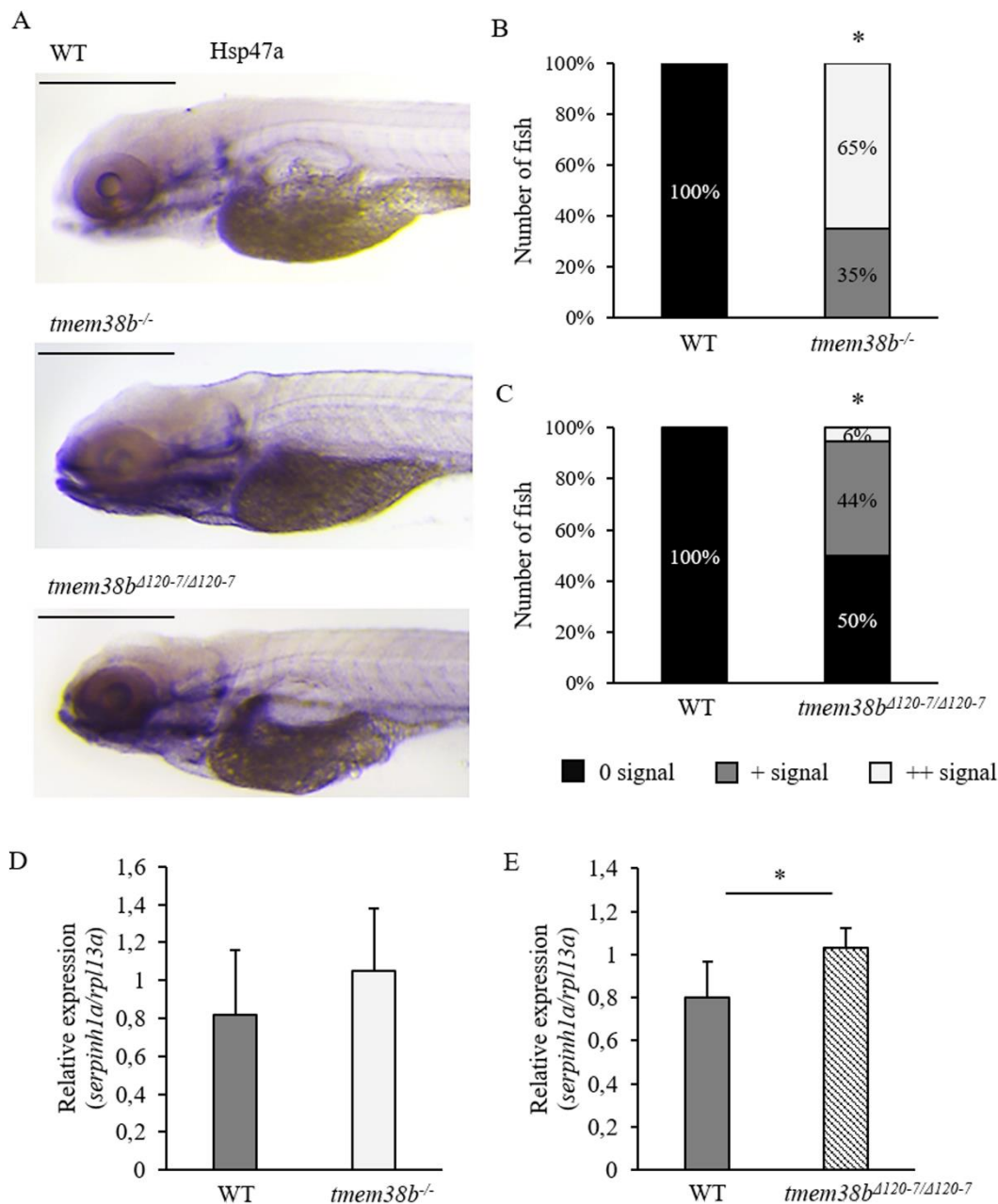


Figure 22. Expression of Hsp47a in WT and both *tmem38b* mutants. **A.** Representative images of 5 dpf fish after whole mount immunohistochemistry with Hsp47a antibody. Scale bar: 500 μ m. **B-C.** Whole mount immunohistochemistry evaluation of Hsp47a expression in WT and mutant fish at 5 dpf. Hsp47a was significantly more expressed in both mutant fish compared to WT. 0, + and ++ indicate the intensity of the signal, from null to high (Hsp47a: WT n= 17, *tmem38b^{-/-}* n=20; WT n= 17, *tmem38b^{Δ120-7/Δ120-7}* n=18) **D.** *serpinh1a* expression was slightly increased in *tmem38b^{-/-}* fish compared to WT (WT n= 3, *tmem38b^{-/-}* n= 3) **E.** *serpinh1a* expression was significantly increased in *tmem38b^{Δ120-7/Δ120-7}* fish compared to WT (WT n= 2, *tmem38b^{Δ120-7/Δ120-7}* n= 2) (*P<0.05).

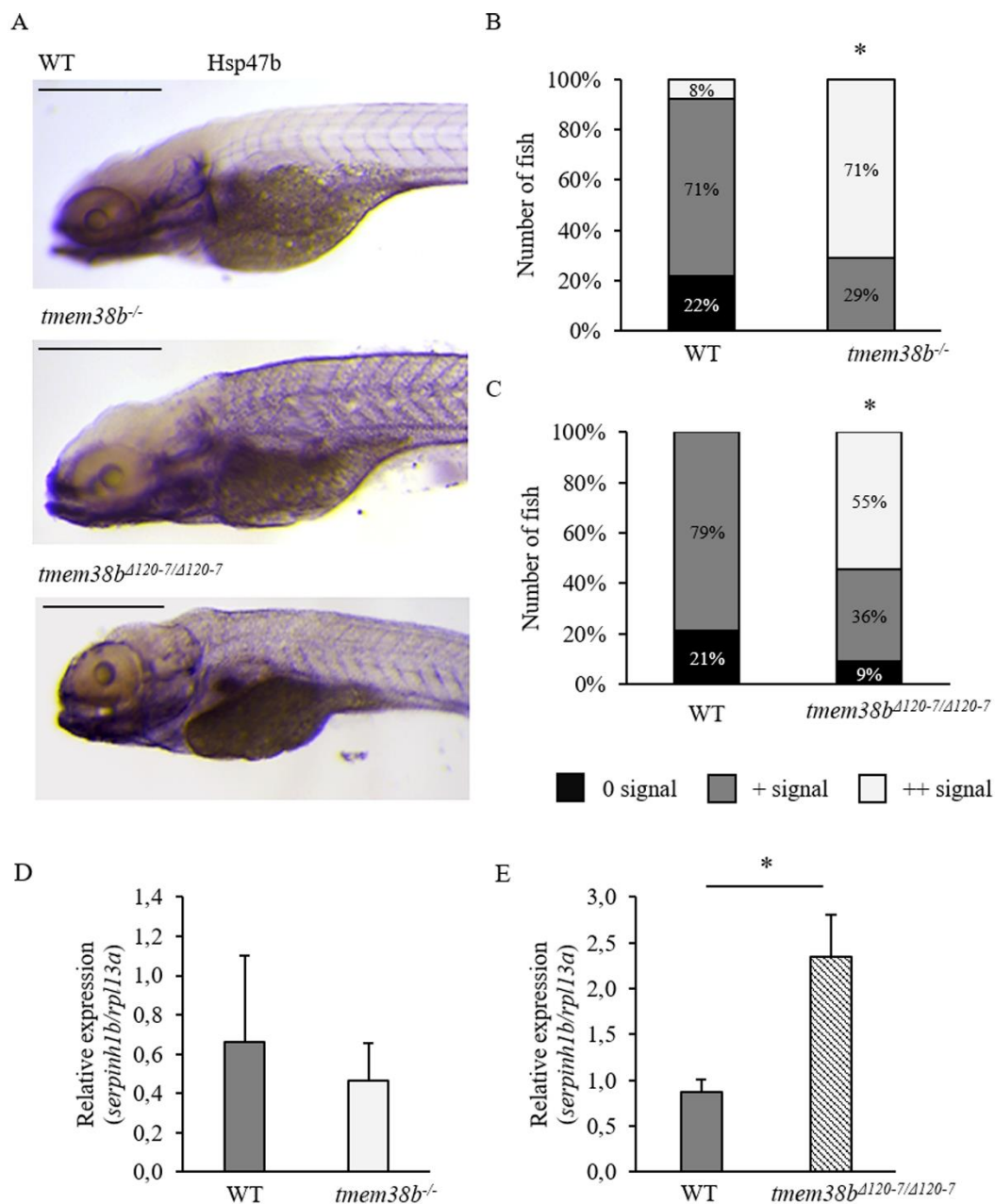


Figure 23. Expression of Hsp47b in WT and both *tmem38b* mutants. **A.** Representative images of 5 dpf fish after whole mount immunohistochemistry with Hsp47b antibody. Scale bar: 500µm. **B-C.** Whole mount immunohistochemistry evaluation of Hsp47b expression in WT and mutant fish at 5 dpf. Hsp47b was significantly more expressed in both mutant fish compared to WT. 0, + and ++ indicate the intensity of the signal, from null to high (Hsp47b: WT n= 51, *tmem38b^{-/-}* n=48; WT n= 14; *tmem38b^{Δ120-7/Δ120-7}* n=11). **D.** *serpinh1b* was similarly expressed in *tmem38b^{-/-}* fish with respect to WT (WT n= 3, *tmem38b^{-/-}* n= 3). **E.** *serpinh1b* expression was significantly increased in *tmem38b^{Δ120-7/Δ120-7}* fish compared to WT (WT n= 2, *tmem38b^{Δ120-7/Δ120-7}* n= 2) (*P<0.05).

Discussion

My main PhD project was focused on the generation and characterization of zebrafish models for OI type XIV to better elucidate the mechanism behind the onset of the pathology and likely to create a valid tool for drug screening approaches. Two zebrafish models for *tmem38b* have been successfully generated by CRISPR/Cas9 gene editing and then morphologically, biochemically and intracellularly characterized.

Generation of OI type XIV zebrafish models

OI type XIV is caused by mutations in *TMEM38B*, encoding for the trimeric intracellular cation channel B (TRIC-B). TRIC-B allows the potassium ions transport across the ER membrane, modulating calcium flux and maintaining the intracellular ion homeostasis. Indeed, the decreased cytoplasmic calcium concentration $[Ca^{2+}]_i$ and the reduced calcium flux release from ER, observed in OI type XIV patients, indicate a dysregulation in calcium homeostasis (Cabral et al. 2016). A similar condition is detected in *Tric-b* knock-out murine osteoblasts, where Ca^{2+} flux through inositol trisphosphate phosphate receptor (IP_3R) is significantly reduced, although with normal resting Ca^{2+} concentrations (Zhao et al. 2016). Since no information about zebrafish *tmem38b* was yet available, synteny analysis of the chromosomal region surrounding the gene and Blastp analysis of the protein were necessary to better elucidate chromosomal region and protein structure conservation, respectively with mammals. Interestingly, the 7 transmembrane domains as well as the KEV motif, important for pore channel formation (Catterall 2010), are conserved between teleosts and mammals (**Figure 4B**).

Two different mutant lines for *tmem38b* have been successfully generated by CRISPR/Cas9. The *tmem38b*^{-/-} carries a 7 nucleotides deletion resulting in the introduction of a premature stop codon, as often reported in patients, while the *tmem38b* ^{Δ 120-7/ Δ 120-7} carries an in frame 24 nucleotides deletion, which includes the conserved KEV motif. Unfortunately, the lack of specific zebrafish antibody against *Tric-b*, did not allow to demonstrate the presence or absence of the protein in both generated models. Indeed, the limited availability of antibodies against zebrafish proteins represents a severe drawback in the characterization of zebrafish disease models.

Nevertheless, the *tmem38b*^{-/-} mutant shows 90% reduction in transcript expression, suggesting the activation of non-sense mediated decay. On the contrary, no reduction in transcript expression is detected in the *tmem38b* ^{Δ 120-7/ Δ 120-7} (**Figure 7**).

Given that the calcium flux has not yet been evaluated *in vivo*, the generation of transgenic zebrafish reporter could lead to an improvement in knowledge concerning the molecular basis of OI type XIV. A double transgenic line that exploits the Gal4/UAS system and the calcium indicator GCaMP (a calcium binding element) (Muto et al. 2011; Chen et al. 2017) will allow to follow Ca²⁺ flux *in vivo* under fluorescence microscope. The matings are ongoing in the lab.

OI type XIV zebrafish models present a mild bone phenotype

OI type XIV is characterized by a high degree of phenotypical variability: the clinical phenotype ranges from asymptomatic to severe. The patients show various levels of bone deformities, low bone mass, recurrent fractures, growth retardation and short stature (Lv et al. 2016).

Since the *Tmem38b* knock-out mouse died at birth due to a reduction in surfactant production, which leads to respiratory insufficiency, new animal models to investigate the role of TRIC-B in the onset of the skeletal phenotype are required (Yamazaki et al. 2011; Zhao et al. 2016). Among these, we decided to use zebrafish, whose swim bladder has the same evolutionary origin as the mammal lungs without the need for surfactant production (Graham 1997).

tmem38b zebrafish mutants are viable and they develop normally until 14 days post fertilization (dpf). At 21 dpf and 1 month post fertilization (mpf) *tmem38b*^{-/-} are shorter than WT (**Figure 9**) and present body disproportions (**Figure 10**).

Interestingly, at 21 dpf, when the swim bladder usually becomes completely developed, a significant decreased level of insufflation is detected in *tmem38b*^{-/-} fish, likely due to a delay during the juvenile developmental stage, since anyway fish reach adult age. The expression of *tmem38b* in the swim bladder (**Figure 5B**) opens the intriguing hypothesis that impaired

inflation may resemble the respiratory insufficiency of murine model, pointing to a possible effect of mutant collagen in the tissue.

On the other hand, no differences in the standard length and in morphometric parameters are observed in the *tmem38b*^{A120-7/A120-7}. In this model the transcript has normal level (**Figure 7B**) and the protein could be translated, although the formation of the channel should be compromised by the lack of the KEV tripeptide, but we cannot exclude a partial compensatory mechanism (or functional retaining).

OI type XIV zebrafish models show impaired vertebral column mineralization at juvenile developmental stage

The investigation of bone mineralization during embryonic development is difficult in humans for ethical reasons, but it is also extremely complex in murine models for which C-section of the females at different pregnancy stages is necessary to collect embryos at various days post fertilization. On the contrary, in zebrafish, thanks to the external fertilization and the availability of easy whole mount alizarin red staining technique, the bone mineralization level can be easily investigated since first stages of skeletal development (Tonelli, Bek, et al. 2020). Using this approach, no differences in cranial bones mineralization are detected at 7 and 14 dpf in *tmem38b* mutants in comparison to WT.

Since in some patients the presence of vertebral abnormalities, fractures and low mineral density was detected, the dimensions of alizarin red stained vertebral bodies were measured at juvenile stages (21 dpf, 1 mpf and 2 mpf) in *tmem38b*^{-/-} mutants. The significant reduction in vertebral dimensions respect to WT suggests the presence of a delay in column mineralization (**Figure 13**). A reduction in vertebral dimensions was also found in *tmem38b*^{A120-7/A120-7} mutant at 21 dpf and 1 mpf.

In *tmem38b*^{-/-} the reduction in vertebral bodies size is still evident at 4 mpf (**Figure 14**), but starting from 6 mpf, the gap between mutant and WT is fulfilled. It is intriguing to hypothesize that, as described in the Brtl mouse model for dominant OI (Kozloff et al. 2004), also in OI type XIV zebrafish a matrix adaptation occurs with the ages. This finding parallels clinically observed decreases in OI patient fracture rate after puberty with a mechanism not yet well understood.

Indeed, microCT analysis of adult *tmem38b*^{-/-} revealed normal vertebral body length, BV/TV, BV and vertebral thickness (**Figure 15, Table 7**).

The zebrafish notochord sheath is segmented into alternating mineralizing and cartilage-like domains prior to vertebral body formation (Wopat et al. 2018). Mineralized notochord sheath domains recruit osteoblasts which produce collagen type I and start to ossify forming vertebral bodies (Inohaya, Takano, and Kudo 2007).

The recruitment of osteoblasts prior to form the vertebral body starts in zebrafish at the standard length of 5.0 mm, corresponding to fish from 14 to 21 dpf. Later, at 7.5 mm length, the osteoblasts cover all mineralized sheath domain, forming the entire vertebral body (chordacentrum) (Wopat et al. 2018).

The reduced size of mineralized vertebrae could be related to an impairment in osteoblast recruitment or in their differentiation, leading to a delay in mutants' bone matrix deposition respect to WT. Interestingly, the early osteoblastic markers *RUNX2* and *SP7* are less expressed in OI type XIV patients (Webb et al. 2017), likely supporting the mineralization defect observed in our models.

OI type XIV zebrafish mutants' collagen type I leads to ER stress condition

The dysregulation of intracellular Ca²⁺ dynamics, may impair the expression of collagen modifying enzymes, such as lysyl hydroxylases, thus affecting collagen post-translational modifications (Cabral et al. 2016). Indeed, one of the typical features of OI type XIV is an under-modified collagen type I, likely due to a decrease in triple helix hydroxylysines content (Cabral et al. 2016), which leads to a reduced level of glycosylation and a faster migration in SDS-PAGE analysis.

The zebrafish *lh1* and *lh2* genes have similar organizations to their human orthologues as well as, based on protein sequence similarities, comparable enzymatic activities (Schneider and Granato 2007). Nevertheless, no difference in α bands collagen electrophoretic migration is detected in *tmem38b* mutants respect to WT, although the Hyl percentage (Hyl/(Lys+Hyl)) in *tmem38b*^{A120-7/ Δ A120-7} bone is significantly decreased with respect to WT, but the data is indeed limited to a single sample (**Table 6**). It is important to remind that the under-modified collagen secreted by OI type XIV patients' osteoblasts is not incorporated

in the extracellular matrix and our data further confirm the absence or undetectable presence of mutant collagen in bone tissue (Cabral et al. 2016).

Preliminary transmission electron microscopy data reveal a reduced amount of secreted collagen fibers in *tmem38b*^{*Δ120-7/Δ120-7*} osteoblasts extracellular matrix compared to WT, suggesting collagen retention in the ER which leads to extracellular matrix insufficiency (**Figure 20, Table 8**). This feature parallels the described matrix insufficiency in OI patients (Cabral et al. 2016) and, consistently, the endoplasmic reticulum collagen type I retention is observed in *tmem38b* KO murine osteoblasts (Zhao et al. 2016). Surprisingly, in *tmem38b*^{-/-} zebrafish no significant reduction of extracellular collagen fibers is present.

Similarly, to knock-out murine osteoblasts, *tmem38b* zebrafish mutants show a higher number of slightly enlarged ER cisternae, suggesting that mutant collagen accumulates intracellularly leading to activation of cell stress.

In OI patients' cells collagen retention and accumulation in the ER cisternae is the main cause of the unfolded protein response activation. Nevertheless, the expression of *HSPA5*, encoding for the UPR master regulator BIP is decrease in patients' cells, although an increase of the protein was reported (Cabral et al. 2016). No change in *hspa5* expression was detected in RNA extracted from the knock-out mice bone. Indeed, also in dominant and recessive OI cells with structural collagen mutation BIP expression is known to be variable (Besio et al. 2019; Besio et al. 2018). In the *tmem38b*^{*Δ120-7/Δ120-7*} mutant *hspa5* is overexpressed, whereas its slight decrease is found in *tmem38b*^{-/-} (**Figure 21**). This variability likely supports the activation of a non-canonical UPR pathway in OI cells (Forlino et al. 2007) as previously hypothesized.

Since impairment in collagen secretion could be hypothesised based on ER cisternae enlargement, and often this is associated to intracellular accumulation of the collagen specific chaperone Hsp47 (Gioia et al. 2012), its expression was evaluated in both mutant zebrafish by whole mount immunohistochemistry using antibodies against the two isoforms present in zebrafish. Hsp47 has a crucial role in binding collagen trimers as soon as they are synthesized, thus preventing premature association of collagen molecule and formation of aggregates in the ER and facilitating the transport of procollagen from the ER to the Golgi.

tmem38b^{A120-7/A120-7} mutant fish show a high expression of Hsp47 protein and increased *serpinh1a/b* expression compared to WT (**Figure 22C-E, 23C-E**), supporting collagen intracellular retention in the ER. No difference in the *serpinh1a/b* gene expression is detected in *tmem38b*^{-/-} mutants compared to WT, while Hsp47 protein is overexpressed (**Figure 22B-D, 23B-D**).

As often happens, the transcript and protein expression levels is not matching (Fukao 2015), but we should also take into account that the expression of Hsp47 in *tmem38b*^{-/-} mutant, at the transcript and the protein level, could be associated to its analysis on different tissues and different stages of development (larvae for protein expression and adult tail fish for transcript analysis). Indeed, it has been demonstrated that the expression of heat shock proteins (Hsp) at the transcript level is lower in mature fish (Murtha and Keller 2003).

Conclusion

In conclusion, two zebrafish models for *tmem38b* were successfully generated and their characterization revealed a very mild bone phenotype, mainly characterized by growth and mineralization delay at the juvenile stage. Moreover, the enlarged ER cisternae suggests the activation of ER stress condition due to altered collagen retention, as supported by the increased level of Hsp47. Interestingly, the two models show some phenotypic differences that could be linked to the diversity of the mutant protein, likely missing in *tmem38b*^{-/-} and translated but not fully functional in *tmem38b*^{A120-7/A120-7}. *tmem38b* specific antibody will be needed to properly address this issue.

Our data confirm that retention of altered collagen causing ER stress condition represents an appealing target for future therapies to cure OI.

Supplementary tables

Supplementary Table 1. Standard length of WT and *tmem38b*^{-/-} fish at different developmental stages. Data are expressed as mean ± SD (dpf= days post fertilization, mpf=months post fertilization). In bold the p value <0.05.

	WT		<i>tmem38b</i> ^{-/-}		p value
	N	Mean ± SD (mm)	N	Mean ± SD (mm)	
5 dpf	13	3.75 ± 0.13	12	3.74 ± 0.24	0.97
7 dpf	19	3.97 ± 0.10	8	3.99 ± 0.13	0.78
14 dpf	33	4.45 ± 0.28	20	4.43 ± 0.33	0.87
21 dpf	32	5.80 ± 0.39	27	5.53 ± 0.59	0.04
1 mpf	27	7.18 ± 1.05	18	6.40 ± 1.35	0.03
2 mpf	18	9.83 ± 1.88	19	9.74 ± 1.75	0.88
4 mpf	15	18.73 ± 2.66	11	18.41 ± 2.11	0.73
6 mpf	15	19.83 ± 2.81	10	20.98 ± 1.77	0.26

Supplementary Table 2. Morphometric parameters evaluated in WT and *tmem38b*^{-/-} fish. Data are expressed as mean ± SD (HAA = Height of Anterior of Anal fin, HE= Height at Eye, SOL= The Snout-Operculum Length) (mpf = months post fertilization). In bold the p value <0.05.

		HAA			HE			SOL		
		N	Mean ± SD (mm)	p value	N	Mean ± SD (mm)	p value	N	Mean ± SD (mm)	p value
1 mpf	WT	25	0.85 ± 0.22	0.08	26	1.23 ± 0.22	0.05	23	1.91 ± 0.29	0.06
	<i>tmem38b</i> ^{-/-}	15	0.71 ± 0.27		15	1.08 ± 0.28		13	1.67 ± 0.44	
2 mpf	WT	18	1.65 ± 0.54	0.96	18	1.81 ± 0.40	0.96	17	2.68 ± 0.48	0.48
	<i>tmem38b</i> ^{-/-}	19	1.65 ± 0.47		19	1.80 ± 0.39		18	2.56 ± 0.52	
4 mpf	WT	15	4.02 ± 0.68	0.55	15	3.16 ± 0.42	0.90	15	4.23 ± 0.52	0.61
	<i>tmem38b</i> ^{-/-}	11	3.87 ± 0.52		11	3.13 ± 0.53		11	4.12 ± 0.57	
6 mpf	WT	15	4.13 ± 0.66	0.61	15	3.07 ± 0.46	0.43	13	4.42 ± 0.88	0.33
	<i>tmem38b</i> ^{-/-}	10	4.26 ± 0.46		10	3.20 ± 0.28		8	4.78 ± 0.74	

Supplementary Table 3. Ratio of morphometric parameters evaluated in WT and *tmem38b*^{-/-} fish. Data are expressed as mean ± SD (mpf = months post fertilization). In bold the p value <0.05.

		SL/HAA			SOL/HE		
		N	Mean ± SD (mm)	p value	N	Mean ± SD (mm)	p value
1 mpf	WT	25	8.98 ± 1.33	0.03	23	1.56 ± 0.07	0.22
	<i>tmem38b</i> ^{-/-}	15	10.07 ± 1.85		12	1.52 ± 0.08	
2 mpf	WT	18	6.26 ± 1.14	0.88	17	1.47 ± 0.09	0.17
	<i>tmem38b</i> ^{-/-}	19	6.20 ± 1.31		18	1.43 ± 0.10	
4 mpf	WT	15	4.70 ± 0.30	0.53	15	1.35 ± 0.10	0.94
	<i>tmem38b</i> ^{-/-}	11	4.77 ± 0.30		11	1.34 ± 0.22	
6 mpf	WT	15	4.81 ± 0.19	0.11	13	1.44 ± 0.17	0.73
	<i>tmem38b</i> ^{-/-}	10	4.94 ± 0.20		8	1.46 ± 0.14	

Supplementary Table 4. Standard length of WT and *tmem38b*^{A120-127/120-12} fish at 21 dpf and 1 mpf. Data are expressed as mean ± SD (dpf= days post fertilization, mpf=months post fertilization).

	WT		<i>tmem38b</i> ^{A120-7/A120-7}		p value
	N	Mean ± SD (mm)	N	Mean ± SD (mm)	
21 dpf	28	5.33 ± 0.80	23	5.38 ± 0.64	0.84
1 mpf	21	5.61 ± 1.08	13	5.49 ± 0.77	0.72

Supplementary Table 5. Morphometric parameters evaluated in WT and *tmem38b*^{A120-127/120-127} fish at 1 mpf. Data are expressed as mean ± SD (HAA = Height of Anterior of Anal fin, HE= Height at Eye, SOL= The Snout-Operculum Length) (mpf = months post fertilization).

1 mpf	HAA			HE			SOL		
	N	Mean ± SD (mm)	p value	N	Mean ± SD (mm)	p value	N	Mean ± SD (mm)	p value
WT	17	0.52 ± 0.21	0.63	17	0.89 ± 0.23	0.81	13	1.53 ± 0.26	0.38
<i>tmem38b</i> ^{A120-7/A120-7}	11	0.49 ± 0.13		11	0.87 ± 0.15		7	1.42 ± 0.28	

Supplementary Table 6. Ratio of morphometric parameters evaluated in WT and *tmem38b* ^{Δ 120-127/120-127} fish. Data are expressed as mean \pm SD (mpf = months post fertilization).

1 mpf	SL/HAA			SOL/HE		
	N	Mean \pm SD (mm)	p value	N	Mean \pm SD (mm)	p value
WT	13	11.5 \pm 1.82	0.88	13	1.58 \pm 0.06	0.89
<i>tmem38b</i> ^{Δ120-7/Δ120-7}	7	11.7 \pm 1.50		7	1.57 \pm 0.07	

Chapter III
Prolyl 3-hydroxylation complex: new insight from
zebrafish OI models

Prolyl 3-hydroxylation complex

The proline hydroxylation is the post-translational modification required for proper procollagen folding and collagen fibril assembly. While 4-hydroxyprolines (4Hyp) increase the triple helix stability and guarantee collagen folding (Berg and Prockop 1973), the role of 3-hydroxyproline (3Hyp) is not completely clarified yet (Jenkins et al. 2003).

Proline 986 of the $\alpha 1$ chain of collagen types I and II and proline 707 of $\alpha 2$ chain of collagen type I are the only proline residues subjected to 3-hydroxylation. This reaction is catalysed by the endoplasmic reticulum resident Prolyl 3-hydroxylation complex, which is composed by the cartilage-associated protein (CRTAP), the prolyl 3-hydroxylase 1 (P3H1) and the cyclophilin B (CyPB), associated with a 1: 1: 1 ratio (Vranka, Sakai, and Bächinger 2004; Morello et al. 2006). P3H1 is the active enzyme responsible for proline 3-hydroxylation, CRTAP plays a role as a helper protein within the complex and CyPB is a peptidyl-prolyl *cis-trans* isomerase which controls collagen folding by promoting *trans* configuration of peptide bonds involving proline residues (Marini, Cabral, et al. 2007).

Since 2006, nonsense and missense mutations in *CRTAP*, *P3H1* and *PPIB* have been discovered in patients with osteogenesis imperfecta type VII, VIII and IX, respectively (Valadares et al. 2014).

CRTAP is the cartilage associated protein, first discovered in cultured chick chondrocytes and high expressed during development (Castagnola et al. 1997). In addition, CRTAP is expressed in proliferating chondrocytes of the growth plate, in the bone collar and in calcified cartilage (Morello et al. 1999). The proof of the relevant role of this protein in bone development came by the generation and characterization of a *Crtap*^{-/-} mouse model showing a severe osteopenia, rhizomelia and kyphosis, typical features of OI type VII patients (Morello et al. 2006).

P3H1 is a multifunctional protein, belonging to the 2-oxoglutarate dioxygenase family, first isolated from chick embryos ER-enriched extract. Further study in rats revealed that *P3h1* is localized in the basement membrane of small vessels and smooth muscle in kidney, skeletal muscle, liver and skin and also in the pericellular material surrounding individual chondrocytes in the trachea, but not in the tracheal cartilage matrix (Marini, Cabral, et al. 2007). *P3h1*^{-/-} mice are characterized by growth deficiency, rhizomelia, reduced bone

mineral density, abnormal hypertrophic chondrocytes and delayed secretion of over-modified collagen, as observed from cultured cells (Baldrige et al. 2008).

CyPB is the peptidyl-prolyl isomerase, required for procollagen folding in the ER. *In vitro* studies show that CyPB is not necessary for full 3-prolyl hydroxylation activity, but probably enhances the complex stability. However, the activity of the complex in the absence of CyPB is sufficient to normally 3-hydroxylate $\alpha 1(I)$ Pro986 (Cabral et al. 2014). Interestingly, it was observed that in CRTAP null cells P3H1 expression is absent and vice versa, indicating that CRTAP and P3H1 are mutually stabilized in the collagen prolyl 3-hydroxylation complex (Chang et al. 2010). By contrast, the absence of CyPB does not alter CRTAP or P3H1 expression.

Recently, it has been demonstrated that Prolyl 3-hydroxylation complex is not only responsible for the 3-hydroxylation of specific proline residues in the chains of fibrillar collagens, but it also acts as a molecular chaperone (Iannitti and Palmieri 2011).

As part of my PhD activity I contributed to the characterization of zebrafish knock-out models for *crtap* and *p3h1*, mainly dealing with the analysis of morphometric parameters, skeletal staining, SDS-PAGE of skin and bone extracted collagen.

These models were generated by CRISPR/Cas9 gene editing in the laboratory of Professor Forlino, in order to better elucidate the relationship between the correct function of the complex and the mechanisms of the disease. In human and in mice, mutations in both genes lead to a loss of 3-Hyp in collagen type I. Nevertheless, mass spectrometry data revealed that the highly conserved target sequence at the Pro986 site in the $\alpha 1(I)$ chain is not 3-hydroxylated in zebrafish collagen type I (Hudson et al. 2014)(Weis and Eyre, unpublished data).

crtap^{-/-} and *p3h1*^{-/-} zebrafish models present a severe skeletal phenotype, characterized by reduced size, body disproportion, altered mineralization and their collagen type I is overmodified, as observed also in OI patients and murine models. For these reasons, the two knock-out lines represent valuable models for human OI type VII and VIII forms, respectively, reproducing their main skeletal, biochemical, and cellular features. The lack of zebrafish 3-hydroxylation supports the defective chaperone role of 3-hydroxylation complex as the primary cause of the OI bone phenotype.



Crtap and *p3h1* knock out zebrafish support defective collagen chaperoning as the cause of their osteogenesis imperfecta phenotype



F. Tonelli^a, S. Cotti^{a,1}, L. Leoni^{a,1}, R. Besio^a, R. Gioia^a, L. Marchese^a, S. Giorgetti^a, S. Villani^b, C. Gistelink^c, R. Wagener^d, B. Kobbe^d, I.A.K. Fiedler^e, D. Larionova^f, B. Busse^e, D. Eyre^c, A. Rossi^a, P.E. Witten^f and A. Forlino^a

a - Department of Molecular Medicine, Biochemistry Unit, University of Pavia, Pavia, Italy

b - Department of Public Health and Experimental and Forensic Medicine, Unit of Biostatistics and Clinical Epidemiology, University of Pavia, Pavia, Italy

c - Department of Orthopedics and Sports Medicine, University of Washington, Seattle, WA, United States

d - Medical Faculty, Center for Biochemistry, Center for Molecular Medicine, University of Cologne, Cologne, Germany

e - Department of Osteology and Biomechanics, University Medical Center Hamburg-Eppendorf, Hamburg, Germany

f - Department of Biology, Ghent University, Ghent, Belgium

Corresponding author. aforlino@unipv.it.

<https://doi.org/10.1016/j.matbio.2020.03.004>

Abstract

Prolyl 3-hydroxylation is a rare collagen type I post translational modification in fibrillar collagens. The primary 3Hyp substrate sites in type I collagen are targeted by an endoplasmic reticulum (ER) complex composed by cartilage associated protein (CRTAP), prolyl 3-hydroxylase 1 (P3H1) and prolyl *cis/trans* isomerase B, whose mutations cause recessive forms of osteogenesis imperfecta with impaired levels of $\alpha 1(I)3\text{Hyp}986$. The absence of collagen type I 3Hyp in wild type zebrafish provides the unique opportunity to clarify the role of the complex in vertebrate. Zebrafish knock outs for *crtap* and *p3h1* were generated by CRISPR/Cas9. Mutant fish have the typical OI patients' reduced size, body disproportion and altered mineralization. Vertebral body fusions, deformities and fractures are accompanied to reduced size, thickness and bone volume. Intracellularly, collagen type I is overmodified, and partially retained causing enlarged ER cisternae. In the extracellular matrix the abnormal collagen type I assembles in disorganized fibers characterized by altered diameter. The data support the defective chaperone role of the 3-hydroxylation complex as the primary cause of the skeletal phenotype.

© 2020 Elsevier B.V. All rights reserved.

Introduction

3-Hydroxyproline (3Hyp) is a rare collagen amino acid modification first identified in the early 60's [1]. It is found in the Xaa-position of the triplet -Gly-Xaa-Yaa- in the sequence -Gly-3Hyp-4Hyp-Gly- and its amount varies in the different collagens types, being more abundant in collagen IV and V and present only at one residue per $\alpha 1$ chain in collagen I and II [2–4]. Hydroxylation of proline in C-3 requires the activity of prolyl 3-hydroxylases (P3Hs), that in the human genome are encoded by three genes, *P3H1*, *P3H2* and *P3H3* and are characterized by tissue specific expression [5–7]. 3Hyp is already present in porifera, indicating that it is highly important for proper extracellular matrix of

multicellular animals [8]. Nevertheless, the exact role of the 3-hydroxylation of proline residues in collagen is still not completely understood. In general, proline hydroxylation is known to be necessary for proper procollagen folding and collagen fibril assembly. 4-Hydroxyprolines (4Hyp) in the Yaa positions increase the triple helix stability by forming water-bridged intramolecular hydrogen bonds or by stereoelectric effect and represent key elements for collagen folding [9]. Initially, a role for 3Hyp in collagen stability was also hypothesized based on the analysis of collagen mimetic peptides that, in presence of 3Hyp in Xaa-position, showed reduced thermal stability [10]. This finding was not confirmed in a follow up analysis where a small increase of stability was instead associated to

3Hyp containing synthetic peptides [11]. Furthermore, since 3Hyp is scarce and this residue never exceeds 10% of the total proline in collagen molecules, its effect on triple helix stability seems unlikely and a function in super molecular assembly or in the interaction with non collagenous proteins has been proposed [4]. In 2006, the severe bone phenotype associated with a lack of this 3Hyp in collagen type I both in human and mice as a consequence of a loss-of-function of cartilage associated protein (CRTAP) turned again on the attention on this rare post translational collagen modification [12,13]. In collagen type I the only fully occupied 3Hyp site is Pro986 in $\alpha 1(I)$ and its synthesis is catalyzed by the endoplasmic reticulum (ER) complex constituted by CRTAP, prolyl 3-hydroxylase 1 (P3H1) and cyclophilin B (CyPB) associated in a 1:1:1 ratio [7,12]. CRTAP acts as a helper protein within the complex, while P3H1, carrying a KEDL ER retention signal, has enzymatic activity and CyPB is a prolyl peptidyl *cis/trans* isomerase (PPIase) involved in the rate limiting step of triple helical folding. When acting on pro α chains, the complex proved to have both an enzymatic and a chaperone function, whereas when acting on the folded triple helix it inhibited fibril formation [14]. CyPB does not contribute to the latter function, which seems associated with CRTAP and P3H1, only. Interestingly, CRTAP and P3H1 in the complex are stabilizing each other and the lack of one protein is compromising the stability of the other, without affecting cyclophilin B. The absence of CyPB also has minimal effect on CRTAP/P3H1 [15].

Soon after the identification of CRTAP mutations as cause for osteogenesis imperfecta (OI) type VII, defects in the other two components of the complex P3H1 and CyPB were shown to be responsible for rare recessive forms of OI, classified as OI type VIII and IX, respectively and characterized by skeletal deformity and extreme bone fragility [16]. An absence of 3Hyp and overglycosylation of collagen type I are typical features of OI type VII and OI type VIII and a reduced level of 3Hyp986 in collagen type II is also reported in the murine models of the diseases [17,18]. Indeed, affected individuals suffer from osteochondrodystrophy with neonatal fractures and broad undertubulated long bones, white sclerae, and rhizomelia [19,20]. Mutations affecting the third member of the complex, cyclophilin B, cause a biochemically and phenotypically distinct OI variant. In OI type IX individuals $\alpha 1(I)$ 3Hyp986 content is reduced, but never absent and in milder forms is almost normal [13,21] and patients do not have rhizomelia. Levels of CRTAP and P3H1 proteins are only slightly reduced in CyPB-null cells, supporting a role for CyPB in protein folding and delivery of the complex to the nascent collagen chains through its

PPIase activity, rather than directly in the 3-hydroxylation [21].

What is responsible for the OI phenotype when the 3-hydroxylation complex is malfunctioning is still unclear. The question whether a lack of $\alpha 1(I)$ 3Hyp986 or impaired chaperone function of the complex caused bone fragility was addressed using a murine model in which the enzymatic activity was inactivated by a single amino acid substitution in the active site of *P3h1*, without compromising the complex assembly. Only a mild bone phenotype with decreased trabecular bone mass was detectable [17,18]. Interestingly, although the mutant mice showed a marked reduction in $\alpha 1(I)$ 3Hyp986, they were of normal appearance and size, with no growth plate abnormalities and normal collagen I post translational modification [17,18]. These findings suggest a limited role for 3Hyp in collagen intracellular folding and a potential role in collagen fibril assembly and/or extrafibrillar protein interaction [18].

The substrate motif for P3H1 activity in $\alpha 1(I)$, $\alpha 1(II)$, $\alpha 1(V)$ GXXGPIGPPGPR (A1 clade) had already appeared in primitive vertebrates [22], but exactly when the hydroxylation of this site first occurred during evolution is not clear. The site is present in zebrafish (*Danio rerio*) $\alpha 1(I)$, but we knew as background that no 3Hyp residues were formed here or at other known 3Hyp sites in zebrafish or other teleost type I or II collagen chains ([23]; Weis and Eyre, unpublished data). Nevertheless, in the zebrafish genome *crtap*, *p3h1* and *ppib* are present each as a single copy and expressed early during development [24,25] making this model a unique tool to understand the chaperone role of the complex in collagen type I and II biosynthesis. In the present study we successfully knocked out the *crtap* and *p3h1* genes in *D. rerio* by CRISPR/Cas9 and we used their deep molecular, biochemical and phenotypic characterization to investigate the role of the 3-hydroxylation complex in determining the skeletal phenotype. The results of this study shed new light on the molecular basis of the recessive OI type VII and VIII.

Results

Similarities and differences between zebrafish and mammal cartilage associated protein and prolyl 3-hydroxylase 1

An analysis of the human, mouse and zebrafish genomic regions surrounding the cartilage associated protein (*crtap*) and prolyl 3-hydroxylase 1 (*p3h1*) genes revealed shared synteny, supporting the presence of a common ancestral chromosomal origin. A unique orthologue of the human *CRTAP*

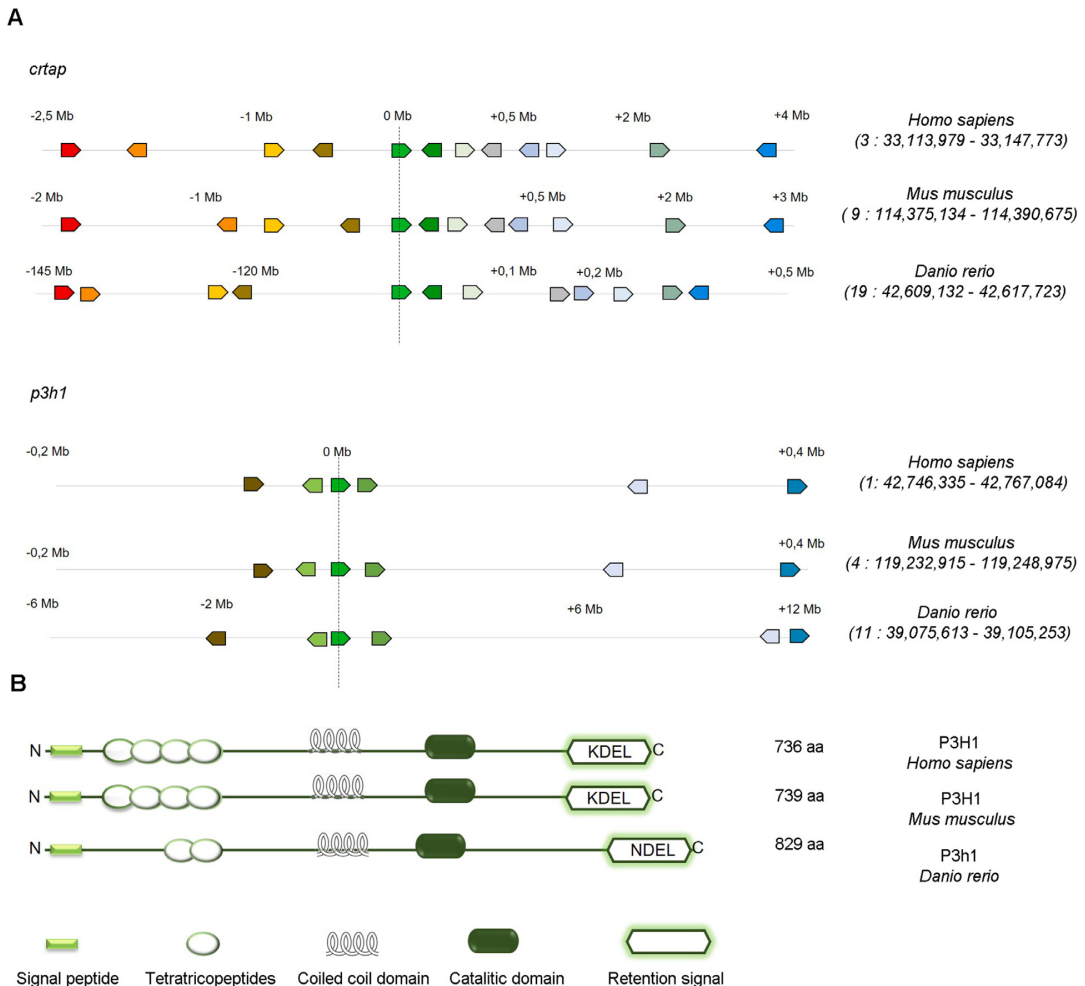


Fig. 1. *In silico* analysis of cartilage associated protein and prolyl 3-hydroxylase 1 among different species. (A) The synteny analysis performed on human (*H. sapiens*), murine (*M. musculus*) and zebrafish (*D. rerio*) cartilage associated protein (Crtap) and prolyl 3-hydroxylase 1 (P3h1) reveals the existence of a common ancestral chromosomal origin. Each color corresponds to a gene, the list of the genes is indicated in Supplementary Tables 1 and 2. (B) Prolyl 3-hydroxylase 1 domains are conserved among human, mouse and zebrafish.

gene is present in *D. rerio* on chromosome 19 and 11 genes are conserved in the region surrounding the zebrafish and human/murine *CRTAP* locus. Similarly, a unique orthologue of the human *P3H1* gene is present on chromosome 11 of *D. rerio* genome and the region surrounding the zebrafish and human/murine *P3H1* locus shows 5 conserved coding genes (Fig. 1A, Supplementary Tables 1 and 2).

The zebrafish Crtap (Q1L8P0) consists of 396 amino acids (aa) and shows 56.7% and 65.4% identity with the two human CRTAP isoforms of 358 (C9JP16) and 401 (O75718) aa, respectively, and

68% identity with the 400 aa murine CRTAP (Q9CYD3).

In zebrafish a single P3h1 isoform (A0A0R419E8) of 829 aa is present and it has 52.3% identity with the human P3H1 (Q32P28), containing the endoplasmic reticulum signal KDEL at the C-terminal end and associated to OI type VIII. The murine P3h1 (Q3V1T4) with the same domain structure as human P3H1, consists of 739 aa and shares 54% identity with the zebrafish protein. Considering the specific functional domains, the zebrafish P3h1 shares 52.2% and 54% identity in the prolyl 3-hydroxylase domain and 85.7% and

86% identity in the coiled coil domain with the human and mouse proteins, respectively. Only two of the four human and murine tetratricopeptide repeat-containing domains (TPR) are present in the zebrafish orthologue. Finally, the KDEL retention signal in zebrafish is replaced with a NDEL sequence (Fig. 1B, Supplementary Table 3). Considering the role of these domains in protein-protein interaction it can be speculated a different affinity of P3h1 for its partner Crtap.

Generation of the OI type VII and VIII zebrafish models by CRISPR/Cas9

The general strategy adopted to generate the *crtap* and *p3h1* knock out zebrafish models for osteogenesis imperfecta type VII and VIII, respectively is outlined in Fig. 2A. Two specific RNA guides (gRNAs) targeting exon 1 of *crtap* gene and exon 2 of *p3h1* gene, respectively were microinjected in 1–2 cell stage zebrafish fertilized embryos together with *in vitro* transcribed Cas9 mRNA. F0 mosaic zebrafish were screened for specific targeting at 1 day post fertilization (dpf) by T7 endonuclease I (T7EI) assay and by Sanger sequencing (Fig. 2B). The mutagenesis rate was 92% for *crtap* and 77% for *p3h1*.

The F0 mosaic zebrafish were outcrossed to wild type (WT) AB zebrafish. Several pools of embryos were collected at 1 dpf and screened by T7EI assay to identify the F0 germ line zebrafish, that were further outcrossed to AB WT. F1 progeny was initially screened by T7 endonuclease assay to discriminate the WT from the heterozygous mutant animals and the mutants finally confirmed by Sanger sequencing. Several insertions, deletions and *indel* mutations were identified (Supplementary figure 1) and among them, one for each gene of interest was selected to generate a *crtap* and a *p3h1* knock out zebrafish line. The mutant F1 zebrafish carrying the c.199_202delTTTCinsAG in *crtap* (Fig. 2C), predicted to insert a premature stop codon at amino acid 80 of Crtap was chosen to obtain the F2 *crtap* knock out model (*crtap*^{-/-}). The mutant F1 zebrafish carrying the c.645delCinsGGAGAA in *p3h1* (Fig. 2C), predicted to insert a premature stop codon at amino acid 266 of P3h1 protein was selected to generate the F2 *p3h1* knock out model (*p3h1*^{-/-}). Because of the two specific mutations, genotyping of the mutant zebrafish by restriction enzyme digestion of the amplicon of the region surrounding the target sequence could be performed. *BpmI* and *Eco0109I* were used for *crtap*^{-/-} and *p3h1*^{-/-} genotyping, respectively (Fig. 2D). qPCR analysis revealed about 50% reduction of mutant *crtap* expression (WT: 0.80 ± 0.30, *crtap*^{-/-}: 0.44 ± 0.10) in *crtap*^{-/-} zebrafish and normal level for *p3h1* (WT: 0.77 ± 0.32, *p3h1*^{-/-}: 1.15 ± 0.46) in *p3h1*^{-/-} zebrafish compared to WT. Nevertheless, no Crtap

and P3h1 were translated due to the introduction of a premature stop codon in both proteins, as demonstrated by western blot analysis using specific antibodies (Fig. 2E, Supplementary figure 2).

Growth and mineralization delay in *crtap*^{-/-} and *p3h1*^{-/-} resemble human OI type VII and VIII outcome

Osteogenesis imperfecta type VII and VIII are characterized both in humans and murine models by growth delay and altered mineralization. Gross observation of the homozygous *crtap*^{-/-} and *p3h1*^{-/-} zebrafish clearly revealed a reduced size compared to WT (Fig. 3A). To provide quantitative data the zebrafish growth curve was evaluated by measuring the standard length (SL) of WT, *crtap* and *p3h1* heterozygous and homozygous mutant zebrafish from 1 to 8 weeks post fertilization (wpf). A significant growth delay in both homozygous *crtap*^{-/-} and *p3h1*^{-/-} zebrafish compared to WT and heterozygous animals was evident, which reproduced the findings in human (Fig. 3B).

Interestingly, a complete loss of Crtap resulted in a 50% lethality by 3 wpf (1 wpf: WT *n* = 24, *crtap*^{+/-} *n* = 57, *crtap*^{-/-} *n* = 14; 2 wpf: WT *n* = 28, *crtap*^{+/-} *n* = 55, *crtap*^{-/-} *n* = 20; 3 wpf: WT *n* = 25, *crtap*^{+/-} *n* = 46, *crtap*^{-/-} *n* = 10, WT *n* = 13, *crtap*^{+/-} *n* = 27, *crtap*^{-/-} *n* = 10), whereas no effect on the survival was evident in absence of P3h1.

Alizarin red staining revealed a delay in the mineralization of the cranial bones at 1 and at 2 wpf in homozygous *crtap*^{-/-} and *p3h1*^{-/-} zebrafish compared to WT. The analysis was performed for two bones that form around a cartilaginous anlage, the hyomandibular (HM) and ceratohyal (CHB), and on the vertebral centra that are established by direct mineralization of the notochord sheath [26] (Fig. 3C). At 1 wpf, *crtap*^{-/-} mutants showed a borderline significant or significant mineralization impairment in all analyzed bones compared to WT (NC: p Fisher's exact test=0.07, HM: p Fisher's exact test=0.007 and CHB: p Fisher's exact test=0.005, respectively), whereas only a slightly reduced mineralization was observed in *p3h1* mutants, compared to controls. (Fig. 3D). Precisely, the quote of *p3h1*^{-/-} with a notochord (NC) complete mineralization was the half of WT, but the difference was not significant (chi2 = 1.87, *p* = 0.17) (Fig. 3D). The *p3h1*^{-/-} with a complete mineralization were less than WT without differences between groups (p Fisher's exact test = 0.49). Contrary to previous bones, CHB showed a beginning in mineralization in both WT and *p3h1*^{-/-}, even if it was higher in the last (Fig. 3D). The delay in mineralization was greater in *p3h1*^{-/-} than in WT, but not statistically relevant (p Fisher's exact test = 0.58) (Fig. 3D).

At 2 wpf a significantly lower mineralization was detectable in *p3h1*^{-/-} compared to WT only for NC

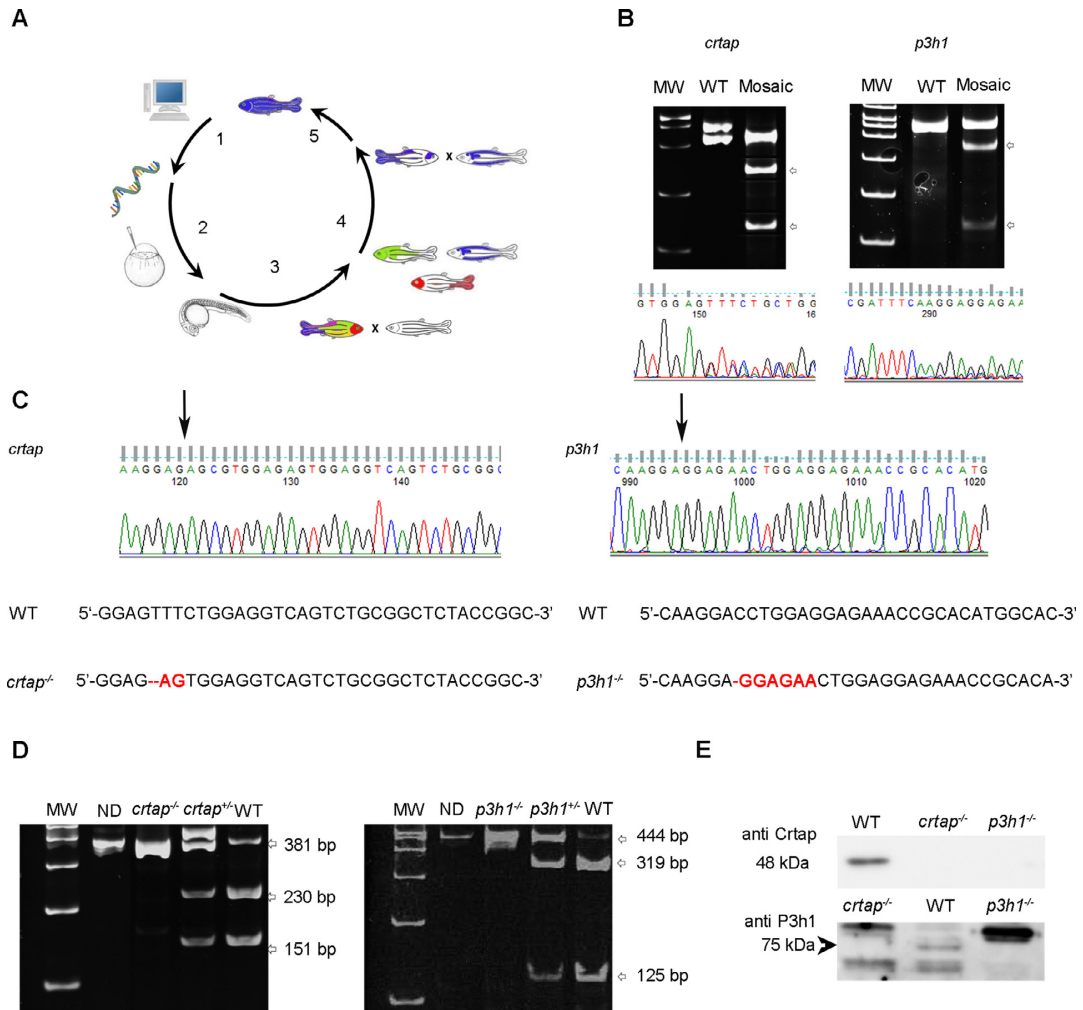


Fig. 2. Generation of OI type VII and VIII zebrafish models using CRISPR/Cas9. (A) Strategy used to generate mutants: 1. *In silico* target sequence identification; 2. gRNAs and Cas9 mRNA *in vitro* transcription and microinjection in fertilized zebrafish embryos; 3. Targeting evaluation and F0 mosaic fish screening; 4. Generation of F1 heterozygote fish; 5. Generation of F2 homozygote mutant fish. (B) F0 mosaic fish screening using T7 endonuclease assay followed by Sanger sequencing. Amplicons are digested by T7 endonuclease in presence of heterozygosity. (C) DNA sequences of F1 heterozygotes selected to generate knock out fish. Black arrows indicate mutation sites, red dashes indicate deletions, red bolded nucleotides indicate insertions. (D) Restriction enzyme-based screening to genotype *crtap* (left) and *p3h1* (right) WT and mutant alleles. PCR amplicon of the region surrounding the mutation was digested with *BpmI* (left) and *EcoO109I* (right), that specifically cut the wild type sequence, generating 230 and 151 bp fragments and 319 and 125 bp fragments, respectively. Mutant alleles lack the restriction site and are left undigested. MW: molecular weight, ND: not digested. (E) Western blots performed on proteins extracted from WT ($n=3$), *crtap*^{-/-} ($n=3$) and *p3h1*^{-/-} ($n=3$) skin reveal the absence of Crtap in *crtap*^{-/-} and P3h1 in *p3h1*^{-/-}. Moreover, Crtap is absent in *p3h1*^{-/-} and P3h1 is absent in *crtap*^{-/-}. The arrowhead point to the P3h1 specific band. (For interpretation of the references to color in this figure legend, the reader is referred to the web version of this article.)

(p Fisher's exact test = 0.006) and CHB (p Fisher's exact test = 0.003) (Fig. 3D). Whereas in *crtap* mutant the delay in mineralization was significant with respect to WT for all bones (NC: p Fisher's exact test < 0.001, HM: Fisher's exact test = 0.019

and CHB: p Fisher's exact test = 0.001, respectively).

Alizarin red staining of 1 month post fertilization (mpf) WT and *p3h1*^{-/-} larvae revealed reduced vertebral centrum length (WT = 0.156 ± 0.015 mm;

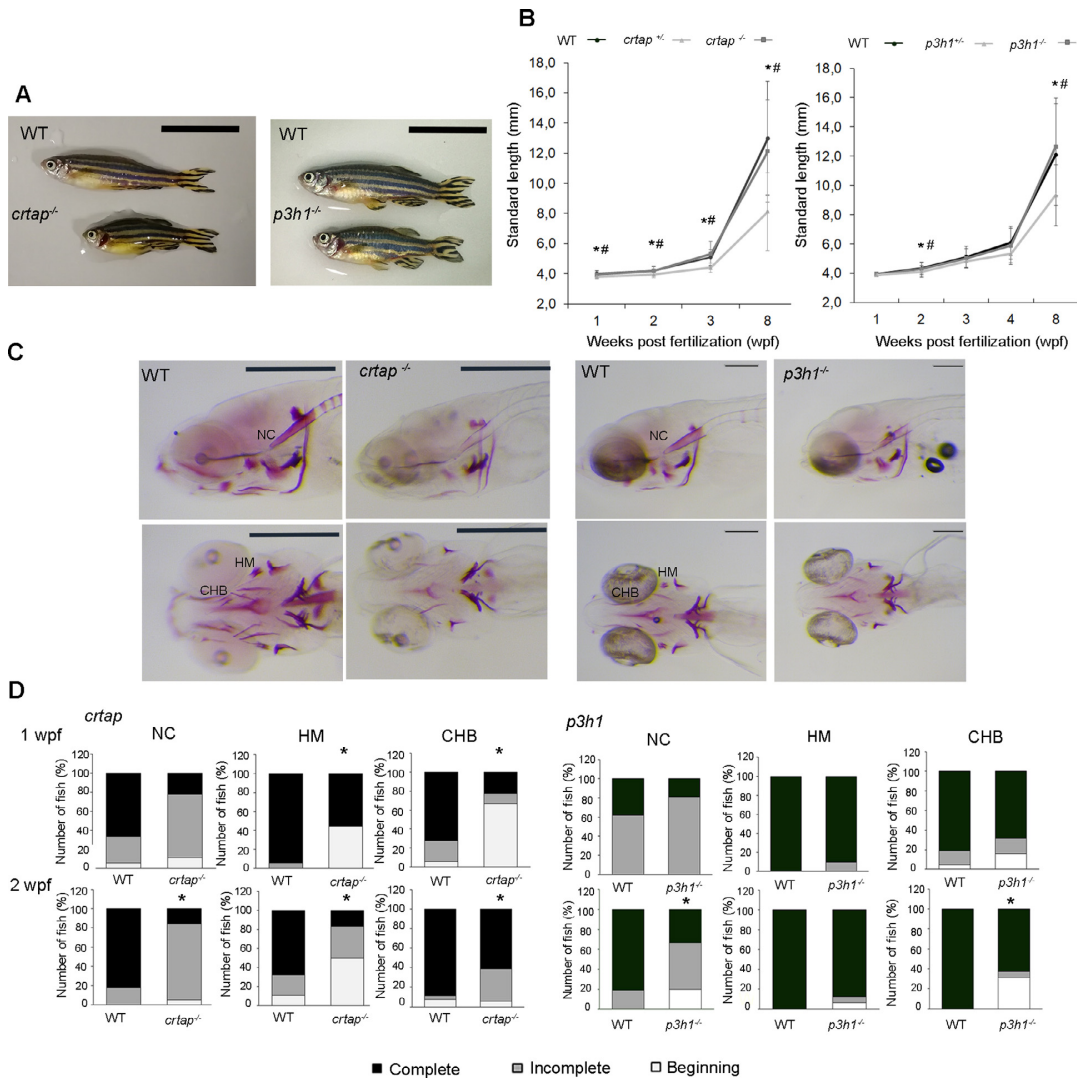


Fig. 3. *crtap*^{-/-} and *p3h1*^{-/-} mutants present reduced length and delayed mineralization compared to WT. (A) Adult WT, *crtap*^{-/-} and *p3h1*^{-/-} fish bright field images. Scale bar: 1 cm. (B) Growth curves representing WT, heterozygotes and homozygotes standard length measured from 1 to 8 wpf for *crtap*^{-/-} (WT *n* ≥ 13, *crtap*^{+/-} *n* ≥ 27, *crtap*^{-/-} *n* ≥ 10) and from 1 to 8 wpf for *p3h1*^{-/-} (WT *n* ≥ 19, *p3h1*^{+/-} *n* ≥ 34, *p3h1*^{-/-} *n* ≥ 14). *crtap*^{-/-} and *p3h1*^{-/-} fish are shorter than WT and heterozygotes. *: *p* < 0.05 between WT and homozygous mutants; #: *p* < 0.05 between heterozygous and homozygous mutants. (C) Lateral and ventral views of alizarin red stained WT, *crtap*^{-/-} and *p3h1*^{-/-} fish. The notochord is shown in the lateral view, while the hyomandibular and the ceratohyal bones are represented in the ventral view. Scale bar: 500 μm for WT and *crtap*^{-/-}, 200 μm for WT and *p3h1*^{-/-}. (D) Level of bone mineralization analyzed in WT, *crtap*^{-/-} and *p3h1*^{-/-} fish. A delayed mineralization is evident at 1 and at 2 wpf in *crtap*^{-/-} while only at 2 wpf in *p3h1*^{-/-}, respect to controls. NC: notochord, HM: hyomandibular, CHB: ceratohyal. 1 wpf (*crtap* matings: WT *n* = 22, *p3h1*^{-/-} *n* = 21) and 2 wpf (*crtap* matings: WT *n* = 28, *crtap*^{-/-} *n* = 20; *p3h1* matings: WT *n* = 22, *p3h1*^{-/-} *n* = 16). Data information: values are expressed as mean ± standard deviation and statistical significance (*p* < 0.05) determined by One way Anova in panel B and by Chi-squared test or the Fisher's exact test in panel D.

Table 1. Morphometric analysis of 2 mpf WT, *crtap*^{-/-} and *p3h1*^{-/-} zebrafish.

	WT		p value	<i>crtap</i> ^{-/-}		p value	WT		p value	<i>p3h1</i> ^{-/-}	
	Mean ± SD			Mean ± SD			Mean ± SD				
N	13	10		28	14		12.11 ± 3.46	9.34 ± 2.08	0.005		
SL (mm)	12.99 ± 3.77	8.12 ± 2.59	0.004	12.11 ± 3.46	9.34 ± 2.08	0.005					
N	13	6		25	14		2.51 ± 0.87	1.89 ± 0.65	0.02		
HAA (mm)	2.95 ± 0.8	2.02 ± 0.52	0.06	2.51 ± 0.87	1.89 ± 0.65	0.02					
N	13	7		25	14		2.34 ± 0.56	2.02 ± 0.47	0.1		
HE (mm)	2.47 ± 1	1.69 ± 1.13	0.13	2.34 ± 0.56	2.02 ± 0.47	0.1					
N	13	4		23	12		3.21 ± 0.71	2.68 ± 0.54	0.03		
SOL (mm)	3.09 ± 1.15	2.79 ± 0.82	0.46	3.21 ± 0.71	2.68 ± 0.54	0.03					
N	13	6		25	14		5.54 ± 0.73	5.17 ± 0.73	0.78		
SL/HAA	4.38 ± 0.45	6.03 ± 2.88	0.31	5.54 ± 0.73	5.17 ± 0.73	0.78					
N	13	4		23	12		1.32 ± 0.10	1.26 ± 0.07	0.08		
SOL/HE	1.29 ± 0.16	1.11 ± 0.05	0.04	1.32 ± 0.10	1.26 ± 0.07	0.08					

p3h1^{-/-} = 0.133 ± 0.015 mm, $p < 0.05$) and area (WT = 0.018 ± 0.003 mm²; *p3h1*^{-/-} = 0.014 ± 0.003 mm², $p = 0.056$), further confirming a delay in bone mineralization during development.

crtap^{-/-} and *p3h1*^{-/-} zebrafish display body disproportion

Morphometric analyses, performed on lateral bright field images of adult *crtap*^{-/-}, *p3h1*^{-/-} and WT zebrafish, were used to evaluate the presence of body disproportion, a common feature in the more severe OI forms [27]. At 2 mpf, *crtap*^{-/-} were not only shorter than WT, as already revealed by the growth curve (SL: $p = 0.002$, Fig. 3B, Table 1), but showed a reduced body height compared to the littermates, as demonstrated by measuring the dorsal-ventral distance (Height at Anterior margin of Anal fin, HAA: $p = 0.06$). The height (Height at Eye, HE), the length (Snout-Operculum Length, SOL) of the head and the SL/HAA ratio were not significantly reduced in *crtap*^{-/-} with respect to WT, nevertheless, the significant reduction of the SOL/HE ratio ($p = 0.04$) in *crtap*^{-/-} zebrafish revealed the presence of a chunky head (Table 1). Similarly, the *p3h1*^{-/-} at 2 mpf displayed decreased body length ($p = 0.009$, Fig. 3B, Table 1) and reduced HAA compared to WT zebrafish ($p = 0.02$) (Table 1). In the head of *p3h1*^{-/-} zebrafish the height (HE) was not significantly reduced, whereas the SOL was significantly decreased compared to WT ($p = 0.03$) (Table 1). On the contrary to *crtap*^{-/-}, the SL/HAA and SOL/HE ratios were similar in *p3h1*^{-/-} and WT zebrafish, demonstrating normal body proportion. Nevertheless, at 6 mpf the *p3h1* mutant phenotype worsened, the knock out zebrafish were drastically shorter ($p = 0.004$) with severe disproportions both in the head and in the body (Supplementary Table 4).

Skeletal deformities and altered vertebral bone morphology in the knock out models

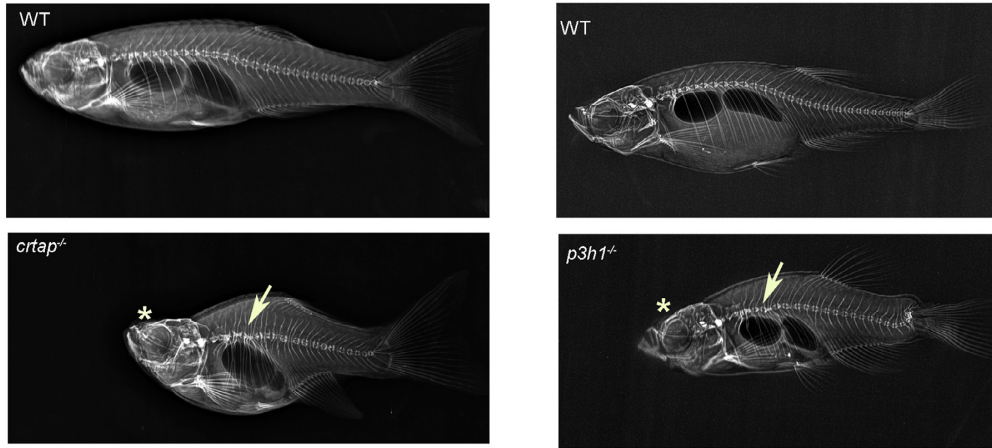
Severely deformed spinal columns with vertebral body compression, distortion and misalignment along the antero-posterior axis were detected in both *crtap*^{-/-} and *p3h1*^{-/-} zebrafish by X-ray imaging. The presence of the chunky head shape of *crtap*^{-/-} was also confirmed (Fig. 4A). μ CT, performed at 10 mpf, revealed in both knock out models severe spine and body deformities and the presence of calli in the ribs (Fig. 4B). An evaluation of bone properties by high-resolution μ CT was possible only for *p3h1*^{-/-}, due to the high mortality of *crtap*^{-/-}, that limited the availability of a proper number of animals for statistical analysis.

μ CT of WT and *p3h1*^{-/-} at 8 mpf revealed deformities in the vertebral column of *p3h1*^{-/-} including the presence of several ribs attached to one vertebral body (Fig. 4C). Morphometric analysis of the first precaudal vertebral body ($n = 5$ fish/group) revealed a similar vertebral body length in the study groups, but significantly reduced bone volume (0.009 ± 0.002 mm³ vs. 0.014 ± 0.003, $p < 0.05$), mean vertebral thickness (14.6 ± 1.1 μ m vs. 17.8 ± 0.6 μ m, $p < 0.001$) and polar moment of inertia, a surrogate measure for the resistance against torsion (0.29 ± 0.05 ($\times 10^{-3}$ mm⁴) vs. 0.48 ± 0.20 ($\times 10^{-3}$ mm⁴), $p < 0.05$) compared to WT. Also, the estimated vertebral diameter (0.199 ± 0.009 mm vs. 0.243 ± 0.010 mm, $p < 0.001$) and cross sectional bone area were reduced in mutants compared to WT (0.017 ± 0.002 mm² vs. 0.022 ± 0.003 mm², $p < 0.05$) (Fig. 4D).

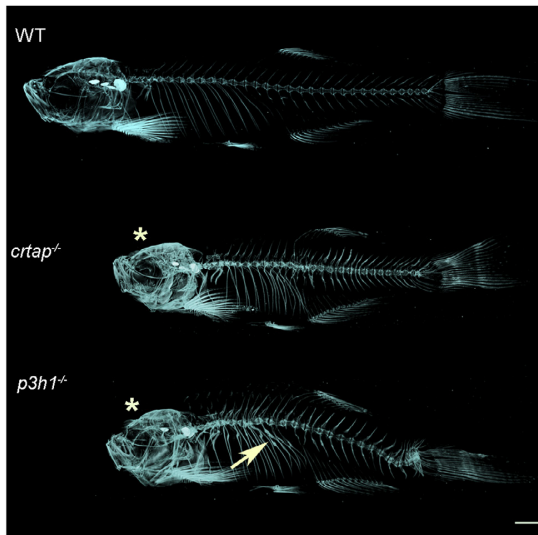
crtap^{-/-} and *p3h1*^{-/-} have a delay in the inflation of the swim bladder

The teleost swim bladder is located at the dorso-anterior part of the abdominal cavity and it is evolutionary derived from the lungs of basal osteichthyans

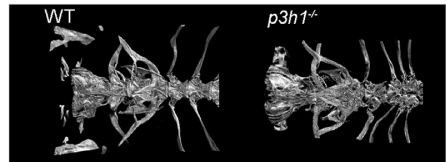
A



B



C



D

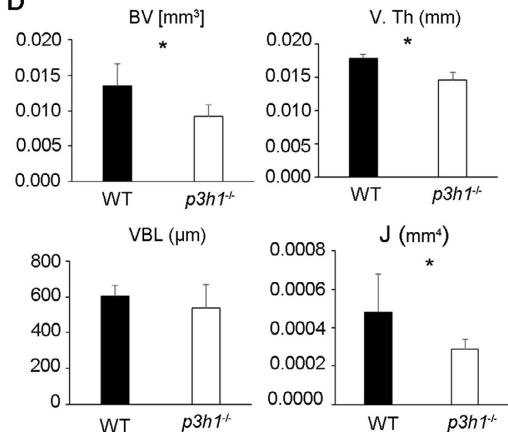


Fig. 4. *crtap*^{-/-} and *p3h1*^{-/-} have skeletal deformities and impaired bone properties. (A) X-rays of 2 mpf (*crtap* matings: WT *n* = 5, *crtap*^{-/-} *n* = 5; *p3h1* matings: WT *n* = 28, *p3h1*^{-/-} *n* = 15), 4 mpf (*crtap* matings: WT *n* = 2, *crtap*^{-/-} *n* = 3) and 6–12 mpf (*p3h1* matings: WT *n* = 33, *p3h1*^{-/-} *n* = 8) zebrafish show a severe skeletal phenotype both at the level of the skull (asterisk) and at the level of vertebral column (arrow) in mutants with respect to controls. Magnification 5x. (B) μ CT scans of adult WT (*n* = 5), *crtap*^{-/-} (*n* = 3) and *p3h1*^{-/-} (*n* = 5) confirmed the skeletal deformities observed by X-rays (asterisks). The presence of calli at the level of the ribs of mutant fish suggests also bone fragility. Scale bar: 2 mm. (C) Ventral view of the first vertebrae in WT and *p3h1*^{-/-}, including weberian and precaudal vertebrae with attached ribs. In *p3h1*^{-/-}, the presence of several ribs attached to the second precaudal vertebral body was frequently observed. (D) Morphometric analysis of the first precaudal vertebral body (*n* = 5 fish/group) resulted in significantly smaller bone volume (BV) and smaller thickness of the vertebral bone (V.Th), similar vertebral body length (VBL) and smaller polar moment of inertia (J, surrogate measure for the resistance against torsion) in *p3h1*^{-/-} compared to WT controls. Data information: in panel D values are expressed as mean \pm standard deviation and statistical significance, determined by two-tailed unpaired T-test, is indicated by **p* < 0.05.

[28]. It is composed by a first lobe which is inflated at the end of the first week post fertilization. The development of this organ continues until the second lobe becomes inflated at 3 wpf [29] (**Supplementary figure 3**). Analysis of the swim bladder in WT and mutant zebrafish revealed a delay in its initial inflation at 1 wpf in *crtap*^{-/-} (MW=3.16, $p=0.002$) and *p3h1*^{-/-} (MW=2.78, $p=0.005$) compared to WT zebrafish. Starting from 2 wpf, the gap disappeared between WT and *crtap*^{-/-} (MW=1.92, $p=0.06$): the first lobe became inflated in WT and this happened also in *p3h1*^{-/-} mutant. At 3 wpf both WT and mutant zebrafish showed a similar level of inflation for both lobes (*crtap*^{-/-}: MW=1.33, $p=0.18$; *p3h1*^{-/-}: MW=0.96, $p=0.34$).

Impairment of the collagen chaperone activity of the complex

Type I collagen extracted from bone and skin of WT and mutant knock out fish was analyzed by SDS-Urea-PAGE. A slight slower migration and broadening of the electrophoretic bands corresponding to the type I collagen α chains were evident in mutant samples (**Fig. 5A**) supporting the presence of collagen overmodification, a typical feature in OI type VII and VIII patients and murine models. ³H-proline labelled type I collagen was also obtained from the tail of adult WT, *crtap*^{-/-} and *p3h1*^{-/-} fish, as described in methods and analyzed by SDS-Urea-PAGE. Even stronger delay in migration and broadening of the α bands was evident in mutant samples confirming the synthesis of collagen overmodification (**Fig. 5B**).

Electrophoretic delay and/or broadening of the collagen I α bands is usually caused by excessive lysine hydroxylation and glycosylation [30], as a result of delayed collagen triple-helix folding in the endoplasmic reticulum (ER). To explore this, the amino acid composition of collagen type I extracted from bone and skin of WT, *crtap*^{-/-} and *p3h1*^{-/-} fish was analyzed. The Hyl/Lys-ratio was increased in both bone and skin of knock out fish compared to controls, although the difference was limited due to the high level of lysine hydroxylation in control

zebrafish collagen type I, whose value was very closed to the maximum theoretical one (**Table 2, Supplementary Table 5**). Hyp/Pro-ratio was also significantly increased in mutant samples (**Table 2**).

Mass spectrometric analyses of the $\alpha 1-\alpha 3$ bands of collagen type I extracted from vertebral columns of WT and *p3h1* mutant fish revealed a complete absence of prolyl-3-hydroxylation of the specific Pro986 residue in both fish (**Fig. 5C**). This is consistent with our known lack of prolyl 3-hydroxylation at any site in normal teleost fibrillary type I collagen ([23]; Weis and Eyre, unpublished data). The mass spectral results also showed no difference between WT and mutant zebrafish bone collagen in the level of hydroxylation and glycosylation of lysine 87 and of the hydroxylation of the telopeptide (C-telopeptide) cross-linking lysine. The N-telopeptide Lys- and the Lys930 sites could not be detected in the assay (**Supplementary figure 4**).

Of relevance, the mutual protection of Crtap and P3h1 was demonstrated in zebrafish skin by western blotting. Crtap was absent in *p3h1*^{-/-} and P3h1 in *crtap*^{-/-} lysates, as reported by Chang W et al. in humans [15], thus supporting a defective chaperone role of the complex (**Fig. 2E, Supplementary figure 2**).

Collagen type I intracellular retention causes enlarged endoplasmic reticulum in *crtap*^{-/-} and *p3h1*^{-/-} zebrafish

Electron microscopy analysis of the notochord sheath was performed to evaluate the endoplasmic reticulum cisternae size in WT and knock out zebrafish. ER cisternae were clearly larger in osteoblasts (**Fig. 6A**) and chondroblasts (**Fig. 6B**) of *crtap*^{-/-} and *p3h1*^{-/-} compared to WT zebrafish.

Collagen type I fibers are disorganized and characterized by altered diameter in *crtap*^{-/-} and *p3h1*^{-/-} zebrafish

In OI type VII and VIII the overmodified collagen type I in the extracellular matrix self assembles into altered collagen fibers, thus histological analysis of

Table 2. Collagen type I lysine/hydroxylysine and proline/hydroxyproline ratios of mutant fish compared to WT.

	Hyl/(Hyl+Lys) mean \pm SD	p value	Hyp/(Hyp+Pro) mean \pm SD	p value
Bone				
WT	37.9% \pm 0.57%		45.2% \pm 0.27%	
<i>p3h1</i> ^{-/-}	39.2% \pm 0.41%	0.032	46.33% \pm 0.15%	0.003
<i>crtap</i> ^{-/-}	40.31% \pm 2.05%	0.12	46.79% \pm 0.08%	0.0006
Skin				
WT	32.3% \pm 0.34%		45.38% \pm 0.08%	
<i>p3h1</i> ^{-/-}	33.65% \pm 0.62%	0.023	46.79% \pm 0.09%	3.5E-05
<i>crtap</i> ^{-/-}	40.73% \pm 0.53%	2E-05	46.92% \pm 0.24%	2.8E-05

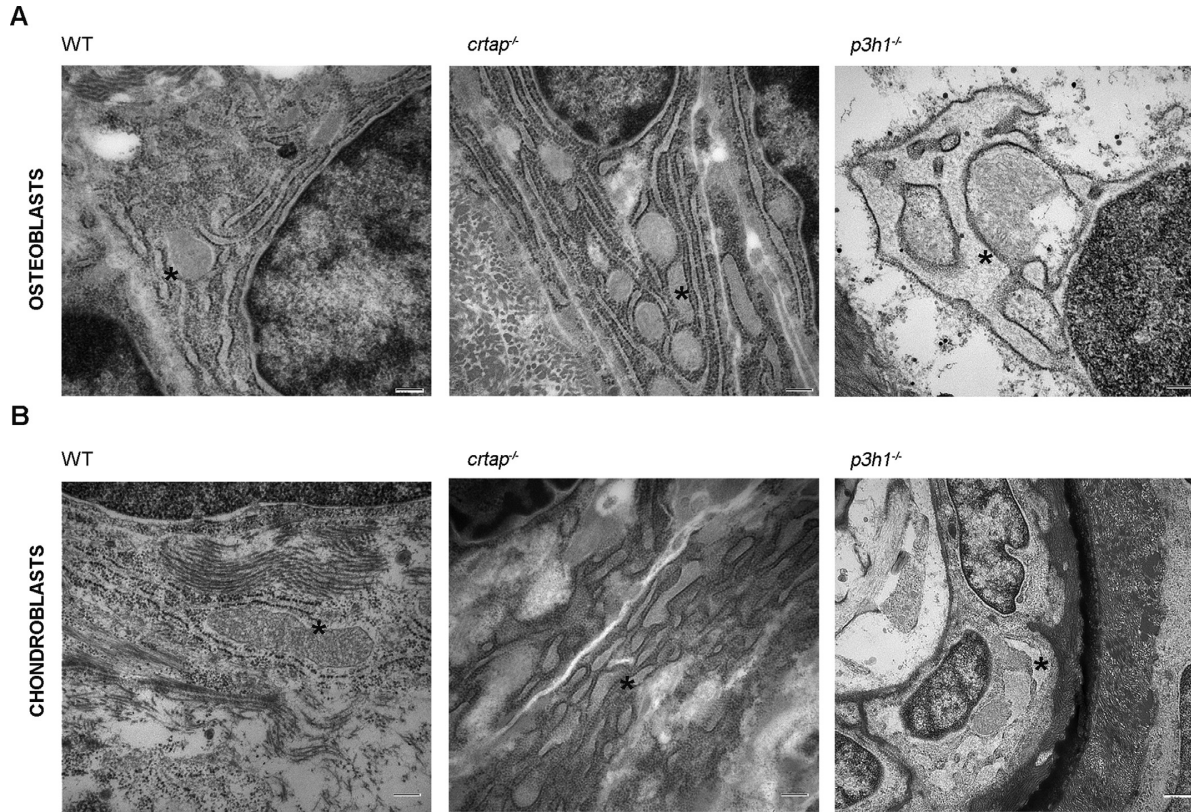


Fig. 6. *crtap*^{-/-} and *p3h1*^{-/-} cells show an endoplasmic reticulum cisternae enlargement. (A) Transmission electron microscopy images of osteoblasts at the level of the notochord sheath of 3 mpf *crtap*^{-/-} and 1 mpf *p3h1*^{-/-} show an endoplasmic reticulum cisternae (asterisk) enlargement with respect to 1 mpf WT. Scale bar: 200 nm. (B) Transmission electron microscopy images of chondroblasts at the level of the notochord sheath of 3 mpf *crtap*^{-/-} and 1 mpf *p3h1*^{-/-} show an endoplasmic reticulum (asterisk) cisternae enlargement with respect to 1 mpf WT. Scale bar: 200 nm for WT and *crtap*^{-/-} and 500 nm for *p3h1*^{-/-}.

skeletal tissue was performed on *crtap*^{-/-} and *p3h1*^{-/-} zebrafish models.

Histological analysis of toluidine blue stained semi-thin sections of young adult *crtap*^{-/-}, *p3h1*^{-/-} zebrafish and controls was performed. In *crtap*^{-/-} the vertebral body endplates were severely malformed. The notochord tissue in the intervertebral space took on a cartilaginous phenotype and became keratinized, typical reactions of damaged notochord tissue [31]. The bone volume of the vertebral body endplates was increased, albeit the bone structure was poorly organized (Fig. 7A). The notochord sheath appeared thinner in *p3h1*^{-/-} than in WT zebrafish, particularly in the intervertebral space and the analysis under polarized light showed the absence of birefringent staining in mutant zebrafish indicating the absence of organized collagen type I fiber bundles in the bone of neural arches, in the notochord sheath of the vertebral column and in the enlarged notochord sheath of the intervertebral space (Fig. 7B, Supplementary figure 5).

Electron microscopy analysis of the corresponding ultra-thin sections revealed significantly larger collagen type I fiber diameters in *crtap*^{-/-} compared to WT zebrafish (WT: 46.47 ± 7.38 nm, *crtap*^{-/-}: 49.11 ± 11.13 nm, $p < 0.05$) and smaller collagen type I fiber diameters in *p3h1* knock out zebrafish compared to WT (WT = 19.86 ± 3.63 nm; *p3h1*^{-/-} = 18.62 ± 3.52 nm, $p < 0.001$) (Fig. 7C). Interestingly, patches of fibers interspersed in the extracellular matrix of the inner site of the notochord containing collagen type II fibrils were present only in *p3h1*^{-/-}, but absent in WT zebrafish (Fig. 7D).

Cranial bone from adult *crtap*^{-/-} and *p3h1*^{-/-} zebrafish were also analyzed to evaluate collagen type I fibril size and patterning in mature bone matrix. Interestingly, the collagen type I fiber diameter was significantly reduced in both knock out lines compared to WT zebrafish (WT = 54.31 ± 10.47 nm, *crtap*^{-/-} = 29.91 ± 4.03 nm, *p3h1*^{-/-} = 32.17 ± 7.09 nm, $p < 0.001$). Irregular D-period patterning was also evident in both mutant lines compared to age matched WT controls (Fig. 7E).

Discussion

The endoplasmic reticulum prolyl 3-hydroxylation complex constituted by the 1:1:1 assembly of cartilage associated protein, prolyl 3-hydroxylase 1 and cyclophilin B is known to be crucial for proper bone formation [27]. Indeed, mutations in any of its three components are responsible for moderate to lethal recessive osteogenesis OI, namely OI type VII, VIII and IX [12,13,19,21]. Both an enzymatic and a chaperone function have been associated with the complex, but what is really causing the bone phenotype in OI patients is still unclear [14].

By CRISPR/Cas9 gene editing we generated zebrafish knock out models for *crtap* and *p3h1* carrying frameshift mutations that cause lack of protein translation. Deep molecular, morphological, biochemical and histomorphometric characterization of two knock out lines revealed a milder phenotype compared to that seen in OI patients probably due to the low weight bearing of zebrafish skeleton compared to tetrapodes. Nevertheless, different from the expected 1:2:1 (WT: *crtap*^{+/+}: *crtap*^{-/-}) Mendelian ratio a 50% lethality for *crtap*^{-/-} is observed in the first 3 weeks of age. Indeed, children with null mutation in *CRTAP* mostly die during infancy [20]. The survival rate of *p3h1*^{-/-} zebrafish is normal in contrast to what reported for infants with mutations in *P3H1* that often die in the perinatal period [19].

Overall, the phenotype of *crtap*^{-/-} and *p3h1*^{-/-} zebrafish is more in line with the milder OI phenotype described in the murine models that is worsening with aging. Viable knock out mice for OI type VII and VIII had been generated [12, 18]. Both *Crtap* and *P3h1* null mice are smaller than control littermates, develop progressive and severe kyphoscoliosis and show severe rhizomelia. In both murine models reduced bone density is described [12, 18].

Both zebrafish models recapitulate the growth delay and the bone phenotype typical of OI type VII and VIII. *Crtap*^{-/-} is already significantly shorter at 1 wpf and both models remain smaller throughout life, never reaching the size of control littermates.

Head and body disproportions are evident in both zebrafish models. Disproportion is already detectable at 2 mpf in *crtap*^{-/-}, and present at older age also in *p3h1*^{-/-}, again supporting the more severe outcome in zebrafish lacking *Crtap* protein. X-ray and μ CT scans show skeletal defects in *crtap*^{-/-} and *p3h1*^{-/-} compared to controls. Mutant zebrafish reveal deformed vertebral column, vertebral fusions and compressions, similar to the skeletal phenotype described in patients [32], but not detectable in the murine OI models [12, 18]. Indeed, vertebral compressions and vertebral fractures in human OI individuals are possible consequences of poor quality of bones that are unable to sustain the mechanical loading [27]. Interestingly, none of the murine OI models reproduce the vertebral phenotype, mainly because, being quadrupeds, they have a different spine structure and the impact of gravity is quite different from that in humans. Zebrafish instead bear cranial to caudal spinal loads caused by swimming forward through water coupled with a caudal propulsion. These loads are quite comparable to the gravitational load to which humans are exposed [33]. This makes zebrafish a reasonable model to analyze phenotype in bone diseases affecting vertebral column.

p3h1^{-/-} alizarin red staining reveals reduced vertebral size and μ CT of the vertebral bones shows reduced size, bone volume and thickness again resembling the human phenotype.

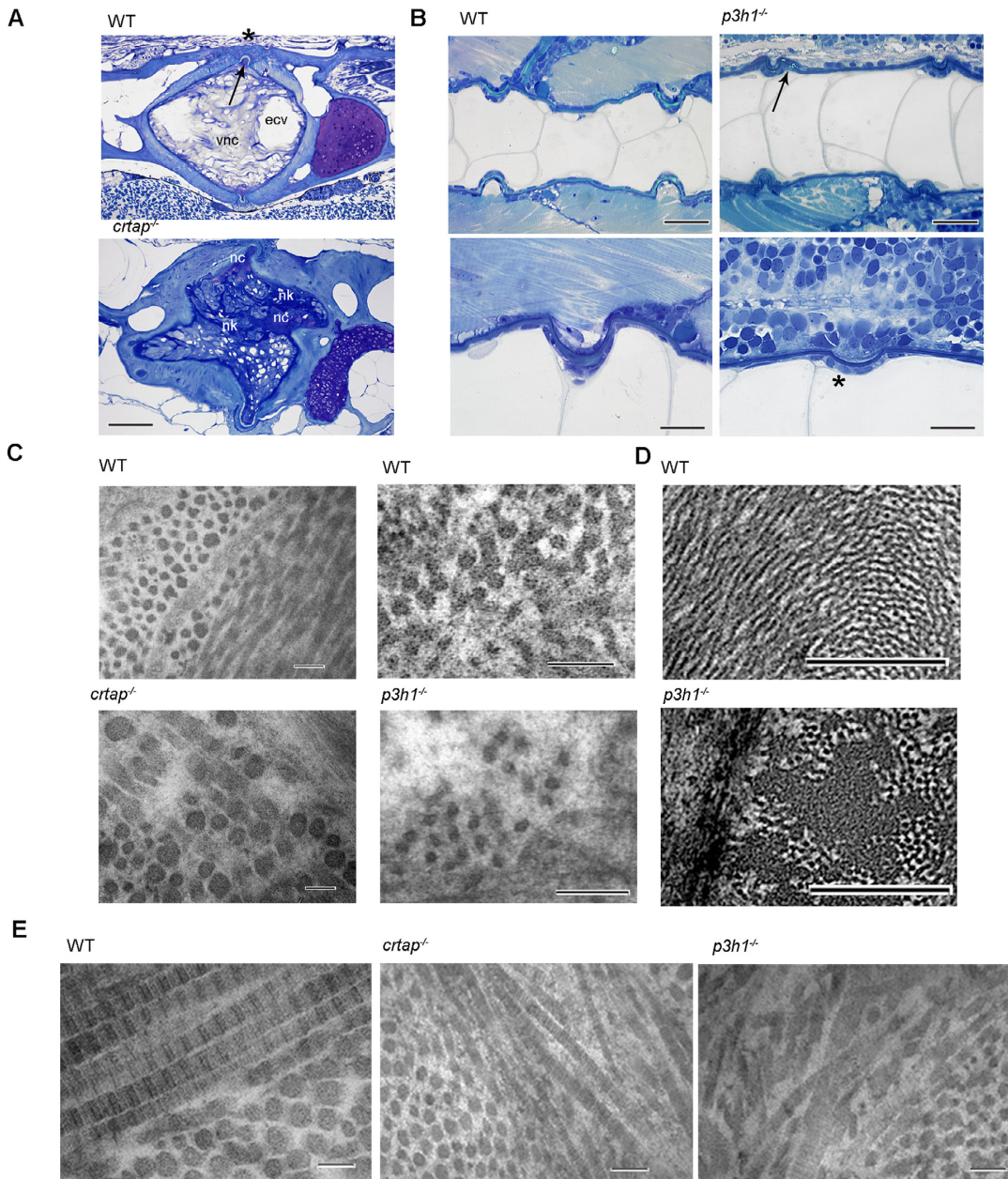


Fig. 7. *crtap*^{-/-} and *p3h1*^{-/-} collagen fibers abnormality in the notochord sheath region. (A) Toluidine blue stained sagittal sections of 3 mpf WT and *crtap*^{-/-} vertebral body endplates of two adjoined abdominal vertebral bodies. Top panel: In WT animals the intervertebral tissue consists of centrally located vacuolated notochord cells (vnc) and extracellular vacuoles (ecv). Black arrow indicates intervertebral space. The edges of the vertebral body endplates are connected by a ligament composed of the thickened collagen type II based notochord sheath and collagen type I fibers on the outside. Bottom panel: same location as above. Vertebral body endplates are severely malformed. The notochord tissue in the intervertebral space takes on a cartilaginous phenotype (nc) and becomes keratinized (nk), typical reactions of damaged notochord tissue. The bone volume of the vertebral body endplates is increased, albeit the bone structure is unorganized. Scale bar: 100 μ m. (B) Toluidine blue stained sagittal sections of WT and *p3h1*^{-/-}. Top panels: under birefringent light an

One of the advantages of zebrafish models for skeletal diseases is the possibility to evaluate bone mineralization very early during development simply by whole mount alizarin red staining of fixed specimens, without the need to sacrifice pregnant female to obtain mutant embryos and to perform embedding and sectioning. Cranial bone mineralization is decreased in both *crtap*^{-/-} and *p3h1*^{-/-} models compared to WT, thus demonstrating that Crtap and P3h1 are indispensable for proper bone mineralization during development.

The overmodified collagen type I is present in skin and bone tissues of *crtap*^{-/-} and *p3h1*^{-/-} zebrafish. The vertebral collagen fibrils are characterized by significantly larger diameter in *crtap*^{-/-} compared to WT zebrafish recapitulating what was previously reported for patients and murine models. On the contrary, the collagen fibrils in human and mice lacking P3h1 are characterized by irregular size rather than the reduced size present in the *p3h1*^{-/-} fish. Nevertheless, the results indicate a different role for the two proteins beside their function in the ER. Indeed, CRTAP is known to be secreted probably influencing collagen fibrils size [34]. Of note, fibrils size is smaller in both knock out zebrafish in cranial bone at adult age suggesting a site and/or time dependent effect of Crtap and P3h1 absence during bone remodeling. Further investigation on zebrafish in different bones and at different ages will be useful to elucidate this finding.

Interestingly, in mutant zebrafish the D-periodic pattern is also compromised.

In *p3h1*^{-/-} collagen type II fibrils show a peculiar appearance with the presence of patches of smaller fibers interspersed within regular ones. This observation is not surprising since P3h1 was first described as an extracellular proteoglycan in hyaline cartilage [35]. The presence of abnormal collagen type II fibrils in *p3h1*^{-/-} but not in *crtap*^{-/-} zebrafish, suggests a tissue specific role of the two proteins independently from their intracellular function [36,37].

In zebrafish the notochord, the main axial support during early development, [38] is surrounded by a notochord sheath which is composed of a thin inner layer of elastin, a thick lamellar collagen type II containing layer and an outer elastin containing elastica externa. Osteoblasts and collagen type I are localized outside the elastica externa, while chondroblasts reside below at the level of collagen type II

fibers [39,40]. Thus, notochord sheath represents a perfect region to investigate skeletal cells.

Enlargement of intracellular endoplasmic reticulum cisternae in *crtap*^{-/-} and *p3h1*^{-/-} osteoblasts indicate a partial mutant collagen retention, that is a common feature in dominant and recessive OI caused by misfolded collagen type I [41,42]. Also, chondroblasts around the notochord show enlarged ER in both mutants, likely supporting a function of the complex on the intracellular folding of collagen type II. Indeed, the lack of the 3-hydroxylation complex in OI type VII and VIII murine models is associated to reduced $\alpha 1$ (II)3Hyp986 and to growth plate disorganization, likely responsible for the peculiar skeletal phenotype involving also cartilage abnormalities [17,18].

Here we show that the lack of Crtap impairs the stability of P3h1 and vice versa in zebrafish. This observation is consistent with their presence in a complex like that demonstrated in the human ER [15]. Mass spectrometry analysis shows that the highly conserved target sequence at the Pro986 site in the $\alpha 1$ (I) chain is not 3-hydroxylated in zebrafish whether from WT, *crtap*^{-/-} or *p3h1*^{-/-} mutant tissue, confirming the lack of 3-hydroxylation in fibrillar collagens previously observed in zebrafish ([23]; Weis and Eyre, unpublished data)

Despite that, in both models, when the complex is not functioning, the collagen type I is overmodified, as evident by its delayed electrophoretic migration. Considering the limited increase in lysine hydroxylation, due to the already high basal level of Hyl in zebrafish collagen type I, the increase glycosylation is likely the main cause for collagen overmodification. The presence of overmodified collagen supports a major role of the two proteins in collagen folding in determining the collagen I overmodification and the bone phenotype. This observation nicely complement and strengthen the normal collagen post translational modification and the very mild bone phenotype observed in mice lacking P3h1 activity, but conserving the 3-hydroxylation complex integrity [17] and in the new knock in mice in which the Pro986 target site was substituted with an Alanine [43]. Based on the severe electrophoretic shift of the collagen type I α bands observed for tritiated collagen extracted from fish tail following 24 h of labelling compared to the collagen extracted from bone and skin it is tempting to speculate that the incorporation of the abnormal collagen in the extracellular matrix is limited. Indeed MS analysis of bone collagen did not revealed increased glycosylation at least at Lys87,

abnormal collagen fibers organization is detectable in mutant (arrow). Scale bar: 25 μ m. Bottom panels: a thinner notochord sheath (asterisk) is evident in mutant with respect to WT. Scale bar: 10 μ m. (C) Transmission electron microscopy analysis showed increased collagen type I fibers diameter in *crtap*^{-/-} and reduced cross section size in *p3h1*^{-/-} in comparison to WT. $n \geq 200$, scale bar: 100 nm. (D) Transmission electron microscopy analysis revealed collagen type II fibers disorganization in mutants *p3h1*^{-/-} with respect to WT, as observed by fiber clusters interspersed in the extracellular matrix. Scale bar: 200 nm. (E) Transmission electron microscopy analysis demonstrated a disorganized D-period patterning in both mutant zebrafish models with respect to WT. Scale bar: 100 nm. Data information: values are expressed as mean \pm standard deviation and statistical significance, determined by two-tailed unpaired T-test in panel C, is indicated by * $p < 0.05$.

although we cannot exclude effects on other sites as well as on other collagen types, such as type V known to play a relevant role in collagen type I fibril formation [44] and indeed potentially affecting bone extracellular matrix organization. Likely, the overmodified collagen is partially intracellularly retained as already reported in dominant and recessive OI in presence of misfolded collagen type I [41,42]. Indeed, the endoplasmic reticulum cisternae enlargement in *crtap*^{-/-} and *p3h1*^{-/-} osteoblasts support such hypothesis. Also, chondroblasts around the notochord show enlarged ER in both mutants likely supporting a function of the complex on the intracellular folding of collagen type II.

The most common causes of death in individuals with severe OI are linked to respiratory problems. Lung stroma contains collagen fibrils and hence they may also be affected by mutations in genes involved in collagen biosynthesis. *Crtap*^{-/-} mice showed increased airways space in the lungs, leading to a reduction in the thickness of alveolar walls [34]. In zebrafish, similarly to mammalian lungs, the swim bladder derives from an extension of the foregut endoderm and the presence of collagen type I has been described in seabass (*Lates calcarifer*) [45]. Indeed, exploiting the transparency of embryo and larvae, the evaluation of swim bladder reveals a delay in the inflation of the first lobe of the swim bladder at 7 dpf in both zebrafish mutants compared to WT, suggesting that prolyl 3-hydroxylation complex can play an essential role also in non-skeletal tissues in zebrafish, as already demonstrated in rats and chick embryos [46] and described in the OI murine models [34,47].

In conclusion, the *crtap*^{-/-} and *p3h1*^{-/-} zebrafish characterization supports the defective chaperone role of 3-hydroxylation complex as the primary cause of the OI bone phenotype. The two knock out lines represent valuable models for the human OI type VII and VIII forms, respectively, reproducing their main skeletal features. Both models are characterized by partial retention of mutant collagen in the ER, a common feature in various OI forms, and recently indicated as target for possible common chaperone pharmacological therapy [41,42,48]. Thus, *p3h1*^{-/-}, and limited to early developmental stages *crtap*^{-/-} due to increase lethality, will be valid tools for drug screening using chemical chaperones, considering the advantage of using zebrafish models to reduce amount of drug needed and cost and to increase sample number and statistical power.

Materials and methods

Zebrafish husbandry and ethical statement

WT AB zebrafish were obtained by European Zebrafish Research Center (Germany). Zebrafish embryos were kept in petri dishes in zebrafish water

(1.2 mM NaHCO₃, 0.1 g/L instant ocean, 1.4 mM CaSO₄, 0.00002% w/v methylene blue) at 28 °C until 6 days post fertilization (dpf), then housed in ZebTEC semi-closed recirculation housing systems (Techniplast, Buguggiate, Italy) at 28 °C, pH 7.5 and conductivity 500 μS on a 14/10 light/dark cycle. Zebrafish were fed three times a day alternating dry food and brine shrimps. For the experiments, larvae and adult zebrafish were anesthetized using 0.016% w/v tricaine (3-amino benzoic acid ethylester, Sigma Aldrich, Darmstadt, Germany) in zebrafish water and sacrificed by tricaine overdose (0.4% w/v). All the experiments were performed in agreement with EU Directive 2010/63/EU. The experimental protocol was approved by Italian Ministry of Health (Approval Animal Protocol No.1191/2016-PR).

In silico analysis

Synteny maps of the chromosomal regions surrounding cartilage associated protein and prolyl 3-hydroxylase 1 genes in *D. rerio*, *H. sapiens* and *M. musculus* were generated using the human genes as reference by combining PhyloView and AlignView from Genomicus 93.01 (<http://www.genomicus.biologie.ens.fr>) with Ensembl Comparative Genomics data. Conserved domains between zebrafish, human and mouse proteins were identified using UniProt (<https://www.uniprot.org>) and Motif Search (<https://www.genome.jp/tools/motif/>). The percentage of protein identity was estimated using Lalign (https://embnet.vital-it.ch/software/LALIGN_form.html).

Generation of zebrafish *crtap* and *p3h1* knock out using CRISPR/Cas9

A single guide RNA (gRNA) for each gene (*crtap*, ENSDARG00000018010; *p3h1*, ENSDARG00000071212) was designed using the online freely available software CHOPCHOP (<https://chop.chop.rc.fas.harvard.edu>) [49]. For both genes the target sequence was selected at the 5'- end; for *crtap* in exon 1 (5'-ggagagcgtggagtttctggaggG-GAGAGCGTGGAGTTTCTGGAGG-3', 174–196 nt, ENSDART00000010104.6) and for *p3h1* in exon 2 (5'-ggagaccgatttcaaggacctggGGAGACCGATT-CAAGGACCTGG-3', 570–592 nt, ENSDART000000102827.5). The synthesis of target oligonucleotides (Eurofins Genomics, Vimodrone, Italy) and the preparation of gRNAs were carried out as described in [50].

For the Cas9 mRNA *in vitro* transcription, the pT3TS-nCas9n vector (Addgene, # 46757) was linearized by *Xba*I (New England BioLabs, Ipswich, Massachusetts, USA) digestion and purified using the Nucleospin Gel and PCR Clean-up Kit (Macherey-Nagel, Düren, Germany). DNA was transcribed using mMACHINE mMESSAGE T3 Kit (Invitrogen, Carlsbad, California, USA). mRNA

polyadenylation was performed using the Poly(A) Tailing Kit (Ambion, Waltham, Massachusetts, USA) and the Cas9 transcript was purified by RNeasy Mini Kit (Qiagen, Hilden, Germany) [50]. The mRNA quality was checked by electrophoresis on 1% (w/v) formaldehyde agarose gel. The gRNA (12.5 ng/ μ L) and Cas9 mRNA (300 ng/ μ L) were mixed in Danieau solution (58 mM NaCl, 0.7 mM KCl, 0.4 mM MgSO₄, 0.6 mM Ca(NO₃)₂, 5 mM Hepes, pH 7.6) with a tracer dye (0.5 mg/mL, dextran conjugated with tetramethylrhodamine, Molecular Probes, Carlsbad, California, USA) in a final volume of 5 μ L and pre-heated at 60 °C for 10 min. Microinjection was carried out using an InjectMan micromanipulator (Eppendorf, Hamburg, Germany) assembled on a Leica M165 FC stereomicroscope. Injection pressure and time were modulated to calibrate the injected volume, ranging from 2 to 4 nL per embryo. After 24 h the DNA from single embryos was extracted by proteinase K digestion (2.5 mg/mL, Sigma Aldrich, Darmstadt, Germany) in lysis buffer (100 mM Tris HCl, pH 8.5, 5 mM EDTA, 0.2% (w/v) SDS, 200 mM NaCl) overnight (o/n) at 55 °C, followed by isopropanol precipitation and resuspension in 20 mM Tris-HCl, 1 mM EDTA, pH 8.0. To evaluate targeting efficiency T7 Endonuclease Assay was performed. The genomic region surrounding the target sequences was PCR amplified using the following primers: for *crtap*: forward 5'-GTCCCTCGCGCAGTATGAGAA-3' (673 – 692 nt) and reverse 5'-CAGGTACTTGTATGGCTCCCG-3' (1033 – 1053 nt) generating a 381 bp amplicon and for *p3h1*: forward 5'-CTACACTAACATGTACATGTATGC-3' (5356 – 5379 nt) and reverse 5'-ACAGTGTGTATATTCTGCATCCC-3' (5777 – 5799 nt) generating a 444 bp amplicon. Briefly, 10 μ L of each PCR amplicon underwent a denaturing/annealing cycle consisting of 5 min at 94 °C, followed by cooling to 85 °C, at –2 °C per sec and further to 25 °C, at –0.1 °C per sec. The annealed amplicon was then digested with 0.2 U/ μ L T7 endonuclease I (New England BioLabs) at 37 °C for 1 h. The sample was run on 8% (v/v) polyacrylamide gel. T7 only cuts heteroduplex amplicons. The targeting was confirmed by Sanger Sequencing.

T7 endonuclease assay, as described above, was also used to identify F0 mosaic zebrafish using DNA extracted from pools of embryos obtained from the progeny of F0 mosaic zebrafish outcrossed with AB WT zebrafish. The mutations in the heterozygous F1 zebrafish was determined by DNA extraction from tail clip of adult zebrafish followed by Sanger sequencing of the region surrounding the targeting.

Genotyping of the *crtap* and *p3h1* knock out zebrafish

To genotype the *crtap* and *p3h1* knock out zebrafish, the DNA was extracted by tail clip as described

above, PCR amplified with the above reported primers and the amplicon digested by restriction endonucleases. For *crtap* mutant zebrafish carrying the c.199_202delTTTCinsAG mutation the PCR amplicon was digested with *BpmI* (New England BioLabs) which only cuts the WT allele producing two bands of 151 and 230 bp. For *p3h1* mutant zebrafish carrying the c.645delCinsGGAGAA mutation the PCR amplicon was digested with *EcoO109I* (New England BioLabs) which only cuts the WT allele producing two bands of 125 and 319 bp. The digested products were analysed by 8% (v/v) polyacrylamide gel. The embryos generated from pairwise breeding were grown to 3 weeks post fertilization (wpf) and the genotyping data were used to analyze for Mendelian ratios of surviving homozygous knock out zebrafish compared to WT and heterozygous zebrafish. Under the null hypothesis of no viability selection, progeny genotypes should conform to an expected Mendelian ratio of 1:2:1. Deviations from expected number of homozygous knock out were tested with goodness-of-fit Chi-square statistical analysis.

qPCR

RNA was extracted from skin of adult WT ($n=2$), *crtap* ($n=1$) and *p3h1* ($n=3$) knock out mutants using Qiazol (Qiagen) following manufacturer's instructions. RNA quantity was determined by NanoDrop spectrophotometer and RNA quality by agarose gel electrophoresis. cDNA was synthesized from 2 μ g of RNA using the High Capacity cDNA Transcription kit (Applied Biosystems, Waltham, Massachusetts, USA) according to manufacturer's protocol in a final volume of 20 μ L. qPCR for *crtap*, *p3h1* and β -actin was performed in 25 μ L reaction mixtures with 12.5 μ L SYBR Green Master mix (Applied Biosystems) using the QuantStudio 3 thermocycler and the QuantStudio Design & analysis software (Applied Biosystems). The following primers were used: for *crtap* (ENSDART0000010104.6) forward, 5'-GAGCTGGCACTGAGAGACTT-3' (676-695 nt) and reverse, 5'-TAATGATCTGCGATGGACGGG-3' (768-788 nt), for *p3h1* (ENSDART00000102827.5) forward, 5'-ACATCACGAAAGAGAGGTGG-3' (1055-1075 nt) and reverse, 5'-GTGTCTGGATCAACAAACGCT-3' (1146-1166 nt) and for β -actin (ENSDART00000054987.7) forward, 5'-GAAGGAGATCACCTCTCTTGCTC-3' (942-964 nt) and reverse, 5'-GTTCTGTTTAGAAGCACTTCTGTG-3' (1111-1135 nt). The annealing temperature was 60 °C for *crtap* and 66 °C for *p3h1*. Samples were run in triplicate and $\Delta\Delta$ Ct was used for quantitation.

Expression and purification of recombinant zebrafish Crtap and P3h1 proteins and generation of specific antibodies

cDNA constructs were generated by RT-PCR on total zebrafish RNA. Suitable primers introduced 5'

terminal NheI or XbaI and 3' terminal NotI restriction sites. Crtap primer sequences were 5'-caa tgc tag cCA GTA TGA GAA ATA TAA CTT TCG C-3' (forward) and 5'-caa tgc gg ccg ctt aAT CCA GAT ATT CAT CAA GAA AC-3' (reverse), P3h1 primer sequences were 5'-caa ttc tag aGA CCC TCA AAT CAA TGC-3' (forward) and 5'-caa tgc ggc cgc tta GTG TTT TTC AGC TTT GGA G-3' (reverse). The amplified PCR products were inserted into a modified pCEP-Pu vector containing an N-terminal BM-40 signal peptide and N-terminal One-STrEP tag [51]. The recombinant plasmids were introduced into human embryonic kidney 293-EBNA cells (Invitrogen, Carlsbad, California, USA) using FuGENE 6 transfection reagents (Roche, Darmstadt, Germany). The cells were selected with puromycin (1 μ g/mL). After filtration and centrifugation (30 min, 10,000 \times g), the cell culture supernatants were applied to a StrepTactin column (IBA Lifesciences, Göttingen, Germany) and eluted following the supplier's protocol. The purified recombinant proteins were used to immunize rabbits and guinea pigs.

Western blotting

Proteins were extracted from adult WT, *crtap*^{-/-} and *p3h1*^{-/-} skin (n=3 per genotype). Following zebrafish sacrifice, skin was dissected and collected in 200 μ L of Laemmli buffer (SDS 10% w/v, glycerol 20% v/v, 0.2 M TrisHCl, pH 6.8) pre-heated at 70 °C. Samples were minced using scissors, heated for 5 min at 95°, centrifuged at maximum speed for 15 min at RT and supernatant transferred in a new tube. Proteins were quantified by RC-DC Protein Assay (Bio-Rad, Segrate, Italy). For each sample 30 μ g were separated on 10% or 6% SDS-PAGE for Crtap and P3h1, respectively. The proteins were electrotransferred to a PVDF membrane (GE Healthcare, Chicago, Illinois, USA) at 100 Volt for 2 h on ice in 19 mM Tris-HCl, 192 mM glycine and 20% (v/v) methanol. The uniform transfer was evaluated by Swift Membrane Stain kit (G-Biosciences, St. Louis, Missouri, USA). The membranes were blocked with 5% (w/v) milk in 20 mM Tris-HCl, 500 mM NaCl, pH 7.5 (TBS), 0.05% (v/v) Tween-20 (Sigma-Aldrich) (TBS-T) at RT for 1 h. After washing with TBS-T the membranes were incubated with 1:500 primary antibody against the specific proteins Crtap (anti-Crtap, provided by PRIMM, Milan, Italy and anti-Crtap generated in house) or P3h1 (anti-P3h1, provided by PRIMM and anti-P3h1 generated in house), in 2.5% milk in TBS-T o/n at 4 °C. The appropriate secondary antibody, anti-rabbit IgG-HRP (Cell Signaling, Danvers, Massachusetts, USA) was added at dilution of 1:10,000 in 2% milk in TBS-T for 1 h at RT. The signal was detected by ECL western blotting detection reagents (GE Healthcare) or Westar Supernova (Cyanagen, Bologna, Italy) and images were acquired with ImageQuant

LAS 4000 (GE Healthcare), using the ImageQuant LAS 4000 1.2 software.

Morphometric analysis

Images of anesthetized post hatching stages (1, 2, 3 wpf and 1, 2, 6 mpf) larvae and adult zebrafish were acquired with M165FC stereomicroscope (Leica, Wetzlar, Germany) connected to DFC425C digital camera (Leica, Wetzlar, Germany). Measurements were performed as described [52] using the LAS v4.5 software (Leica).

Using lateral images the following parameters were measured: Standard Length (SL), defined as the distance from the snout to the caudal peduncle or, in pre-flexion larvae that do not have a caudal peduncle, to the posterior tip of the notochord; Height at Anterior of Anal fin (HAA), defined as the distance from ventral to dorsal, measured immediately anteriorly to the anal fin and perpendicularly to the axis defined by SL; Snout–Operculum Length (SOL), defined as the distance from snout to the most posterior point of operculum; Height at Eye (HE), defined as the distance from ventral to dorsal, measured immediately posteriorly to the eye and perpendicularly to the axis defined by SL (*crtap* matings: WT n \geq 13, *crtap*^{+/-} n \geq 27, *crtap*^{-/-} n \geq 10; *p3h1* matings: WT n \geq 19, *p3h1*^{+/-} n \geq 34, *p3h1*^{-/-} n \geq 14). Vertebral length, height and area were evaluated in WT (n = 9) and *p3h1*^{-/-} (n = 7) at 1 mpf. For each vertebra, the mean of the length measured dorsally and ventrally and the mean of the height measured anteriorly and posteriorly to the vertebral centrum were evaluated using the LAS v4.5 software (Leica). The first 10 vertebrae articulated with the ribs were considered. In addition, the level of insufflation of the swim bladder was evaluated in larvae by counting the numbers of lobes on lateral transmission images at 1 wpf (*crtap* matings: WT n = 25, *crtap*^{-/-} n = 14; *p3h1* matings: WT n = 37, *p3h1*^{-/-} n = 31), 2 wpf (*crtap* matings: WT n = 28, *crtap*^{-/-} n = 20; *p3h1* matings: WT n = 31, *p3h1*^{-/-} n = 25) and 3 wpf (*crtap* matings: WT n = 25, *crtap*^{-/-} n = 10; *p3h1* matings: WT n = 22, *p3h1*^{-/-} n = 20).

Skeletal staining

Following sacrifice 1 wpf (*crtap* matings: WT n = 18, *crtap*^{+/-} n = 43, *crtap*^{-/-} n = 9; *p3h1* matings: WT n = 22, *p3h1*^{+/-} n = 47, *p3h1*^{-/-} n = 21) and 2 wpf (*crtap* matings: WT n = 28, *crtap*^{+/-} n = 54, *crtap*^{-/-} n = 20; *p3h1* matings: WT n = 22, *p3h1*^{+/-} n = 63, *p3h1*^{-/-} n = 16) zebrafish were fixed overnight in 4% (w/v) paraformaldehyde (PFA, Merck KGaA, Darmstadt, Germany) at 4 °C and stained in 0.01% (w/v) Alizarin Red S (Sigma Aldrich) as described in [48]. Images were acquired on ventral, dorsal and lateral orientation using M165 FC stereomicroscope (Leica) connected to

DFC425C digital camera (Leica). The mineralization of the notochord (NC), of the hyomandibular bone (HM) and of the ceratohyal bone (CHB) in 1 and 2 wpf larvae was evaluated independently by three operators blinded to the zebrafish genotype. An interobserver agreement was reached. Mineralization levels were classified as beginning, incomplete or complete based on the extent of the alizarin red staining [48].

X-ray

X-ray of 2 mpf (*crtap* matings: WT $n=5$, *crtap*^{-/-} $n=5$; *p3h1* matings: WT $n=28$, *p3h1*^{-/-} $n=15$), 4 mpf (*crtap* matings: WT $n=2$, *crtap*^{-/-} $n=3$) and 6–12 mpf (*p3h1* matings: WT $n=33$, *p3h1*^{-/-} $n=8$) zebrafish were acquired by Faxitron Mx-20 (Faxitron, Tucson, Arizona, USA), using 25 kV for 10 s. The Kodak DirectView Elite CR System and k-Pacs software (Kodak, Rochester, New York, USA) were used for images digitalization.

μCT

WT, *crtap*^{-/-} and *p3h1*^{-/-} littermate zebrafish grown in the same tank at identical zebrafish density to minimize variability were analyzed by μCT. For qualitative analysis 5 WT, 3 *crtap*^{-/-} and 5 *p3h1*^{-/-} at 10 mpf were selected, whereas for quantitative evaluation 5 WT and 5 *p3h1*^{-/-} at 8 mpf were analyzed. Zebrafish were sacrificed, fixed overnight at 4 °C in 4% (w/v) PFA. Zebrafish were kept hydrated in parafilm and placed in a sample holder during μCT acquisitions (Skyscan 1272, Bruker, Kontich, Belgium). Whole body scans were acquired at 55 kV and 166 μA with a 0.25 mm aluminum filter and at an isotropic voxel size of 5 μm. For high-resolution scans and quantitative analysis of the first precaudal vertebrae, zebrafish were scanned at 50 kV and 176 μA with a 0.25 mm aluminum filter at an isotropic voxel size of 2.5 μm. For all samples, ring artifact and beam hardening correction was kept constant and no smoothing was applied during reconstruction (NRecon, Bruker). After applying a constant global threshold to all samples, the morphological properties: bone volume (BV, mm³), vertebral thickness (V, Th, mm) and polar moment of inertia (MMI_p, surrogate measure for resistance against torsion, mm⁴), estimated vertebral diameter (ECDa, area-equivalent circle diameter, mm) and cross-sectional bone area (B.Ar, mm²) were determined in the high-resolution scans according to previously established protocols [53,54].

Collagen extraction from tissues

Skin and bone were dissected from adult WT ($n=5$), *crtap*^{-/-} ($n=1$) and *p3h1*^{-/-} ($n=5$) zebrafish following sacrifice. The tissues were defatted for 6 h

in 0.1 N NaOH at 4 °C. The bone was decalcified for 48 h in 0.5 M EDTA pH 7.4 at 4 °C. The pepsin-soluble collagen fraction (PSC) was obtained by digesting the tissues with 0.1 mg/mL pepsin in 0.5 M acetic acid at 4 °C for 48 h. The PSC was precipitated by 0.9 M NaCl in 0.5 M acetic acid o/n at 4 °C and quantified using Sircol Soluble Collagen assay (Biocolor, Carrickfergus, UK). Equal amount of collagen from each sample (3 μg) was loaded on 6% SDS-Urea-PAGE in non-reducing conditions. Gels were stained overnight with 0.08 M picric acid, 0.04% Coomassie Brilliant Blue R250 (Sigma Aldrich, Darmstadt, Germany), destained in water and acquired with Versadoc3000 (Bio-Rad) [48].

Steady state collagen analysis

Caudal fins from anesthetized adult WT ($n=3$), *crtap*^{-/-} ($n=3$) and *p3h1*^{-/-} ($n=3$) zebrafish were cut and plated into 24 wells plate in Dulbecco's Modified Eagle Medium (D-MEM, Lonza Biosciences, Basel, Switzerland) containing 4 mM glutamine (Euroclone, Pero, Italy), 100 μg/ml penicillin, 100 μg/ml streptomycin (Euroclone), 100 μg/mL (+)-sodium L-ascorbate (Sigma Aldrich) and 1% fetal bovine serum (FBS, Euroclone). For collagen labelling 100 μCi/mL of L-[2,3,4,5-³H]-proline (PerkinElmer, Milan, Italy) was added per well and samples were incubated for 24 h at 28 °C in humidified incubator in presence of 5% CO₂. The tails were then digested with 0.2 mg/mL pepsin in 0.5 M acetic acid o/n at 4 °C in presence of 20 μg of bovine collagen (Sigma Aldrich) as carrier. Collagen was precipitated with 2 M NaCl, 0.5 M acetic acid and resuspended in Laemmli sample buffer [55]. The radioactivity (counts for minute, CPM) of the collagen samples was quantified using a liquid scintillation analyser (TRI-CARB 2300 TR). Equal amounts of ³H-labeled collagen from each sample was loaded on 6% SDS-Urea-PAGE gel in non-reducing conditions. The gels were incubated for 1 h with enhancer solution (EN³HANCE, PerkinElmer, 6NE9701, Milan; Italy), washed in deionized water, and dried. Dried gels were exposed to hyperfilm (Amersham Chicago, Illinois, USA,) at -80 °C [56]. The radiography films were digitalized by VersaDoc 3000 (Bio-Rad, Segrate, Italy).

Amino acid analysis

Collagen type I extracted from skin and bone of WT, *crtap*^{-/-} and *p3h1*^{-/-} (30 μg) as described above was hydrolysed in 6 M HCl at 110 °C under nitrogen and hydrolysates were derivatized with orthophthalaldehyde (OPA) and 9-fluorenyl-methyl-chloroformate (FMOC). OPA and FMOC derivatives were analyzed by Jasco X-LC Amino Acid Analyzer with a fluorescence detector (excitation/emission at 340/446 nm for OPA-amino acids an excitation/emission at 268/

308 nm for FMOc-amino acids). The results are means of three independent analyses.

Mass spectrometry analysis

Vertebral columns from adult WT ($n=3$) and $p3h1^{-/-}$ ($n=3$) zebrafish were dissected, cleaned from surrounding connective tissue, demineralized in 0.1 M HCl at 4 °C overnight, washed and solubilized by heat denaturation in Laemmli buffer [55]. Samples were separated on 6% SDS-PAGE, collagen type I α chains were cut from gel and in-gel trypsin digested. Electrospray mass spectrometry (MS) was performed on tryptic peptides using an LTQ XL ion-trap mass spectrometer (Thermo Scientific, Waltham, Massachusetts, USA) equipped with in-line liquid chromatography using a C45 mm capillary column (300 mm 150 μ m; Higgins Analytical RS-15M3-W045) eluted at 4 mL/min. The liquid chromatography (LC) mobile phase consisted of buffer A (0.1% (v/v) formic acid in MilliQ water) and buffer B (0.1% (v/v) formic acid in 3:1 acetonitrile: n-propanol (v/v)). The LC sample stream was introduced into the mass spectrometer by electrospray ionization (ESI) with a spray voltage of 4 kV. Proteome Discoverer search software (Thermo Scientific) was used for peptide identification using the NCBI protein database. Proline and lysine modifications were examined manually by scrolling or averaging the full scan over several minutes so that all of the post translational variations of a given peptide appeared together in the full scan.

Histological analysis

For histological analysis dissected skeletal tissues from 1–3 mpf WT and $p3h1^{-/-}$ ($n=2$ for genotype), and $crtap^{-/-}$ ($n=1$), and adult WT ($n=4$), $crtap^{-/-}$ ($n=1$) and $p3h1^{-/-}$ ($n=2$) were fixed for 2 h at RT in 1.5% (v/v) PFA (Sigma Aldrich), 1.5% (v/v) glutaraldehyde (Sigma Aldrich), 0.1 M sodium cacodylate buffer (pH 7.4) and 0.001% (w/v) CaCl_2 . The samples were decalcified in 0.1 M EDTA for 5 days at 4 °C. Samples were rinsed in 0.1 M sodium cacodylate buffer containing 10% sucrose and post fixed for 36 h using 1% (w/v) OsO_4 in 0.1 M sodium cacodylate buffer at pH 7.4 containing 0.825% (w/v) $\text{K}_3\text{Fe}(\text{CN})_6$. After rinsing with demineralized water, specimens were dehydrated in presence of CuSO_4 bars. Subsequently, zebrafish were infiltrated with low-viscosity epoxid embedding medium [57].

Parasagittal 1 μ m semi-thin sections of the sites of interest were mounted on superfrost slides stained for 1 min with toluidine blue (0.2% toluidine blue, 2% Na_2CO_3), rinsed with demineralized water, air-dried and mounted with DPX (Fluka, Buchs, Switzerland). A Leitz DL22 microscope (Leica) equipped with a PL APO 63/1.40 Oil lens and a 5MP CCD camera was used for analysis and documentation.

Ultra thin (50–90 nm) sections were cut using a Reichert UltracutS ultramicrotome (Leica) with a diamond knife (Diatome Ltd., Nidau, Switzerland) and mounted on formvar-coated single slot copper grids (Agar Scientific, Brussels, Belgium). The sections were stained with uranyl acetate and lead citrate (EM stain, Leica) and viewed with a Jeol JEM-1010 (Jeol Ltd, Brussels, Belgium) TEM operating at 60 kV. Images were digitalized using the DITABIS drum scan system (Ditabis AG, Pforzheim, Germany) [58].

Transmission electron microscopy (TEM) images were used to measure the diameter of transversal collagen type I fibers and to evaluate the D-period banding and the rough endoplasmic reticulum cisternae size. Diameters were measured by tracing a line using LAS v4.5 software (Leica) on fully transversal collagen type I fibers. The bending periods were not quantified, but qualitatively evaluated.

Statistical analysis

All quantitative variables were expressed as mean \pm standard deviation (SD), while categories using percentage. Two parallel experimental designs were conducted: in the first, $crtap^{-/-}$ mutants were compared to WT, and in the second, $p3h1^{-/-}$ mutants were compared to a different group of WT. Based on this, unpaired parametric *t*-test or the analogous non parametric test (Mann-Whitney or MW) was applied to assess differences in quantitative parameters between each mutants and their respective WT group. One way Anova was applied for the analysis of standard lengths values of WT, heterozygous and homozygous fish. Difference in bones mineralization was evaluated by means of Chi-squared test or the Fisher's exact test. A p-value level less than 0.05 was considered significant. Statistical analyses were performed using Excel, SigmaPlot or STATA®.

Author's contributions

Conceptualization: A.F.; Methodology: F.T., S.C., L.L., R.B., R.G., C.G., K.B., B.B., D.L., I.F.; Formal analysis: A.F., D.L., F.T., P.E.W., B.B., R.W., D.E.; Resources: A.F., R.W., P.E.W., B.B., D.E.; Data curation: F.T., A.F., P.E.W., R.W., B.B., C.G.; Writing - original draft: F.T., A.F.; Writing - review & editing: all the coauthors; Supervision: A.F.; Project administration: A.F.; Funding acquisition: A.F., R.W.

Acknowledgments

We thank Dr. Patrizia Arcidiaco, Centro Grandi Strumenti, University of Pavia, Italy, for amino acid analysis; the animal facility "Centro di servizio per la

gestione unificata delle attività di stabulazione e di radiobiologia” of the University of Pavia, Pavia, Italy to host the animals; the OPBA of the University of Pavia for supporting in animal protocol drawing up and Ilaria Ceppi, Bs for initial characterization of the mutants.

Declaration of Competing Interest

The authors report no conflict of interest.

Funding

This work was supported by Fondazione Cariplo (Grant no. 2013-0612), Telethon (grant no. GGP13098), the European Community, FP7, ‘Sybil’ project (grant no. 602300) and Italian Ministry of Education, University and Research (MIUR) [Dipartimenti di Eccellenza (2018–2022)] to AF and the German Research Council (FOR 2722-B1) to R.W.

Supplementary materials

Supplementary material associated with this article can be found in the online version at doi:10.1016/j.matbio.2020.03.004.

Received 26 November 2019;

Received in revised form 5 March 2020;

Accepted 5 March 2020

Available online 12 March 2020

Keywords:

Recessive osteogenesis imperfecta;
Cartilage associated protein;
Prolyl 3-hydroxylase;
Prolyl 3-hydroxylation complex;
Zebrafish skeletal disease models;
Collagen type I

¹These authors contribute equally to the manuscript

References

- [1] J.D. Ogle, R.B. Arlinghaus, M.A. Lgan, 3-Hydroxyproline, a new amino acid of collagen, *J. Biol. Chem.* 237 (1962) 3667–3673.
- [2] N.A. Kefalides, Structure and biosynthesis of basement membranes, *Int. Rev. Connect. Tissue Res.* 6 (1973) 63–104.
- [3] R.K. Rhodes, E.J. Miller, Physicochemical characterization and molecular organization of the collagen A and B chains, *Biochemistry* 17 (17) (1978) 3442–3448.
- [4] M.A. Weis, et al., Location of 3-hydroxyproline residues in collagen types I, II, III, and V/XI implies a role in fibril supra-molecular assembly, *J. Biol. Chem.* 285 (4) (2010) 2580–2590.
- [5] D.M. Hudson, D.R. Eyre, Collagen prolyl 3-hydroxylation: a major role for a minor post-translational modification? *Connect. Tissue Res.* 54 (4–5) (2013) 245–251.
- [6] P. Tiainen, et al., Characterization of recombinant human prolyl 3-hydroxylase isoenzyme 2, an enzyme modifying the basement membrane collagen IV, *J. Biol. Chem.* 283 (28) (2008) 19432–19439.
- [7] J.A. Vranka, L.Y. Sakai, H.P. Bachinger, Prolyl 3-hydroxylase 1, enzyme characterization and identification of a novel family of enzymes, *J. Biol. Chem.* 279 (22) (2004) 23615–23621.
- [8] H. Ehrlich, et al., Mineralization of the metre-long biosilica structures of glass sponges is templated on hydroxylated collagen, *Nat. Chem.* 2 (12) (2010) 1084–1088.
- [9] R.A. Berg, D.J. Prockop, The thermal transition of a non-hydroxylated form of collagen. Evidence for a role for hydroxyproline in stabilizing the triple-helix of collagen, *Biochem. Biophys. Res. Commun.* 52 (1) (1973) 115–120.
- [10] C.L. Jenkins, et al., Effect of 3-hydroxyproline residues on collagen stability, *J. Am. Chem. Soc.* 125 (21) (2003) 6422–6427.
- [11] K. Mizuno, et al., Effect of the -Gly-3(S)-hydroxyprolyl-4(R)-hydroxyprolyl- tripeptide unit on the stability of collagen model peptides, *FEBS J.* 275 (23) (2008) 5830–5840.
- [12] R. Morello, et al., CRTAP is required for prolyl 3- hydroxylation and mutations cause recessive osteogenesis imperfecta, *Cell* 127 (2) (2006) 291–304.
- [13] A.M. Barnes, et al., Deficiency of cartilage-associated protein in recessive lethal osteogenesis imperfecta, *N. Engl. J. Med.* 355 (26) (2006) 2757–2764.
- [14] Y. Ishikawa, et al., Biochemical characterization of the prolyl 3-hydroxylase 1.cartilage-associated protein.cyclophilin B complex, *J. Biol. Chem.* 284 (26) (2009) 17641–17647.
- [15] W. Chang, et al., Prolyl 3-hydroxylase 1 and CRTAP are mutually stabilizing in the endoplasmic reticulum collagen prolyl 3-hydroxylation complex, *Hum. Mol. Genet.* 19 (2) (2009) 223–234.
- [16] R. Morello, Osteogenesis imperfecta and therapeutics, *Matrix Biol.* 71-72 (2018) 294–312.
- [17] E.P. Homan, et al., Differential effects of collagen prolyl 3-hydroxylation on skeletal tissues, *PLoS Genet.* 10 (1) (2014) e1004121.
- [18] J.A. Vranka, et al., Prolyl 3-hydroxylase 1 null mice display abnormalities in fibrillar collagen-rich tissues such as tendons, skin, and bones, *J. Biol. Chem.* 285 (22) (2010) 17253–17262.
- [19] W.A. Cabral, et al., Prolyl 3-hydroxylase 1 deficiency causes a recessive metabolic bone disorder resembling lethal/severe osteogenesis imperfecta, *Nat. Genet.* 39 (3) (2007) 359–365.
- [20] F.S. Van Dijk, et al., CRTAP mutations in lethal and severe osteogenesis imperfecta: the importance of combining biochemical and molecular genetic analysis, *Eur. J. Hum. Genet.* 17 (12) (2009) 1560–1569.
- [21] F.S. Van Dijk, et al., PPIB mutations cause severe osteogenesis imperfecta, *Am. J. Hum. Genet.* 85 (4) (2009) 521–527.
- [22] R.M. Gryder, M. Lamon, E. Adams, Sequence position of 3-hydroxyproline in basement membrane collagen. Isolation of glycyl-3-hydroxyprolyl-4-hydroxyproline from swine kidney, *J. Biol. Chem.* 250 (7) (1975) 2470–2474.
- [23] D.M. Hudson, R. Werther, M. Weis, J.J. Wu, D.R. Eyre, Evolutionary origins of C-terminal (GPP)n 3-hydroxyproline formation in vertebrate tendon collagen, *PLoS One* 9 (4) (2014) e93467.
- [24] B. Thisse, et al., Expression of the zebrafish genome during embryogenesis, ZFIN on-line publication (2001).
- [25] B. Thisse, C. Thisse, Fast release clones: a high throughput expression analysis, ZFIN on-line publication (2004).

- [26] C.C. Cabbage, P.M. Mabee, Development of the cranium and paired fins in the zebrafish *Danio rerio* (Ostariophysi, Cyprinidae), *J. Morphol.* 229 (2) (1996) 121–160.
- [27] J.C. Marini, et al., Components of the collagen prolyl 3-hydroxylation complex are crucial for normal bone development, *Cell Cycle* 6 (14) (2007) 1675–1681.
- [28] S. Longo, M. Riccio, A.R. McCune, Homology of lungs and gas bladders: insights from arterial vasculature, *J. Morphol.* 274 (6) (2013) 687–703.
- [29] C.L. Winata, et al., Development of zebrafish swimbladder: the requirement of Hedgehog signaling in specification and organization of the three tissue layers, *Dev. Biol.* 331 (2) (2009) 222–236.
- [30] Y. Taga, et al., Site-specific quantitative analysis of overglycosylation of collagen in osteogenesis imperfecta using hydrazide chemistry and Silac, *J. Proteome Res.* 12 (5) (2013) 2225–2232.
- [31] Z. Zeng, et al., Notochord injury assays that stimulate transcriptional responses in Zebrafish larvae, *Bio Protoc.* 8 (23) (2018) e3100.
- [32] R. Besio, A. Forlino, Treatment options for osteogenesis imperfecta, *Expert Opin. Orphan Drugs* 3 (2) (2015) 165–181.
- [33] K.F. Gorman, F. Breden, Teleosts as models for human vertebral stability and deformity, *Comp. Biochem. Physiol. C Toxicol. Pharmacol.* 145 (1) (2007) 28–38.
- [34] D. Baldrige, et al., Generalized connective tissue disease in *Crtap*^{-/-} mouse, *PLoS One* 5 (5) (2010) e10560.
- [35] D.J. Wassenhove-McCarthy, K.J. McCarthy, Molecular characterization of a novel basement membrane-associated proteoglycan, *Leprecan*, *J. Biol. Chem.* 274 (35) (1999) 25004–25017.
- [36] R.V. Iozzo, M.A. Gubbiotti, Extracellular matrix: the driving force of mammalian diseases, *Matrix Biol.* 71–72 (2018) 1–9.
- [37] Y. Krishnan, A.J. Grodzinsky, Cartilage diseases, *Matrix Biol.* 71–72 (2018) 51–69.
- [38] A. Bensimon-Brito, et al., Distinct patterns of notochord mineralization in zebrafish coincide with the localization of Osteocalcin isoform 1 during early vertebral centra formation, *BMC Dev. Biol.* 12 (2012) 28.
- [39] S. Grotmol, et al., Stepwise enforcement of the notochord and its intersection with the myoseptum: an evolutionary path leading to development of the vertebra? *J. Anat.* 209 (3) (2006) 339–357.
- [40] P.E. Witten, A. Huysseune, A comparative view on mechanisms and functions of skeletal remodelling in teleost fish, with special emphasis on osteoclasts and their function, *Biol. Rev. Camb. Philos. Soc.* 84 (2) (2009) 315–346.
- [41] R. Besio, et al., Cellular stress due to impairment of collagen prolyl hydroxylation complex is rescued by the chaperone 4-phenylbutyrate, *Dis Model Mech.* 12 (6) (2019) dmm038521.
- [42] R. Besio, et al., 4-PBA ameliorates cellular homeostasis in fibroblasts from osteogenesis imperfecta patients by enhancing autophagy and stimulating protein secretion, *Biochim. Biophys. Acta Mol. Basis Dis.* 1864 (5 Pt A) (2018) 1642–1652.
- [43] W.A. Cabral, et al., Substitution of murine type I collagen A1 3-hydroxylation site alters matrix structure but does not recapitulate osteogenesis imperfecta bone dysplasia, *Matrix Biol.* (2020), doi: 10.1016/j.matbio.2020.02.003.
- [44] D.E. Birk, Type v collagen: heterotypic type I/IV collagen interactions in the regulation of fibril assembly, *Micron* 32 (3) (2001) 223–237.
- [45] S. Sinthusamran, S. Benjakul, H. Kishimura, Comparative study on molecular characteristics of acid soluble collagens from skin and swim bladder of seabass (*Lates calcarifer*), *Food Chem.* 138 (4) (2013) 2435–2441.
- [46] K. Tryggvason, et al., Partial purification and characterization of chick-embryo prolyl 3-hydroxylase, *Biochem. J.* 183 (2) (1979) 303–307.
- [47] E. Pokidysheva, et al., Prolyl 3-hydroxylase-1 null mice exhibit hearing impairment and abnormal morphology of the middle ear bone joints, *Matrix Biol.* 32 (1) (2013) 39–44.
- [48] R. Gioia, et al., The chaperone activity of 4PBA ameliorates the skeletal phenotype of Chihuahua, a zebrafish model for dominant osteogenesis imperfecta, *Hum. Mol. Genet.* 26 (15) (2017) 2897–2911.
- [49] T.G. Montague, et al., CHOPCHOP: a CRISPR/Cas9 and Talen web tool for genome editing, *Nucl. Acids. Res.* 42 (2014) W401–W407 (Web Server issue).
- [50] L.E. Jao, S.R. Wente, W. Chen, Efficient multiplex biallelic zebrafish genome editing using a Crispr nuclease system, *Proc. Natl. Acad. Sci. U. S. A.* 110 (34) (2013) 13904–13909.
- [51] B. Maertens, et al., Cleavage and oligomerization of gliomedin, a transmembrane collagen required for node of Ranvier formation, *J. Biol. Chem.* 282 (14) (2007) 10647–10659.
- [52] D.M. Parichy, et al., Normal table of postembryonic zebrafish development: staging by externally visible anatomy of the living fish, *Dev. Dyn.* 238 (12) (2009) 2975–3015.
- [53] M.L. Bouxsein, et al., Guidelines for assessment of bone microstructure in rodents using micro-computed tomography, *J. Bone Miner. Res.* 25 (7) (2010) 1468–1486.
- [54] I.A.K. Fiedler, et al., Severely impaired bone material quality in chihuahua zebrafish resembles classical dominant human osteogenesis imperfecta, *J. Bone Miner. Res.* 33 (8) (2018) 1489–1499.
- [55] U.K. Laemmli, Cleavage of structural proteins during the assembly of the head of bacteriophage T4, *Nature* 227 (5259) (1970) 680–685.
- [56] A. Forlino, F. Tonelli, R. Besio, Steady-state and pulse-chase analyses of fibrillar collagen, *Methods Mol. Biol.* (1952) (2019) 45–53.
- [57] A.R. Spurr, A low-viscosity epoxy resin embedding medium for electron microscopy, *J. Ultrastruct. Res.* 26 (1) (1969) 31–43.
- [58] J. Dewit, P.E. Witten, A. Huysseune, The mechanism of cartilage subdivision in the reorganization of the zebrafish pectoral fin endoskeleton, *J. Exp. Zool. B Mol. Dev. Evol.* 316 (8) (2011) 584–597.

Chapter IV
New pharmacological treatment for OI: an in vitro
approach

OI treatment

Nowadays, no definitive pharmacological treatment for OI exists. Nevertheless, several molecules are today tested in clinical trials for OI.

Anti-resorptive therapies

The main drug therapy for OI is based on bisphosphonates prescription. Bisphosphonates interact with hydroxyapatite crystals in bone and accumulate at active bone remodelling sites. They represent a bone anti-reabsorption treatment, based on osteoclasts activity inhibition, thus leading to a delay in bone resorption and improvement of the bone matrix volume (Drake, Clarke, and Khosla 2008; Soares et al. 2016). Patients treated with bisphosphonates show increased bone mineral density, improved mobility, reduced pain and a general improvement in the quality of life (Biggin and Munns 2017). Since bisphosphonates suppress the bone turnover and they can persist in the skeleton for years, a long-term treatment could lead to consequences on skeletal remodelling, such as delayed healing of osteotomies and osteonecrosis of the jaw and atypical femoral fracture. Furthermore, their effect on reducing fracture rate is still controversial (Saita, Ishijima, and Kaneko 2015).

Denosumab is a human monoclonal antibody against the receptor activator of nuclear factor Kappa-B ligand (RANKL). RANKL, mainly secreted by osteoblasts and osteocytes, favours mature osteoclast differentiation from hematopoietic precursors by binding to RANK receptor on their surface and activating the NF- κ B signal transduction pathway (Bargman et al. 2010). Denosumab inhibits RANK-RANKL interaction, blocking osteoclastogenesis and consequently bone resorption (Kostenuik et al. 2009). OI murine models treated with RANKL inhibitor show an improvement in bone biomechanical parameters, such as stiffness and cortical thickness, even if no reduction in bone fractures was observed (Bargman et al. 2010). The first clinical trial for Denosumab, performed on children with mutation in *SERPINF1*, showed improved bone mineral density at the level of lumbar spine, without any adverse effects (Hoyer-Kuhn et al. 2016).

In a phase III clinical trial, where postmenopausal women with osteoporosis have been treated for 10 years, an increased bone mineral density (BMD) with a reduced fracture

incidence was reported with minimal side effects (Bone et al. 2017). Thus, positive skeletal benefit/risk profile supports the use of Denosumab for a long-term treatment in patients at high risk for fracture (Ferrari et al. 2020).

Unfortunately, in some osteoporotic patients treated with denosumab an atypical femur fractures and osteonecrosis of the jaw were found. Moreover, the discontinuation of denosumab therapy is followed by rapidly rising bone turnover markers, decreasing bone density, and vertebral fracture risk that returns to baseline, with a possible increase in the risk of multiple vertebral fractures. Furthermore, the treatment with a bisphosphonate after stopping Denosumab is necessary to stabilize BMD or mitigate bone loss (Lewiecki 2018).

Anabolic therapies

Bone anabolic treatment represent an alternative approach for OI therapy. Teriparatide (TPD) is FDA approved bone anabolic therapy for the treatment of osteoporosis. It is a recombinant form of parathyroid hormone (hPTH), which increases bone remodelling, bone formation and bone density, improves bone microstructure and reduces fracture risk (Neer et al. 2001). The administration of Teriparatide leads to an increase in bone formation, by reducing osteoblast apoptosis in cancellous bone (Jilka et al. 1999) and promoting the differentiation of pre-osteoblasts in the periosteum (Jilka et al. 2009).

Since Teriparatide has not yet been approved for use in children, only few clinical trials on OI adult patients were performed. In addition, anabolic response of osteoblasts (Gatti et al. 2013), significant increase in bone density and in bone strength were demonstrated only in patients with mildest form of OI (Orwoll et al. 2014).

A new promising anabolic treatment is the anti-sclerostin antibody, Evenity. Sclerostin is a small protein expressed in osteocytes after mechanical stress applied to the skeleton (Lewiecki 2014) and plays an important role in the regulation of bone remodelling, being involved in the WNT pathway. Evenity binds to sclerostin, limiting the inhibition of the Wnt/ β -catenin signalling (Li et al. 2005) and thus, favouring osteoblast differentiation, proliferation and activity. Evenity is FDA and EMA approved to treat osteoporosis in postmenopausal women at high risk of bone fractures, although with a warning label for possible cardiovascular complication. These patients show a significant increase in BMD

and a reduction in fracture risk (Recker et al. 2015; Cosman et al. 2016). Evenity has been tested in the OI murine models *Brtl/+* and *Crtap^{-/-}*, favouring the amelioration of bone mass and bone architecture and consequently bone biomechanical parameters (Sinder et al. 2014; Sinder et al. 2015), (Roschger et al. 2014; Grafe et al. 2016). Evenity treatment seems to stimulate bone formation and reduce bone resorption in an ongoing phase II clinical trial on patients affected by mild forms of OI (Glorieux et al. 2017).

TGF- β signalling plays a key role in the temporal and spatial regulation of bone remodelling. TGF- β is secreted by osteoblasts and efficiently stored in the bone matrix, representing a coupling factor between bone resorption and formation (Crane, Xian, and Cao 2016). TGF- β neutralizing antibodies improve trabecular bone mass, cortical thickness and bone strength in *Crtap^{-/-}* and *Colla2^{tm1.1Mcb}* mice, reducing both osteoclast and osteoblast activity (Grafe et al. 2014). Among them, Fresolimumab, which already provided promising results in animal models, is today in phase I clinical trial (<https://clinicaltrials.gov/ct2/show/NCT03064074>).

4-phenylbutyric acid (4-PBA) is an FDA approved molecule for urea cycle disorders due to its ammonia scavenger activity (Matoori and Leroux 2015). In addition, 4-PBA has also chemical chaperon activity by interacting with hydrophobic domains of misfolded proteins, and favouring their folding (Iannitti and Palmieri 2011). Indeed, it has been demonstrated that it is also able to promote proper folding, decreasing the accumulation and aggregation of misfolded proteins in the ER lumen (Iannitti and Palmieri 2011). Interestingly, amelioration of the cellular phenotype upon 4-PBA treatment was reported in dermal fibroblasts with mutations in *COL4A2* (Murray et al. 2014).

Moreover, 4-PBA administration in a zebrafish model for classical OI (*Chi^{+/+}*) increased bone mineralization and ameliorated cellular stress, reducing ER cisternae size, thus favouring collagen secretion (Gioia et al. 2017).

An *in vitro* study which used 4-PBA on primary fibroblasts from patients with dominant form of OI, proved to reduce apoptosis by alleviating cellular stress and increasing protein secretion (Besio et al. 2018).

As part of my PhD research activity I contributed in defining the molecular basis of 4-PBA in ameliorating OI cell homeostasis using primary fibroblasts isolated from patients with recessive form of OI, namely OI type VII, VIII and IX (Besio et al. 2019). In detail, I performed the collagen analysis.

RESEARCH ARTICLE

Cellular stress due to impairment of collagen prolyl hydroxylation complex is rescued by the chaperone 4-phenylbutyrate

Roberta Besio¹, Nadia Garibaldi^{1,2}, Laura Leoni¹, Lina Cipolla³, Simone Sabbioneda³, Marco Biggiogera⁴, Monica Mottes⁵, Mona Aglan⁶, Ghada A. Otaify⁶, Samia A. Temtamy⁶, Antonio Rossi¹ and Antonella Forlino^{1,*}

ABSTRACT

Osteogenesis imperfecta (OI) types VII, VIII and IX, caused by recessive mutations in cartilage-associated protein (*CRTAP*), prolyl-3-hydroxylase 1 (*P3H1*) and cyclophilin B (*PPIB*), respectively, are characterized by the synthesis of overmodified collagen. The genes encode for the components of the endoplasmic reticulum (ER) complex responsible for the 3-hydroxylation of specific proline residues in type I collagen. Our study dissects the effects of mutations in the proteins of the complex on cellular homeostasis, using primary fibroblasts from seven recessive OI patients. In all cell lines, the intracellular retention of overmodified type I collagen molecules causes ER enlargement associated with the presence of protein aggregates, activation of the PERK branch of the unfolded protein response and apoptotic death. The administration of 4-phenylbutyrate (4-PBA) alleviates cellular stress by restoring ER cisternae size, and normalizing the phosphorylated PERK (p-PERK):PERK ratio and the expression of apoptotic marker. The drug also has a stimulatory effect on autophagy. We proved that the rescue of cellular homeostasis following 4-PBA treatment is associated with its chaperone activity, since it increases protein secretion, restoring ER proteostasis and reducing PERK activation and cell survival also in the presence of pharmacological inhibition of autophagy. Our results provide a novel insight into the mechanism of 4-PBA action and demonstrate that intracellular stress in recessive OI can be alleviated by 4-PBA therapy, similarly to what we recently reported for dominant OI, thus allowing a common target for OI forms characterized by overmodified collagen.

This article has an associated First Person interview with the first author of the paper.

KEY WORDS: Osteogenesis imperfecta, Endoplasmic reticulum stress, Chemical chaperone, Unfolded protein response, 4-PBA

¹Department of Molecular Medicine, Biochemistry Unit, University of Pavia, 27100 Pavia, Italy. ²Istituto Universitario di Studi Superiori - IUSS, 27100 Pavia, Italy. ³Istituto di Genetica Molecolare, Consiglio Nazionale delle Ricerche, 27100 Pavia, Italy. ⁴Department of Biology and Biotechnology, University of Pavia, 27100 Pavia, Italy. ⁵Department of Neuroscience, Biomedicine and Movement, University of Verona, 37134 Verona, Italy. ⁶Department of Clinical Genetics, Human Genetics & Genome Research Division, Center of Excellence for Human Genetics, National Research Centre, Cairo 12622, Egypt.

*Author for correspondence (aforlino@unipv.it)

© R.B., 0000-0003-1430-2934; S.S., 0000-0001-8551-5465; M.B., 0000-0003-3834-6712; M.M., 0000-0002-7390-2246; M.A., 0000-0002-0908-0639; G.A.O., 0000-0003-2313-7387; S.A.T., 0000-0002-6452-823X; A.R., 0000-0002-2460-8761; A.F., 0000-0002-6385-1182

This is an Open Access article distributed under the terms of the Creative Commons Attribution License (<https://creativecommons.org/licenses/by/4.0>), which permits unrestricted use, distribution and reproduction in any medium provided that the original work is properly attributed.

Received 8 January 2019; Accepted 20 May 2019

INTRODUCTION

Osteogenesis imperfecta (OI) is a collagen-related heritable disorder affecting several connective tissues, but is mainly characterized by skeletal deformity and bone fragility (Marini et al., 2017). Together with the dominant forms caused by mutations in type I collagen and representing over 85% of OI cases, recessive and X-linked OI have been described since 2006. These forms are characterized by defects in proteins involved in collagen type I folding, post-translational modifications, intracellular trafficking, extracellular processing or osteoblasts maturation (Forlino and Marini, 2016; Lindert et al., 2016).

Synthesis of type I collagen includes a complex intracellular and extracellular series of events preceding mature collagen fibril formation and involves several molecular players. Briefly, two $\alpha 1$ and one $\alpha 2$ chains are synthesized in the endoplasmic reticulum (ER) and linked in a trimeric molecule thanks to specific C-terminal recognition sequences and covalent disulfide bridges occurring in close proximity to the ER membrane. During their translation and before triple-helical folding, the α -chains undergo various post-translational modification events, including hydroxylation of proline in C-4 and C-3 and of lysine residues (Ishikawa and Bächinger, 2013). Proline-4 hydroxylation, catalyzed by prolyl-4-hydroxylase B (P4HB), affects almost all the proline residues placed in the Y position of the collagen triplet unit (Gly-X-Y). 4(R)-hydroxy-L-proline (4-Hyp) residues are fundamental for helix stability by favoring water-bridged intramolecular hydrogen bonding. The hydroxylation of triple helical and telepeptide lysine residues, performed by lysyl hydroxylase 1 and lysyl hydroxylase 2, respectively, provides the substrates for successive intracellular glycosylation and extracellular covalent crosslink formation. The role of 3(S)-hydroxy-L-proline (3-Hyp) instead is still poorly defined (Hudson and Eyre, 2013; Pokidysheva et al., 2014). Very few proline residues in collagen type I are 3-hydroxylated, likely excluding their role in collagen stability (Marini et al., 2007). In $\alpha 1(I)$, only Pro986 is always present as 3-Hyp and this post-translational modification is performed by prolyl-3-hydroxylase 1 (P3H1) that is associated in a 1:1:1 ratio with cartilage-associated protein (CRTAP) and cyclophilin B (CyPB) to form a complex active in the ER (Ishikawa et al., 2009). The relevance of 3-Hyp in collagen folding as well as in proper fibril formation was proposed following the identification of three recessive OI forms characterized by the lack of $\alpha 1(I)$ Pro986 C-3 hydroxylation and caused by mutations in one of the three genes encoding the proteins of the ER complex (Marini et al., 2007). Defects in CRTAP, the helper protein of the complex, are responsible for OI type VII (OMIM # 610682), and patients show a moderate to lethal phenotype with growth deficiency, rhizomelia, severe osteoporosis and neonatal fractures (Morello et al., 2006). OI type VIII (OMIM # 610915) is the consequence of mutations in P3H1, the protein of the complex that catalyzes $\alpha 1(I)$ Pro986 C-3 hydroxylation. OI type VIII patients usually show a severe to lethal phenotype with the symptoms overlapping those of type VII (Cabral

et al., 2007). Importantly, CRTAP and P3H1 are mutually stabilizing in the ER (Chang et al., 2010).

Mutations in *PP1B* are responsible for OI type IX (OMIM # 259440). *PP1B* encodes for CyPB, the peptidyl-prolyl *cis-trans* isomerase that catalyzes the isomerization of the peptide bonds involving proline residues, the rate-limiting step reaction in collagen folding. The phenotype of OI type IX patients ranges from moderate to lethal, partially overlapping OI type VII and VIII forms, but without rhizomelia (Barnes et al., 2010; van Dijk et al., 2009).

The absence of CRTAP, P3H1 and CyPB, associated with complete lack or reduced $\alpha 1(I)3$ -Hyp986, delays collagen type I folding, causing overmodification of the helical region and decreased collagen secretion at least in OI dermal fibroblasts (Marini et al., 2007). A still open question to understand the molecular basis of these OI recessive forms is whether the OI phenotype is caused by the absence of 3-Hyp in the bone matrix or by a defect in intracellular collagen folding and secretion, or a combination of both. Interestingly, in a knock-in mouse in which the P3H1 catalytic site was inactivated, but the enzyme was still able to complex with CRTAP, a mild bone phenotype was present (Homan et al., 2014).

The overmodified collagen molecules secreted in the extracellular matrix (ECM) in OI type VII, VIII and IX assemble in irregular fibrils, which impair proper mineralization, affecting bone properties, but their intracellular effects are still unknown (Forlino et al., 2011).

Interestingly, using a functional proteomic approach on lysates obtained from primary fibroblasts of patients with mutations in *CRTAP*, *P3H1* or *PP1B*, we demonstrated an altered cytoskeleton and altered nucleoskeletal assembly, pointing to an impairment of the intracellular compartment (Gagliardi et al., 2017).

No effective therapy is available for any of the OI forms, and bisphosphonates, the most commonly used drugs, are anti-catabolic molecules that impair osteoclast activity and bone remodeling, improving bone mineral density, but without positive effects on bone properties (Besio and Forlino, 2015). Thus, the search for new and, likely, common pharmacological targets for multiple OI forms is an urgent patient need. We used seven primary fibroblast lines obtained from recessive OI type VII, VIII and IX patients to evaluate how cells react to the presence of overmodified collagen because of mutations in the components of the collagen prolyl-3-hydroxylase complex. We demonstrated that mutant collagen accumulates in the ER, causing unfolded protein response (UPR) activation and apoptotic death. We proved that the administration of the chemical chaperone 4-phenylbutyrate (4-PBA) ameliorates cellular homeostasis by mainly favoring protein secretion.

RESULTS

Primary fibroblasts from seven previously described (*PP1B*) recessive OI patients with mutations in the components of the

Table 1. List of the human primary fibroblast cells used in the study

Patient	Gene	Protein	Gene mutation	Protein mutation	OI type	Clinical phenotype	Reference
CRTAP-1	<i>CRTAP</i>	CRTAP	c.118_133del16insTACCC/ c.118_133del16insTACCC	Glu40Tyrfs*117	VII	Short stature, long-bone fractures and deformities, vertebral deformities, rhizomelia, grayish sclerae	Valli et al., 2012
CRTAP-2	<i>CRTAP</i>	CRTAP	c.-1677_471+1592del/c.-1677_471+1592del	Not reported	VII	Short stature, long-bone fractures and deformities, vertebral deformities, scoliosis, pectus carinatum, wormian bone, osteoporosis, joint hypermobility, rhizomelia, faint blue sclerae at birth	Caparros-Martin et al., 2013
CRTAP-3	<i>CRTAP</i>	CRTAP	c.804_809delAGAAGT/ c.804_809delAGAAGT	Glu269_Val270del	VII	Short stature, long-bone fractures and deformities, rib fractures, vertebral deformities, compression and fractures, scoliosis, osteopenia, no rhizomelia, grayish sclerae	Amor et al., 2011
P3H1-1	<i>P3H1</i>	P3H1	c.2148delC	Glu719Asnfs*747	VIII	Short stature, long-bone fractures and deformities, vertebral deformities, osteopenia	Our unpublished data
P3H1-2	<i>P3H1</i>	P3H1	c.1223+2T>G/c.1223+2T>G	Not reported	VIII	Short stature, long-bone fractures and deformities, pectus carinatum, wormian bones, vertebral deformities, scoliosis, osteoporosis, joint hypermobility, faint blue sclerae at birth	Caparros-Martin et al., 2013
P3H1-3	<i>P3H1</i>	P3H1	c.765C>A/c.2055+18G>A	Tyr255Ter splice site	VIII	22-week-old fetus: severe skeletal dysplasia characterized by short, bowed and deformed long bones	Our unpublished data
CyPB	<i>PP1B</i>	CyPB	c.497A>C/c.497A>C	His166Pro	IX	Short stature, long-bone fractures and deformities, pectus carinatum, flaring of ribs, wormian bones, vertebral deformities, kyphoscoliosis, osteoporosis, joint hypermobility, dusky color of the sclerae	Caparros-Martin et al., 2013

3-hydroxylation complex were selected for the study. Three patients carry mutations in *CRTAP* (CRTAP-1, CRTAP-2 and CRTAP-3), three in *P3H1* (P3H1-1, P3H1-2 and P3H1-3) and one in *PPIB* (CyPB) (Table 1).

In CRTAP-1, in which the mutation is predicted to cause a frameshift resulting in a premature stop codon, and in CRTAP-2, in which a large genomic deletion including exon 1 was described, a strongly reduced (0.036 ± 0.019) and no CRTAP expression, respectively, were detected by quantitative real-time PCR (qPCR), suggesting the activation of nonsense-mediated decay (Fig. 1A). Similarly, a reduced P3H1 expression (0.146 ± 0.03) was present in P3H1-2 cells carrying an intronic mutation in intron 7, predicted to impair normal splicing. Indeed, no exon 6-8 amplicon was detected by reverse-transcription PCR (RT-PCR), but a band with higher molecular weight, compatible with the retention of the intronic sequence, was detected (Fig. 1B).

A reduction of about 50% of *P3H1* transcript was demonstrated in P3H1-3, a compound heterozygous for an allele carrying a missense mutation and a second allele predicted to impair the translation of the KDEL ER-retention signal. The defect in the P3H1-1 patient, the only one not molecularly characterized yet, was identified as a single-nucleotide deletion (c.2148delC) in *P3H1* exon 15. The mutation causes a frameshift and the introduction of a premature stop codon at position 747 (Glu719Asnfs*747). Only a slightly reduced *P3H1* expression (0.78 ± 0.03) was detected (Fig. 1A). As expected,

no impairment of CRTAP expression was found in CRTAP-3, carrying the homozygous deletion of 6 nucleotides (nt) responsible for the in frame removal of amino acids Glu269 and Val270, or in CyPB, carrying a homozygous single base-pair substitution generating the His166Pro in CyPB (Fig. 1A).

At the protein level, all cells from patients carrying mutations in *CRTAP* showed the absence of both CRTAP and P3H1 expression and, similarly, patients with mutations in *P3H1* showed no P3H1 and CRTAP expression, as expected given the mutual protection of these proteins in the complex (Chang et al., 2010). By contrast, the level of the third component, CyPB, was not affected (Fig. 1C). No CyPB expression was detectable in *PPIB* mutant cells despite normal transcript level, but the level of CRTAP and P3H1 proteins were within the normal range (CRTAP 1.00 ± 0.19 ; P3H1 1.00 ± 0.28).

Mutations in the components of the prolyl 3-hydroxylation complex impair collagen structure and cell survival

The impairment of the 3-hydroxylation complex is known to affect type I collagen folding, causing its increased hydroxylation and glycosylation (Forlino and Marini, 2016). In all analyzed OI cells, the presence of collagen overmodification was confirmed by electrophoretic analysis of ^3H -labeled type I collagen. Steady-state collagen gels revealed the typical broadening of the $\alpha(\text{I})$ bands in both cell-layer and medium fractions (Fig. 2A). Furthermore, an increase of collagen retention was detected in mutant cells

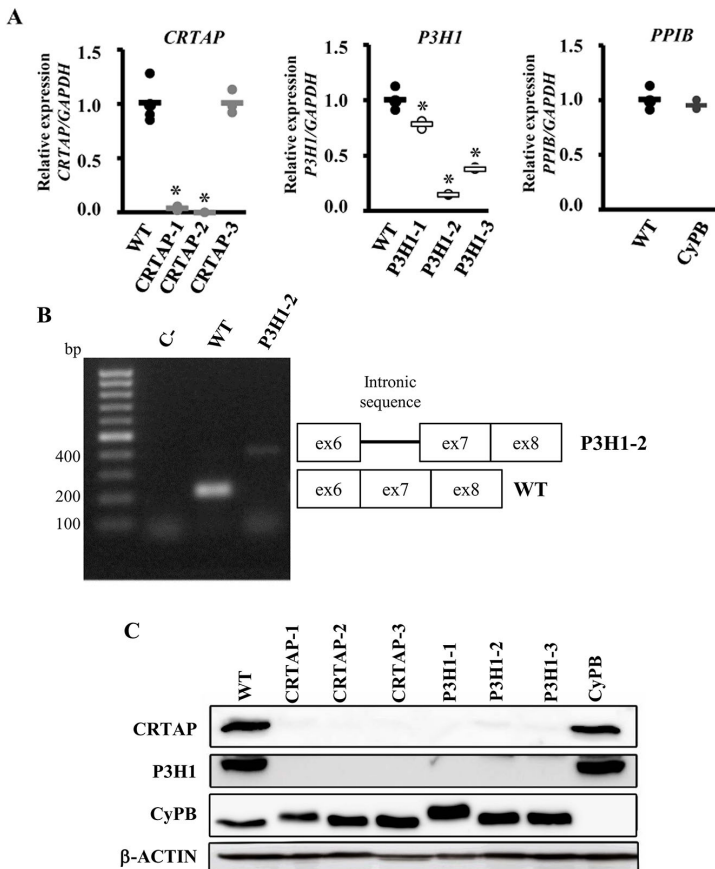


Fig. 1. Loss of mutant CRTAP, P3H1 and CyPB in OI patient fibroblasts. (A) Quantitation of *CRTAP*, *P3H1* and *PPIB* expression evaluated by qPCR. Mutations in *CRTAP*, *P3H1* and *PPIB* caused a close to complete absence of the mutated transcripts in CRTAP-1, CRTAP-2 and P3H1-2 patients, and a reduced mRNA level in P3H1-1 and P3H1-3. * $P < 0.05$. WT values are represented as black dots; CRTAP as gray dots; P3H1 as white dots; CyPB as dark gray dots. (B) Amplification of the exon 6-exon 8 region of *P3H1* transcript generated the expected 217 bp amplicon in control cells (WT), whereas, in the P3H1-2 patient, the presence of a higher molecular weight (~400 bp) band compatible with intronic retention was detected. C-, RT-PCR negative control. (C) Representative western blot to evaluate the expression of CRTAP, P3H1 and CyPB in control (WT) and mutant cell lysate fractions (CRTAP-1, CRTAP-2, CRTAP-3, P3H1-1, P3H1-2, P3H1-3, CyPB). Loss of the mutated protein in patient's cells was demonstrated. Patients with mutations in *CRTAP* showed also no P3H1 expression and patients with mutations in *P3H1* showed no CRTAP expression, as a consequence of their mutual protection in the complex.

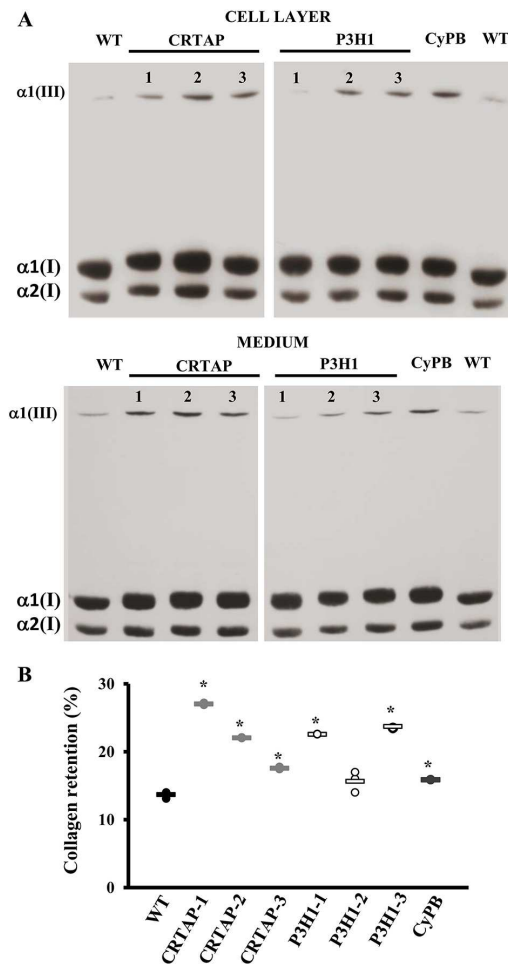


Fig. 2. Mutations in the collagen prolyl-3-hydroxylation complex lead to collagen overmodifications and collagen intracellular retention. (A) Representative SDS-urea-PAGE fluorographies of ^3H -labeled collagen extracted from the cell layer and medium of control (WT) and patient (CRTAP-1, CRTAP-2, CRTAP-3, P3H1-1, P3H1-2, P3H1-3, CyPB) fibroblasts. In mutant samples, broader and slower α (I) bands demonstrated the overglycosylation of type I collagen. (B) The percentage of intracellular collagen retention was evaluated as a ratio between the CPM in the cell layer and in medium plus cell layer. Collagen molecules in mutant cells were more intracellularly retained compared to WT. * $P < 0.05$. WT values are represented as black dots; CRTAP as gray dots; P3H1 as white dots; CyPB as dark gray dots.

compared to controls, and kinetic analysis showed a decrease in collagen secretion (Fig. 2B and Fig. S1).

Electron microscopy imaging revealed the presence of large vacuoles, resembling autophagosome vesicles since double membranes were occasionally detectable, and the ER cisternae were clearly enlarged compared to control cells. The ER looked normal in P3H1-2 cells (Fig. 5B).

Apoptosis occurrence was demonstrated in all OI mutant cells by the increased level of cleaved caspase 3 (Fig. 3A) and confirmed by fluorescence activated cell sorting (FACS) upon annexin V/Dead-positive cell labeling. Indeed, an higher percentage of apoptotic

cells compared to controls ($4.31 \pm 0.78\%$) was detected by FACS in CRTAP-2, CRTAP-3, P3H1-2, P3H1-3 and CyPB fibroblasts ($49.00 \pm 5.2\%$, $35.74 \pm 3.57\%$, $22.86 \pm 2.83\%$, 53.93 ± 2.17 and $20.42 \pm 1.11\%$, respectively) (Fig. 3B and Fig. S2).

UPR is activated in fibroblasts from patients with recessive OI

Given the intracellular presence of overmodified collagen molecules in the recessive patients' fibroblasts, we investigated the expression of the chaperones binding immunoglobulin protein (BIP) and protein disulfide isomerase (PDI) and the activation of the three branches of the UPR: the eukaryotic translation initiation factor 2 alpha kinase 3 (PERK) branch, the inositol-requiring enzyme 1 α (IRE1 α) branch and the activating transcription factor 6 (ATF6) branch.

Four out of seven cell lines showed an increased level of both BIP, the best-characterized activator of the UPR sensors, and PDI, which catalyzes the formation and isomerization of disulfide bonds necessary for protein native state and which is known to interact with single collagen α chains (Fig. 3C) (Wilson et al., 1998).

The phosphorylated PERK (p-PERK):PERK ratio was significantly increased in all mutant cells with the exception of P3H1-2, in which a trend was detectable. Consistently, in these cell lines the expression of activating transcription factor 4 (ATF4), the effector of p-PERK, was also increased (Fig. 3C), confirming the activation of the UPR branch. No activation of the ATF6 and IRE1 α branches was identified since no difference in cleaved ATF6 was detected and the IRE1 α -mediated splicing of *XBP1* in mutants was comparable to controls (Fig. 3D).

Based on these data, we demonstrated that mutations in the prolyl-3-hydroxylation complex, causing the synthesis of overmodified collagen, lead to the disruption of ER homeostasis and consequent activation of the PERK branch of the UPR in OI fibroblasts.

Recessive OI fibroblasts react to cellular stress by activating autophagy

Given the presence and/or intracellular accumulation of overmodified collagen molecules and with autophagy being the first cell response to constitutive dysfunctional cellular components, its activation was investigated, evaluating the expression of the terminal autophagic marker, the microtubule-associated protein 1A/1B-light chain 3 (LC3-II). The expression of LC3-II was upregulated in all cases except in patient P3H1-2 (Fig. 4A). Following chloroquine treatment, the expression of LC3-II was increased compared to wild type (WT) in CRTAP-2, CRTAP-3, P3H1-2 and CyPB cells, indicating a general accumulation of LC3-II due to the block in autophagic flux (Fig. 4B). The quantitation of LC3 immunofluorescence in OI fibroblasts treated with chloroquine was performed to validate the activation of the autophagic pathway by an independent assay. As expected, the LC3 signal was significantly increased compared to controls in CRTAP-2, CRTAP-3, P3H1-2 and CyPB cells, in agreement with the western blot data (Fig. 4C).

4-PBA ameliorates recessive OI fibroblasts homeostasis

To alleviate cellular stress due to intracellular retention of overmodified collagen molecules, patient fibroblasts and control cells were treated with 4-PBA, a well-known chemical chaperone, FDA-approved as an ammonia scavenger for urea cycle disorders (Matoori and Leroux, 2015). The effect of the drug was evaluated following the activation of the PERK branch of the UPR and the activation of caspase 3, as a signature for apoptosis, by western blotting. Their levels were compared in control and OI treated versus untreated cells and in treated OI cells versus untreated controls. None of the selected markers was significantly changed in WT after 4-PBA

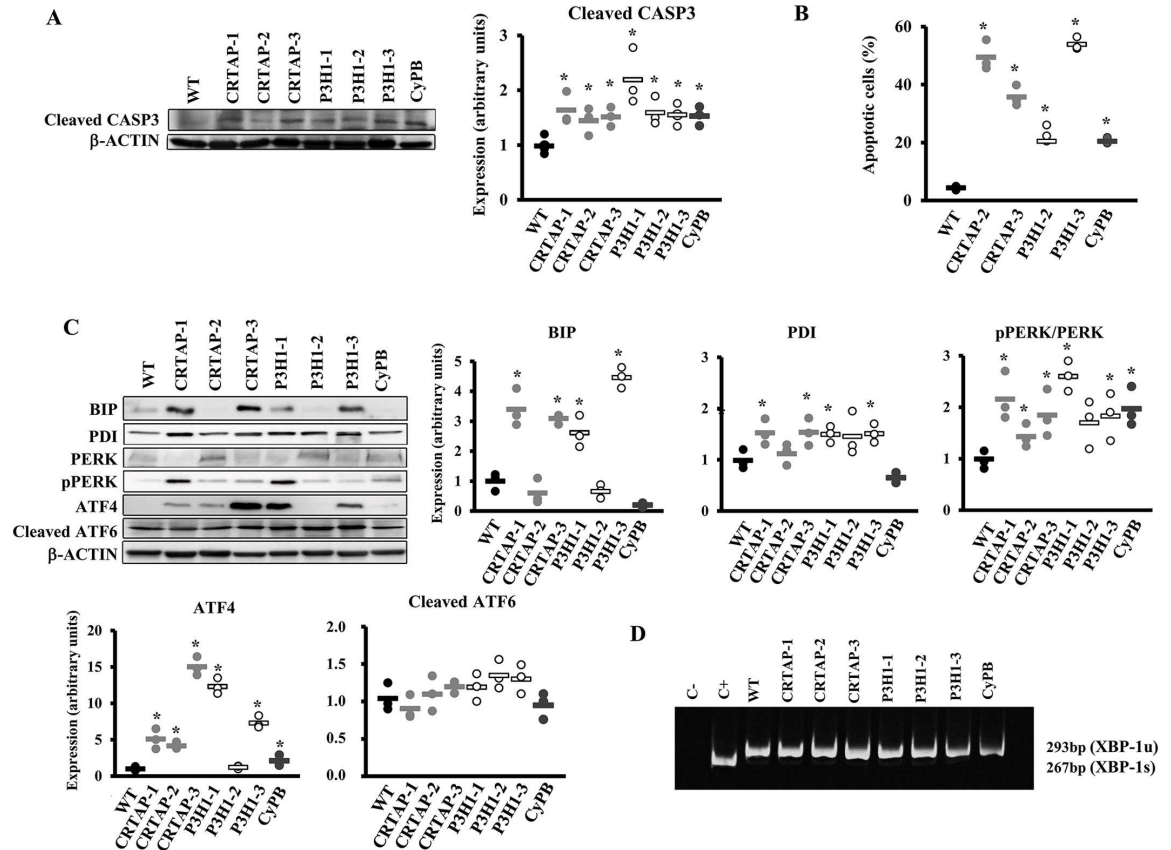


Fig. 3. Activation of apoptosis and the UPR in recessive OI patient fibroblasts. (A) Representative western blot (left) to evaluate the expression of cleaved caspase 3 (CASP3), a terminal marker for apoptosis and the dot plot of the quantitative analysis (right). β -actin was used for normalization. (B) Quantitative analysis of the fraction of apoptotic events in the cell lines following FACS analysis upon cells staining with annexin V (FITC) and propidium iodide (PI). Apoptosis is activated in all tested OI patients' cells. (C) Representative western blots (left) and dot plots of the quantitative analysis (right and bottom) of the collagen chaperone PDI and of proteins involved in the UPR (BIP, PERK, p-PERK, ATF4, ATF6) in control (WT) cells and in cells with mutations in CRTAP, P3H1 or CyPB. The PERK branch of the UPR was upregulated in all patients' fibroblasts with the exception of patient P3H1-2. β -actin was used for normalization. WT values are represented as black dots; CRTAP as gray dots; P3H1 as white dots; CyPB as dark gray dots. * $P < 0.05$. (D) RT-PCR amplification of *XBP1* mRNA from control (WT) and patient cells. The spliced XBP1-1s form of XBP1 transcript (XBP-1u) is not detectable in patient cells. Fibroblasts treated with thapsigargin were used as positive control (C+).

administration (data not shown). Interestingly, following the treatment, p-PERK:PERK and cleaved caspase 3 levels were decreased to or even less than control values in all cases (Fig. 5A). The positive effect of the drug on recessive OI cellular homeostasis was further confirmed by the reduction of ER cisternae size, as evaluated by transmission electron microscopy (Fig. 5B). No rescue of CRTAP and CyPB was instead detected after the treatment in the patients with normal transcript level, indicating that the 4-PBA effect is not due to rescue of folding of the mutant proteins (Fig. 5C).

4-PBA chaperone function rescues recessive OI cell homeostasis

In order to determine the mechanism of action of 4-PBA, we investigated in our system the effect of the drug on collagen secretion and on general protein secretion. Collagen secretion was unaffected by the treatment, as were collagen post-translational modifications (data not shown). However, protein labeling with ^{35}S -L-methionine and ^{35}S -L-cysteine revealed an increased total protein secretion upon 4-PBA administration in all the cells tested in which it was severely

affected in the basal condition, namely CRTAP-1, P3H1-1, P3H1-2 and P3H1-3 (Fig. 6A), indicating its chaperone activity.

Interestingly, an increased LC3-II level in all mutant cells treated with 4-PBA was detected, clearly supporting a 4-PBA stimulatory effect on autophagy in OI recessive cells (Fig. 6B). In order to determine whether the rescue of the cellular homeostasis following 4-PBA treatment was due to its chaperone function or to its autophagy-stimulating ability, ER proteostasis, PERK activation and cell survival were monitored in the absence or presence of chloroquine, a pharmacological inhibitor of autophagy. Thioflavin T (ThT), a small molecule that exhibits increased fluorescence when it binds to protein aggregates, was used to quantify ER proteostasis (Beriault and Werstuck, 2013). Enhanced ThT fluorescence was detectable in mutant cells compared to control, indicating the accumulation of intracellular misfolded material (Fig. 7A). 4-PBA treatment significantly reduced the ThT fluorescence, proving the reduction of protein accumulation (Fig. 7A). Importantly, this effect of 4-PBA was evident also when inhibiting autophagy with chloroquine (Fig. 7A). Furthermore, the p-PERK:PERK ratio and

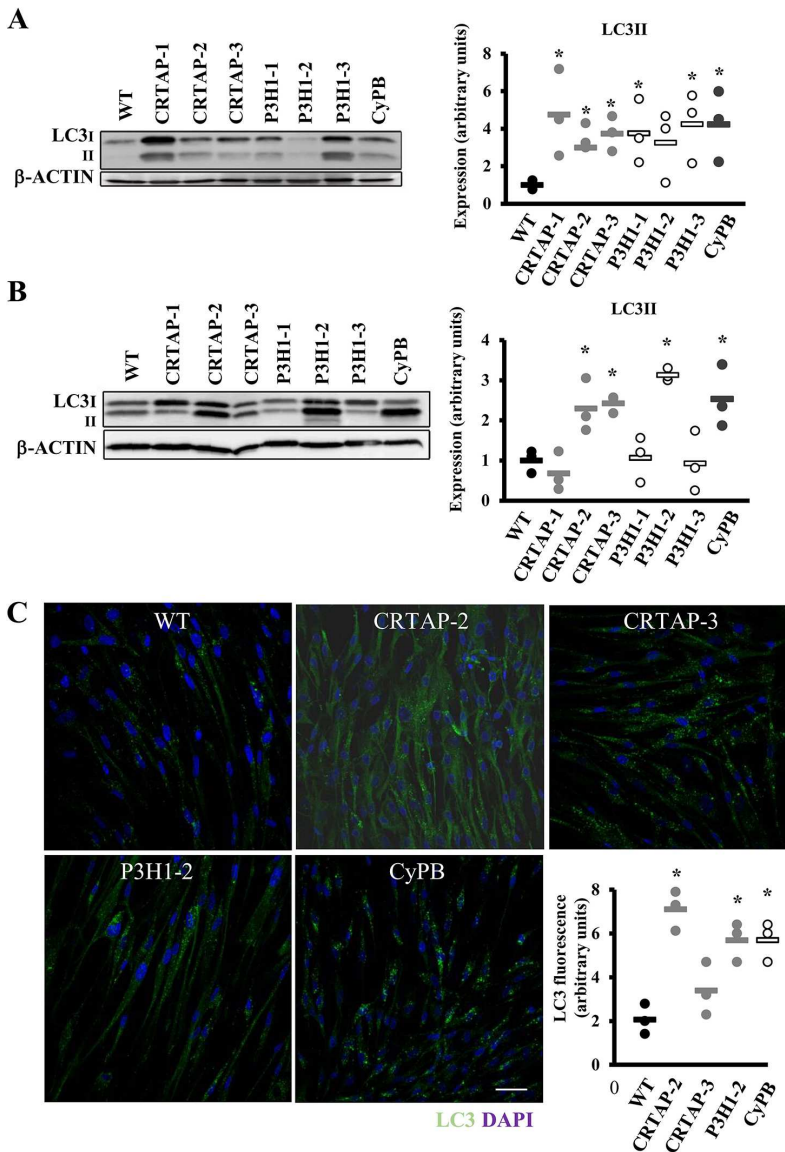


Fig. 4. Recessive OI cells react to cellular stress by activating autophagy.

(A) Representative western blot (left) and dot plot of the quantitative analysis (right) of the terminal autophagic marker LC3 in control (WT) and in cells with mutations in CRTAP, P3H1 or CyPB. LC3-II is upregulated in all cases except in patient P3H1-2. β -actin was used for normalization. (B) Representative LC3 western blot (left) performed on cell lysates obtained following chloroquine incubation from WT and mutant samples, and dot plot of the quantitative analysis (right). The terminal marker of autophagy evaluated in dynamic conditions is increased in CRTAP-2, CRTAP-3, P3H1-2 and CyPB. β -actin was used for normalization. (C) Representative LC3 immunofluorescence images of WT and mutant fibroblasts treated with chloroquine. Quantitation of the total area of punctate signal per cell confirms the activation of autophagy. DAPI (nuclei) in blue and LC3 in green. Magnification 40 \times , zoom 4 \times . WT values are represented as black dots; CRTAP as gray dots; P3H1 as white dots; CyPB as dark gray dots. * P <0.05. Scale bar: 40 μ m.

apoptosis were decreased by 4-PBA when autophagy was impaired, finally corroborating the primary chaperone function of the drug in rescuing cell homeostasis (Fig. 7B,C).

To evaluate whether other chemical chaperones could have a similar effect on OI cells, tauroursodeoxycholic acid (TUDCA), approved for cholestasis (Wagner and Trauner, 2016), was used. TUDCA did not show any effect on p-PERK, apoptosis and autophagy levels, thus suggesting a specificity of 4-PBA in the rescue of recessive OI fibroblasts homeostasis (Fig. S3).

DISCUSSION

In the past 10 years, the prolyl-3-hydroxylation complex has been demonstrated to be crucial for proper type I collagen folding and post-translational modifications (Marini and Blissett, 2013).

Mutations in any of its components, CRTAP, P3H1 and CyPB, are associated with recessive forms of moderate to lethal OI, characterized by the presence of abnormal ECM and impaired mineralization associated with bone fragility (Marini et al., 2017). Here, we move our attention from the extra- to the intracellular space and describe the effect of overmodified type I collagen on cellular homeostasis of seven recessive OI cases, three carrying mutations in CRTAP, three in P3H1 and one in PP1B, using skin fibroblasts in which no mutant protein was detectable (Fig. 1C).

Overmodified type I collagen in recessive OI mutants causes UPR and apoptosis activation

In all cell lines, the presence of overmodified collagen was demonstrated by metabolic labeling and electrophoretic analysis

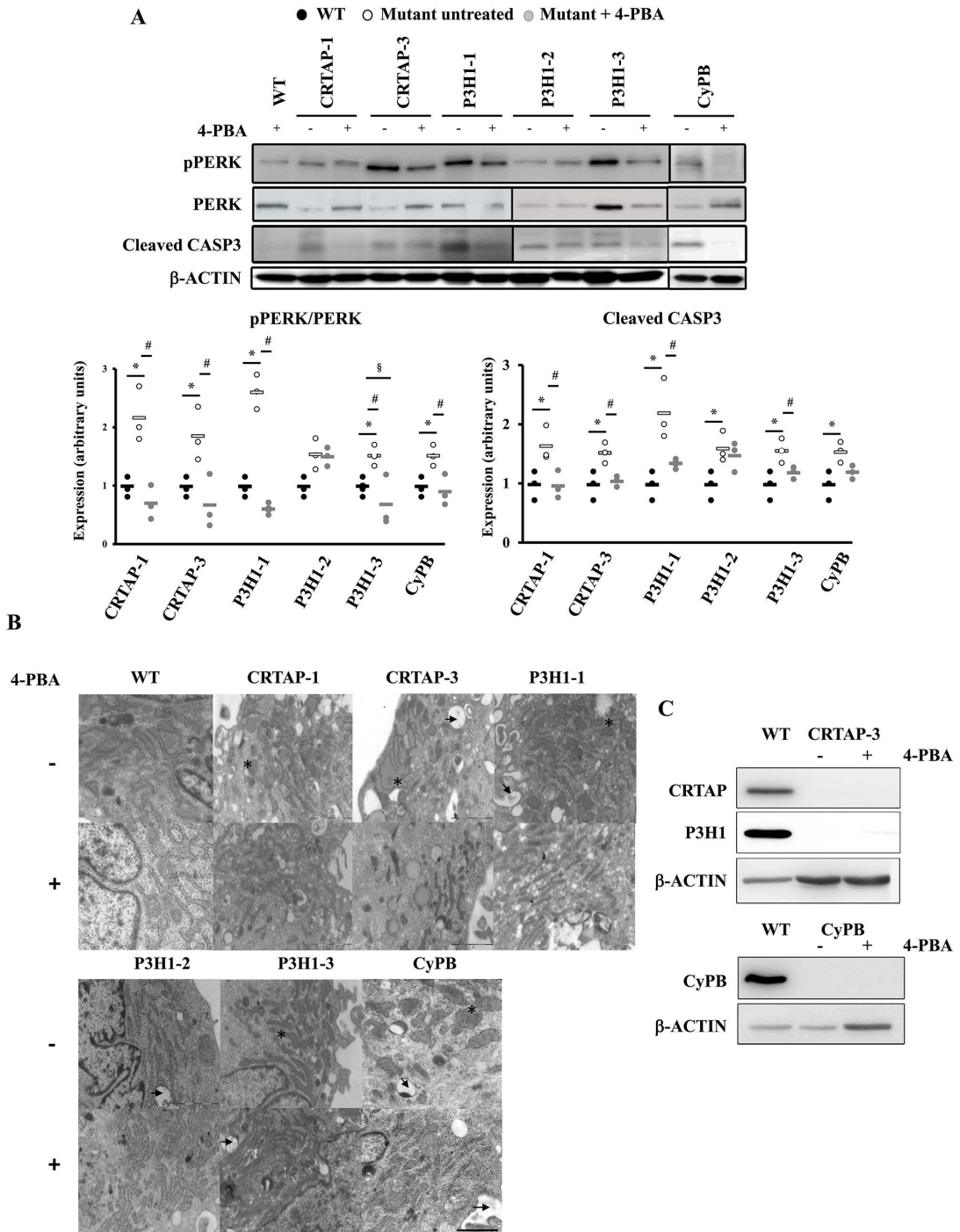


Fig. 5. See next page for legend.

(Fig. 2A). Likely due to the increased accumulation of type I collagen molecules in the ER, cisternae enlargement and cellular vacuolization were detected (Fig. 5B). Interestingly, in the presence

of similar broadening of the α -bands, significant intracellular collagen retention and ER enlargement was not clearly evident in P3H1-2 cells, suggesting a variable ability of the cells to handle

Fig. 5. 4-PBA ameliorates recessive OI fibroblast homeostasis.

(A) Representative western blots (top) and dot plot of the quantitative analysis (bottom) of p-PERK and cleaved caspase 3 (CASP3) in the absence (-) or presence (+) of 4-PBA incubation in control (WT) cells and in cells with mutations in CRTAP, P3H1 or CyPB. The levels of these proteins were compared in treated versus untreated cells and in treated OI cells versus untreated controls. β -actin was used for normalization. * $P < 0.05$ mutant fibroblasts with respect to control fibroblasts. # $P < 0.05$ treated mutant fibroblasts with respect to untreated mutant fibroblasts. § $P < 0.05$ treated mutant fibroblasts with respect to untreated control fibroblasts. p-PERK:PERK and cleaved caspase 3 levels were decreased to or even less than control values in all cases, with the exception of P3H1-2. WT untreated values are shown as black dots, mutants untreated as white dots and mutants treated as gray dots. (B) Transmission electron microscopy representative images of OI patient fibroblasts in the absence (-) or presence (+) of 4-PBA. The analyses revealed ER enlargement (*) and cellular vacuolization (arrow) in mutant cells with the exception of P3H1-2. 4-PBA treatment reduced the ER cisternae enlargement. Magnification 20,000 \times . (C) Representative western blot of CRTAP and P3H1 in control (WT) and CRTAP-3 cell lysates, and of CyPB in WT and CyPB lysates. No protein rescue was detected after the treatment in the two mutant cell lines, in which normal transcript level was detected. β -actin was used for normalization. Scale bar: 2 μ m.

overmodified type I collagen, either due to a different level of collagen overmodification or to the effect of modifiers affecting collagen secretion (Fig. 2, Fig. 5B). Indeed, although collagen electrophoretic analysis is a quick and simple tool to reveal post-translational overmodifications, it does not allow the detection of subtle differences (Barnes et al., 2006; Cabral et al., 2007) that have been previously demonstrated in OI patients and may potentially impact on protein secretion (Amor et al., 2011; Barnes et al., 2006; Marini et al., 2007; Taga et al., 2013). Furthermore, the functional role of collagen O-glycosylation is not clearly defined yet and, if some information is available regarding its possible extracellular effect on increasing collagen stability against proteolytic degradation, control of lateral growth of the fibrils, interaction with non-collagenous proteins and the cross-linking process,

nothing has been reported so far on its intracellular effect (Perdivara et al., 2013).

Following collagen folding in the ER, its secretion requires the assembly of specific large COPII vesicles, whose formation depends on a large number of proteins and lipids. Thus, it is not surprising that the complex collagen secretory machinery may be tuned by the action of modifiers (Vollmann et al., 2017).

To maintain the functional integrity of ER under stress conditions, the evolutionarily conserved adaptive response, the UPR, is generally turned on. Indeed, UPR activation affecting cell homeostasis and likely modulating disease severity was reported in the presence of mutations in ECM molecules, including the fibrillar collagen type II and X (Boot-Handford and Briggs, 2010). In recessive OI cells, the PERK branch of the UPR is activated, as demonstrated by an increased p-PERK:PERK ratio and upregulation of its effector ATF4 (Fig. 3C). In the presence of ER stress, BIP, the master regulator of activation of the UPR branches, is released from the UPR sensors to favor protein folding and this event activates the specific ER cellular response. Interestingly, three out of seven OI cell lines did not show upregulation of BIP, hinting at other regulatory proteins being involved in the ER stress response in the presence of overmodified type I collagen retention, as suggested in previous reports (Besio et al., 2018; Forlino et al., 2007; Mirigian et al., 2016). UPR activation is not sufficient for cell homeostasis and CRTAP-2, CRTAP-3, P3H1-2 and CyPB recessive OI fibroblasts also showed upregulated autophagy (Fig. 4), which is often activated to regulate the lysosome-dependent turnover of cell materials to reduce the ER overload (Galluzzi et al., 2017; Green and Levine, 2014). Surprisingly, autophagy was also stimulated in P3H1-2 cells in which no reduction of collagen secretion, no UPR activation and no ER cisternae enlargement were detectable. The splice-site mutation in this cell line (c.1223+2T>G), predicted to cause exon 7 removal, should result in the translation of a shorter P3H1 (p.Asp391Valfs46) that could indeed be eliminated through

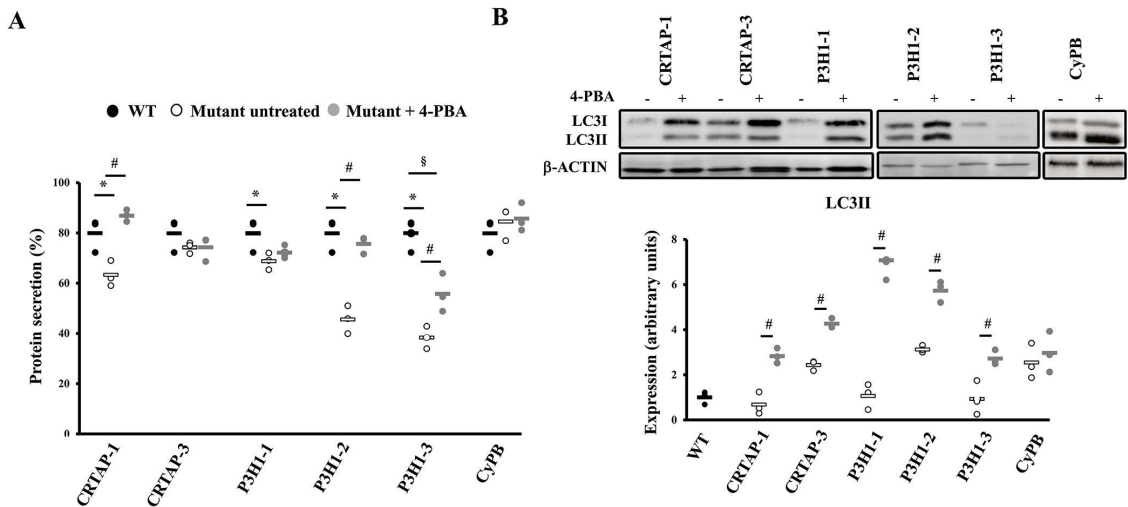


Fig. 6. 4-PBA stimulates protein secretion and autophagy. (A) Dot plot representing the amount of general protein secreted in the absence or presence of 4-PBA treatment in WT and OI patient fibroblasts. In the samples in which protein secretion was impaired in the basal condition, it was rescued by 4-PBA treatment. (B) Representative western blot to evaluate LC3 expression (top) in control (WT) and patient cells in the absence (-) and presence (+) of 4-PBA, and dot plot of the quantitative analysis (bottom). An increase of LC3-II levels in cells after 4-PBA treatment was detected. * $P < 0.05$ mutant fibroblasts with respect to control fibroblasts. # $P < 0.05$ treated mutant fibroblasts with respect to untreated mutant fibroblasts. § $P < 0.05$ treated mutant fibroblasts with respect to untreated control fibroblasts. β -actin was used for normalization. WT untreated values are shown as black dots, mutants untreated as white dots and mutants treated as gray dots.

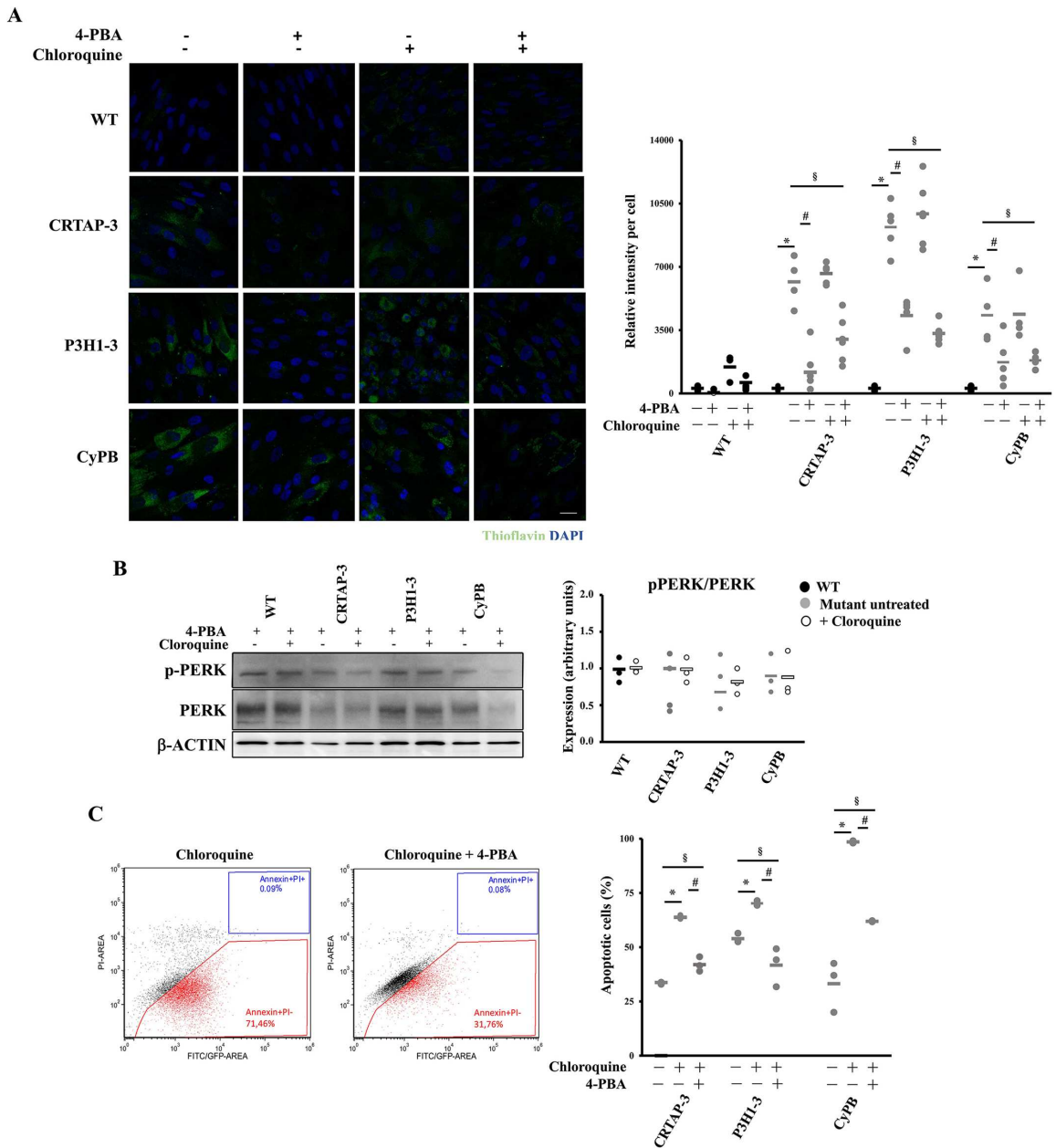


Fig. 7. 4-PBA chaperone function is mainly responsible for homeostasis rescue in the recessive OI cells. (A) ER proteostasis was evaluated using thioflavin T (ThT). Representative immunofluorescence images are shown on the left and the fluorescence quantitation graph is reported on the right. Mutant cells revealed an increased fluorescence compared to control, indicating the intracellular accumulation of misfolded proteins. 4-PBA treatment significantly reduced the ThT fluorescence, proving its chaperone role also following autophagy inhibition with chloroquine. WT is shown in black, mutants in gray. (B) Representative western blot to evaluate pPERK:PERK expression in the absence (–) and presence (+) of 4-PBA and of chloroquine and quantitative analysis. 4-PBA normalized the p-PERK:PERK ratio even when autophagy was impaired. β-actin was used for normalization. WT untreated values are shown as black dots, mutants untreated as gray dots, cells treated with chloroquine as white dots. (C) Representative FACS plots and quantitative analysis of the fraction of apoptotic events following staining with annexin V (FITC) and propidium iodide (PI) in the absence (–) and presence (+) of chloroquine and of 4-PBA. Even when autophagy was impaired, 4-PBA decreased apoptosis. * $P < 0.05$ mutant fibroblasts treated with chloroquine with respect to untreated. # $P < 0.05$ mutant fibroblasts treated with 4-PBA and chloroquine with respect to treated with chloroquine. § $P < 0.05$ mutant fibroblasts treated with 4-PBA and chloroquine with respect to untreated fibroblasts. Scale bar: 20 μm.

autophagy. Nevertheless, the strong reduction of RNA expression demonstrated the activation of nonsense-mediated decay, likely minimizing the amount of protein synthesis. Despite autophagy activation, apoptosis was promoted in all analyzed cell lines (Fig. 3A).

Common pathways are activated in recessive and classical forms of OI

The reported overmodified collagen retention, UPR activation and cell death found in recessive OI type VII, VIII and IX resemble what was previously detected in the OI forms due to mutations in *COL1A1* and *COL1A2* genes and characterized by the synthesis of structurally altered collagen molecules. In particular, in fibroblasts from patients with classical OI forms, we recently demonstrated that the intracellular-retained overglycosylated collagen causes ER cisternae enlargement, and the inefficiency of the UPR to counteract the constitutive synthesis of mutant collagen brought cells to death (Besio et al., 2018). In our system, we also described autophagy activation as a general mechanism associated with *COL1A1* mutations, but detectable only in few cases with mutations in *COL1A2* (Besio et al., 2018). We hypothesized that endogenous autophagy in OI cells could be linked to the presence of a higher amount of mutant collagen since, due to its stoichiometry, 75% of trimers will be overmodified in the presence of mutant $\alpha 1$, versus 50% when $\alpha 2$ chains are mutated. Interestingly, in the analyzed recessive cells, in which all the collagen type I is overmodified, not all patients had the same autophagic response. Although we cannot exclude a mutation or site-dependent effect of structural defects in collagen chains, these new results support the hypothesis of a role for modifiers in modulating cell response to stress. Indeed, in a previous study using skin and bone samples from the Brl mouse, a model for dominant OI carrying a G349C substitution in $\alpha 1(I)$ and either a moderate or a lethal outcome, we found in mice with non-lethal outcome a better ability to react to mutant collagen retention. Such capacity was associated with an increased expression of chaperone proteins (Bianchi et al., 2012; Forlino et al., 2007). Some years later, we confirmed a different ability to manage cell stress and thus to guarantee cell homeostasis in patients cells carrying identical mutation, but different outcome (Besio et al., 2018).

Of note, independently from the autophagic cellular response, apoptosis is upregulated in both dominant and recessive mutant cells. Thus, apoptotic pathway activation represents a hallmark of unsolved cell stress, both in dominant and in recessive forms of the disease (Besio et al., 2018; Bianchi et al., 2012; Galluzzi et al., 2017; Green and Levine, 2014; Mirigian et al., 2016). P3H1-2 represents an exception to this rule since, in this cell line, apoptosis is not activated by sustained ER stress due to mutant collagen retention, but possibly as a consequence of sustained autophagy.

4-PBA: a potential common therapy for recessive and classical forms of OI

The identification of novel targets for disease treatment is of valuable significance to develop novel therapies. The recognition of altered pathways common to several diseases is even more relevant for rare diseases with a limited number of affected patients. We previously proved that 4-PBA successfully ameliorates classical OI cell homeostasis *in vitro* using OI patients' fibroblasts, and bone phenotype *in vivo* using the OI zebrafish model *Chihuahua* (Besio et al., 2018; Gioia et al., 2017). The drug activated autophagy and increased general protein secretion in OI dominant fibroblasts, and improved bone mineralization and bone histomorphometric parameters in the zebrafish model. 4-PBA is an FDA-approved drug

for urea cycle disorders; thus, its repositioning for a different disease will definitely speed up the bench-to-bedside transition (Matoori and Leroux, 2015). Nevertheless, the multiple recognized functions of 4-PBA need to be taken into consideration for a proper data interpretation. Associated to its ammonia scavenger role, 4-PBA has a recognized chaperone function, favoring ER protein folding and thus attenuating the UPR in the presence of ER stress caused by misfolded protein accumulation (Pettit and Feller, 2014), and it acts as a histone deacetylase inhibitor, modulating chromatin accessibility and thus gene expression (Butchbach et al., 2016). Interestingly, at least in yeast cells, 4-PBA attenuates the UPR by accelerating the degradation of the ER-stress sensor Ire1, rather than by restoring the global protein folding; indeed, UPR attenuation was detectable even in the absence of ER stress (Daosukho et al., 2007; Mai et al., 2018).

Here, we dissected whether the positive effect of 4-PBA was due to its autophagy-stimulating ability or to its chaperone function, and finally proved its relevance in assisting protein secretion.

Taking all these findings into consideration, our results prove and extend the potential use of 4-PBA as chemical chaperone to the OI forms characterized by overmodified collagen production. For the first time, we demonstrated the potential pharmacological benefit of this drug for the recessive forms of OI with defects in the 3-hydroxylation complex. In almost all the analyzed fibroblasts carrying mutations in the P3H1 complex, 4-PBA administration reduced PERK activation and decreased apoptosis (Fig. 5A). The improved general protein secretion detected in the recessive OI resembles the findings described in dominant cases. The restoration of normal ER cisternae size (Fig. 5B) and the reduced ThT fluorescence (Fig. 7A) further supports the reduction of misfolded protein accumulation.

Of note, treatment of CyPB mutant cells seems to act in a different way. Drug administration reduced apoptotic death, but neither autophagy nor protein secretion were significantly augmented. CyPB is involved in other intracellular complexes. It is a binding partner for lysyl hydroxylase isoforms, thus affecting collagen hydroxylation and crosslinks, and interacts with BIP and PDI, thus having a relevant role in the folding of the collagen C-propeptides and on the kinetics of collagen chain association (Gruenwald et al., 2014; Heard et al., 2016; Terajima et al., 2016). Indeed, *PP1B*-null cells showed a delay in trimer association together with the increased post-translational modification present also in *CRTAP*- and *P3H1*-null cells (Pyott et al., 2011; van Dijk et al., 2009). With the limit of the use of a single cell line, mainly due to the extreme rarity of OI type IX, we can hypothesize that the multiple roles of CyPB may be differentially and specifically affected/modulated by 4-PBA treatment, and further experiments will be necessary to shed light on the mechanism.

Study limitations

As a cellular model, we used primary fibroblasts from recessive OI patients. Since skin biopsy has limited invasiveness, a large body of literature is available on OI biochemical characterization based on this cell type, and fibroblasts share with osteoblasts the production of a high amount of collagen type I and several biochemical pathways (Bianchi et al., 2012). Furthermore, a skin phenotype is often described in OI patients (Balasubramanian et al., 2016). Nevertheless, OI is mainly a bone disorder and the bone-forming cells are known to produce even higher amounts of collagen type I, with a higher glycosylation level compared to fibroblasts (Sarafova et al., 1998). Indeed, how osteoblasts react to mutant collagen retention has been recently addressed using calvarial osteoblasts

from the OI knock-in murine model $\alpha 2(I)$ -G610C. The misfolded procollagen was found accumulated in the ER, causing an unusual cell stress, which was neither activating a conventional UP \mathcal{R} nor causing ER overload, although EIF2 α was found phosphorylated (Mirigian et al., 2016). Interestingly, in a more recent paper using the same OI murine model, ER-stress-related genes were found upregulated in hypertrophic chondrocytes expressing type I collagen (Scheiber et al., 2019). Further investigation in different murine models and, likely, in human osteoblasts are necessary.

For proper interpretation of our results, it should also be considered that the *in vitro* growth and expansion of the cells could have imposed an artificial ‘stress’ that we cannot exclude to have some effects on the activation of specific UP \mathcal{R} branches. Anyway, all controls and mutant cell lines were similarly expanded, likely supporting the truthfulness of the described differences. To properly translate *in vitro* data to patients, *in vivo* validation is needed. We recently demonstrated in osteoblasts from the OI zebrafish model *Chihuahua* an ER cisternae enlargement associated with mutant collagen type I synthesis and we proved that 4-PBA was indeed restoring ER cisternae size, likely favoring collagen secretion (Gioia et al., 2017). The identification of the involved pathways in mammals needs further investigation.

In conclusion, we identified ER stress as a common potential target for the treatment of recessive OI carrying mutations in components necessary for collagen post-translational modifications and for the cure of classical dominant OI. The finding that the same chemical chaperone is effective in cells synthesizing overmodified collagen increases the potential clinical use of 4-PBA for multiple OI forms.

MATERIALS AND METHODS

Human fibroblasts

Seven human primary dermal fibroblasts from skin biopsies of OI patients carrying mutations in one of the genes coding for the three members of the collagen prolyl 3-hydroxylation complex – *CRTAP* (*CRTAP*-1, *CRTAP*-2, *CRTAP*-3) (Amor et al., 2011; Caparros-Martin et al., 2013; Valli et al., 2012), *P3H1* (*P3H1*-1, *P3H1*-2 and *P3H1*-3) (Caparros-Martin et al., 2013) and *PPIB* (*CyPB*) (Caparros-Martin et al., 2013) – and three pediatric controls (Promo Cell) were obtained after informed consent and used up to passage 10 (P10) (Table 1). Cells were grown at 37°C in humidified atmosphere containing 5% CO $_2$ and cultured in Dulbecco’s modified Eagle’s medium (DMEM; 4.5 g/l glucose; Lonza) supplemented with 10% fetal bovine serum (FBS; Euroclone), 4 mM glutamine (Euroclone), 100 μ g/ml penicillin and streptomycin (Euroclone). No ascorbic acid was added to expansion media. For each experiment, except where differently stated, 2.5×10^4 cells/cm 2 were plated and harvested after 5 days with no media change. For drug treatment, cells were incubated for 15 h with 5 mM 4-PBA (Sigma-Aldrich) or with 0.96 mM TUDCA (Sigma-Aldrich). The lysosome fusion with autophagosome was blocked using 10 μ M chloroquine (Sigma-Aldrich) for 6 h.

Sequencing

Genomic DNA from *P3H1*-1 was extracted from fibroblasts by standard procedure. Exons were amplified by PCR and Sangers’ sequencing was performed.

Expression analysis

Total RNA was extracted from patients’ fibroblasts using TriReagent (Sigma-Aldrich) according to the manufacturer’s protocol. DNase digestion was performed using the Turbo DNA Free Kit (Ambion, Applied Biosystems), and RNA integrity was verified on agarose gel. cDNA was synthesized and qPCR was performed on the Mx3000P Stratagene thermocycler using Syber Green Master Mix (Applied Biosystems) with custom primers. For *CRTAP* (NM_006371.4) the forward primer was 5’-CCCAGACCTGAAGCAGTT-3 (nt 1180-1197) and the reverse

primer was 5’-TTCTCCCTCATCATCCATT-3’ (nt 1278-1257). The *PPIB* (NM_000942.4) forward primer was 5’-GGAGAGAAAGGATTGGCTAC-3’ (nt 413-433) and the reverse primer was 5’-CAGGCTGCTTACTGTCGTGA-3’ (nt 651-630). The *P3H1* (NM_001243246.1) forward primer was 5’-CGGGTGGCTGGCGGTTCCG-3’ (nt 78-96) and the reverse primer was 5’-ACCTCGGCTGGGAGGCAGC-3’ (nt 184-165). All reactions were performed in triplicate. *GAPDH* was used as normalizer. The *GAPDH* (NM_002046.5) forward primer was 5’-ATAC-CAGGAAATGAGCTTGACAAA-3’ (nt 1035-1057) and the *GAPDH* reverse primer was 5’-TCCTCTGACTTCAACAGCGACAC-3’ (nt 1130-1107). Relative expression levels were calculated using the $\Delta\Delta C_t$ method.

Protein lysates

Fibroblasts were washed and scraped in PBS, centrifuged at 1000 g for 4 min, lysed and sonicated in RIPA buffer (150 mM NaCl, 1% IGEPAL $^{\text{®}}$ CA-630, 0.5% sodium deoxycholate, 0.1% SDS, and 50 mM Tris, pH 8) supplemented with protease inhibitors (13 mM benzamide, 2 mM N-ethylmaleimide, 5 mM ethylenediaminetetraacetic acid, 1 mM phenylmethylsulfonyl fluoride and 2 mM NaVO $_3$). Proteins were quantified by RC DC Protein Assay (Bio-Rad). Bovine serum albumin (BSA) (Sigma-Aldrich) was used as standard.

Western blot

Proteins from human fibroblast lysates (10-50 μ g) were separated on SDS-PAGE with acrylamide percentage ranging from 6 to 15%, depending on the size of the analyzed protein (Table S1). The proteins were electrotransferred to a PVDF membrane (GE Healthcare) at 100 V for 2 h on ice in 19 mM Tris-HCl, 192 mM glycine and 20% (v/v) methanol. The membranes were then blocked with 5% (w/v) BSA in 20 mM Tris-HCl, 500 mM NaCl, pH 7.5 (TBS), 0.05% (v/v) Tween-20 (Sigma-Aldrich) (TBS-T) at room temperature (RT) for 1 h. After washing with TBS-T, the membranes were incubated with 1:1000 primary antibody against the specific proteins *CRTAP* (generously provided by Dr Lee Brendan, Baylor College of Medicine, TX, USA), *P3H1* (NovusBio), *CyPB* (Proteintech), *BIP* (Cell Signaling), *PERK* (Cell Signaling), *PDI* (Cell Signaling), *p-PERK* (Thr980; Cell Signaling), *LC3A/B* (Cell Signaling), cleaved caspase-3 (Cell Signaling), *ATF4* (Novus Biological), *ATF6* (Abcam) in 5% BSA in TBS-T overnight at 4°C. The appropriate secondary antibody anti-mouse (Cell Signaling), anti-rabbit (Cell Signaling) or anti-goat (Santa Cruz Biotechnology) was added at dilution of 1:2000 in 5% BSA in TBS-T for 1 h at RT. Anti- β -actin antibody (Santa Cruz Biotechnology) diluted 1:1000 in 5% BSA in TBS-T was used for protein loading normalization. The signal was detected by ECL western blotting detection reagents (GE Healthcare) and images were acquired with ImageQuant LAS 4000 (GE Healthcare), using the ImageQuant LAS 4000 1.2 software. Band intensities were evaluated by densitometry, using ImageQuant TL analysis software. For each gel, the intensity of the control band was set equal to one, and the expression of the mutant samples was expressed as fold difference. For each cell line, three independent lysates were collected and technical triplicates were performed.

Collagen analysis

Labeling of collagen with L-[2,3,4,5- 3 H]-proline (PerkinElmer) was used to evaluate collagen overmodification and secretion. A total of 2.5×10^4 fibroblasts/cm 2 were plated into 6-well plates and grown for 24 h. Cells were then incubated for 2 h with serum-free DMEM containing 4 mM glutamine, 100 μ g/ml penicillin and streptomycin, and 100 μ g/ml (+)-sodium L-ascorbate (Sigma-Aldrich) to stimulate collagen production. For steady-state experiments, the labeling was performed for 18 h in the same media using 28.57 μ Ci of 3 H-Pro/ml. For chase experiments, the labeling was performed for 4 h using 47.14 μ Ci of 3 H-Pro/ml, then the labeling media was replaced with serum-free DMEM containing 2 mM proline (Sigma-Aldrich), 4 mM glutamine, 100 μ g/ml penicillin and streptomycin, and 100 μ g/ml (+)-sodium L-ascorbate (chase media). Collagen was collected at 0.5, 1, 2 and 3 h after the chase. Collagen extraction was performed as previously reported (Forlino et al., 2019; Valli et al., 1991). Briefly, medium and cell lysate fractions were digested overnight with 100 ng/ml of pepsin in 0.5 M acetic acid at 4°C. Collagen was then precipitated using 2 M NaCl, 0.5 M acetic acid. Collagen was resuspended in Laemmli buffer (62 mM Tris-HCl, pH 6.8, 10% glycerol, 2% sodium dodecyl sulfate, 0.02% Bromophenol Blue) and

the radioactivity [counts per minute (CPM)] was measured using a liquid scintillation analyzer (PerkinElmer TRI-CARB 2300 TR).

For steady-state analyses, equal amounts of ^3H -labeled collagen from each patient's cells were loaded on 6% urea-SDS gels in a non-reducing condition. For chase analyses, the same volume of ^3H -labeled collagens from each time point was electrophoresed. The gels were fixed in 45% methanol, 9% glacial acetic acid, incubated for 1 h with enhancer (PerkinElmer, 6NE9701), washed in deionized water and dried. ^3H gel radiographs were obtained by direct exposure of dried gels to hyperfilm (Amersham) at -80°C . The radiography films were digitalized by VersaDoc 3000 (Bio-Rad). To quantify the intracellular collagen retention, the ratio between the CPM in the cell layer and the CPM in medium plus cell layer was evaluated. To quantify the percentage of collagen secretion, the ratio between the density of the $\alpha 1(\text{I})$ band in the media and the total collagen (medium plus cell layer) was evaluated by Quantity One software (Bio-Rad) (Ciccocioppo et al., 2013).

To analyze the effect of 4-PBA on collagen secretion, cells were labeled for 18 h in the absence or presence of 5 mM 4-PBA using 28.57 μCi of ^3H -Pro/ml. Collagen extraction from the media was performed as previously reported and an equal volume was loaded on the SDS-urea-PAGE. The ratio between the density of the $\alpha 1(\text{I})$ band in the medium was evaluated on the digitalized fluorography, and the value was normalized to the DNA extracted from the cell layer.

Transmission electron microscopy analysis

For transmission electron microscopy analysis, fibroblasts from controls and patients were trypsinized and centrifuged at 1000 g for 3 min. The pellet was fixed with 1% glutaraldehyde in the culture medium for 2 h at RT. The cells were rinsed in PBS and then in H_2O . Finally, the fibroblasts were fixed in 2% (w/v) OsO_4 in H_2O for 2 h at RT, rinsed in distilled water and embedded in 2% agarose. The specimens were dehydrated in acetone and finally infiltrated with epoxy resin overnight and polymerized in gelatin capsules at 60°C for 24 h. Thin sections (60–70 nm thick) were cut on a Reichert OM-U3 ultramicrotome with a diamond knife and collected on 300-mesh nickel grids. The grids were stained with saturated aqueous uranyl acetate by lead citrate and observed with a Zeiss EM900 electron microscope, operated at 80 kV with objective aperture of 30 μm .

XBPI splicing analyses

cDNA from control and patients cells was used for PCR amplification across the region of the *XBPI* cDNA (NM_005080.3) containing the intronic target of IRE1 α ribonuclease using 0.3 μM sense (nt 396–425; 5'-TCAGCTTTTACGAGAGAAAACATGGCCT-3') and antisense (nt 696–667; 5'-AGAACATGACTGGGTCCAAGTTGTCAGAA-3') primers. Following a 30 min incubation at 50°C , reactions were cycled 30 times at 94°C , 60°C and 72°C for 30 s at each temperature. Reaction products were electrophoresed on 8% TBE acrylamide gels and visualized by ethidium bromide staining.

LC3 immunofluorescence

A total of 1.5×10^4 fibroblasts were plated on sterile glass coverslips (Marienfeld) in 24-well plates in triplicate. After 5 days, cells were treated for 6 h with 10 μM chloroquine. Following the treatment, the medium was removed and cells were fixed with cold 100% CH_3OH for 15 min at -20°C , washed three times with PBS and blocked for 1 h in 1% BSA in PBS containing 0.3% Triton X-100. Then, cells were incubated with LC3 primary antibody (Cell Signaling) diluted 1:500 in 1% BSA, 0.3% Triton X-100 in PBS overnight at 4°C . Cells were washed three times with PBS and incubated with secondary antibody [Alexa-Fluor-488-conjugated F(ab') fragment anti-rabbit IgG, Immunological Sciences] diluted 1:2000 in 1% BSA, 0.3% Triton X-100 in PBS for 2 h at RT. Nuclei were stained with 4',6-diamidino-2-phenylindole (DAPI; Sigma-Aldrich). The samples were analyzed using an SP5-Leica confocal microscope (Leica). The total area of punctate signal per cell was measured by the Leica software LAS4.5.

Thioflavin-T labeling

A total of 1.5×10^4 fibroblasts were plated on sterile glass coverslips (Marienfeld) in 24-well plates. After 4 days, cells were incubated with 5 μM

Thioflavin T (ThT; Sigma-Aldrich) for 15 h in the presence or absence of 4-PBA and in the presence or absence of chloroquine. The medium was removed and cells were fixed with 4% paraformaldehyde in PBS for 20 min at RT. Nuclei were stained with DAPI (Sigma-Aldrich). The samples were analyzed using an SP8-Leica confocal microscope (Leica). The excitation and emission settings were: DAPI (Ex. MP laser 800 nm, Em. 410–530 nm), ThT (Ex. 458 nm, Em. 480–520 nm). The total area of punctate signal per cell was measured using the Leica software LAS4.5.

Fluorescence activated cell sorting (FACS)

To analyze apoptosis, the FACS Annexin V/Dead Cell Apoptosis Kit (Invitrogen) was used following the manufacturer's instructions. As positive control for the activation of apoptosis, cells were treated with 20 μM thapsigargin (Sigma-Aldrich) for 24 h in serum-free DMEM. Samples were analyzed by Cell Sorter S3 (Bio-Rad); 1×10^4 events for each sample were considered measuring the fluorescence emission at 510–540 nm and >565 nm. For autophagy inhibition, 50 μM chloroquine was used.

Protein secretion

OI patients' fibroblasts were plated in 24-well plates and labeled with 5 μCi /ml [^{35}S] EXPRESS35S Protein Labeling Mix (PerkinElmer) in DMEM without L-methionine, L-cystine and L-glutamine for 1 h at 37°C . Total proteins from medium and cell layer were precipitated with 10% trichloroacetic acid. Proteins were washed with acetone twice and resuspended in 60 mM Tris-HCl, pH 6.8, 10% sodium dodecyl sulphate. The radioactivity (CPM) of the samples was measured using a liquid scintillation analyzer (TRI-CARB 2300 TR). The percentage of protein secretion was calculated based on the ratio between the CPM in the media and the CPM in medium and cell layer, evaluated in five technical replicates.

Statistical analysis

Statistical differences between patients and controls were evaluated by two-tailed Student's *t*-test. Statistical differences between controls, patients and treated patients and between the different treatments were evaluated by one-way ANOVA using Sigma plot 11.0 (Fisher). All data passed tests for normality and equal variance. Technical triplicates were performed and values were expressed as mean \pm s.d. A *P*-value <0.05 was considered significant.

Acknowledgements

We thank Prof. Brendan Lee (College of Medicine Houston, TX, USA) for providing the anti-CRTAP antibody; Prof. Roy Morello for providing the CRTAP-3 cell line; Dr Patrizia Vaghi (Centro Grandi Strumenti, University of Pavia, Italy) for technical assistance with confocal microscopy; and Mr Angelo Gallanti for technical assistance with cell culture.

Competing interests

The authors declare no competing or financial interests.

Author contributions

Conceptualization: R.B., A.F.; Methodology: R.B., N.G., L.L., L.C., S.S., M.B.; Validation: R.B., N.G., L.L., L.C., S.S., M.B.; Formal analysis: R.B., A.F.; Investigation: R.B., A.F.; Resources: M.M., M.A., G.A.O., S.A.T., A.F.; Data curation: R.B., A.F.; Writing - original draft: R.B., A.R., A.F.; Writing - review & editing: R.B., N.G., L.L., L.C., S.S., M.B., M.M., M.A., G.A.O., S.A.T., A.R., A.F.; Supervision: A.F.; Project administration: A.F.; Funding acquisition: A.F., A.R.

Funding

The work was supported by Fondazione Cariplo [grant no. 2013-0612], Fondazione Telethon [grant no. GGP13098] and the FP7 Ideas: European Research Council "Sybil" project [grant no. 602300].

Supplementary information

Supplementary information available online at <http://dmm.biologists.org/lookup/doi/10.1242/dmm.038521.supplemental>

References

- Amor, I. M. B., Rauch, F., Gruenwald, K., Weis, M., Eyre, D. R., Roughley, P., Glorieux, F. H. and Morello, R. (2011). Severe osteogenesis imperfecta caused by a small in-frame deletion in CRTAP. *Am. J. Med. Genet. A* **155**, 2865–2870. doi:10.1002/ajmg.a.34269
- Balasubramanian, M., Sobey, G. J., Wagner, B. E., Peres, L. C., Bowen, J., Bexon, J., Javadi, M. K., Arundel, P. and Bishop, N. J. (2016). Osteogenesis

- imperfecta: ultrastructural and histological findings on examination of skin revealing novel insights into genotype-phenotype correlation. *Ultrastruct. Pathol.* **40**, 71-76. doi:10.3109/01913123.2016.1140253
- Barnes, A. M., Chang, W., Morello, R., Cabral, W. A., Weis, M. A., Eyre, D. R., Leikin, S., Makareeva, E., Kuznetsova, N., Uveges, T. E. et al. (2006). Deficiency of cartilage-associated protein in recessive lethal osteogenesis imperfecta. *N. Engl. J. Med.* **355**, 2757-2764. doi:10.1056/NEJMoa063804
- Barnes, A. M., Carter, E. M., Cabral, W. A., Weis, M. A., Chang, W., Makareeva, E., Leikin, S., Rotimi, C. N., Eyre, D. R., Raggio, C. L. et al. (2010). Lack of cyclophilin B in osteogenesis imperfecta with normal collagen folding. *N. Engl. J. Med.* **362**, 521-528. doi:10.1056/NEJMoa0907705
- Beriault, D. R. and Werstuck, G. H. (2013). Detection and quantification of endoplasmic reticulum stress in living cells using the fluorescent compound, Thioflavin T. *Biochim. Biophys. Acta* **1833**, 2293-2301. doi:10.1016/j.bbamcr.2013.05.020
- Besio, R. and Forlino, A. (2015). Treatment options for osteogenesis imperfecta. *Expert Opin. Orphan Drugs* **3**, 165-181. doi:10.1517/21678707.2015.1006197
- Besio, R., Iula, G., Garibaldi, N., Cipolla, L., Sabbioneda, S., Biggiogera, M., Marini, J. C., Rossi, A. and Forlino, A. (2018). 4-PBA ameliorates cellular homeostasis in fibroblasts from osteogenesis imperfecta patients by enhancing autophagy and stimulating protein secretion. *Biochim. Biophys. Acta* **1864**, 1642-1652. doi:10.1016/j.bbdis.2018.02.002
- Bianchi, L., Gagliardi, A., Gioia, R., Besio, R., Tani, C., Landi, C., Cipriano, M., Gimigliano, A., Rossi, A., Marini, J. C. et al. (2012). Differential response to intracellular stress in the skin from osteogenesis imperfecta Brtl mice with lethal and non lethal phenotype: a proteomic approach. *J. Proteomics* **75**, 4717-4733. doi:10.1016/j.jprot.2012.01.038
- Boot-Handford, R. P. and Briggs, M. D. (2010). The unfolded protein response and its relevance to connective tissue diseases. *Cell Tissue Res.* **339**, 197-211. doi:10.1007/s00441-009-0877-8
- Butchbach, M. E. R., Lumpkin, C. J., Harris, A. W., Saieva, L., Edwards, J. D., Workman, E., Simard, L. R., Pellizzoni, L. and Burghes, A. H. M. (2016). Protective effects of butyrate-based compounds on a mouse model for spinal muscular atrophy. *Exp. Neurol.* **279**, 13-26. doi:10.1016/j.expneurol.2016.02.009
- Cabral, W. A., Chang, W., Barnes, A. M., Weis, M. A., Scott, M. A., Leikin, S., Makareeva, E., Kuznetsova, N. V., Rosenbaum, K. N., Tiff, C. J. et al. (2007). Prolyl 3-hydroxylase 1 deficiency causes a recessive metabolic bone disorder resembling lethal/severe osteogenesis imperfecta. *Nat. Genet.* **39**, 359-365. doi:10.1038/ng1968
- Caparros-Martin, J. A., Valencia, M., Pulido, V., Martinez-Glez, V., Rueda-Arenas, I., Amr, K., Farra, C., Lapunzina, P., Ruiz-Perez, V. L., Temtamy, S. et al. (2013). Clinical and molecular analysis in families with autosomal recessive osteogenesis imperfecta identifies mutations in five genes and suggests genotype-phenotype correlations. *Am. J. Med. Genet. A* **161**, 1354-1369. doi:10.1002/ajmg.a.35938
- Chang, W., Barnes, A. M., Cabral, W. A., Bodurtha, J. N. and Marini, J. C. (2010). Prolyl 3-hydroxylase 1 and CRTAP are mutually stabilizing in the endoplasmic reticulum collagen prolyl 3-hydroxylation complex. *Hum. Mol. Genet.* **19**, 223-234. doi:10.1093/hmg/ddp481
- Ciccocioppo, R., Vanoli, A., Klersy, C., Imbesi, V., Boccaccio, V., Manca, R., Betti, E., Cangemi, G. C., Strada, E., Besio, R. et al. (2013). Role of the advanced glycation end products receptor in Crohn's disease inflammation. *World J. Gastroenterol.* **19**, 8269-8281. doi:10.3748/wjg.v19.i45.8269
- Daosukho, C., Chen, Y., Noel, T., Sompol, P., Nithipongvanit, R., Velez, J. M., Oberley, T. D. and St Clair, D. K. (2007). Phenylbutyrate, a histone deacetylase inhibitor, protects against Adriamycin-induced cardiac injury. *Free Radic. Biol. Med.* **42**, 1818-1825. doi:10.1016/j.freeradbiomed.2007.03.007
- Forlino, A. and Marini, J. C. (2016). Osteogenesis imperfecta. *Lancet* **387**, 1657-1671. doi:10.1016/S0140-6736(15)00728-X
- Forlino, A., Tani, C., Rossi, A., Lupi, A., Campari, E., Gualeni, B., Bianchi, L., Armini, A., Cetta, G., Bini, L. et al. (2007). Differential expression of both extracellular and intracellular proteins is involved in the lethal or nonlethal phenotypic variation of BrtlIV, a murine model for osteogenesis imperfecta. *Proteomics* **7**, 1877-1891. doi:10.1002/pmic.200600919
- Forlino, A., Cabral, W. A., Barnes, A. M. and Marini, J. C. (2011). New perspectives on osteogenesis imperfecta. *Nat. Rev. Endocrinol.* **7**, 540-557. doi:10.1038/nrendo.2011.81
- Forlino, A., Tonelli, F. and Besio, R. (2019). Steady-state and pulse-chase analyses of fibrillar collagen. *Methods Mol. Biol.* **1952**, 45-53. doi:10.1007/978-1-4939-9133-4_4
- Gagliardi, A., Besio, R., Carnemolla, C., Landi, C., Armini, A., Aglan, M., Otaify, G., Temtamy, S. A., Forlino, A., Bini, L. et al. (2017). Cytoskeleton and nuclear lamina affection in recessive osteogenesis imperfecta: a functional proteomics perspective. *J. Proteomics* **167**, 46-59. doi:10.1016/j.jprot.2017.08.007
- Galluzzi, L., Bravo-San Pedro, J. M., Levine, B., Green, D. R. and Kroemer, G. (2017). Pharmacological modulation of autophagy: therapeutic potential and persisting obstacles. *Nat. Rev. Drug Discov.* **16**, 487-511. doi:10.1038/nrd.2017.22
- Gioia, R., Tonelli, F., Ceppi, I., Biggiogera, M., Leikin, S., Fisher, S., Tenedini, E., Yorgan, T. A., Schinke, T., Tian, K. et al. (2017). The chaperone activity of 4PBA ameliorates the skeletal phenotype of Chihuahua, a zebrafish model for dominant osteogenesis imperfecta. *Hum. Mol. Genet.* **26**, 2897-2911. doi:10.1093/hmg/ddx171
- Green, D. R. and Levine, B. (2014). To be or not to be? How selective autophagy and cell death govern cell fate. *Cell* **157**, 65-75. doi:10.1016/j.cell.2014.02.049
- Gruenewald, K., Castagnola, P., Besio, R., Dimori, M., Chen, Y., Akel, N. S., Swain, F. L., Skinner, R. A., Eyre, D. R., Gaddy, D. et al. (2014). Sc65 is a novel endoplasmic reticulum protein that regulates bone mass homeostasis. *J. Bone Miner. Res.* **29**, 666-675. doi:10.1002/jbmr.2075
- Heard, M. E., Besio, R., Weis, M. A., Rai, J., Hudson, D. M., Dimori, M., Zimmerman, S. M., Kamykowski, J. A., Hogue, W. R., Swain, F. L. et al. (2016). Sc65-null mice provide evidence for a novel endoplasmic reticulum complex regulating collagen lysyl hydroxylation. *PLoS Genet.* **12**, e1006002. doi:10.1371/journal.pgen.1006002
- Homan, E. P., Lietman, C., Grafe, I., Lenington, J., Morello, R., Napierala, D., Jiang, M.-M., Munivez, E. M., Dawson, B., Bertin, T. K. et al. (2014). Differential effects of collagen prolyl 3-hydroxylation on skeletal tissues. *PLoS Genet.* **10**, e1004121. doi:10.1371/journal.pgen.1004121
- Hudson, D. M. and Eyre, D. R. (2013). Collagen prolyl 3-hydroxylation: a major role for a minor post-translational modification? *Connect. Tissue Res.* **54**, 245-251. doi:10.3109/03008207.2013.800867
- Ishikawa, Y. and Bächinger, H. P. (2013). A molecular ensemble in the rER for procollagen maturation. *Biochim. Biophys. Acta* **1833**, 2479-2491. doi:10.1016/j.bbamcr.2013.04.008
- Ishikawa, Y., Wirz, J., Vranka, J. A., Nagata, K. and Bächinger, H. P. (2009). Biochemical characterization of the prolyl 3-hydroxylase 1, cartilage-associated protein cyclophilin B complex. *J. Biol. Chem.* **284**, 17641-17647. doi:10.1074/jbc.M109.007070
- Lindert, U., Cabral, W. A., Ausavarat, S., Tongkobpetch, S., Ludin, K., Barnes, A. M., Yeetong, P., Weis, M., Krabichler, B., Srichomthong, C. et al. (2016). MBTPS2 mutations cause defective regulated intramembrane proteolysis in X-linked osteogenesis imperfecta. *Nat. Commun.* **7**, 11920. doi:10.1038/ncomms11920
- Mai, C. T., Le, Q. G., Ishiwata-Kimata, Y., Takagi, H., Kohno, K. and Kimata, Y. (2018). 4-Phenylbutyrate suppresses the unfolded protein response without restoring protein folding in *Saccharomyces cerevisiae*. *FEMS Yeast Res.* **18**, doi:10.1093/femsyr/foy016
- Marini, J. C. and Blissett, A. R. (2013). New genes in bone development: what's new in osteogenesis imperfecta. *J. Clin. Endocrinol. Metab.* **98**, 3095-3103. doi:10.1210/jc.2013-1505
- Marini, J. C., Cabral, W. A., Barnes, A. M. and Chang, W. (2007). Components of the collagen prolyl 3-hydroxylation complex are crucial for normal bone development. *Cell Cycle* **6**, 1675-1681. doi:10.4161/cc.6.14.4474
- Marini, J. C., Forlino, A., Bächinger, H. P., Bishop, N. J., Byers, P. H., Paeppe, A. D., Fassier, F., Fratzi-Zelman, N., Kozloff, K. M., Krakow, D. et al. (2017). Osteogenesis imperfecta. *Nat. Rev. Dis. Primers* **3**, 17052. doi:10.1038/nrdp.2017.52
- Matoori, S. and Leroux, J.-C. (2015). Recent advances in the treatment of hyperammonemia. *Adv. Drug Deliv. Rev.* **90**, 55-68. doi:10.1016/j.addr.2015.04.009
- Mirigian, L. S., Makareeva, E., Mertz, E. L., Omari, S., Roberts-Pilgrim, A. M., Oestreich, A. K., Phillips, C. L. and Leikin, S. (2016). Osteoblast malfunction caused by cell stress response to procollagen misfolding in alpha2(I)-G610C mouse model of osteogenesis imperfecta. *J. Bone Miner. Res.* **31**, 1608-1616. doi:10.1002/jbmr.2824
- Morello, R., Bertin, T. K., Chen, Y., Hicks, J., Tonachini, L., Monticone, M., Castagnola, P., Rauch, F., Glorieux, F. H., Vranka, J. et al. (2006). CRTAP is required for prolyl 3-hydroxylation and mutations cause recessive osteogenesis imperfecta. *Cell* **127**, 291-304. doi:10.1016/j.cell.2006.08.039
- Perdivara, I., Yamauchi, M. and Tomer, K. B. (2013). Molecular characterization of collagen hydroxylysine O-glycosylation by mass spectrometry: current status. *Aust. J. Chem.* **66**, 760-769. doi:10.1071/CH13174
- Pettit, R. S. and Fellner, C. (2014). CFTR modulators for the treatment of cystic fibrosis. *P. T.* **39**, 500-511.
- Pokidysheva, E., Boudko, S., Vranka, J., Zientek, K., Maddox, K., Moser, M., Fassler, R., Ware, J. and Bächinger, H. P. (2014). Biological role of prolyl 3-hydroxylation in type IV collagen. *Proc. Natl. Acad. Sci. USA* **111**, 161-166. doi:10.1073/pnas.1307597111
- Pyott, S. M., Schwarze, U., Christiansen, H. E., Pepin, M. G., Leistritz, D. F., Dineen, R., Harris, C., Burton, B. K., Angle, B., Kim, K. et al. (2011). Mutations in PPIB (cyclophilin B) delay type I procollagen chain association and result in perinatal lethal to moderate osteogenesis imperfecta phenotypes. *Hum. Mol. Genet.* **20**, 1595-1609. doi:10.1093/hmg/ddr037
- Sarafova, A. P., Choi, H., Forlino, A., Gajko, A., Cabral, W. A., Tosi, L., Reing, C. M. and Marini, J. C. (1998). Three novel type I collagen mutations in osteogenesis imperfecta type IV probands are associated with discrepancies between electrophoretic migration of osteoblast and fibroblast collagen. *Hum. Mutat.* **11**, 395-403. doi:10.1002/(SICI)1098-1004(1998)11:5<395::AID-HUMU7>3.0.CO;2-4
- Scheiber, A. L., Guess, A. J., Kaito, T., Abzug, J. M., Enomoto-Iwamoto, M., Leikin, S., Iwamoto, M. and Otsuru, S. (2019). Endoplasmic reticulum stress is induced in growth plate hypertrophic chondrocytes in G610C mouse model of

- osteogenesis imperfecta. *Biochem. Biophys. Res. Commun.* **509**, 235-240. doi:10.1016/j.bbrc.2018.12.111
- Taga, Y., Kusubata, M., Ogawa-Goto, K. and Hattori, S.** (2013). Site-specific quantitative analysis of overglycosylation of collagen in osteogenesis imperfecta using hydrazide chemistry and SILAC. *J. Proteome Res.* **12**, 2225-2232. doi:10.1021/pr400079d
- Terajima, M., Taga, Y., Chen, Y., Cabral, W. A., Hou-Fu, G., Srisawasdi, S., Nagasawa, M., Sumida, N., Hattori, S., Kurie, J. M. et al.** (2016). Cyclophilin-B modulates collagen cross-linking by differentially affecting lysine hydroxylation in the helical and telopeptidyl domains of tendon type I collagen. *J. Biol. Chem.* **291**, 9501-9512. doi:10.1074/jbc.M115.699470
- Valli, M., Mottes, M., Tenni, R., Sangalli, A., Gomez Lira, M., Rossi, A., Antoniazzi, F., Cetta, G. and Pignatti, P. F.** (1991). A de novo G to T transversion in a pro-alpha 1 (I) collagen gene for a moderate case of osteogenesis imperfecta. Substitution of cysteine for glycine 178 in the triple helical domain. *J. Biol. Chem.* **266**, 1872-1878. doi:10.1007/bf00219169
- Valli, M., Barnes, A. M., Gallanti, A., Cabral, W. A., Viglio, S., Weis, M. A., Makareeva, E., Eyre, D., Leikin, S., Antoniazzi, F. et al.** (2012). Deficiency of CRTAP in non-lethal recessive osteogenesis imperfecta reduces collagen deposition into matrix. *Clin. Genet.* **82**, 453-459. doi:10.1111/j.1399-0004.2011.01794.x
- van Dijk, F. S., Nesbitt, I. M., Zwikstra, E. H., Nikkels, P. G. J., Piersma, S. R., Fratantoni, S. A., Jimenez, C. R., Huizer, M., Morsman, A. C., Cobben, J. M. et al.** (2009). PPIB mutations cause severe osteogenesis imperfecta. *Am. J. Hum. Genet.* **85**, 521-527. doi:10.1016/j.ajhg.2009.09.001
- Vollmann, E. H., Cao, L., Amatucci, A., Reynolds, T., Hamann, S., Dalkilic-Liddle, I., Cameron, T. O., Hossbach, M., Kauffman, K. J., Mir, F. F. et al.** (2017). Identification of novel fibrosis modifiers by in vivo siRNA silencing. *Mol. Ther. Nucleic Acids* **7**, 314-323. doi:10.1016/j.omtn.2017.04.014
- Wagner, M. and Trauner, M.** (2016). Recent advances in understanding and managing cholestasis. *F1000Res* **5**, 705. doi:10.12688/f1000research.8012.1
- Wilson, R., Lees, J. F. and Bulleid, N. J.** (1998). Protein disulfide isomerase acts as a molecular chaperone during the assembly of procollagen. *J. Biol. Chem.* **273**, 9637-9643. doi:10.1074/jbc.273.16.9637

Chapter V
Early fracture healing is delayed in the $Colla2^{+/G610C}$
osteogenesis imperfecta murine model

Early Fracture Healing in OI murine model

Bone fractures healing is a biological process starting with the formation of hematoma followed by the recruitment of inflammatory cells, which are involved primarily in the innate immune response. Then a vascularization phase leads to a recruitment of skeletal stem cells, which differentiate in chondrocytes and create the cartilaginous callus. After callus formation, the stem cells are recruited to form new bone progressively substituting the cartilage template. Following this step, the bone remodelling phase takes place, involving osteoclasts, which resorb mineralized cartilage and primary bone (Morgan, De Giacomo, and Gerstenfeld 2014).

The uncoupling between bone formation and resorption process, as well as impaired osteoblasts differentiation and increased osteoclasts activity, are typical of bone diseases (Rauch et al. 2000; Uveges et al. 2008; Li et al. 2010). Thus, a deep knowledge of the bone healing and bone formation will have great impact both in helping patients fracture care and in understanding OI bone biology.

The investigation of bone healing in OI patients is a difficult task, due to the invasiveness required to deeply evaluate this process at organ, tissue, and cellular levels. In particular, the early healing steps characterized by cartilaginous callus formation cannot be followed either by radiography or by quantitative tomography without the help of appropriate contrast agents (Kulmala et al. 2010). Therefore, OI animal models could represent the valid tool to better understand the healing process of the bone fractures healing.

Colla2^{+/*G610C*}, also known as Amish mouse, has a moderate severe OI, caused by a glycine substitution in the $\alpha 2(I)$ chain and represents a valid model for classical dominant OI (Daley et al. 2010; Masci et al. 2016). Morphometric, μ CT, histological, and biochemical approaches were used for a deep investigation of early and late steps of bone healing after tibia fracture. At 2 weeks post fracture (wpf), the *Colla2*^{+/*G610C*} mice showed a smaller callus, bone surface and bone volume with respect to WT mice. Furthermore at 2 wpf, histological analysis revealed a significant increment of cartilaginous tissue associated to reduce bone in mutant compared to WT littermates, indicating an impaired healing process. Moreover, the biochemical analysis of collagen extracted from callus at 2 wpf revealed in mutants an

increased amount of type II cartilage specific collagen instead of type I bone specific collagen.

In conclusion, this mouse model showed a delay in the initial phase of bone fracture repair probably due to a reduced osteoblastic differentiation of the stem cells recruited at the fracture site following the formation of the cartilage callus. This finding can be of great impact and suggest the use of osteoblastic differentiation stimulating drugs during OI patients fractures healing process

During the first year of my PhD I contributed to the revision of the Besio and Maruelli et al. 2018 manuscript.



Early Fracture Healing is Delayed in the *Col1a2*^{+G610C} Osteogenesis Imperfecta Murine Model

Roberta Besio¹ · Silvia Maruelli¹ · Severine Battaglia² · Laura Leoni¹ · Simona Villani³ · Pierre Layrolle² · Antonio Rossi¹ · Valerie Trichet² · Antonella Forlino¹

Received: 15 May 2018 / Accepted: 30 July 2018 / Published online: 3 August 2018
© Springer Science+Business Media, LLC, part of Springer Nature 2018

Abstract

Osteogenesis imperfecta (OI) is a rare heritable skeletal dysplasia mainly caused by type I collagen abnormalities and characterized by bone fragility and susceptibility to fracture. Over 85% of the patients carry dominant mutations in the genes encoding for the collagen type I $\alpha 1$ and $\alpha 2$ chains. Failure of bone union and/or presence of hyperplastic callus formation after fracture were described in OI patients. Here we used the *Col1a2*^{+G610C} mouse, carrying in heterozygosis the $\alpha 2(I)$ -G610C substitution, to investigate the healing process of an OI bone. Tibiae of 2-month-old *Col1a2*^{+G610C} and wild-type littermates were fractured and the healing process was followed at 2, 3, and 5 weeks after injury from fibrous cartilaginous tissue formation to its bone replacement by radiography, micro-computed tomography (μ CT), histological and biochemical approaches. In presence of similar fracture types, in *Col1a2*^{+G610C} mice an impairment in the early phase of bone repair was detected compared to wild-type littermates. Smaller callus area, callus bone surface, and bone volume associated to higher percentage of cartilage and lower percentage of bone were evident in *Col1a2*^{+G610C} at 2 weeks post fracture (wpf) and no change by 3 wpf. Furthermore, the biochemical analysis of collagen extracted from callus 2 wpf revealed in mutants an increased amount of type II collagen, typical of cartilage, with respect to type I, characteristic of bone. This is the first report of a delay in OI bone fracture repair at the modeling phase.

Keywords Osteogenesis imperfecta · Fracture repair · Callus · μ CT · Collagen

Roberta Besio and Silvia Maruelli have contributed equally to this work.

Electronic supplementary material The online version of this article (<https://doi.org/10.1007/s00223-018-0461-x>) contains supplementary material, which is available to authorized users.

✉ Antonella Forlino
aforlino@unipv.it

Roberta Besio
roberta.besio@unipv.it

Silvia Maruelli
silvia.maruelli01@universitadipavia.it

Severine Battaglia
severine.battaglia@univ-nantes.fr

Laura Leoni
laura.leoni02@universitadipavia.it

Simona Villani
simona.villani@unipv.it

Pierre Layrolle
pierre.layrolle@univ-nantes.fr

Antonio Rossi
antrossi@unipv.it

Valerie Trichet
valerie.trichet@univ-nantes.fr

¹ Department of Molecular Medicine, Biochemistry Unit, University of Pavia, Via Taramelli 3B, 27100 Pavia, Italy

² INSERM, UMR 1238, PHY-OS, Bone sarcomas and remodeling of calcified tissues, Faculty of Medicine, University of Nantes, Nantes, France

³ Department of Public Health and Experimental and Forensic Medicine, Unit of Biostatistics and Clinical Epidemiology, University of Pavia, Pavia, Italy

the patients carry dominant mutations in the *COL1A1* or *COL1A2* gene, encoding for the collagen $\alpha 1(I)$ or $\alpha 2(I)$ chains, respectively, responsible for quantitative or qualitative type I collagen alterations. Recessive and X-linked mutations have also been described in the more recently identified OI forms, due to mutations in proteins important for type I collagen post-translational modifications, secretion, processing, or for osteoblasts activity and/or differentiation [2]. Thus, OI is a molecular heterogeneous group of diseases, but all forms share several common clinical features such as growth delay, skeletal deformity, and bone fragility associated to susceptibility to fracture even in the absence of trauma [2]. The management of multiple fractures and the related pain are among the main challenges the OI patients need to face throughout life [3, 4].

Bone healing is a well-characterized biological process starting, soon after injury, with the initial formation of a hematoma followed by the recruitment of inflammatory cells, involved primarily in the innate immune response. Soon after, a vascularization phase guarantees the recruitment of skeletal stem cells differentiating in chondrocytes, which create the cartilaginous callus. Then, cartilage is progressively substituted by primary bone formation, in which stem cells are recruited to form bone. Following this modeling phase, bone remodeling, involving osteoclasts, takes place, during which osteoclasts resorb mineralized cartilage and primary bone [5]. These steps happen sequentially, although with a certain overlap, as it can be expected considering the number of different cell types involved in the process and the complexity of signaling factors regulating vascularization, cell recruitment, and differentiation [6]. Healing time is variable depending on fracture site and age of the patient. The persistence of the fractured line and the small size or absence of the callus may indicate the occurrence of healing at much slower rate than normal [7]. Diseases, such as OI, characterized by uncoupling between bone formation and resorption, as well as by impaired osteoblasts differentiation and increased osteoclasts activity, may indeed be associated to alterations of fracture repair [8–10].

Since fracture healing is in general referred as normal in OI patients, bone repair has been very poorly investigated. Nevertheless, osteotomies and non-union fractures are not rare events in OI (prevalence 15–20%) [11, 12]. Several reports had been published describing failure of bone union in OI patients and/or presence of hyperplastic callus formation [11–17]. Also, a delay in osteotomy union was reported following administration of bisphosphonate [18], the most common drug used for OI treatment [19]. Furthermore, the use of a modified Radiographic Union Score for Tibial Fractures (RUST) has been recently proposed to better evaluate osteotomy and fracture union in the setting of OI [20].

A deep investigation of bone healing in OI will be useful not only to better characterize the main clinical outcome of

the patients, but also to appropriately evaluate the goodness of the available treatment options and likely to identify new ones. To date, the available information addressing OI fracture repair at organ, tissue, cell, and molecular levels comes from very few studies performed in two OI murine models, in which fracture healing was used as model for bone modeling and remodeling in order to evaluate the effect of bisphosphonates or anti-RANKL antiresorptive treatments [21, 22]. Of note, several animal models for classical dominant as well as recessive OI forms are now available [23] and murine background and type of causative mutation can indeed affect bone repair. Thus, the investigation of different models offers the opportunity to reproduce the heterogeneity of the patients' population. To this purpose, we evaluated the healing process in a third OI model for dominant OI and we compared the data to the ones available in the literature. We studied the *Colla2*^{+G610C} mouse, carrying in heterozygosis the $\alpha 2(I)$ -G610C substitution [24]. Tibiae of *Colla2*^{+G610C} and WT littermates were fractured at 2 months of age and the healing process was analyzed at 2, 3, and 5 weeks after injury by means of complementary radiography, μ -computed tomography, histological and biochemical methods.

Materials and Methods

Mouse Strain and Genotyping

The *Colla2*^{+G610C} mice (CD1/CH3/B6), carrying in heterozygosis the G610C substitution in the $\alpha 2$ chain of type I collagen, were kindly provided by Prof Charlotte Phillips, University of Missouri-Columbia, USA [24]. Littermates were used as controls. The animals were housed in the animal facility of the Department of Molecular Medicine, University of Pavia. All the experiments were approved by the OPBA (Office for the Animals Welfare) of the University of Pavia and by the Italian Ministry of Health (protocol n. 1116/2015-PR, 21/10/2015), complied with the ARRIVE guidelines and carried out in accordance with the EU Directive 2010/63/EU for animal experiments. Genomic DNA was extracted from tail clip and genotyping was performed by PCR as previously described [24].

Study Design

Following the validation of the fracture system on WT (CD1/CH3/B6) mice (Supplementary Methods, Supplementary Results, Supplementary Fig. 1), males *Colla2*^{+G610C} and wild-type (WT) littermates obtained from matings of heterozygous male or female *Colla2*^{+G610C} with WT mice were used for the study. The animals were divided in 3 groups ($n = 7/9$ mice for each group) and were subjected to surgery at 2 months of age. Before surgery, the mice

were anesthetized with Zooletil (40 mg/kg) intramuscularly administered after local lidocaine treatment. After shaving and disinfection, a small skin cut was made in the knee joint region in order to visualize the proximal tibia epiphysis. A non-locked intramedullary pin (Fine Science Tools Austerlitz insect pins FST-26000-25) was inserted in an anterograde manner in the intramedullary canal of both tibiae. The injury was sutured with a resorbable suture thread (Ethicon). Using a home-made device, which exploits a three-point force theory, a bilateral composed fracture approximately at ¼ of distance from the distal proximity of the mice tibiae was performed. All the animals were allowed full weight bearing and unrestricted activity after awakening from anesthesia and they were able to ambulate independently. Mice were sacrificed by cervical dislocation 2, 3, and 5 weeks post fracture (wpf).

X-Rays

Lateral radiographs with the hindlimbs in external rotation were performed post-surgery to ensure the correct positioning of the pin and to categorize the fracture pattern as oblique, transverse, or comminuted, following the classification system of the Orthopaedic Trauma Association [25]. After sacrifice at the indicated time points from surgery, tibiae were harvested bilaterally and carefully cleaned from soft tissues. Digital radiographs (Faxitron X-ray corporation) were obtained in the mediolateral plane. Callus perimeter and callus area were measured using Leica application suite V 4.5. No spontaneous fractures were detected in the experimental mice.

Micro-Computed Tomography Analysis

One fractured tibia from each mouse (WT $n=8$, *Col1a2^{+G610C}* $n=7$ at 2 wpf; WT $n=9$, *Col1a2^{+G610C}* $n=7$ at 3 wpf; WT $n=8$, *Col1a2^{+G610C}* $n=8$ at 5 wpf) was dissected, cleaned from soft tissues, fixed in 4% paraformaldehyde (PFA) for 24 h, washed with phosphate buffered saline (PBS), and stored at 4 °C until analysis. The tibiae were scanned at a pixel size of 9 µm with the SkyScan1076 *in-vivo* micro-CT (Bruker). The X-ray tube voltage was set at 49 kV and the X-ray intensity was 200 µA. Each tibia was scanned in air, and an aluminum filter was used to remove image noise. Average scan duration was 21 min with 360° of rotation. The ring artifact correction was 6, and the beam hardening correction was 10%.

Bone parameters were calculated using the Skyscan CT Analyzer (CTAn) software. Using this software, the volume of interest was manually defined as callus formation. Binarized images were performed: an upper threshold of 255 and a lower threshold of 35 were used to delineate each pixel as “bone” or “non-bone.” A set of 2 hydroxyapatite (HA)

phantoms was scanned and used for calibration to Bone Mineral Density (BMD), Bone Surface (BS), Bone Volume (BV), Total Volume (TV), BV/TV, Intersection Surface (IS), BS/BV, BS/TV, and BMD were evaluated.

Histological Analysis

For histological studies, fractured tibiae at 2 (WT $n=9$, *Col1a2^{+G610C}* $n=7$), 3 (WT $n=8$, *Col1a2^{+G610C}* $n=8$) and 5 wpf (WT $n=7$, *Col1a2^{+G610C}* $n=8$) were dissected and cleaned from surrounding connective tissue. Intramedullary pins were removed prior to fixation in 4% PFA in PBS for 24 h. Bones were then decalcified in 14% EDTA pH 7.1 for 21 days and embedded in paraffin following standard procedures. Longitudinal tibia sections (7 µm) were cut using a RM2265 microtome (Leica Microsystems srl), mounted on Superfrost Plus slides (Menzel-Glaser, VWR), and stained with Alcian Blue Hematoxylin and Orange G/Eosin Counterstain [26]. Images were acquired using a DFC480 digital camera (Leica Microsystems srl) connected to a light microscope (DM5500B, Leica, Microsystems srl). To achieve a whole callus view, 5X magnification images of portions of the callus were acquired and merged by the Leica software LAS 4.5. The amount of cartilage was measured by quantitation of the proteoglycan staining, which appeared as blue color, whereas the amount of bone was evaluated by measuring the amount of red color staining the type I collagen matrix. The blue and red areas were automatically quantified using Leica application suite V 4.5, while the callus area was manually defined. Five sections of the inner part of the callus were analyzed for each mouse. The pin hole was considered as the reference position to ensure the comparison of the same region of the callus in the different samples. The cartilage and bone amount were expressed as percentage of the total callus area.

Collagen Analysis

For protein analysis, collagen was extracted from callus at 2 wpf (WT $n=13$, *Col1a2^{+G610C}* $n=12$) and at 3 wpf (WT $n=6$, *Col1a2^{+G610C}* $n=8$). The callus, cleaned from surrounding soft tissue, was washed in PBS and minced after pin removal. The sample was then decalcified in 0.5 M EDTA pH 7.1 at 4 °C for 7 days, changing the solution every other day. Collagen was extracted by means of pepsin digestion. Briefly, after wash with PBS, the bone chips were digested with 0.1 mg/ml pepsin in 0.5 M acetic acid at 4 °C for 7 days. The collagen was precipitated with 0.9 M NaCl in 0.5 M acetic acid, washed in 70% EtOH and lyophilized. The pellet was resuspended in 0.5 M acetic acid and 5 µl was lyophilized and resuspended in 10 µl of 1 X Laemmli buffer (62.5 mM Tris HCl, pH 6.8, 10% glycerol, 2% sodium dodecyl sulfate (SDS), 0.02% bromophenol blue), denatured

at 80 °C for 5 min, and run on 6% polyacrylamide-urea-SDS gels (SDS-Urea-PAGE). The gel was stained with Coomassie Picric Staining [27] and acquired by Versadoc (Biorad). The band intensity was measured using Quantity one software (Biorad). Based on the results obtained from the 1D SDS-Urea-PAGE, an equal amount of each sample was loaded to obtain an equal loading for all the samples. The gel was then stained with Coomassie Blue. The $\alpha 1(I)$ band was cut and digested for 2 h with a solution 25% cyanogen bromide (CNBr) and 75% formic acid under steering. The band was then washed with water, incubated with 1 X Laemmli buffer for 10 min at 90 °C, and loaded on 12% SDS-Urea-PAGE. The gel was stained with Coomassie Picric Staining and acquired by Versadoc (Biorad). The intensity of the bands corresponding to the collagen CB peptides $\alpha 1(II)$ -CB10 and $\alpha 1(I)$ -CB6 was determined using Quantity one software (Biorad). For the identification of the exact position in SDS-Urea-PAGE of CB10 peptide of type II collagen [$\alpha 1(II)$ -CB10] and of the CB6 peptide of type I collagen [$\alpha 1(I)$ -CB6] in our samples, type II and type I collagens were extracted from calf cartilage and murine tail, respectively, and digested by cyanogen bromide. The type II and type I collagens CB bands identified on SDS-Urea-PAGE were used as reference standard for our callus samples.

Statistical Analysis

Categorical variables were reported as percentages. Quantitative variables were expressed as mean \pm standard deviation (SD). One-way repeated measures ANOVA was applied to evaluate changing during time after fracture (2, 3, 5 wpf) within each genotype (WT and *Colla2*^{+/*G610C*}) followed by post hoc tests with the Bonferroni's correction for multiple comparisons. Similarly, two-way repeated measures ANOVA was used to analyze differences between the two genotypes at the different time after fracture, followed by post hoc contrast, if it was indicated. If the sphericity assumption of ANOVA was violated, the opportune correction on degrees of freedom was used (Greenhouse-Geisser

[GG] or Huynh-Feldt [HF]). When necessary, parametric or equivalent non-parametric unpaired t test (Mann-Whitney) was applied.

A $p < 0.05$ was considered significant, apart from the post hoc contrast analysis in which the correction for multiple comparison tests was used (assuming $k = 3$ contrast: $p \leq 0.017$). The analyses were performed using STATA 14®.

Results

Bilateral fractures of tibiae from *Colla2*^{+/*G610C*} and control mice were performed after the insertion of a steel pin in the medullary canal to generate a comminuted fracture associated to endochondral ossification [28]. Tibiae were then collected 2, 3, and 5 weeks post fracture (wpf) to evaluate the healing process (Fig. 1).

Post-Fracture Radiographs Revealed a Smaller Callus Area in the Early Phase of the Healing Process in *Colla2*^{+/*G610C*}

X-rays performed after surgery showed no difference in the type of fracture, namely comminuted (WT: 3.85%, *Colla2*^{+/*G610C*}: 4.17%), oblique (WT: 42.30%, *Colla2*^{+/*G610C*}: 41.66%), or transverse (WT: 53.85%, *Colla2*^{+/*G610C*}: 54.17%) between mutant and WT (Fig. 2a).

Callus perimeter and area were evaluated on lateral X-rays of both legs 2, 3, and 5 wpf (Fig. 2b). The perimeter was similar in mutant and WT mice at all examined time points (Fig. 2c). However, a different change over time was observed in WT and mutant mice ($F_{2,34} = 2.74$, p for interaction with HF correction = 0.08). Interestingly, WT mice showed a significant linear decline in the callus perimeter over the time ($p = 0.0006$) (Fig. 2c, Supplementary Fig. 2a) that was not present in *Colla2*^{+/*G610C*} animals ($p > 0.05$ both for linear and quadratic effect).

Callus area was significantly smaller in *Colla2*^{+/*G610C*} mice with respect to WT littermates only at 2 wpf

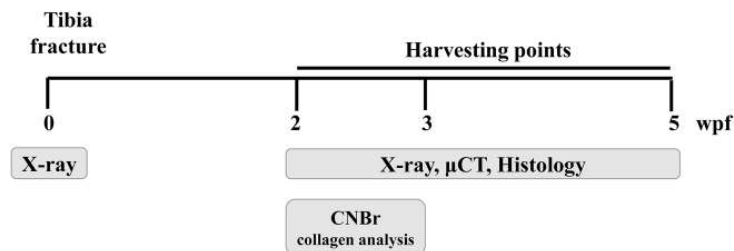


Fig. 1 Study design. A total of 45 WT and 43 *Colla2*^{+/*G610C*} mice underwent surgery at 2 months of age. Mice were sacrificed and calluses collected 2, 3, and 5 weeks post fracture (wpf) for X-ray, μ CT,

and histology. Cyanogen Bromide (CNBr) collagen analyses was performed on calluses collected at 2 and 3 wpf

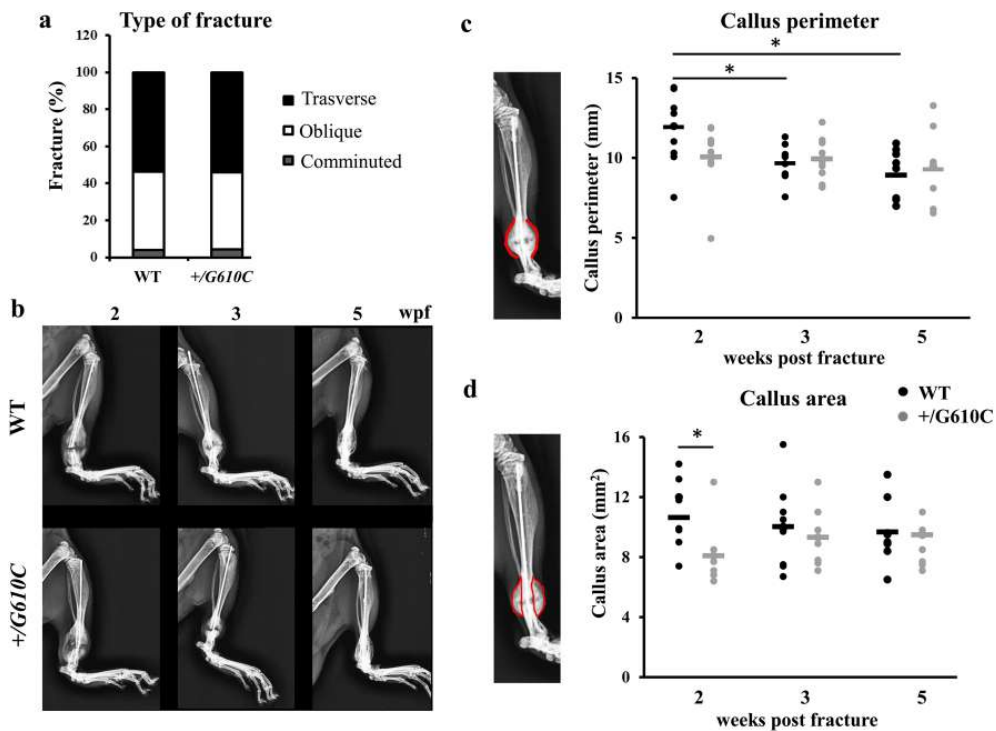


Fig. 2 X-ray analysis of the tibiae fracture healing. **a** Analyses of the type of fracture. **b** Representative X-ray images of the tibia healing process 2, 3, and 5 weeks post fracture (wpf) in WT and *Col1a2*^{+G610C} mice. **c, d** Measurement of the callus perimeter and

area 2, 3, and 5 wpf. Perimeter and area are indicated by red lines in the representative images on the left of the panels. * $p < 0.05$. (Color figure online)

($8.09 \pm 2.27 \text{ mm}^2$ and $10.64 \pm 2.26 \text{ mm}^2$, respectively; $MW = 2.3$, $p = 0.02$) and similar at 3 and 5 wpf (Fig. 2d). Of note, a decreased trend of callus area was evident only in WT animals although without reaching significance.

μ CT Analysis of Tibiae Callus Revealed a Delayed Healing Process in *Col1a2*^{+G610C}

Micro-Computed Tomography (μ CT) was performed to evaluate the callus properties during the healing process (Fig. 3a–c). One tibia from each mouse ($n = 7–9$ per genotype and time point) was used. No differences were detectable at the last time point (5 wpf) for any of the analyzed parameters. Significant differences were instead identified 2 and 3 wpf.

In *Col1a2*^{+G610C}, the bone surface (BS) was significantly smaller compared to WT 2 wpf (*Col1a2*^{+G610C}: $231.44 \pm 92.81 \text{ mm}^2$, WT: $343.34 \pm 99.21 \text{ mm}^2$; $MW = 2.08$, $p = 0.037$), whereas a significant increase was detectable 3 wpf (*Col1a2*^{+G610C}: $409.58 \pm 105.39 \text{ mm}^2$; WT: $289.82 \pm 74.98 \text{ mm}^2$; $MW = -2.38$, $p = 0.017$) (Fig. 3c).

BS showed a different modification over time in WT and *Col1a2*^{+G610C} mice ($F_{2,27} = 8.74$, p for interaction with HF correction = 0.0012). In WT, the change was not relevant ($p > 0.05$), while in *Col1a2*^{+G610C} the bone surface was higher at 3 wpf with respect to 2 wpf ($p = 0.001$) (Supplementary Fig. 2b).

Similarly, a smaller bone volume (BV) was present 2 wpf in mutant mice compared to WT (*Col1a2*^{+G610C}: $6.65 \pm 2.92 \text{ mm}^3$; WT: $11.81 \pm 4.073 \text{ mm}^3$; $MW = 1.97$, $p < 0.05$) (Fig. 3c).

Time after fracture and genotype had an independent effect on bone volume ($F_{2,26} = 2.26$, p for interaction with HF correction = 0.13). Only in *Col1a2*^{+G610C} animals, BV significantly increased from 2 to 3 wpf ($p = 0.007$) (Supplementary Fig. 2c). Of note, the trend of both BS and BV was opposite in mutant compared to WT. In mutant animals, the smaller callus BS and BV at 2 wpf suggest a delay in the bone healing process.

BS/BV, representing the ratio of bone surface to the bone volume also called specific bone surface, was significantly larger in *Col1a2*^{+G610C} compared to WT

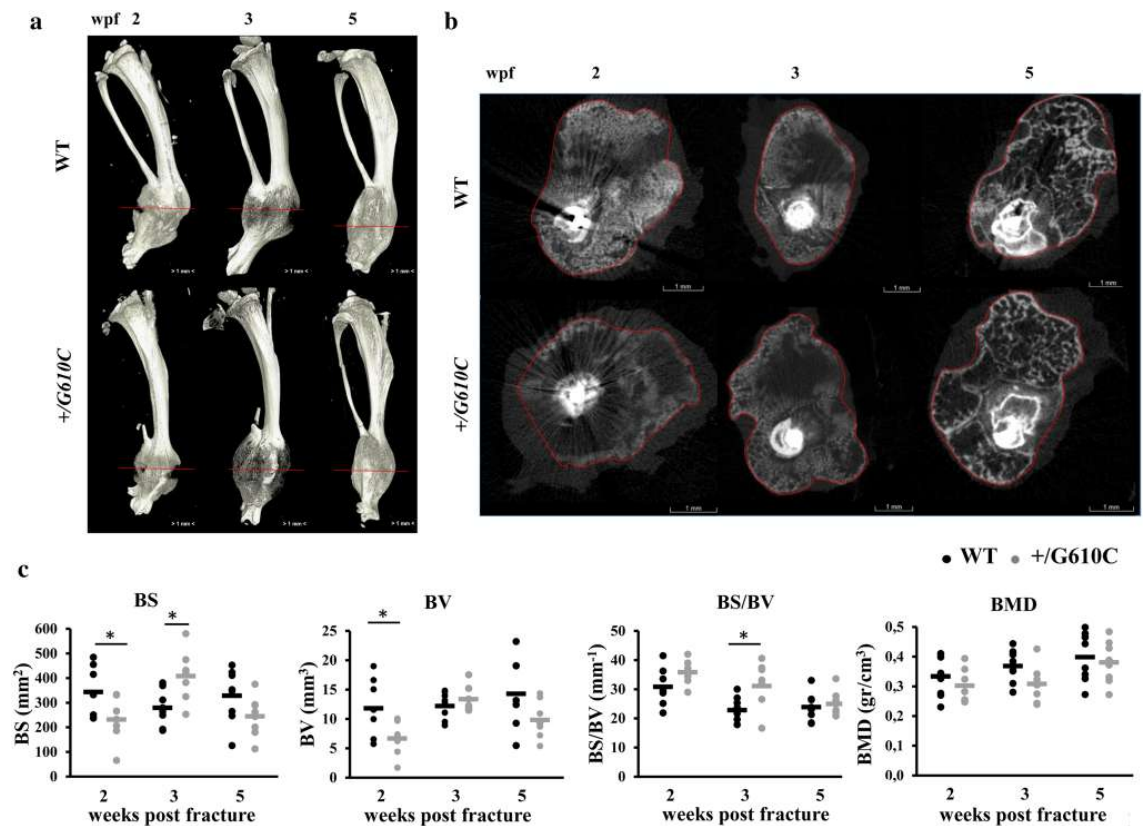


Fig. 3 Callus structural properties evaluated by μ CT. μ CT analyses of callus 2, 3, and 5 weeks after fracture ($n=7-9$ per time point and genotype). (a) Representative μ CT whole tibia scans. Red lines indicate the position of the transaxial images shown in panel B. (b)

Representative μ CT transaxial images of the middle of the callus. (c) Quantitation of the bone surface (BS), bone volume (BV), BS/BV, and bone mineral density (BMD) at 2, 3, and 5 weeks post fracture (wpf). * $p < 0.05$. (Color figure online)

mice 3 wpf ($Col1a2^{+/G610C}$: $31.03 \pm 8.53 \text{ mm}^{-1}$; WT: $22.78 \pm 3.73 \text{ mm}^{-1}$; $MW = -2.17$ and $p = 0.03$) (Fig. 3c).

Time and genotype showed an independent effect on BS/BV ($F_{2,26} = 11.38$, $p = 0.0003$) that was linearly decreased only in mutant mice ($p = 0.0006$) and U-shaped in WT ($p = 0.013$). In mutant animals, BS/BV at 5 wpf was significantly decreased with respect to 2 wpf ($p = 0.001$) and with respect to 3 wpf ($p = 0.024$). In WT animals, the BS/BV significantly declined at 5 wpf ($p = 0.003$) and at 5 wpf ($p = 0.012$) compared to 2 wpf, but no difference was detectable between 3 and 5 wpf (Supplementary Fig. 2d).

The bone mineral density (BMD) was similar in $Col1a2^{+/G610C}$ and WT mice at all examined time points. An overall significant linear trend in time was found ($F_{2,26} = 5.12$, $p = 0.013$) for WT ($p = 0.047$) as well as for mutant mice ($p = 0.022$) (Fig. 3c).

Quantitative Histology Confirmed the Delayed Healing in $Col1a2^{+/G610C}$

During fracture healing, cartilage is progressively substituted by bone, and thus callus at 2, 3, and 5 wpf underwent histological evaluation to follow this process. Alcian Blue Hematoxylin and Orange G/Eosin staining [26] was used to specifically stain cartilage (blue) and bone (red) in callus sections from mutant and WT mice (Fig. 4a, Supplementary Fig. 3).

At 2 wpf, the percentage of cartilage in $Col1a2^{+/G610C}$ was larger compared to WT ($Col1a2^{+/G610C}$: $46.04 \pm 8.27\%$; WT: $32.70 \pm 15.78\%$, $p = 0.06$), whereas the percentage of bone was significantly smaller ($Col1a2^{+/G610C}$: $17.15 \pm 7.66\%$; WT: $28.83 \pm 8.14\%$, $p < 0.05$) (Fig. 4b, c). No difference at the other time points was detected.

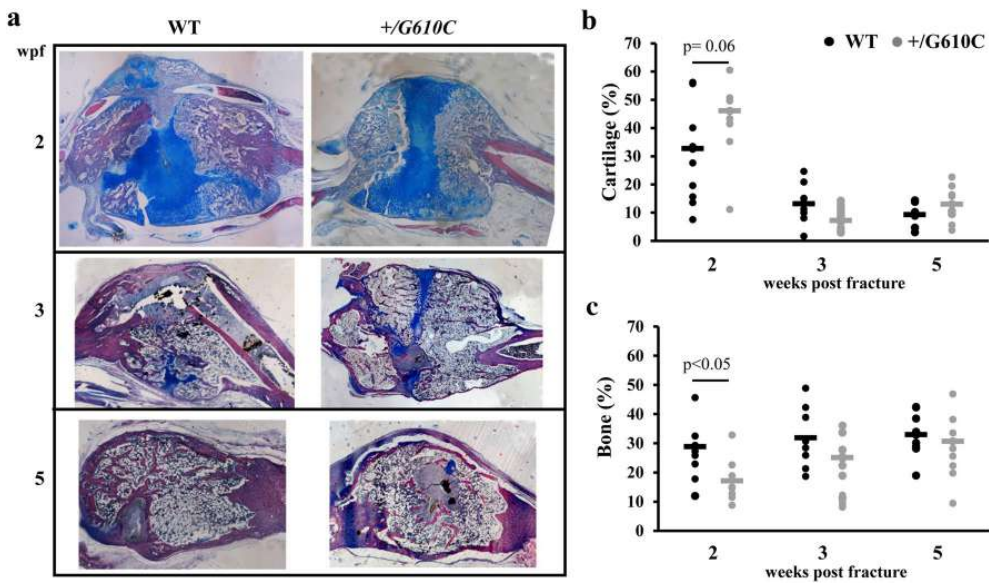


Fig. 4 Callus histological analysis during the healing process. **a** Representative images of the Alcian Blue, Hematoxylin Orange G staining of WT and *Col1a2*^{+G610C} callus sections at 2, 3, and 5 weeks after fracture staining cartilage and bone, respectively ($n=7$ per time point and genotype). The amount of cartilage was measured by quan-

titation of the proteoglycan staining, which appears as blue color (**b**), whereas the amount of bone was evaluated by measuring the amount of red color staining the type I collagen matrix (**c**). (Color figure online)

A significant difference in time between genotypes was found for cartilage percentage ($F_{2,26}=8.46$, p for interaction with HF correction = 0.0015). In WT mice, the percentage of cartilage linearly decreased ($p=0.0002$) and the decline was significant from 2 wpf both to 3 and 5 wpf ($p<0.005$). On the contrary, in mutant animals the percentage of cartilage showed a marked U-shaped variation in time ($p<0.00005$) (Supplementary Fig. 2e).

The data supported again a compromised early phase bone healing in mutant compared to control demonstrated by a delay in fibrous cartilaginous callus substitution with bone tissue.

CNBr Collagen Peptides Analysis Showed a Prevalence of Collagen II in *Col1a2*^{+G610C} Callus

To confirm the delay in the early phase of fracture healing observed by μ CT and histological evaluation, the fibrillar collagens present at callus site were quantified. The main collagens in cartilage and bone are type II and type I collagen, respectively. Both collagens were extracted from callus following bone demineralization by means of pepsin digestion. SDS-Urea-PAGE was used to separate the monomer α chains of the collagen types, namely $\alpha 1(I)$, $\alpha 2(I)$, and $\alpha 1(II)$. Since the $\alpha 1(II)$ and $\alpha 1(I)$ chains are known to migrate together, the band was cut and in gel-digested using

cyanogen bromide (CNBr). A peculiar feature of collagen α chains is to have a discrete number of methionine residues in the triple helical domain that, following digestion using CNBr, generate a CNBr peptides map specific for the various collagen types [29]. The CNBr peptides derived from the $\alpha 1(I)$ and $\alpha 1(II)$ chains are different (Fig. 5a). Following in gel-digestion, the $\alpha 1$ band was loaded in a second SDS-Urea-PAGE to discriminate the different CB peptides (Fig. 5b). To evaluate the amount of cartilaginous tissue in the callus, the intensity of the peptide bands corresponding to the cyanogen bromide peptide 10 (CB10) specific for the $\alpha 1(II)$ and the CB6 belonging to $\alpha 1(I)$ were evaluated and their ratio calculated. The $\alpha 1(II)$ -CB10/ $\alpha 1(I)$ -CB6 ratio was significantly higher in mutant with respect to control samples (*Col1a2*^{+G610C}: 5.34 ± 3.68 ; WT: 2.45 ± 1.27 , $p<0.05$) 2 weeks after fracture. No differences were detected 3 weeks after fracture further confirming a delay limited to the early bone repair phase (Fig. 5c).

Discussion

Osteogenesis imperfecta patients face multiple fractures during their life due to the extreme fragility of their skeleton and to the frequent osteotomies required for rodding their long bones in order to improve bone strength and ameliorate their

to favor fracture healing [35]. Interestingly, transgenic mice with enhanced osteoblast differentiation are also characterized by accelerated fracture repair [36]. Of note, in support of our hypothesis Mirigian LS et al reported an impairment of *Col1a2^{+G610C}* stem cell differentiation toward mature osteoblasts [37].

On the other hand, a similar impaired osteoblastogenesis was described also *in vitro* in the OI *Brtll/+* [38] and *oim/oim* mice [10], but in these models no early delay in fracture healing was described [21, 22]. Of course the type of mutation can account for such differences. In *Brtll/+* mice, the glycine substitution is in the $\alpha 1(I)$ chain (G349C) and more toward the first half of the type I collagen trimer with respect to *Col1a2^{+G610C}* mice bearing the mutation at the glycine 610 of the $\alpha 2(I)$. In *oim/oim*, the mutation impairs the incorporation of the $\alpha 2(I)$ in the trimer.

Also the site and type of bone fracture may be relevant for the healing process. In *oim/oim*, an open transverse osteotomy was obtained at the mid-shaft of the femur, whereas in *Brtll/+* and *Col1a2^{+G610C}* the fracture occurred at the tibia although in mid-position in *Brtll/+* and toward the proximal end in *Col1a2^{+G610C}*. Another important difference between our study and the previous ones is the presence of bilateral versus unilateral fracture.

The three OI murine models analyzed are in different genetic backgrounds, being *oim/oim* in B6C3FeF1/J, *Brtll/+* in a mixed outbred strain C57Bl/6J, FVBN, and CD-1, and the *Col1a2^{+G610C}* in a mix CD1/CH3/B6. We cannot exclude a role of the mouse genetic background in determining the fracture healing differences, and this will definitely need to be considered in human patients. Indeed, mice of different strains are reported to have differences in skeletal properties and this affect also bone repair [39, 40].

Also, we cannot exclude that the delay in the early repair phase detected in *Col1a2^{+G610C}* mice was not recognized in *Brtll/+* and *oim/oim* mice due to technical limitations. Indeed, only histological evaluation was used in the previous studies to determine cartilage persistence in the callus. Given the well-recognized heterogeneous and asymmetrical nature of the callus tissues, histological analysis alone may not provide definitive results. The biochemical analysis used in our study to evaluate the collagen type composition in callus is definitely a complementary and more quantitative analysis since it overcomes the problem of tissue heterogeneity.

Another issue to be considered is the effect of different dyes used to stain cartilage/bone tissue. In the *oim/oim* study, Alcian Blue was used to stain cartilage, whereas in *Brtll/+* and in *Col1a2^{+G610C}* Sufranin-O/Fast Green and Alcian Blue/Orange G staining were used, respectively. Different sensitivities have been reported for the different staining dyes, but a direct comparison among these three has not been reported yet [41].

We did not detect any difference in the type of fracture obtained in mutant and WT littermates, similar to what was observed in *Brtll/+* mice, a model of similar OI severity. On the contrary, the bone of the *oim/oim* mouse, a model for a more severe OI, revealed a higher percentage of shredding following osteotomy and indeed in this model spontaneous fractures are also normally present.

In conclusion, our results showed for the first time a delay in the early phase of OI bone fracture repair possibly due to impaired osteoblastic differentiation of the stem cells recruited at the fracture site following cartilaginous callus formation. This finding can be of great value to better take care of fracture in OI patients pointing to the possible use of drug or biomaterials stimulating osteoblastic differentiation together with the general procedure adopted for OI fracture fixation or during osteotomy.

Acknowledgements The work was supported by Care4BrittleBone (2015-0003) and the European Community, FP7, ‘Sybil’ project (Grant No. 602300).

Compliance with Ethical Standards

Conflict of interest Roberta Besio, Silvia Maruelli, Severine Battaglia, Laura Leoni, Simona Villani, Pierre Layrolle, Antonio Rossi, Valerie Trichet, Antonella Forlino declared that they have no competing interest.

Ethical Approval All applicable international, national, and/or institutional guidelines for the care and use of animals were followed, all procedures performed in studies involving animals were in accordance with the ethical standards of the institution or practice at which the studies were conducted.

References

- Forlino A, Marini JC (2016) Osteogenesis imperfecta. *Lancet* 387:1657–1671
- Marini JC, Forlino A, Bachinger HP, Bishop NJ, Byers PH, Paepe A, Fassier F, Fratzl-Zelman N, Kozloff KM, Krakow D et al (2017) Osteogenesis imperfecta. *Nat Rev Dis Primers* 3:17052
- Mehlman CT, Shepherd MA, Norris CS, McCourt JB (2012) Diagnosis and treatment of osteopenic fractures in children. *Curr Osteoporos Rep* 10:317–321
- Besio R, Forlino A (2015) Treatment options for osteogenesis imperfecta. *Expert Opin Orphan D* 3:165–181
- Morgan EF, De Giacomo A, Gerstenfeld LC (2014) Overview of skeletal repair (fracture healing and its assessment). *Methods Mol Biol* 1130:13–31
- Marsell R, Einhorn TA (2011) The biology of fracture healing. *Injury* 42:551–555
- Morshed S (2014) Current options for determining fracture union. *Adv Med* 2014:708574
- Rauch F, Travers R, Parfitt AM, Glorieux FH (2000) Static and dynamic bone histomorphometry in children with osteogenesis imperfecta. *Bone* 26:581–589
- Uveges TE, Collin-Osdoby P, Cabral WA, Ledgard F, Goldberg L, Bergwitz C, Forlino A, Osdoby P, Gronowicz GA, Marini

- JC (2008) Cellular mechanism of decreased bone in *Brtl* mouse model of OI: imbalance of decreased osteoblast function and increased osteoclasts and their precursors. *J Bone Miner Res* 23:1983–1994
10. Li H, Jiang X, Delaney J, Franceschetti T, Bilic-Curcic I, Kalinovsky J, Lorenzo JA, Grcevic D, Rowe DW, Kalajzic I (2010) Immature osteoblast lineage cells increase osteoclastogenesis in osteogenesis imperfecta murine. *Am J Pathol* 176:2405–2413
 11. Gamble JG, Rinsky LA, Strudwick J, Bleck EE (1988) Non-union of fractures in children who have osteogenesis imperfecta. *J Bone Joint Surg* 70:439–443
 12. Agarwal V, Joseph B (2005) Non-union in osteogenesis imperfecta. *J Pediatr Orthop B* 14:451–455
 13. Hsiao MS, Mormino MA, Esposito PW, Burke BA (2013) Distal humerus atrophic nonunion in a child with osteogenesis imperfecta. *J Pediatr Orthop* 33:725–729
 14. Cheung MS, Glorieux FH, Rauch F (2007) Natural history of hyperplastic callus formation in osteogenesis imperfecta type V. *J Bone Miner Res* 22:1181–1186
 15. Brenner RE, Vetter U, Nerlich A, Worsdorfer O, Teller WM, Muller PK (1989) Biochemical analysis of callus tissue in osteogenesis imperfecta type IV. Evidence for transient overmodification in collagen types I and III. *J Clin Invest* 84:915–921
 16. Ramirez N, Vilella FE, Colon M, Flynn JM (2003) Osteogenesis imperfecta and hyperplastic callus formation in a family: a report of three cases and a review of the literature. *J Pediatr Orthop B* 12:88–96
 17. Cheung MS, Azouz EM, Glorieux FH, Rauch F (2008) Hyperplastic callus formation in osteogenesis imperfecta type V: follow-up of three generations over ten years. *Skeletal Radiol* 37:465–467
 18. Munns CF, Rauch F, Zeitlin L, Fassier F, Glorieux FH (2004) Delayed osteotomy but not fracture healing in pediatric osteogenesis imperfecta patients receiving pamidronate. *J Bone Miner Res* 19:1779–1786
 19. Dwan K, Phillipi CA, Steiner RD, Basel D (2016) Bisphosphonate therapy for osteogenesis imperfecta. *Cochrane Database Syst Rev* 10:CD005088
 20. Franzone JM, Finkelstein MS, Rogers KJ, Kruse RW (2017) Evaluation of fracture and osteotomy union in the setting of osteogenesis imperfecta: Reliability of the modified radiographic union score for tibial fractures (RUST). *J Pediatr Orthop*. (in press)
 21. Delos D, Yang X, Ricciardi BF, Myers ER, Bostrom MP, Camacho NP (2008) The effects of RANKL inhibition on fracture healing and bone strength in a mouse model of osteogenesis imperfecta. *Journal of Orthop Res* 26:153–164
 22. Meganck JA, Begun DL, McElderry JD, Swick A, Kozloff KM, Goldstein SA, Morris MD, Marini JC, Caird MS (2013) Fracture healing with alendronate treatment in the *Brtl/+* mouse model of osteogenesis imperfecta. *Bone* 56:204–212
 23. Enderli T, Burtch S, Templet J, Carriero A (2016) Animal models of osteogenesis imperfecta: applications in clinical research. *Orthop Res Rev* 8:41–55
 24. Daley E, Streeten EA, Sorkin JD, Kuznetsova N, Shapses SA, Carleton SM, Shuldiner AR, Marini JC, Phillips CL, Goldstein SA et al (2010) Variable bone fragility associated with an Amish COL1A2 variant and a knock-in mouse model. *J Bone Miner Res* 25:247–261
 25. Marsh JL, Slongo TF, Agel J, Broderick JS, Creevey W, DeCoster TA, Prokuski L, Sirkin MS, Ziran B, Henley B et al (2007) Fracture and dislocation classification compendium—2007: Orthopaedic Trauma Association classification, database and outcomes committee. *J Orthop Trauma* 21:S1–S133
 26. Nowalk JR, Flick LM (2008) Visualization of different tissues involved in endochondral ossification with alcian blue hematoxylin and orange G/eosin counterstain. *J Histochem* 31:19–21
 27. Stephano JL, Gould M, Rojas-Galicia L (1986) Advantages of picric acid fixation for staining polypeptides in polyacrylamide gels. *Anal Biochem* 152:308–313
 28. Ford JL, Robinson DE, Scammell BE (2004) Endochondral ossification in fracture callus during long bone repair: the localisation of ‘cavity-lining cells’ within the cartilage. *J Orthop Res* 22:368–375
 29. Miller EJ, Rhodes RK (1982) Preparation and characterization of the different types of collagen. *Methods Enzymol* 82 Pt A:33–64
 30. Kulmala KA, Korhonen RK, Julkunen P, Jurvelin JS, Quinn TM, Kroger H, Toyras J (2010) Diffusion coefficients of articular cartilage for different CT and MRI contrast agents. *Med Eng Phys* 32:878–882
 31. Ferguson C, Alpern E, Miclau T, Helms JA (1999) Does adult fracture repair recapitulate embryonic skeletal formation? *Mech Dev* 87:57–66
 32. Bargman R, Posham R, Boskey AL, DiCarlo E, Raggio C, Pleshko N (2012) Comparable outcomes in fracture reduction and bone properties with RANKL inhibition and alendronate treatment in a mouse model of osteogenesis imperfecta. *Osteoporos Int* 23:1141–1150
 33. Silience DO, Senn A, Danks DM (1979) Genetic heterogeneity in osteogenesis imperfecta. *J Med Genet* 16:101–116
 34. Masci M, Wang M, Imbert L, Barnes AM, Spevak L, Lukashova L, Huang Y, Ma Y, Marini JC, Jacobsen CM et al (2016) Bone mineral properties in growing *Col1a2(+)/G610C* mice, an animal model of osteogenesis imperfecta. *Bone* 87:120–129
 35. Pountos I, Panteli M, Lampropoulos A, Jones E, Calori GM, Giannoudis PV (2016) The role of peptides in bone healing and regeneration: a systematic review. *BMC Med* 14:103
 36. Zhang M, Ho HC, Sheu TJ, Breyer MD, Flick LM, Jonason JH, Awad HA, Schwarz EM, O’Keefe RJ (2011) *EP1(-/-)* mice have enhanced osteoblast differentiation and accelerated fracture repair. *J Bone Miner Res* 26:792–802
 37. Mirigian LS, Makareeva E, Mertz EL, Omari S, Roberts-Pilgrim AM, Oestreich AK, Phillips CL, Leikin S (2016) Osteoblast malfunction caused by cell stress response to procollagen misfolding in *alpha2(I)-G610C* mouse model of osteogenesis imperfecta. *J Bone Miner Res* 31:1608–1616
 38. Gioia R, Panaroni C, Besio R, Palladini G, Merlini G, Giansanti V, Scovassi IA, Villani S, Villa I, Villa A et al (2012) Impaired osteoblastogenesis in a murine model of dominant osteogenesis imperfecta: a new target for osteogenesis imperfecta pharmacological therapy. *Stem Cells* 30:1465–1476
 39. Jepsen KJ, Pennington DE, Lee YL, Warman M, Nadeau J (2001) Bone brittleness varies with genetic background in *A/J* and *C57BL/6J* inbred mice. *J Bone Miner Res* 16:1854–1862
 40. Manigrasso MB, O’Connor JP (2008) Comparison of fracture healing among different inbred mouse strains. *Calcif Tissue Int* 82:465–474
 41. Ji H, Li J, Shao J, He D, Liu Y, Fei W, Luo E (2017) Histopathologic comparison of condylar hyperplasia and condylar osteochondroma by using different staining methods. *Oral Surg Oral Med Oral Pathol Oral Radiol* 123:320–329

Chapter VI
Zebrafish: a resourceful vertebrate model to
investigate skeletal disorders

Zebrafish: A Resourceful Vertebrate Model to Investigate Skeletal Disorders

The using of animal models is essential to better study the pathophysiology of several diseases. In recent years, zebrafish has been proven an excellent model organism, because it has several advantages including external fertilization, large number of offspring from a single mating and rapid development. Furthermore, the zebrafish is also a powerful model for bone pathologies, since it shares the same bone cells as well as the same ossification processes with mammals. In Tonelli et al. 2020 review, for which I contributed to text revision, design images and edit tables, zebrafish bone biology and an updated list of generated and deeply characterized models of skeletal disorders, have been described. The review was also focused on highlighting the importance of already available zebrafish transgenic models to dynamically dissect the nature of tissue development, molecular transduction pathways activity and regeneration. Finally, several tools are nowadays available to evaluate the embryos development and to characterized different zebrafish models bone phenotypes both at microscopical and macroscopical point of view. MicroCT, X-ray, and whole mount stainings allow a macroscopic view of the bone elements, while techniques such as Transmission Electron Microscopy (TEM) and immunohistochemistry allow to elucidate cells phenotype and their intracellular features.



Zebrafish: A Resourceful Vertebrate Model to Investigate Skeletal Disorders

Francesca Tonelli^{1†}, Jan Willem Bek^{2†}, Roberta Besio^{1†}, Adelbert De Clercq^{2†}, Laura Leoni¹, Phil Salmon³, Paul J. Coucke², Andy Willaert^{2‡} and Antonella Forlino^{1*‡}

¹ Biochemistry Unit, Department of Molecular Medicine, University of Pavia, Pavia, Italy, ² Department of Biomolecular Medicine, Center of Medical Genetics, Ghent University-University Hospital, Ghent, Belgium, ³ Bruker microCT, Kontich, Belgium

OPEN ACCESS

Edited by:

Wim Van Hul,
University of Antwerp, Belgium

Reviewed by:

Christoph Winkler,
National University of
Singapore, Singapore
Michaël R. Laurent,
University Hospitals Leuven, Belgium

*Correspondence:

Antonella Forlino
aforlino@unipv.it

[†] These authors have contributed
equally to this work

[‡] These authors share last authorship

Specialty section:

This article was submitted to
Bone Research,
a section of the journal
Frontiers in Endocrinology

Received: 25 April 2020

Accepted: 22 June 2020

Published: 31 July 2020

Citation:

Tonelli F, Bek JW, Besio R, De
Clercq A, Leoni L, Salmon P,
Coucke PJ, Willaert A and Forlino A
(2020) Zebrafish: A Resourceful
Vertebrate Model to Investigate
Skeletal Disorders.
Front. Endocrinol. 11:489.
doi: 10.3389/fendo.2020.00489

Animal models are essential tools for addressing fundamental scientific questions about skeletal diseases and for the development of new therapeutic approaches. Traditionally, mice have been the most common model organism in biomedical research, but their use is hampered by several limitations including complex generation, demanding investigation of early developmental stages, regulatory restrictions on breeding, and high maintenance cost. The zebrafish has been used as an efficient alternative vertebrate model for the study of human skeletal diseases, thanks to its easy genetic manipulation, high fecundity, external fertilization, transparency of rapidly developing embryos, and low maintenance cost. Furthermore, zebrafish share similar skeletal cells and ossification types with mammals. In the last decades, the use of both forward and new reverse genetics techniques has resulted in the generation of many mutant lines carrying skeletal phenotypes associated with human diseases. In addition, transgenic lines expressing fluorescent proteins under bone cell- or pathway- specific promoters enable *in vivo* imaging of differentiation and signaling at the cellular level. Despite the small size of the zebrafish, many traditional techniques for skeletal phenotyping, such as x-ray and microCT imaging and histological approaches, can be applied using the appropriate equipment and custom protocols. The ability of adult zebrafish to remodel skeletal tissues can be exploited as a unique tool to investigate bone formation and repair. Finally, the permeability of embryos to chemicals dissolved in water, together with the availability of large numbers of small-sized animals makes zebrafish a perfect model for high-throughput bone anabolic drug screening. This review aims to discuss the techniques that make zebrafish a powerful model to investigate the molecular and physiological basis of skeletal disorders.

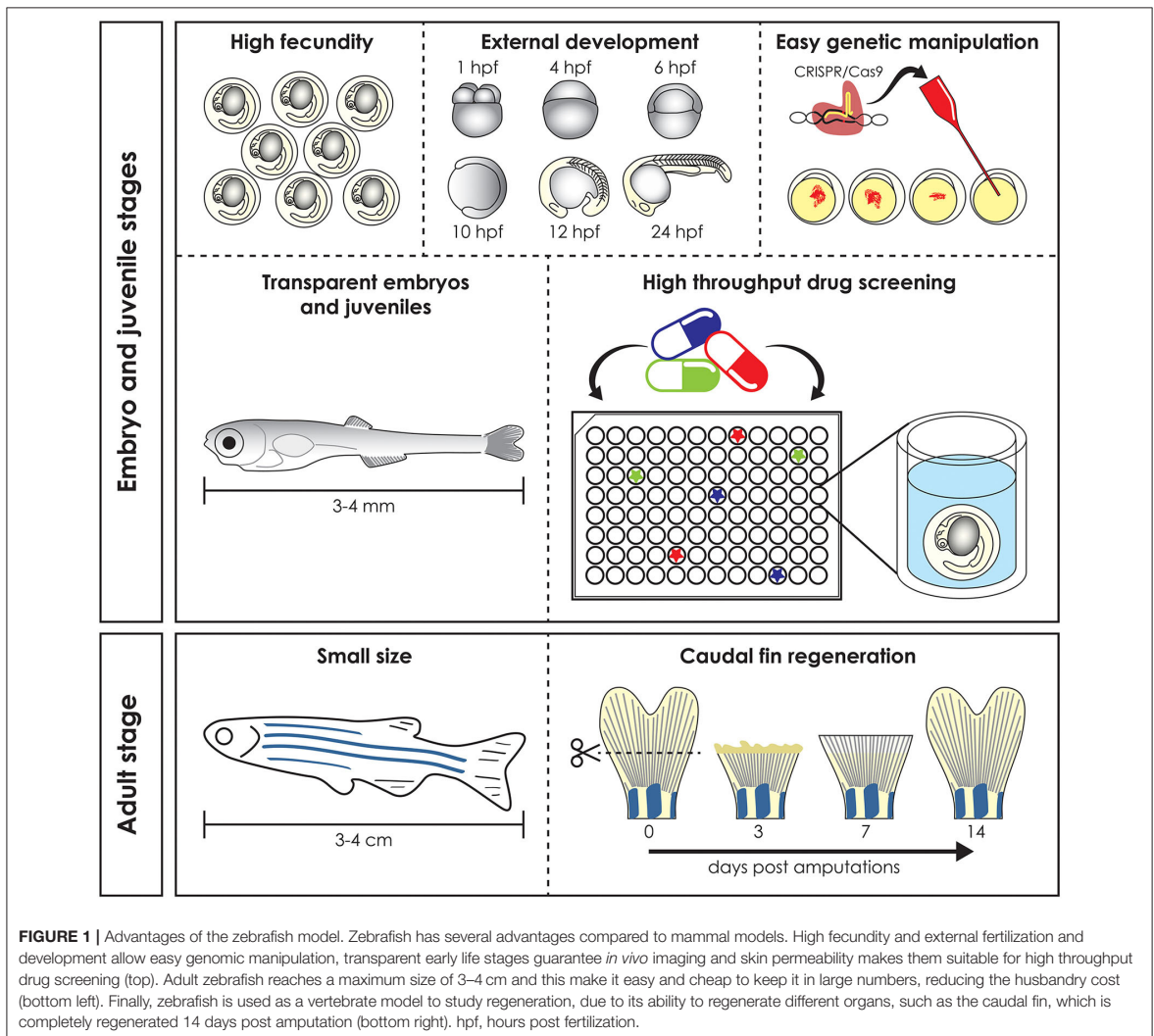
Keywords: zebrafish, skeletal system, x-ray, microCT analyses, imaging techniques, skeletal diseases

INTRODUCTION

Preclinical animal models can be used to elucidate gene and protein function in ways often impossible in humans, by means of genome sequencing, advances in DNA manipulation and high resolution live-imaging (1). Mammals such as mice and non-human primates are traditionally the preferred models for biomedical research due to their close evolutionary relationship with humans.

However, their use is costly and studies at early developmental stages raise ethical concerns. Furthermore, in most countries the adoption of the “Three R’s” principles: Replacement, Reduction, and Refinement (2) for animal research is mandatory and encourages the use of alternative models, such as *Danio rerio* (zebrafish), *Xenopus laevis/tropicalis* (clawed toad), *Drosophila melanogaster* (fruit fly), and *Caenorhabditis elegans* (nematode). In these organisms *in vivo* techniques can be applied with the simplicity and versatility of *in vitro* assays and therefore they are frequently used in fundamental and biomedical research to quickly define gene functions and to develop novel therapeutic options (3). Zebrafish, the most frequently employed non-mammalian vertebrate animal model, is a freshwater bony fish, belonging to the Cyprinidae family and to the Teleostei infraclass

of ray-finned fish which arose ~340 million years ago (4). This species was initially described by the Scottish physician and naturalist Hamilton (5) in a survey on South Asian flora and fauna. Starting from the pioneering research of George Streisinger in the 70s–80s, who was the first to clone a zebrafish and in this way demonstrated the easy genetic manipulation of this species (6), zebrafish became a powerful model organism for developmental studies, genetic research, drug and toxicology screenings and for understanding tissue regeneration and repair (7–9). In contrast to other vertebrate models such as mice, fertilization occurs externally, which together with transparency and rapid embryo to larval transition permits easy access and visualization of development (10) (Figure 1). Moreover, due to its rapid growth, a recognizable and complete vertebrate body



plan is already in place by 1 day post fertilization (dpf) and embryogenesis is complete by 3 dpf (11). In contrast to other vertebrate models such as rodents, the small size and large number of offspring of zebrafish allow for increased sample numbers, thereby increasing the statistical power of experiments (3). Finally, the relatively low husbandry cost further contributed to the increasing popularity of the zebrafish as a model for research (11).

Besides developmental studies, the zebrafish is an established research model in many other research fields. During the last 20 years, the zebrafish has proven itself as a useful model to study disease mechanisms (1). This is due to its physiological relevance and genetic tractability to model genetic variation in humans. Compared to mammalian model organisms, the zebrafish genome underwent an extra (third) whole duplication about 350 million years ago, with the result that for many genes in humans, there may be two copies (paralogues) in zebrafish. Despite this there is a relatively high level of genome conservation between zebrafish and humans with more than 70% of human protein-coding genes having at least one zebrafish ortholog. The haploid zebrafish genome has 25 chromosomes containing 1.7 billion base pairs (4). Various forward and reverse genetic approaches have been applied to generate mutant lines that mimic many different human diseases, including skeletal diseases ranging from secondary osteoporosis (OP) to rare disorders such as osteogenesis imperfecta (OI) (12–20). A major benefit of zebrafish is the simplicity of combining mutant and transgenic lines that express fluorescent reporter proteins under the control of responsive elements for signaling pathways or promoters of cell-type-specific markers. This in turn allows for *in vivo* investigation of the effect of a disease mutation on the spatio-temporal expression of specific genes, and on cell differentiation and signaling pathways.

Zebrafish larvae have been intensively used for pharmacological and toxicological screens, because of their small size (easy distribution in microtiter well plates), high abundance and their ability to absorb small compounds from the water through the skin and gills (21). Together with the availability of many different disease models, the zebrafish is a unique tool to develop novel targeted pharmacological approaches (Figure 1) (21).

Finally, their ability to regenerate some cells and tissues, such as fins and scales, makes the zebrafish a valuable model for understanding organ repair mechanisms during healthy and pathological conditions (Figure 1) (22).

This review, after providing a brief overview of zebrafish bone biology, will focus on the description and use of the various techniques and approaches which make *Danio rerio* a powerful model organism to investigate the molecular and physiological basis of skeletal disorders.

ZEBRAFISH BONE BIOLOGY

The Skeleton

Skeletal development and gene expression and the general inventory of bone types are conserved between zebrafish and mammals, nevertheless few differences need to be considered

when using this animal as model for skeletal study. Osteocytes are not present in all bones and/or at all developmental stages, endochondral ossification is rare in zebrafish and vertebral body do not build on a cartilaginous anlage (23, 24). The common perception of mammals being more complex than “lower” organisms, such as teleosts, is false, especially concerning the skeleton. Certain characteristics of the teleost skeleton are more advanced and elaborate compared to mammals, such as the zebrafish skull that contains at least twice the number of bones (24). At the tissue level, the mammalian skeleton mostly consists of cellular bone and hyaline cartilage. While other types of bone, such as hyperostotic and acellular bone and cartilage (i.e., fiber cartilage), can be present in mammalian skeletons, they are often associated with pathological processes. However, in teleosts many different bone and cartilage types with different cellularity and matrix composition exist in wild type conditions not related to disease (25). The zebrafish skeleton consists of a dermal skeleton and an endoskeleton. Scales, polarized structures of the exoskeleton, teeth, and fin rays are part of the dermal skeleton and are distinctive as skeletal structures in their ability to regenerate (25–27). In fish, teeth, scales, and fin rays can all be traced back in evolution to a single structure, called the odontode (28), and they arise at the epithelial-mesenchymal border (29, 30). It has been shown that the mesenchymal tissues that engender these skeletal elements have a neural crest origin (29, 31, 32).

The endoskeleton consists of cranial, axial, and appendicular skeletal elements (33). As in all vertebrates, the zebrafish cranial skeleton arises mostly from the cranial neural crest, while the appendicular skeleton develops from somite-derived paraxial mesoderm (31, 33). In contrast with tetrapods, in which vertebral centrum formation is controlled by somites patterned along the vertebral column, in teleosts the notochord has an instructive role in vertebral centrum patterning as the centra start out as mineralization foci in the notochord sheath (34, 35).

Skeletal Cells

The teleost and mammalian skeletal systems share similar cell types (Figure 2A). In cartilage there are (i) chondroblasts as the cartilage forming cells and (ii) chondrocytes maintaining the cartilage matrix. In bone there are (i) osteoblasts as the bone forming cells, (ii) osteocytes that act as the mechanosensors regulating osteoblast and osteoclast activity and (iii) osteoclasts which are the bone resorbing cells (24, 37). Similar to mammals, teleost skeletal histogenesis involves the differentiation of chondroblasts and osteoblasts, that secrete the collagen extracellular matrix, from mesenchymal stem cells (38, 39). Both in mammals and fish, skeletal cells are formed by a complex interplay of intracellular molecular pathways and secreted factors that regulate the timing, location, and pathway by which bone cells differentiate (40–42). Although not investigated in mammals before, in zebrafish osteoblasts are present in clusters at the end of growing bones and can be classified in two different groups (type I and type II) based on cell cluster size, location, and nuclei shape, although they have overlapping functions (36). Type I osteoblasts are located at the edges of growing flat bones, such as the dentary, maxillary, and frontal bone, in large clusters with more than 25 cells with a wide oval, round, or

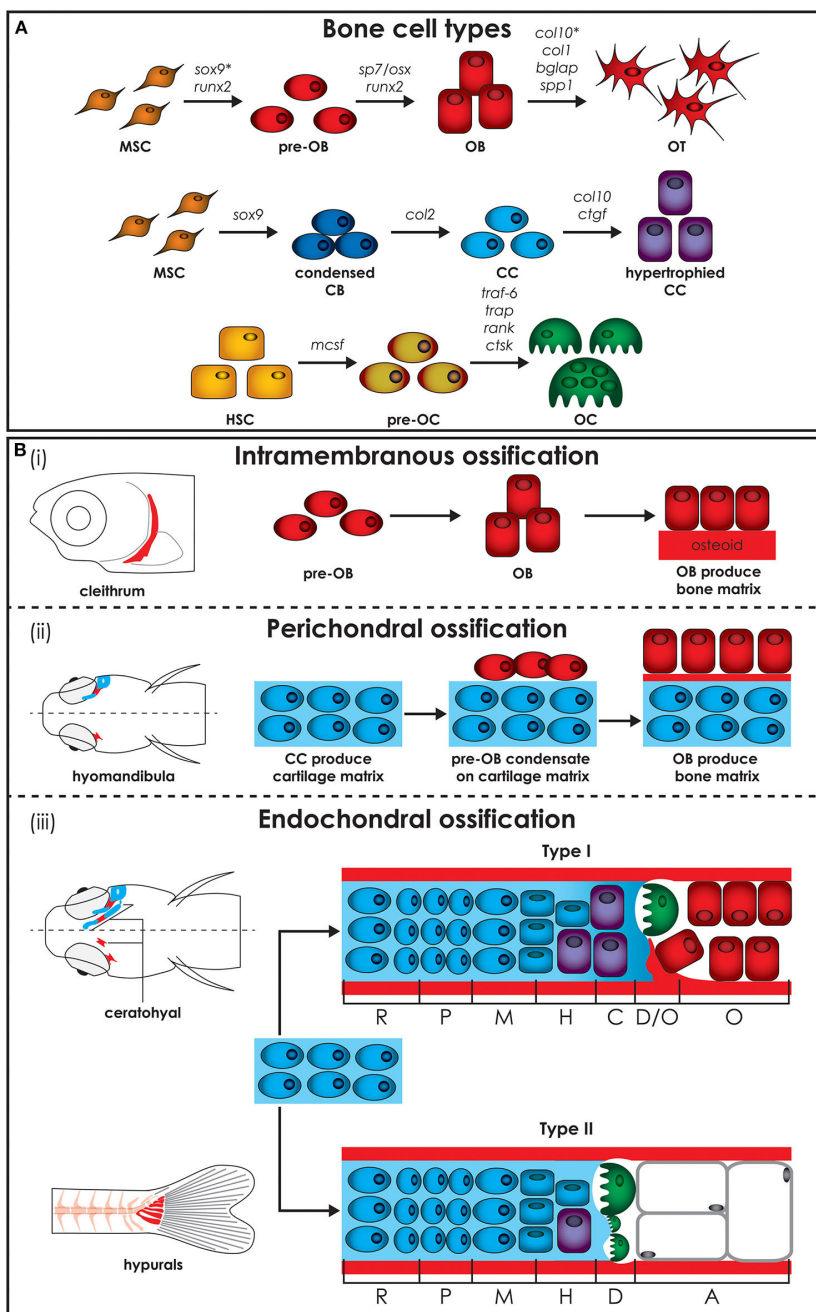


FIGURE 2 | Zebrafish bone cells and ossification types. **(A)** Bone is formed by osteoblasts and osteocytes, while cartilage is formed by chondroblasts and chondrocytes, and both bone and cartilage are degraded by osteoclasts. All bone cell types develop from progenitors similar to the mammalian counterpart and share similar gene expression profiles (genes are indicated above arrows). Note however that HSCs in zebrafish are not present in the bone marrow but in the head kidney. In addition, the genes for collagen X, encoded by *col10*, and SRY-box transcription factor 9 (indicated by*), encoded by *sox9*, are expressed during osteoblasts differentiation in zebrafish, but not in humans. **(B)** Three types of ossification are present in zebrafish: (i) intramembranous ossification, (ii) perichondral ossification, (Continued)

FIGURE 2 | present in teleosts but not in humans, and (iii) endochondral ossification. (i) During intramembranous ossification mesenchymal stem cells condensate and differentiate into pre-osteoblasts and finally into mature osteoblasts that deposit bone matrix (osteoid) that subsequently mineralizes. (ii) Perichondral ossification starts at the surface of a cartilaginous template where osteoblasts deposit bone matrix without replacing the cartilage. (iii) Endochondral ossification is the process by which growing cartilage is replaced by bone to allow the skeleton to grow. For ossification to start, matrix surrounding the chondrocytes must calcify so that osteoclasts can break down the cartilage. In teleost two types of endochondral ossification exist. Type I endochondral ossification, typical in the ceratohyal, resembles the mammalian endochondral ossification process. This is characterized by a hypertrophic zone, where the cartilage matrix calcifies, followed by a degradation zone where osteoclasts (also referred to as chondroclasts) degrade the cartilaginous matrix, and a bone formation zone. Type II ossification, in the hypurals, is characterized by a lack of the calcification and ossification zones, leading to tubular concave bones filled with adipose tissue. Schematics based on detail description in Weigle and Franz-Odenaal (36). A, adipose zone; C, calcification zone; CB, chondroblasts; CC, chondrocytes; D, degradation zone; H, hypertrophic zone; HSC, hematopoietic stem cell; M, maturation zone; MSC, mesenchymal stem cell; O, ossification zone; OB, osteoblasts; OC, osteoclasts; OT, osteocytes; P, proliferation zone; R, rest zone.

irregularly shaped nucleus. Laterally to these cells there is a zone of differentiating osteoblasts where cells are smaller and more elongated, assuming the typical spindle shape of osteoblast-like cells, which cover all zebrafish bones with a monolayer at the level of the perichondrium (36). Type II osteoblast clusters are smaller (4–12 cells) and are distributed throughout the skeleton. These osteoblasts have a reduced size, elongated nucleus and are present throughout the bony trabecular network of spongy bones. Type II osteoblast clusters can also be detected at the edges of cartilage break down zones and lateral to the epiphysial growth plate, at the outer surface of tubular bones (36).

Most skeletal elements in the adult zebrafish skeleton contain osteocytes, but with a smaller volume and less canaliculi compared to mice and humans (36). The mechanosensing ability of osteocytes in zebrafish is not fully understood yet, but it was shown that osteocytes have a preferred orientation in adult zebrafish vertebrae (36). Acellular bone, without trapped osteocytes, can be found in many zebrafish cranial bones. Contrary to expectations, acellular bone does not appear to be stiffer due to the lack of osteocyte lacunae, making the role of acellular bone unclear (43). It is important to note that both cellular and acellular bone can occur within the same bony element. Osteon-like structures in zebrafish have been reported (for the lateral ethmoid bone) but these structures, composed of a central Haversian canal and bone lamella, do not have osteocytes (36).

In mammals, bone resorbing cells are multinucleated macrophages originating from the fusion and maturation of peripheral blood monocytes differentiated from hematopoietic bone marrow cells (44). Multinucleated osteoclasts can also be found in teleosts, especially in basal teleosts, such as salmonids and cyprinids (45). Nevertheless, in teleosts, smaller and mononucleated osteoclasts are predominant, but they retain the molecular regulators of mammalian osteoclast function (37). Examples include receptor activator of nuclear factor kappa-B (Rank) and Rank-ligand (Rankl) which are important for osteoclast maturation. Mature osteoclasts become tartrate-resistant acid phosphatase (Trap) and cathepsin K (CtsK) positive, which are both required for the cells to be able to degrade bone matrix components (37, 46). Zebrafish are characterized by an ontogenic change at 30 dpf when mononucleated osteoclasts evolve to multinucleated osteoclasts, which perform lacunar resorption and bone remodeling (37).

Each cell type achieves and performs its function by involving specific genes, acting as molecular fingerprints. All three bone

cell types develop from similar progenitors as their mammalian counterpart and share similar profiles of gene expression (Figure 2A) (36). Gene expression of zebrafish collagen and transcription factor in skeletal cells of cartilage and bone are not completely conserved with mammals. Unlike mammals, zebrafish osteoblasts express collagen type X and various teleosts have been shown to have collagen type II in their bone matrix (47, 48). In addition, *Sox9* expression, which is required for differentiation of chondrocytes, but not of osteoblasts in mammals, has been reported to be involved in bone development in teleosts (49). Unlike tetrapods, zebrafish type I collagen, the most abundant protein in bone, has three instead of two different α chains, namely $\alpha 1$, $\alpha 3$, and $\alpha 2$ encoded by *coll1a1a*, *coll1a1b*, and *coll1a2*, respectively (50). Based on the amino acid sequence, the $\alpha 3$ chain is phylogenetically similar to $\alpha 1$, supporting the common origin of their coding genes, which derive from a genome duplication that occurred at an early stage in teleost evolution (51). Importantly, all amino acid residues involved in human/mouse collagen type I cross-links are conserved in zebrafish, suggesting the existence of similar extracellular assembly (50).

Bone Ossification

Bone formation starts in zebrafish around 4–5 dpf. The bony elements can have three modes of ossification: intramembranous, perichondral, or endochondral. Intramembranous ossification starts with mesenchymal cell condensation and differentiation into osteoblasts, without the need of a cartilage template (Figure 2Bi) (45). This type of ossification occurs in the skull, for example in the cranial roof and opercular bones, in the vertebral column, where most of the vertebral body is formed by this type of ossification, in scales and in the fin rays (45). In mammals, this ossification is mostly restricted to bones of the cranial vault and the dentary (52).

Perichondral ossification, characterized by bone formation in the perichondrium, is more common in the teleost compared to the mammalian skeleton, where it has been considered as a form of intramembranous ossification (45). In teleosts perichondral ossification is present in the hyomandibula and Meckel's cartilage, where osteoblasts aggregate on the surface of the cartilaginous template and deposit bone matrix into the perichondrium (Figure 2Bii).

Endochondral ossification, which is the main type of ossification in mammals, is uncommon in teleosts. In this type of ossification, mesenchymal cells condense and differentiate

into chondroblasts and chondrocytes, which then secrete an extracellular cartilage matrix that functions as a template that is replaced by bone matrix (Figure 2Biii). In teleosts, two types of endochondral ossification exist. In a few bones, such as the ceratohyal and the radials in the pectoral fin, type I endochondral ossification takes place at the level of epiphysis and of the epiphysial growth plate resembling the mammalian endochondral ossification process. It is characterized by a resting zone, a proliferation zone with columnar cartilage, and a hypertrophic zone followed by a region in which cartilage matrix calcifies (36). Finally, chondroclasts degrade the cartilaginous matrix (degradation zone), allowing osteoblasts to lay down bone matrix (ossification zone). In the hyomandibula, branchial arches, ethmoid and hypuralia type II endochondral ossification takes place. Here, the calcification and ossification zones are absent and the cartilage template is replaced by adipose cells, leading to tubular concave bones filled with adipose tissue (36, 37).

Because the cranial skeleton is often too complex for screening by high throughput methods, the zebrafish vertebral body is the most investigated component of the skeleton both in early and adult life stages. Although the vertebrae in both mammals and teleosts consist of notochord and bone, there are a few key differences. First, the notochord is the *de facto* vertebral column in early teleost life stages and persists throughout life, while it only forms the intervertebral disc in mammals (53, 54). The notochord consists of a core of large and vacuolated chordocytes which is surrounded by an epithelial layer of chordoblasts that secrete the notochord sheath. This sheath is a stratified structure, composed of a thin external membrane containing elastin, covering a thicker layer of mainly collagen type II (54). Second, while the vertebrae in mammals have a cartilaginous precursor which endochondrally ossifies, zebrafish vertebrae form initially through direct mineralization of the notochord sheath, called chordacentra, in the absence of a cartilaginous precursor (55, 56). To this day, the exact cellular involvement of this notochord sheath mineralization remains unresolved. Third, the teleost vertebra is subsequently built via intramembranous ossification outside the notochord onto the chordacentrum, consisting of a compact autocentrum and trabecular arcocentrum, which forms the neural and haemal arches (56, 57). The osteoblasts produce collagen type I bone matrix and start to ossify the autocentrum at the level of the intervertebral disc, which acts as the growth center of the vertebral centrum (34).

GENERATION OF KNOCK-OUT AND KNOCK-IN ZEBRAFISH MODELS

Forward Genetic Approach

Different methods to generate zebrafish models of human disorders have been explored over the last decades. Initially, a number of large-scale forward genetic screens, based on random mutagenesis with radiation, chemicals, or insertional mutagenesis, revealed zebrafish mutants affecting different aspects of embryonic development and biological processes (58–60). This phenotype-driven approach was also applied

to screen for genes involved in skeletal development and diseases (Table 1). Several mutants with defects in craniofacial cartilage elements and with mineralized tissue phenotypes (119), or with changes in the shape of the skeleton (96) were identified in large scale forward genetic screens. Mapping of the causative change established some of these mutants as models for human skeletal disorders. For instance, in a study by Gistelincx et al. (120), several type I collagen zebrafish mutants, previously discovered in a forward genetic screen (96), were established as representative models for the brittle bone disorder osteogenesis imperfecta.

Reverse Genetic Approach: Morpholino Knockdown and Gene Editing

Although forward genetics brought great progress to the field of disease modeling, still, for many causal human disease genes, this approach did not reveal corresponding zebrafish mutants, as there is incomplete genome coverage of mutagenesis. Consequently, the need to investigate the function of relevant candidate genes for specific diseases or developmental pathways, sparked the expansion of reverse genetic approaches in the zebrafish field.

The assessment of candidate gene function was initially enabled via knockdown through the use of antisense morpholinos (MO). Their ease of use made this approach increasingly popular for gene function analysis, and several early studies demonstrated that MO-mediated knockdown (“morphants”) recapitulated known mutant phenotypes (121, 122). Over the past years, MOs have also been used in zebrafish modeling of skeletal disorders (Table 1). An example includes the monogenetic form of X-linked osteoporosis, caused by loss-of-function variants in *PLS3* encoding for plastin 3, a cytoskeletal protein involved in bone homeostasis. MO-mediated knockdown of *pls3* in zebrafish (18) induced malformations of the developing craniofacial bone structure, which could be reversed by the administration of human *PLS3* mRNA. Another example by Flores et al. (68) shows that depletion of *runx2b* by MO injection severely compromised craniofacial cartilage formation, phenocopying the human dominantly inherited disorder cleidocranial dysplasia, a condition characterized by impaired ossification and multiple skeletal abnormalities (68). Nevertheless, problems with the application of MOs in zebrafish emerged, such as the frequent occurrence of p53-dependent apoptosis (123–125), and off-target effects resulting in so-called “pseudophenotypes” (126, 127), but also MO-induced phenotypes that cannot be recapitulated in existing mutants (128). The latter issue has recently been studied in more detail leading to the insight that, at least for some genes, the phenotypic differences between morphants and mutants can be due to genetic compensation in the latter, but not in the former (129).

Definitive reverse genetic approaches in zebrafish recently became available in the form of site-specific nucleases enabling targeted gene modification. Initial work utilized zinc finger nucleases (ZFNs) (130, 131), and transcription activator-like effector nucleases (TALENs) (132). However, CRISPR/Cas9 genome editing is currently the most versatile and frequently

TABLE 1 | Zebrafish models for skeletal disorders.

Disorder	Gene	Type	Origin	References
Acrocapitofemoral dysplasia	<i>lh</i>	KO	ENU	(40)
Alagille syndrome	<i>jag1b</i>	KO	ENU	(61)
Amelogenesis imperfecta	<i>slc10a7</i>	KD	MO	(62)
Auriculocondylar syndrome	<i>mef2ca</i>	KO	ENU	(63)
Bruck syndrome	<i>Plod2</i>	KO	ENU	(16)
Campomelic dysplasia	<i>sox9a, sox9b</i>	KO	ENU	(64)
Cartilage-Hair Hypoplasia	<i>rmp</i>	KO	CR	(65)
Cenani-Lenz syndactyly	<i>lrp4</i>	KD	MO	(66)
Chordoma	<i>HRASV12</i>	OE	Tol2	(67)
Cleidocranial dysplasia	<i>runx2b</i>	KD	MO	(68)
Craniofacial defects	<i>tgfb2</i>	KD	MO	(69)
Craniofacial defects	<i>fgf10a</i>	KD	MO	(69)
Craniosynostosis	<i>tcf12</i>		Tol2	(70)
Craniosynostosis	<i>cyp26b1</i>	KO	ENU	(71)
Craniosynostosis	<i>cyp26b1</i>	KO	ENU	(72)
Culler-jones syndrome	<i>gll2</i>	KO	Tol2	(73)
Delayed mineralization	<i>Pth4</i>			(74)
Delayed mineralization			TR	(75)
Ehlers-Danlos syndrome	<i>b4galt7</i>	KD	MO/CR	(76)
Fibrodysplasia	<i>acvr1</i>	CE	Tol2	(77)
Ossificans Progressiva				
Gaucher disease	<i>gba1</i>	KO	ENU	(78)
Holoprosencephaly	<i>ptch1</i>	KO	ENU	(40)
Hyperosteoegeny	<i>n1alcd</i>	OE	Tol2	(79)
Hyperthyroidism	<i>tshr</i>	KO	ENU	(80)
Hypohidrotic ectodermal dysplasia	<i>eda, edar</i>	KO	ENU	(81)
Joint disease	<i>scxa</i>	KO	CR	(82)
Klippel Feil syndrome	<i>meox1</i>		ENU	(83)
Multiple hereditary exostoses	<i>ext2, papst1</i>	KO	ENU	(84)
No mineralization	<i>entpd5</i>	KO	ENU	(85)
Oculodentodigital dysplasia	<i>cx43</i>	KO	ENU	(86)
Orofacial cleft	<i>tgfb3</i>	KD	MO	(87)
Orofacial cleft	<i>mir140</i>	KD	MO	(88)
Orofacial cleft	<i>faf1</i>	KD	MO	(89)
Orofacial cleft	<i>wnt9a, irf6</i>	KO	Tol2	(90)
Osteoarthritis	<i>col11a2</i>	KO	ENU	(91)
Osteoarthritis	<i>prg4a, prg4b</i>	KO	TA	(92)
Osteogenesis imperfecta	<i>col1a1a</i>	MM	ENU	(14, 15, 93)
Osteogenesis imperfecta	<i>bmp1</i>	KO	ENU	(94)
Osteogenesis imperfecta	<i>sp7/osx</i>	KO	ENU	(95)
Osteogenesis imperfecta	<i>col1a1a, col1a1b, col1a2</i>	MM	ENU	(96)

(Continued)

TABLE 1 | Continued

Disorder	Gene	Type	Origin	References
Osteopetrosis	<i>m-csf</i>	KO	ENU	(97)
Osteoporosis			TR	(98)
Osteoporosis			TR	(99)
Osteoporosis	<i>gpr137b</i>	KO	CR	(100)
Osteoporosis			TR	(101)
Osteoporosis			TR	(102)
Osteoporosis	<i>atp6v1h</i>	KO	CR	(20)
Osteoporosis	<i>lgmn</i>	KO	TA	(103)
Osteoporosis	<i>lrp5</i>	KD	MO	(19)
Osteoporosis	<i>pls3</i>	KD	MO	(18)
Osteoporosis			TR	(104)
Pseudoxanthoma elasticum	<i>enpp1</i>	KO	ENU	(105)
Pseudoxanthoma elasticum	<i>abcc6a</i>	KO	ENU	(106)
Saethre-Chotzen syndrome	<i>twist, tcf12</i>	KO	TA	(107)
Saul-Wilson syndrome	<i>cog4</i>	KO	CR	(108)
Spine curvature disorders	<i>kif6</i>	KO	TA	(109)
Spine curvature disorders	<i>ptk7</i>	KO	ZFC	(110)
Spine curvature disorders	<i>slc39a8</i>	KO	CR	(111)
Spine curvature disorders	<i>col8a1a</i>	KO	ENU	(112)
Spine curvature disorders	<i>tbx6, her1, her7, hes6</i>	KO	TA	(35)
Spine curvature disorders	<i>uts2ra</i>	KO	TA	(113)
Spine curvature disorders			TR	(114)
Sponastrime dysplasia	<i>tonsl</i>	KO	CR	(115)
Stickler/Marshall syndrome	<i>col11a1a, col11a1b</i>	KD	MO	(116)
Tumoral calcinosis	<i>golgb1</i>	KO	TA	(117)
Vertebral fractures			TR	(118)

KO, Knockout; KD, knockdown; MO, morpholino; CE, cell ablation; MM, missense mutation; ENU, N-ethyl-N-nitrosourea; CR, CRISPR; Tol2, transposon-mediated integration; TR, treatment, meaning OP models induced by microgravity, drugs, aging, physical exercise, iron stress, microRNA, mechanical loading; TA, talen; ZFN, zinc finger nuclease.

employed reverse genetic technology for the creation of both knock-out and knock-in disease models. The CRISPR/Cas9 system induces a double-stranded DNA break (DSB), carried out by the Cas9 nuclease, at a specific target site, recognized by the binding of a single-guide RNA (sgRNA) molecule. Following DSB, different endogenous repair mechanisms can be initiated. On one hand, the error-prone non-homologous end joining (NHEJ) pathway can be activated, often leading to the introduction of *indel* mutations due to imprecise repair, resulting in gene knock-out. The generation of gene knock-outs in zebrafish is relatively straightforward and efficient. In a study

by Zhang et al. (20) for instance, mutations in the *ATP6V1H*, coding for vacuolar ATPase, were identified in patients with short stature and osteoporosis. Loss-of-function mutants in *atp6v1h* were generated in zebrafish through CRISPR/Cas9-mediated gene knock-out (20). These mutants demonstrated loss of bone mass and increased expression of matrix metalloproteases *mmp9* and *mmp13*. Indeed, pharmacological inhibition of *mmp9* and *mmp13* rescued the bone phenotype, suggesting that blockade of collagen degradation can be a valid therapeutic target. CRISPR/Cas9 gene editing has been recently used to generate knock-out zebrafish for *crtap* and *p3h1*, two genes that are part of a protein complex which is involved in prolyl 3-hydroxylation and proper folding of collagen type I. Loss-of-function mutations in the human ortholog genes cause recessive forms of OI. These zebrafish models faithfully mimic the human disease and support the defective chaperone role of the 3-hydroxylation complex as the primary cause of the skeletal phenotype (17).

In general, reverse genetic approaches are limited by the time required to generate mutant lines, where stable knock-out zebrafish are mostly obtained and analyzed from the F2 generation on. Therefore, an approach for rapid CRISPR-based reverse genetic screens was developed in which phenotyping is performed directly in F0 (mosaic) founders, which are called “crispants” (133, 134). This enables moderate to rapid throughput reverse genetic screens of candidate genes, contributing to skeletal disease. In a study by Watson et al. (133), the comparison between somatic, CRISPR-generated F0 mutants and homozygous germline mutants for *plod2* and *bmp1*, two genes implicated in recessive OI, revealed phenotypic convergence, suggesting that CRISPR screens of F0 animals may faithfully recapitulate the phenotype of skeletal disease models (133).

As an alternative to NHEJ-mediated repair of CRISPR/Cas9-induced DSB, the homology-directed repair (HDR) pathway can be initiated, but only in the presence of a homologous repair template. In physiological circumstances, HDR occurs between sister chromatids during the G2 and S phase of the cell cycle. The knock-in modeling procedure exploits this mechanism by supplying the CRISPR/Cas9 system with an artificial repair template, homologous to the target sequence and containing a specific variant of interest. For the generation of knock-in models, mostly single-stranded oligodeoxynucleotide (ssODN) repair templates are used (135) mainly because the design and production of ssODNs is easier, cheaper and results in higher HDR efficiencies compared to double-stranded templates such as plasmids (136, 137). The need to complement knock-out models with these more precise knock-in disease models is growing, for various reasons. Firstly, specific point mutations may cause a highly divergent pathobiology compared to loss-of-function mutations modeled by knock-out models. More specifically, certain missense mutations may cause a gain-of-function rather than a loss-of-function, while missense mutations in genes encoding proteins included in protein complexes may exercise a dominant negative effect and change the function of the whole protein complex. For instance, in dominant types of OI caused by mutations in the genes encoding the type I collagen α chains, depending on the type of mutation, either the quantity or the structure of type I procollagen is

altered (138). The “quantitative” mutations, mostly resulting in a null *COL1A1* allele, typically cause mild forms of OI, while “qualitative or structural” defects, frequently associated with glycine substitutions, can be responsible for lethal, severe or moderate forms of the disease.

Also, missense mutations in vital developmental genes may be hypomorphic while their loss-of-function counterparts result in early lethality, as reported in the *cdc6* zebrafish mutant for Meier-Gorlin syndrome. Hypomorphic mutations in the *cdc6* gene recapitulate the patient’s phenotype, while the knock-out mutants are embryonically lethal. In these cases, the introduction of such point mutations is a prerequisite to faithfully recapitulating human disease. Secondly, as mentioned before, several zebrafish knock-out models failed to generate a phenotype, which can be due to mRNA decay-induced genetic compensation (139), a phenomenon that is not expected to occur in knock-in models.

Nevertheless, several drawbacks mitigate the straightforward use of HDR knock-in zebrafish models. Firstly, HDR pathways have proved highly inefficient for genome editing (140) even despite proposed modifications, such as repair template modification (141, 142), cell cycle arrest (143) and chemical compound administration (144–151). Secondly, CRISPR/Cas9-mediated HDR mechanisms have been shown to be error-prone (152, 153). These issues hindered the development of knock-in zebrafish models and only a limited number have been reported, in contrast to numerous knock-outs. For instance, CRISPR/Cas9-mediated point mutation knock-ins have been generated for genetic variants implicated in inherited cardiac diseases (154–156), although to our knowledge none have been described so far for skeletal diseases. Different recently developed DSB-free alternatives for precise base pair substitution, such as programmable base editing (157–159) and prime editing (160) promise to be more efficient and versatile approaches, but more research is needed to further improve these methods for application to the zebrafish model system.

TRANSGENIC LINES

Transgenic Zebrafish to Trace Bone Cells and Pathways

Despite the development of new approaches in large-scale and more recently single-cell transcriptomics, genomics, epigenomics, and proteomics (161), these techniques are time consuming, expensive and only available in specialized laboratories (162–164). Furthermore, retrospective -omic analyses exclude cells that do not survive to the point of cell harvest, a common and necessary event in growth and regeneration. Therefore, to be able to understand the dynamic nature of tissue development and regeneration, *in vivo* time-lapse imaging is essential.

The recent evolution of genetic engineering has allowed the generation of transgenic animal models, expressing fluorescent proteins under cell- or pathway- specific promoters, enabling *in vivo* imaging of differentiation and signaling (165). However, the generation of transgenic murine models remains technically demanding, time consuming and expensive (166). In addition,

since mice develop *in utero*, it is almost impossible to investigate early developmental processes in real time and the visualization at cellular level usually requires post-mortem analyses (167).

Zebrafish, with its fast external development, transparent early life stages and relative easy genetic manipulation, is rapidly becoming the model of choice for examining developmental processes via time-lapse microscopy. The introduction of reporter genes downstream of a specific promoter makes it possible to produce site-directed indicators in different organs, tissues or cells and permits real time imaging in developing embryos or post-hatch stages; or even in mature zebrafish by fluorescent microscopy on whole mount specimens (168, 169). A variety of transgenic reporter lines have been generated to mark skeletal cell lineages at different stages of differentiation and signal transduction pathways, by using the conserved regulators of skeletal development (Table 2). The availability of fluorescent reporter lines, together with the use of powerful techniques such as two or multi-photon or light sheet microscopy, has allowed imaging of tissues and organs at a cellular and subcellular level, especially by exploiting the transparency of early life stages (218).

Transgenic Lines to Trace Bone Cells

The most frequently used lines expressing fluorophores in chondrocytes include Tg(-4.9sox10:egfp)^{ba2} and Tg(Col2a1aBAC:mcherry)^{hu5910} (Table 2). The Tg(-4.9sox10:egfp)^{ba2} was employed to detect *sox10* expression in head cartilage during embryo development and to follow migration of neural crest cells during cranium morphogenesis (175). The Tg(Col2a1aBAC:mcherry)^{hu5910} reporter line allowed impaired cartilage patterning and loss of chondrocyte organization to be shown in a zebrafish model of a recessive form of Ehlers-Danlos syndrome with partial loss of B4gal7, a transmembrane Golgi enzyme that plays a pivotal role in proteoglycan biosynthesis (76).

In order to trace the differentiation of bone forming cells, transgenic lines for both early and late osteoblast markers, expressing fluorophores under the *osterix/sp7* and *osteocalcin/bglap* promoters, have been generated (Table 2). The Tg(sp7:EGFP)^{b1212} line allowed osteoblast behavior to be studied during both intramembranous and endochondral ossification. Moreover, this line was used to investigate the abnormal perichondral ossification in the RNA component of the mitochondrial RNA-processing endoribonuclease (*rmrp*) knock-out zebrafish model of cartilage hair hypoplasia (65). Tg(Ola.sp7:mCherry)^{zf131} was crossed with the OI type XIII zebrafish model *frilly fins* to elucidate the role of the bone morphogenic protein 1, encoded by *bmp1a* gene, in osteoblast differentiation and localization (94).

The Tg(Ola.bglap.1:EGFP)^{hu4008} line was used to understand the fundamental role of osteoblast dedifferentiation during bone healing in response to traumatic injury, and to show that adult zebrafish osteoblasts display an elevated cellular plasticity compared to their mammalian counterpart (195).

Despite the conservation of most of the osteoblastogenic markers, in zebrafish the expression of *col10a* is not limited to chondrocytes as in mammals, but is also present in osteoblasts (203). The transgenic line Tg(-2.2col10a1a:GFP)^{tk3}, expressing GFP under *col10a1* promoter, has therefore been used to

investigate molecular events driving both chondrocyte and osteoblast development (203).

An interesting application of the transgenic reporter lines is their use in combination with a mineral stain, imaged at different fluorescent wavelengths, enabling the combined study of osteoblast dynamics and bone mineralization (196). For instance, alizarin red staining of the transgenic zebrafish Tg(Ola.sp7:NLS-GFP)^{zf132} localized *osterix/sp7* positive osteoblasts in the mineralized bone and revealed the absence of *osterix/sp7* expression in the anterior notochord region at 8 dpf (104). Similarly, mineral staining in combination with Tg(*osx:Kaede*)^{pd64} confirmed the osteoblast independent mineralisation of the notochord (196).

Most of the available osteoclast reporter lines express fluorophores under control of the promoter of cathepsin K (*Ctsk*), the osteoclast collagenase that mediates bone resorption (Table 2) (46). Chatani et al. (97) proved the absence of osteoclasts in the *panther* mutant, which lacks a functional receptor for the macrophage colony stimulator factor, taking advantage of the Tg(*ctsk:mEGFP*) transgenic line. A significantly reduced number of GFP-positive osteoclasts was found in the neural and haemal arches in *panther* larvae, indicating a crucial role of the protein in osteoclast proliferation and differentiation. Additionally, the medaka, another well-characterized teleost bony fish used for developmental and biomedical studies, was used to study osteoclasts by placing the gene encoding for the receptor activator of nuclear factor kappa-B ligand, *rankl*, a key osteoclast differentiation factor, under the control of a heat shock element (23). Increased osteoclast differentiation induced upon Rankl activation in this Tg(*rankl:HSE:CFP*) line resulted in an osteoporotic phenotype (46).

Transgenic Lines to Trace Signal Transduction Pathways

Zebrafish transgenic lines expressing *in vivo* reporter proteins under the control of signaling pathway responsive elements are a powerful tool to dissect dynamically the *in vivo* activation or repression of endogenous signaling pathways in real time (210, 219–221). Calcium, Bmp and Wnt pathways are crucial players during bone formation (222–224). Transgenic lines to further investigate these pathways have been generated (Table 2). The Tg(*hsp70:bmp2b-GFP*) line was used to analyze the role of the Bmp2 signaling pathway in an enteric disease, but the transgenic model could be employed to dissect BMP2b signaling in bone (225). To investigate Wnt pathway activation the Tg(7xTCF-Xla.Siam:GFP)^{ia4} and Tg(7xTCF-Xla.Siam:nlsmCherry)^{ia5} transgenic lines, which contain multimerized *tcf/lef* binding sites for the transcription factor activated by β -catenin upstream to a siamois minimal promoter, were generated allowing the dynamics of neural crest-derived cell migration to be traced during development (211). Using the Tg(7xTCF-Xla.Siam:nlsmCherry)^{ia5} transgenic line it was also possible to elucidate important regulatory steps in the osteogenic differentiation process of mesenchymal stem cells (73).

Finally, the unfolded protein response (UPR) was shown to play an important role in the modulation of the phenotype in rare

TABLE 2 | Transgenic lines employed to study zebrafish skeleton.

Cell type	Gene/pathway	Transgenic line	References	Applications	
Neural crest-derived skeletal cells	<i>sox10</i>	Tg(<i>sox10:GFP</i>) ^{ba5}	(170)	(170) [#] , (19) [*]	
	<i>sox10</i>	Tg(<i>sox10:kaede</i>) ^{zf393}	(171)	(90, 171) [#]	
	<i>sox10</i>	Tg(<i>sox10:mRFP</i>) ^{vu234}	(172)	(78, 172) [*]	
	<i>sox10</i>	Tg(-4725 <i>sox10:Cre</i>) ^{ba74}	(173)	(173, 174) [#]	
	<i>sox10</i>	Tg(-4.9 <i>sox10:egfp</i>) ^{ba2}	(175)	(175–177) [#]	
	<i>fli1</i>	Tg(<i>fli1:EGFP</i>) ^{v1}	(178)	(19, 78, 89, 178, 179) [*]	
Cartilaginous cells	<i>foxp2</i>	Tg(<i>foxp2-enhancerA:EGFP</i>) ^{zc42}	(180)	(180, 181) [#]	
	<i>col2a1a</i>	Tg(<i>Col2a1aBAC:mcherry</i>) ^{hu5910}	(40)	(78, 91, 105) [*] , (40, 182) [#] , (76) [*]	
	<i>col2a1a</i>	Tg(-1.7 <i>col2a1a:EGFP-CAAX</i>) ^{hu12}	(183)	(183, 184) [#] , (112) [*]	
	<i>col18a1</i>	Tg(16Hsa.COL18A1-Mmu.Fos:EGFP) ^{zf215}	(185)	(185) [#]	
Preosteoblasts	<i>cyp26b1</i>	Tg(<i>cyp26b1:YFP</i>) ^{hu5786}	(72)	(72) [#]	
	<i>cyp26b1</i>	Tg(<i>cyp26b1:YFP</i>) ^{hu7426}	(186)	(186) [#]	
Branchial arches and notochord cells	<i>cyp26a1</i>	Tg(<i>cyp26a1:eYFP</i>) ^{nu1/+}	(187)	(187, 188) [#]	
Intervertebral disc cells	<i>shhb</i>	Tg(-5.2 <i>shhb:GFP</i>) ^{mb1}	(189)	(189) [#]	
	<i>twist</i>	Tg(<i>Ola.twist1:EGFP</i>) ^{ca104}	(190)	(190) [#]	
Early osteoblasts	<i>osx/sp7</i>	Tg(<i>sp7:EGFP</i>) ^{b1212}	(181)	(73, 181) [#] , (112, 179, 191, 192) [*] , (193) [§] , (65) [*]	
	<i>osx/sp7</i>	Tg(<i>Ola.sp7:mCherry</i>) ^{zf131}	(72)	(94) [*] , (72) [#]	
	<i>osx/sp7</i>	Tg(<i>Ola.sp7:NLS-GFP</i>) ^{zf132}	(72)	(194) [§] , (72, 195) [#] , (78, 85) [*] , (196) [#]	
	<i>osx/sp7</i>	Tg(<i>osterix:mCherry-NTR</i>) ^{pd46}	(197)	(197, 198) [§]	
	<i>osx/sp7</i>	Tg(<i>osx:Kaede</i>) ^{pd64}	(198)	(196, 199) [#] , (198) [§]	
	<i>osx/sp7</i>	Tg(<i>osx:CFP-NTR</i>)	(200)	(200) [#]	
	<i>osx/sp7</i>	Tg(<i>osx:H2A-mCherry</i>) ^{pd310}	(198)	(198) [§]	
	<i>osx/sp7</i>	Tg(<i>osterix:Lifeact-mCherry</i>) ^{cu2032}	(201)	(201) [§]	
	<i>col10a1</i>	Tg(<i>Col10a1BAC:mCitrine</i>) ^{hu7050}	(202)	(78, 91, 105) [*] , (202) [#]	
	<i>col10a1</i>	Tg(-2.2 <i>col10a1a:GFP</i>) ^{ck3}	(203)	(203, 204) [#]	
	<i>runx2</i>	Tg(<i>Hsa.RUNX2-Mmu.Fos:EGFP</i>) ^{zf259}	(205)	(95, 195) [#] , (205) [§]	
	<i>runx2</i>	Tg(<i>RUNX2:egfp</i>)	(31)	(31) [#] , (182) [*]	
	<i>osc/bglap</i>	Tg(<i>Ola.bglap.1:EGFP</i>) ^{hu4008}	(205)	(105, 195) [*] , (205) [§]	
	Mature osteoblasts	<i>entpd5a</i>	TgBAC(<i>entpd5a:YFP</i>) ^{hu5939}	(85)	(35) [#] , (85) [*]
		<i>entpd5a</i>	TgBAC(<i>entpd5a:Kaede</i>) ^{hu6867}	(195)	(195) [*] , (35) [#]
<i>col1a1</i>		Tg(<i>col1a1:EGFP</i>) ^{zf195}	(31)	(31) [#] , (18) [*]	
<i>rankl</i>		Tg(<i>rankl:HSE:CFP</i>)	(46)	(46) [*]	
<i>notch1a</i>		Tg(<i>Ola.sp7:N1a(CD)</i>) ^{cy31}	(79)	(79) [#]	
Osteoclasts	<i>ctsk</i>	TgBAC(<i>ctsk:Citrine</i>) ^{zf336}	(206)	(105) [*]	
	<i>ctsk</i>	Tg(<i>ctsk:YFP</i>)	(206)	(105) [*]	
	<i>ctsk</i>	Tg(<i>ctsk:DsRed</i>)	(207)	(207) [#]	
	<i>ctsk</i>	Tg(<i>CTSK-DsRed</i>)	(97)	(97) [#]	
	<i>ctsk</i>	Tg(<i>Ola.ctsk:EGFP</i>) ^{zf305}	(97)	(97) [#]	
	<i>ctsk</i>	Tg(<i>ctsk:mEGFP</i>)	(46)	(46, 208) [*]	
	<i>trap</i>	Tg(<i>TRAP:GFP</i>)	(97)	(97) [#]	
	<i>trap</i>	Tg(<i>trap:GFP-CAAX</i>) ^{cu2031}	(201)	(201) [§]	
Bmp responsive cells	Bmp pathway	Tg(<i>Bre:GFP</i>) ^{pf77}	(209)	(209) [#]	

(Continued)

TABLE 2 | Continued

Cell type	Gene/pathway	Transgenic line	References	Applications
β-catenin activated cells	Bmp pathway	Tg(<i>bre:egfp</i>) ^{pt510}	(210)	(177, 210) [#]
	Bmp pathway	Tg(<i>BMPRE:EGFP</i>) ^{ia18}	(169)	(169) [#] , (78) [*]
	Wnt pathway	Tg(<i>7xTCF-Xla.Siam:GFP</i>) ^{ia4}	(211)	(211) [#] , (78) [*]
	Wnt pathway	Tg(<i>7xTCF-Xla.Siam:nlsmCherry</i>) ^{ia5}	(211)	(73, 211) [#]
	Wnt pathway	Tg(<i>hsp70l:wnt8a-GFP</i>) ^{w34}	(212)	(213) [#]
	Wnt pathway	Tg(<i>hsp70l:dkk1-GFP</i>) ^{w32}	(214)	(73) [#] , (214) [§]
Stress responsive cells	Wnt pathway	Tg(<i>myl7:EGFP</i>) ^{hw34}	(215)	
	UPR pathway	Tg(<i>ef1α:xbp1δ-gfp</i>) ^{mb10}	(216)	(216) [#]
	UPR pathway	Tg(<i>Hsa.ATF6RE:d2GFP</i>) ^{mw85}	(217)	(217)
	UPR pathway	Tg(<i>Hsa.ATF6RE:eGFP</i>) ^{mw84}	(217)	(217)

*Transgenic lines used to characterize mutants with skeletal pathologies, #transgenic lines used to analyse skeletal development and molecular pathways, §transgenic lines used to study skeletal regeneration, Medaka transgenic lines are reported in bold.

skeletal diseases (226, 227). Interestingly, transgenic zebrafish lines allowing different branches of this pathway to be followed are already available (216, 217, 228, 229). For instance, the transgenic zebrafish model Tg(*ef1α:xbp1δ-gfp*)^{mb10} has been used to trace *in vivo* the splicing of *xbp1*, one of the terminal effectors of the UPR (216).

Live Imaging of Bone Regeneration

Tracing bone cells *in vivo* using transgenic lines in adult zebrafish is challenging due to tissue depth and complexity, but is possible in external structures such as fin rays or scales, which are easily accessible and suitable for regeneration studies (198, 230, 231). Indeed, the available panel of transgenic lines expressing fluorescent and photo-switchable reporter genes in bone cells is useful to trace regeneration *in vivo* (198). This strategy has clarified important biological aspects such as the cellular basis of integumentary bone regeneration. *In vivo* imaging of the Tg(*sp7:EGFP*)^{b1212} transgenic line during caudal fin regeneration showed the presence of GFP positive cells at the amputation plane starting from 2 days post amputation (dpa) and their association with the formation of newly mineralized matrix by 5 dpa (181). Osteoblast lineage tracing in the Tg(*osx:Kaede*)^{pd64} clarified migration and dedifferentiation of scleroblasts during fin regeneration (196).

However, the slow rates of regeneration require long-term live imaging to capture dynamic cellular events to improve the understanding of development, homeostasis, and regeneration by stem cell populations (232). Thus, to enable up to 24 h of continuous live imaging, specific protocols for long-term anesthesia of adult zebrafish have been optimized (198). Indeed, the transgenic line Tg(*osx:H2A-mCherry*)^{pd310} allowed spatio-temporally distinct cell division, motility, and death dynamic within a founder osteoblast pool to be imaged as bone regenerates (198).

Transgenic Lines as Tool for Drug Screening

Transgenesis is not only used to analyze bone development over time, to assess a mutant phenotype or track cell signaling, but also

to evaluate drug screening effects (98, 104). Huang and colleagues employed the transgenic line Tg(*Ola.sp7:NLS-GFP*)^{zfl32} to test anti-osteoporosis chemical drugs. This line, that expresses GFP under control of *osterix/sp7*, allowed for a faster *in vivo* evaluation of drug effects on bone mass and density compared to traditional staining methods. In another study, the *osteocalcin/bglap* reporter transgenic line Tg(*Ola.Bglap:EGFP*)^{hu4008} was employed to test chlorpropamide effects on the nuclear factor kappa-light-chain-enhancer of activated B cells (NF-κB). The drug negatively regulated osteoblast-like cell dedifferentiation, thus helping to maintain bone forming cells in an active state promoting caudal fin ray regeneration (233).

Tips for Transgenic Lines Selection

For the proper selection of transgenic lines there are some aspects that require consideration. First, the choice of the reporter protein is influenced by differences such as color, brightness, toxicity, tissue penetration, subcellular localization, as well as the stability of the fluorescent protein. For instance, in order to study cell signaling dynamics or when performing prolonged cell lineage tracing, the use of long half-life fluorescent proteins is recommended. Furthermore, differences in signal pattern and intensity can be found among transgenic progeny possibly due to multiple insertions in the same founder, thus complicating the analysis (169). This aspect can be ameliorated by diluting the number of transgenic copies through subsequent generations.

Finally, in order to verify the localization of the reporter protein, the use of dual color analysis in the same transgenic line is recommended (196, 199) by for example complementary secondary techniques such as immunohistochemistry or *in situ* hybridization (169, 199).

X-RAY IMAGING

One of the more frequently used techniques to visualize the human skeleton is x-ray imaging. Classic x-ray systems for human and veterinary purposes need to limit radiation exposure to the patient, and therefore have limited exposure settings, that

is their range of tube accelerating voltage (kV), current (mA), and time of exposure. These parameters are set to optimize the image of the skeleton while keeping the radiation exposure to the patient as low as possible and cannot be easily changed. Consequently, these medical appliances are not appropriate to image the small zebrafish skeletons. Examples of x-ray sources that have a wide range of possible x-ray output settings are small manual units used to scan museum artifacts and fossils, a small animal radiation research platform (SARRP; Xstrahl, Surrey, UK) and the Faxitron[®] x-ray cabinets. Specifically, these sources can be set to low power but long exposure time parameters, and can be used in combination with high resolution technical film such as mammography film or x-ray film (e.g., AGFA D2) used in aerospace and petroleum factory applications. A Faxitron x-ray cabinet in combination with mammography film was used by Fisher et al. (93) to image the skeleton of WT and *chihuahua* mutant zebrafish to screen for skeletal abnormalities (Table 2).

With the revolution of digital sensors capturing the x-ray signal, it has become straightforward to take an x-ray image of a small or large part of the human skeleton. The use of digital x-ray sensors is however more challenging when using zebrafish (24, 234) as the resolution is too low in most cases to capture a quality image of the small zebrafish skeleton. A modern system such as a Faxitron Ultrafocus x-ray cabinet can provide digital x-ray images up to a 5 μm spatial resolution which can be geometrically magnified (Faxitron[®]) (Figure 3A). This technique was used to screen for deformed and fragile bones in *chihuahua* mutant zebrafish (15) and to assess the gross skeletal anatomy of *prg4a*^{-/-}; *prg4b*^{-/-} mutant zebrafish (92). Although these digital images may look clean and sharp, the thinner less mineralized bones may not be present in the image, which represents a loss of information about the zebrafish skeleton (234). In contrast, technical film such as AGFA D2 can theoretically capture extremely high-resolution images. Such technical film works well in combination with low energy settings needed for optimal imaging of the zebrafish skeleton. Moreover, this film is able to capture an image of smaller bones, which is not always possible when using a digital sensor.

The main advantage of using x-rays to image the zebrafish skeleton is that it is a cheap and quick methodology. Furthermore, x-ray imaging can be repeated on live organisms and can be used as a preliminary diagnostic tool for skeletal imaging before applying a more specialized method such as micro computed tomography (microCT) or mineral staining (Figures 3B,C). For instance, x-ray imaging is frequently used in aquaculture related research where it is a first line tool to assess skeletal deformities (235, 236). Although x-ray imaging can be employed to assess skeletal deformities in adult zebrafish, its use for juvenile zebrafish, where the skeleton is too small to be captured on film or digitally, is not feasible. In addition, x-ray images of zebrafish are not suitable for quantification of tissue or bone mineral densities. MicroCT currently provides a better solution to estimate these bone parameters (80, 120).

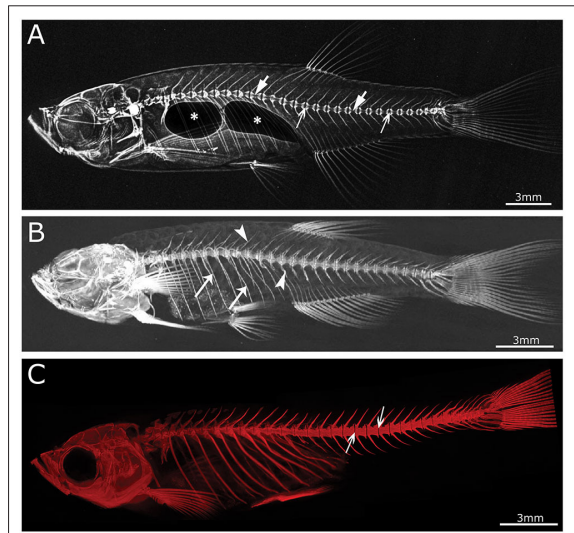


FIGURE 3 | Imaging techniques in zebrafish. **(A)** Lateral x-ray image of a wild type zebrafish acquired with a Faxitron tabletop X-ray cabinet. Notice the outline of the major bones in the skull and vertebral column and the outline of the double chambered swim bladder (indicated by asterisks) in the abdominal cavity. The tissue inside the vertebrae (indicated by block arrows) and intervertebral spaces (indicated by line arrows), i.e., the notochord, can be easily assessed for the presence of mineral. **(B)** Lateral view of a 3D reconstructed microCT scanned adult zebrafish at 21 μm . More details are visible in the skull and especially the vertebral column compared to the x-ray image (neural and haemal arch are indicated by arrow heads and the ribs with a small arrows). **(C)** Lateral image in the fluorescent channel of a zebrafish whole mount cleared and stained with alizarin red for mineralized tissues. Compared to the images above, more details of the skeleton can be observed, especially in the vertebral column where all individual bones and their outlines can be noticed. The alizarin red image also allows to assess the presence of mineral in the intervertebral space (indicated by arrows). All images were taken of wild type zebrafish.

MICRO COMPUTED TOMOGRAPHY

Computed tomography (CT) is a non-invasive technology based on x-ray analysis that allows detailed 3D reconstructions of large specimens. The generation of CT images involves the capturing and recording of x-rays that pass through the sample onto a detector. This process is repeated several times for multiple angles, followed by the virtual reconstruction into a 3D image (237). The required resolution for zebrafish imaging is beyond the capabilities of medical CT machines ($\geq 70 \mu\text{m}$), requiring higher resolutions, which can be obtained by microCT (Figure 3B) (237). The resolutions that can be achieved with modern microCT scanners vary from relatively low resolutions ($\geq 20 \mu\text{m}$), with quick scan times and large sample size, to higher resolutions ($\leq 10 \mu\text{m}$), with longer scanning durations and smaller sample size. It is important to note that the magnification, often described as the size of the voxels (3D pixels) is not identical to spatial resolution, which is roughly 2–3 times larger

(238). MicroCT is less time consuming and provides excellent 3D resolution compared to optical microscopy/histology. Although mainly mineralized tissues are recorded, resulting in a loss of information on aspects such as cells and non-mineralized tissues, the use of contrast agents allows visualization of different tissues such as adipose or epithelial tissue and can even enhance the signal of poorly mineralized bone (239, 240). For example, scanning of juvenile stages can be performed by staining the samples with silver nitrate beforehand, allowing for visualization of early bone development where only low amounts of mineral are present (241). However, with this approach only relative mineralization densities can be determined, and not absolute hydroxyapatite levels, which is an important parameter when modeling skeletal disorders. The amount of hydroxyapatite present in samples can be determined by performing a calibration microCT scan of a reference object (phantom) with a known hydroxyapatite concentration. This approach was used in a study of the effect of aging on bone mineral density (BMD) in zebrafish, revealing progressively increased BMD with age, in contrast to humans (101). When interpreting skeletal phenotypes, it is important not to rely on a single method, because certain phenotypes can be better detected using other methods. For example, a mineralized notochord leading to completely solid centra is easier to assess using microCT compared to mineral staining (72). In addition to 3D renderings, microCT data allows the creation and viewing of individual slices throughout the sample, similar to histological sections. Histology of mineralized tissues is notoriously difficult and requires special protocols because samples cannot be demineralized for sectioning. As an example, a complementary approach of both histology and high resolution microCT ($6\ \mu\text{m}$) was used in a zebrafish model for craniosynostosis revealing fusion of the coronal suture (107).

Although low resolution microCT ($\geq 20\ \mu\text{m}$) does not allow the detection of subtle skeletal changes, such as fusions between adjacent bones, it is perfectly suitable for whole-body scanning and phenotyping of adult zebrafish with a moderate throughput (Figure 3B). Such a procedure was applied by Gistelink et al. (120), where individual vertebral bodies (neural/haemal arches and centrum) of different OI zebrafish models were manually segmented. Subsequently, tissue mineral density (TMD), vertebral length, bone volume, and thickness were determined for each component (80). Manual segmentation is a laborious process and possibly introduces human bias into the analysis, which can be overcome by semi-automated segmentation algorithms such as FishCut (80). FishCut enables the measuring of a large number of parameters in the vertebral column, and is supplemented by a statistical approach for analysis (80). Models for Bruck syndrome, osteogenesis imperfecta and hyperthyroidism have been successfully analyzed by this high-throughput pipeline, thereby standardizing zebrafish skeletal analyses (80, 120). High resolution microCT ($\leq 10\ \mu\text{m}$) on the other hand, allows for more detailed analysis, but is very time consuming and limits the scanning to only small segments of the skeleton (Figure 4). MicroCT scans of a vertebral body at $1\ \mu\text{m}$ voxel size revealed osteocyte lacunae, which is beyond the resolution range of whole body microCT scans (Figures 4B,D) (242). In a study by Newham et al. (118), high

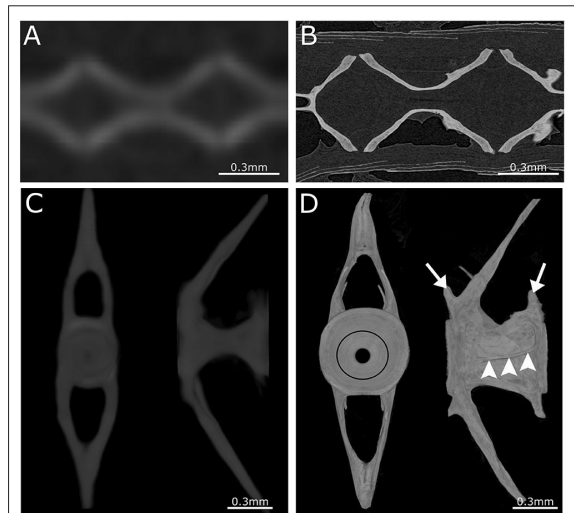


FIGURE 4 | Comparison between low- and high-resolution microCT. **(A)** Image of parasagittal microCT plane at $21\ \mu\text{m}$. **(B)** Similar structure as in **(A)** but scanned at $0.75\ \mu\text{m}$. Comparison between low-resolution and high-resolution microCT clearly demonstrates the ability to distinguish separate vertebrae and compact bone only using high-resolution microCT. **(C)** Anterior and lateral view of a 3D maximal projection surface render of a vertebrae scanned at $21\ \mu\text{m}$. **(D)** Similar structure as in **(C)** but scanned at $0.75\ \mu\text{m}$. Notice the difference in detail where the growth rings (black circle) are visible in the vertebral endplate on the anterior view. The lateral view of high-resolution microCT shows the outline of the vertebra with the pre- and post-zygapophyses (white arrows), and an antero-posterior running medial vertebral trabecula (white arrowheads).

resolution scans of vertebral bodies before and after mechanical compression were analyzed via geometric morphometrics. The obtained measurements were successfully used to determine the deformation zones and subsequently used to predict the deformation and strain during loading (118).

BONE HISTOLOGY: FROM WHOLE MOUNT TO SECTIONS

Whole mount staining and high-resolution section analysis of the zebrafish skeleton represent complementary techniques, commonly used to describe bone development and structure at tissue and cellular levels.

Whole Mount Mineral and Cartilage Staining

In biomedical research, where the zebrafish is used as a model organism, whole mount staining is generally used to study the morphology of the skeleton (Table 3). The most commonly used techniques are staining of mineralized tissues with alizarin red S (ARS), staining of cartilage matrix with alcian blue (AB) or staining both tissues with a combination of both ARS and AB (Figure 5). These staining methods are based on well-established protocols, where a specimen is made translucent to transparent

TABLE 3 | Techniques applied to evaluate bone phenotype in zebrafish models.

Disorder	Stage	AR	AB	Dual stain	Calcein	Morphology	Histology	TEM	SEM	ISH	Transgenics	MicroCT	X-Ray	AFM	qBei	Nanoindentation	FTIR	References
Acrocapitofemoral dysplasia	L			x							x							(40)
Alagille syndrome	L			x	x					x								(61)
Amelogenesis imperfecta	L	x	x															(62)
Auriculocondylar syndrome	L			x		x												(63)
Bruck syndrome	L-J-A	x	x			x	x	x				x						(16)
Campomelic dysplasia	L		x		x	x				x								(64)
Cartilage-Hair Hypoplasia	L	x		x		x				x	x							(65)
Cenani-Lenz syndactyly	L		x			x				x								(66)
Chordoma	L						x	x			x							(67)
Cleidocranial dysplasia	L		x				x			x								(68)
Craniofacial defects	L			x			x											(69)
Craniofacial defects	L			x			x											(69)
Craniosynostosis	L-A	x								x	x							(70)
Craniosynostosis	L			x		x				x								(71)
Craniosynostosis	L-A	x		x	x	x					x	x						(72)
Culler-jones syndrome	A				x		x				x							(73)
Delayed mineralization	L			x			x			x	x							(74)
Delayed mineralization	L-A	x		x		x												(75)
Ehlers-Danlos syndrome	L	x	x			x												(76)
Fibrodysplasia ossificans progressiva	L-A	x				x	x					x						(77)
Gaucher disease	L			x		x		x			x							(78)
Holoprosencephaly	L			x							x							(40)
Hyperosteogeny	L-A			x	x	x	x				x		x					(79)
Hyperthyroidism	A												x					(80)

(Continued)

TABLE 3 | Continued

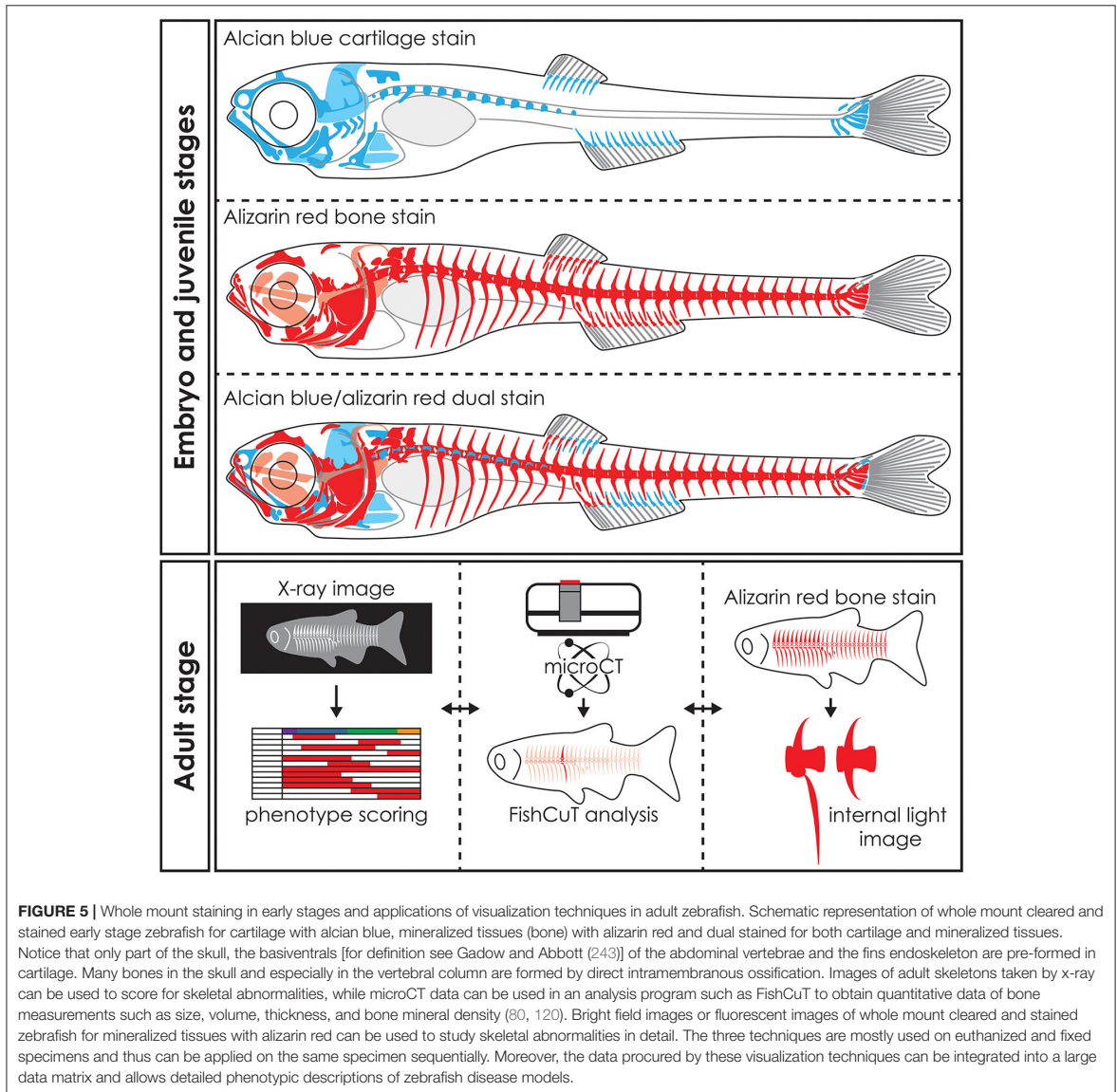
Disorder	Stage	AR	AB	Dual stain	Calcein	Morphology	Histology	TEM	SEM	ISH	Transgenics	MicroCT	X-Ray	AFM	qBei	Nanoindentation	FTIR	References
Hypohidrotic ectodermal dysplasia	A	x		x		x					x	x						(81)
Joint disease	L-A	x		x		x	x			x	x	x						(82)
Klippel Feil syndrome	L A	x																(83)
Multiple hereditary exostoses	L	x	x							x								(84)
No mineralization	L-A	x	x	x		x				x	x							(85)
Oculodentodigital dysplasia	A								x							x		(86)
Orofacial cleft	L	x	x	x		x												(87)
Orofacial cleft	L			x														(88)
Orofacial cleft	L		x			x				x	x							(89)
Orofacial cleft	L		x			x					x							(90)
Osteoarthritis	L-A			x			x				x	x		x				(91)
Osteoarthritis	L-A		x				x			x	x	x	x					(92)
Osteogenesis imperfecta	L-A			x						x			x					(93)
Osteogenesis imperfecta	L-A	x		x		x	x			x	x							(94)
Osteogenesis imperfecta	L-A	x					x	x		x	x							(95)
Osteogenesis imperfecta	L-A	x				x						x						(96)
Osteogenesis imperfecta	L-A			x	x	x						x	x					(15)
Osteogenesis imperfecta	L-A			x	x							x			x	x	x	(14)
Osteopetrosis	L-A	x			x	x	x	x										(97)
Osteoporosis	L				x	x												(98)
Osteoporosis	L	x																(99)
Osteoporosis	A					x	x					x						(100)
Osteoporosis	A					x						x						(101)
Osteoporosis	L	x	x	x	x						x							(102)
Osteoporosis	L-A	x	x	x	x	x						x						(20)
Osteoporosis	L	x				x												(103)

(Continued)

TABLE 3 | Continued

Disorder	Stage	AR	AB	Dual stain	Calcein	Morphology	Histology	TEM	SEM	ISH	Transgenics	MicroCT	X-Ray	AFM	qBei	Nanoindentation	FTIR	References
Osteoporosis	L			x		x	x				x							(19)
Osteoporosis	L										x							(18)
Osteoporosis	L	x				x					x							(104)
Pseudoxanthoma elasticum	L-J	x		x	x	x					x							(105)
Pseudoxanthoma elasticum	L-J	x				x				x	x							(106)
Saethre-Chotzen syndrome	A	x		x				x				x						(107)
Saul-Wilson Syndrome	L		x															(108)
Spine curvature disorders	L-J-A			x		x				x		x						(109)
Spine curvature disorders	L-J-A				x	x						x						(110)
Spine curvature disorders	J-A	x																(111)
Spine curvature disorders	L-A	x	x			x		x			x	x						(112)
Spine curvature disorders	L-A	x			x					x	x							(35)
Spine curvature disorders	L-A					x				x		x						(113)
Spine curvature disorders	A					x	x					x						(114)
Sponastrime dysplasia	L			x														(115)
Stickler/Marshall syndrome	L		x			x	x	x										(116)
Tumoral calcinosis	A								x		x							(117)
Vertebral fractures	A					x						x						(118)

L, Larval stage; J, Juvenile stage; A, Adult stage; AR, Alizarin red; AB, Alcian blue; TEM, Transmission electron microscopy; SEM, Scanning electron microscopy; AFM, Atomic force microscopy; qBei, Quantitative backscattered electron imaging; FTIR, Fourier-transform infrared spectroscopy.



and cartilage matrix or mineralized tissues are stained with a dye. Images of whole mount cleared and stained animals, taken with a modern stereo microscope, have an even higher resolution than standard microCT images (Figures 3B,C). Therefore, the whole mount clearing and staining technique can be considered as the gold standard for observing the whole zebrafish skeleton in detail.

Alizarin Red S

Many different protocols exist for ARS staining of mineralized tissues, however the main steps are based on (i) removing the pigmentation of the tissue with a bleaching solution (basic pH),

(ii) neutralization of depigmentation, (iii) staining the animal with ARS, and (iv) clearing the animal of excess stain (244). The ARS molecule is a dihydroxyanthraquinone, likely binding the Ca^{2+} on the hydroxyapatite surface to form either a salt or a chelate form (245), thus it specifically stains mineralized tissue. In disease models ARS will stain ectopic mineralization in soft tissues. For example, ectopic mineralization was shown surrounding the eye, in the wall of the bulbus arteriosus of the heart and in the ventral skin of the dragon fish ($dgf^{-/-}$), a knock-out zebrafish model for the gene that encodes Enpp1, and modeled for generalized arterial calcification of infancy (GACI)

and pseudoxanthoma elasticum (PXE) (105, 106). Bone collagen in teleosts can also be deposited without being mineralized, as was shown in salmon vertebral bone (246, 247) and in the dentine of replacement teeth of the African bichir (248). It is important to underline that the unmineralized collagen cannot be visualized with ARS, however, mineralization usually quickly follows collagen deposition. Finally, there is also one mineralized collagenous tissue that does not stain with alizarin red S, the hypermineralized enameloid of the tooth cusps (248, 249).

ARS staining for mineralized tissues is frequently used to assess the development of skeletal elements in the head, axial skeleton, and fins at early life stages (Figure 5). In addition, investigating the early skeletal phenotype can be focused on a delay or advance in the development or specifically on the mineralization status of early skeletal elements. Because ARS is autofluorescent in the rhodamine channel (red), it can be used in combination with skeletal transgenic zebrafish reporter lines in which the fluorescent signal of the skeletal cells is in a different light spectrum. Alternatively, a Kaede reporter line, where the spectrum of the fluorescent protein can be changed by exposing the specimen to UV-light, can be used in a more flexible way (196). While most studies using ARS for mineralized tissue examined fixed specimens, ARS can also be used as a live stain especially in early stages where pigmentation does not obscure the underlying skeleton yet [reviewed in (250)]. Staining with ARS can also be employed to assess the juvenile and adult skeleton (Figure 5) because mineralized bone is the main skeletal tissue present at these life stages and is easy to observe with this technique.

Alcian Blue

Staining cartilage whole mounts with AB 8GX, similar to ARS staining, is based on several basic steps including (i) removing the pigmentation of the tissue with a bleaching solution (basic pH), (ii) staining the specimens with AB (acid pH), (iii) rehydration and clearing the specimens of excess stain, and (iv) dehydration and storing the specimens. The AB molecule is part of the phthalocyanine dyes with most often copper (Cu^{2+}) as the central metallic ion which results in a blue stain. AB has specifically four tetramethylisothiouonium solubility groups with S=C bonds that are easily broken to bind an insoluble AB molecule to the tissue (251). The stain binds as a salt to sulfated and carboxylated acid mucopolysaccharides and glycoproteins present in the cartilage matrix (251). Alcian blue is in most cases dissolved in a dehydrating ethanol/acetic acid solution and brought to a specific low pH. This low pH (1.5–2.5) causes AB to stain very specifically to the cartilage matrix (Figure 5).

Cartilage is the main skeletal tissue in early life stages of zebrafish, particularly in the skull (chondrocranium) and fins (252). Therefore, AB staining has been largely used in early life stages, i.e., 2–20 dpf, to study the morphology of the chondrocranium in different skeletal zebrafish models (62, 68) (Figure 5). Developing malformations are mainly defined as the irregular shape of skeletal elements, but can also be defined by the absence of skeletal elements or the incorrect morphogenesis of a single skeletal element (66, 84). Relative to the entire skeleton, not much cartilage is present in later life stages (late juveniles, adults)

of zebrafish, yet AB staining can be used to assess for example cartilaginous joints (92).

Alcian Blue/Alizarin Red S Double Stain

Staining of cartilage and mineralized tissues can also be combined in a single specimen, as described in several papers by Kimmel et al. (253, 254). In this protocol tissues are stained first with AB followed by ARS staining (Figure 5). The dual staining for cartilage and mineralized tissues is similar to the single stain methods, except that AB can also be dissolved in a salt/ethanol solution, where the salts can be sodium acetate or the more commonly used magnesium chloride (244, 255).

The dual staining protocol is mostly used to assess development of malformations of the early skeleton but can also be used to investigate the normal development and developmental sequence of the skeleton (69). More specifically, dual staining has been used to assess ossification and mineralization status of cartilaginous bones (40, 87) and shape morphology of skeletal elements (61, 166).

The main advantage of this staining technique is the visualization of both cartilage and bone in an individual specimen, so that both connective tissues can be studied at the same time. However, this approach has also several disadvantages. First, when an acid/ethanol solution is used for AB staining, this acidic staining solution demineralizes the tissues that are subsequently visualized with ARS. This results in a reduced staining of mineralized tissues compromising the correct phenotypic assessment. This issue was reviewed by Witten et al. (24). Therefore, it is advisable to always use single staining protocols, either as an alternative or as a validation method in parallel to the double staining protocol. Second, dissolving AB in a non-acidic salt/ethanol solution is however challenging because pH higher than 6 decreases the specificity of the staining solution for mucopolysaccharides and glycoproteins (251).

ARS and AB Whole Mount Staining Advantages and Pitfalls

Considering the simplicity and above all the extensive use of the ARS and AB whole mount staining, a brief overview of its general advantages and disadvantages may be useful.

Both the single staining and double staining approaches are cheap and generally fast to use. Specimens that have not developed scales yet, can often be stained in a single day, with observations made the same day or the day after. In contrast, adult specimens can take up to 2 weeks to stain (244). Indeed, staining protocols need to be adapted to the size of the specimens. Therefore, a thorough description of the staining protocol is indispensable for the interpretation and reproducibility of results (251, 256).

Detailed observations of cartilaginous and mineralized connective tissues can be made owing to the high sensitivity and specificity of both the ARS and AB stains. In particular, small mineralized structures such as the initial mineralizations in early life stages and small intermuscular bones or tendons in adult life stages can be visualized by ARS with high fidelity (24, 234), especially when using fluorescent light which greatly enhances the visibility of these small structures (55, 250). Importantly,

ARS stain disappears over time especially in small mineralized structures requiring immediate observation and imaging once the staining procedure is finished. In contrast, when specimens are stored correctly in 100% glycerol, AB staining will remain specific for a longer time (256).

Although AB stains cartilage matrix specifically when the correct pH is used, AB solutions with a pH that is too high or solutions that have a too high or too low salt concentration can result in non-specific staining of non-cartilaginous connective tissue, i.e., collagen type I bone matrix. Non-specific staining can lead to incorrect interpretations of results. Finally, careful interpretation is needed of single AB stained connective tissues in specimens of 15 dpf and older. During the perichondral ossification of cartilaginous bones in zebrafish (**Figure 2Bii**), when a collagenous sheath forms around cartilaginous bone, the AB solution fails to stain the cartilage, and therefore the cartilaginous connective tissue appears absent. The presence of cartilage beneath the collagen can however still be confirmed using oblique light settings.

Histological Stains

Bone histology is often necessary to complement other imaging techniques, such as whole mount imaging, and remains one of the methods of choice to investigate the skeletal phenotype and bone mineralization during developmental stages (**Table 3**). The small size of zebrafish has forced researchers to adapt existing, standard histological procedures performed on human and murine skeletal tissues. High quality histological preparations and extensive knowledge about the zebrafish skeletal anatomy and development are indispensable for a correct skeletal evaluation (36, 45). Since zebrafish share similar bone cell types and cellular markers with mammals, it is possible to apply the standard histological and histomorphometric staining protocols available for mammalian bone, although with some technical optimization. In zebrafish in particular, the cellular composition analysis requires high-magnification imaging because skeletal elements may consist of a very limited number of cells, that are smaller in comparison with mammalian cells (24).

Unlike humans and mice, histology on zebrafish can easily be performed on a whole specimen in different developmental stages. Skeletal development can be followed in early juvenile stages looking at the mineralization of the notochord sheath and of cranial bones, while in adult zebrafish histology is most often performed on the abdominal vertebra (the first 10 vertebrae articulated with ribs, although this number is variable), the scales and the caudal fin rays.

Histological Specimen Preparation

In general, the histological procedure for both whole adult zebrafish and dissected bone samples, involves fixation in 4% paraformaldehyde in phosphate buffer saline (PBS) pH 7.2 overnight at 4°C, decalcification in 10% EDTA pH 7.2 for 7 days at 4°C and dehydration according to standard histological protocols or in a gradient series of acetone solutions (199). Importantly, while no decalcification is required up to 20 dpf, for juvenile to adult life stages the time of decalcification varies and depends on the developmental stage and size. Juveniles from

21 dpf till adulthood are normally decalcified for 4 up to 7 days (257).

According to Oralova et al. (199), paraffin embedding does not provide high quality histological details of zebrafish embryos and of early juvenile stages. In these cases, epoxy, or methacrylate resin embedding media are recommended (258). From epoxy blocks, semi, and ultrathin sections can be obtained for light and transmission electron microscopy, respectively, while methacrylate is more suitable for histochemical reactions (24). When using transgenic zebrafish lines expressing fluorescent reporters, fluorescence is generally lost in paraffin embedded samples. Cryosections preserve fluorescence, but significantly decreases the quality of the morphological structure due to processing artifacts. For this reason, Oralova and colleagues developed a new protocol using glycol methacrylate (GMA) embedding, which preserves both fluorescent labeling, epitopes for immunostaining and morphology, making it a more suitable choice (199).

Staining of Skeletal Sections

Different stains can be applied to histological sections of the zebrafish skeleton. Masson's trichrome and toluidine blue are commonly used and generally allow visualization of collagen and particular aspects of bone. Masson's trichrome, which usually stains muscle fibers red, collagen and bone in blue/green, cytoplasm in light red/pink, and cell nuclei in dark brown to black, reveals much thinner layers of collagen fibrils in a mutant zebrafish model for type I collagenopathies, a heterogeneous group of connective tissue disorders caused by genetic defects in type I collagen (120). Toluidine blue is often used to detect bone cells, but is also a powerful dye to visualize proteoglycans, elastin and, when using birefringent light—collagen type I and type II fiber organization. Toluidine blue was used to detect abnormalities in glycosaminoglycan pattern in the pharyngeal skeleton of a zebrafish model for a recessive OI knock-out of *sec24C/sec24D*, two components of the COPII vesicle complex required for collagen secretion (259). Moreover, sections stained with toluidine blue showed compressed and deformed vertebrae, and excessive bone formation and remodeling at the vertebral endplates in the Bruck syndrome *plod2* mutant, characterized by the loss of type I collagen telopeptide lysyl hydroxylation (16).

The most widely used mineral staining assays include ARS, calcein and von Kossa staining, which specifically bind to calcium in the mineralized bone. In a study by Pasqualetti et al. (260), successive staining with ARS and calcein allowed evaluation of bone formation at the level of the circuli of growing scales in wild-type animals (260). In the *panther* fish, characterized by impaired osteoclast proliferation and differentiation, von Kossa staining enabled detection of altered mineralization of the neural arches (97).

Finally, collagen fiber maturation can be investigated by sirius red staining under polarized light, as performed to study the actinotrichia and lepidotrichia pattern in the *chihuahua* zebrafish, carrying a mutation in collagen type I $\alpha 1$ chain (15, 93, 261).

Transmission Electron Microscopy Analysis

Transmission electron microscopy (TEM) has also been used to investigate zebrafish bone. TEM represents a powerful method to analyze ultrastructural features of tissues since it provides much higher magnification and resolution compared to light microscopy, allowing visualization of cellular and matrix structures at a subnanometer scale. For instance, an altered distribution of bone collagen fiber diameter, a frequently described feature in various skeletal pathological conditions, was detected in the *crtap* and *p3h1* knock-out models of OI type VII and VIII by TEM, revealing the crucial role of the collagen post translational modification complex in bone organization (17). TEM was also used to show enlarged endoplasmic reticulum cisterna in these models, reinforcing ER stress as a key element in the OI phenotype and a potential target for new therapeutic approaches (17, 226, 227).

Immunohistochemistry

Immunohistochemistry (IHC) on zebrafish sections is also possible but limited, compared to mammal specimens, given the reduced availability of specific zebrafish antibodies. Nonetheless, with IHC, the spatiotemporal pattern of distribution of several proteins, a key prerequisite for understanding development, have been elucidated in embryos both in physiological and pathological conditions (199). For example, a structural defect in the extracellular matrix (ECM) has been detected in the *fncl3a^{wue1/wue1}* zebrafish where IHC of type II collagen showed a loss of mature actinotrichia in 52 h post fertilization (hpf) embryos and β -catenin staining revealed divergent ECM assembly in the regenerated adult fin (262).

Determining the exact spatial localization of the protein of interest in immunostained whole mount larvae is difficult, especially for more deeply located tissues. To overcome this limitation, it is possible to perform whole-mount IHC followed by GMA embedding and sectioning, as was shown by Oralova et al. (199). In this way, the distribution of labeled cells was mapped and quantified allowing for close investigation of the cellular behavior during tissue development, cell migration, and adhesion events, as well as growth and differentiation. As an example, the use of a pan cytokeratin antibody on Tg(*sox17:egfp*) embryos allowed the authors to localize the protein of interest, Sox17, and the epidermis in the same section (199).

Finally, alkaline phosphatase (Alp), expressed by osteoblasts and required for the mineralization of extracellular matrix, and Trap, expressed by osteoclasts, and important for bone resorption, can both be immunostained to detect active osteoblasts and osteoclasts, respectively, and have been used for example to follow cell differentiation in scales (260).

Histological Analysis of Tissue Regeneration

Zebrafish's ability to repair caudal fin rays and scales has led to the optimization of specific histological protocols for these tissues involving both tissue sectioning as well as whole organ analysis (263). The analysis of histological sections has made clear that during regeneration in the caudal fin rays, cells near the site of injury can dedifferentiate, proliferate and replace the damaged

or missing cells (196, 264). Furthermore, histological studies have identified a population of *Runx2/Sp7* positive chondrocytes involved in bone repair, and have helped to elucidate the ability of periosteal cells to generate cartilage in response to injury in *indian hedgehog homolog a (Ihha)* mutants (265).

To study mineralization and cellular compositions of caudal fin rays and scales, the tissue can also be isolated and directly stained without the need for dehydration and sectioning. For instance, by using ARS and calcein double staining and ALP immunohistochemistry, the specific mineralization pattern of bone forming cells in different areas of a scale was elucidated (260). Masson's trichrome staining of regenerating ray collagen proved that multiple amputations do not affect the regenerative bone capacity (266).

IS THE MEDAKA AN ALTERNATIVE TOOL IN SKELETAL RESEARCH?

Together with zebrafish, medaka (*Oryzias latipes*) is the other most frequently used small teleost in biomedical research. This species native to East Asia, belongs to the Adrianichthyidae family (order Beloniformes) and had an ancestor living in saltwater (267).

Evolutionarily, zebrafish and medaka are distantly related (268), with the last common ancestor dating back 110–200 million years ago (269). Being a small fish, medaka shares all the advantages already described for zebrafish, although it has a faster generation time, 2 vs. 3 months, shortening genetic experiments (23).

Similar to zebrafish, the medaka shares common skeletal developmental schemes as well as the presence of most of skeletal cells, chondrocytes, osteoblasts, and osteoclasts with tetrapods, but notably is missing osteocytes (23, 24).

The medaka genome, that underwent a whole duplication like that of the zebrafish, is available and easy to manipulate using the same techniques as in zebrafish research allowing easy generation of skeletal disease models and transgenic lines (46, 208, 270–273).

The almost completely conserved phenotypic features between zebrafish and medaka allow researchers to exploit the same imaging techniques to analyze skeletal components in both physiological and pathological conditions, either in terms of x-ray imaging or more specialized methods, such as microCT, whole mount or histological staining methods (23).

LIMITATIONS OF THE ZEBRAFISH MODEL

To take full advantage of the zebrafish as a model of human diseases it is important to be aware of existing drawbacks. Due to the extra whole genome duplication compared to mammals, as mentioned above, about 20% of the zebrafish genes have two functional copies, complicating the generation of knock-out disease models (274). Furthermore, some of the duplicated genes have functionally diverged, thus limiting the use of zebrafish in accurately modeling human diseases (11, 24). Additionally, the limited availability of antibodies against zebrafish proteins and the difficulty in establishing tissue specific primary cell

lines impairs zebrafish use in research. Finally, the generation of conditional knock-outs and knock-ins is still difficult in zebrafish. Although recently a method to integrate *loxP* sequences at specific sites in the zebrafish genome using the CRISPR/Cas9 technology has been developed, and conditional mutants of *tbx20* and *fleer* have been generated employing Cre recombinase technology (275, 276).

CONCLUSIONS

In the last decade the zebrafish has emerged as a unique model to investigate common and rare human skeletal disorders. The advances in gene editing techniques, from the initial insertion of random genomic mutations by exposure to mutagenic substances, to the knockdown expression of specific genes by antisense morpholino oligonucleotides, to the change of the genome at a specific site by nuclease technologies and their simple use in zebrafish, have all allowed research groups to generate new bone disease models. In particular, the versatile and cheap CRISPR/Cas9 system has found a wide use in many laboratories and undergone a series of optimizations allowing an increasingly specific and error-free gene editing. Nevertheless, its use for knock-in mutations still requires further optimization. The combining of zebrafish skeletal disease models with already available or newly generated transgenic lines, has contributed tremendously to the advances made in *in vivo* analysis of bone cells. The advances in confocal microscopy and the emergence of light sheet microscopy allows for better visualization and

characterization of larval phenotypes in skeletal disease models, taking advantage of larvae transparency. X-ray and microCT have been optimized for small adult zebrafish bones, allowing analysis of the whole skeleton or small elements at high resolution. On the other hand, traditional skeletal specific dyes, such as alizarin red and alcian blue remain a valuable tool to study bone in larvae and adults. Finally, biomedical research has an urgent need for high throughput drug screening platforms and zebrafish models of skeletal diseases represent a bridge from *in vitro* to *in vivo* approaches.

In conclusion, ongoing technological advances in analytical techniques are making the zebrafish emerge as a unique and powerful model for the investigation and understanding of human skeletal disorders, and additionally as an efficient platform for compound discovery.

AUTHOR CONTRIBUTIONS

FT, JB, RB, AD, AW, and AF: writing—original draft. All authors: review and editing. LL, JB, and AD: figures.

FUNDING

This work was supported by the Italian Ministry of Education, University and Research (MIUR) [Dipartimenti di Eccellenza (2018–2022)] and the Brittle Bone Foundation Grant-2019 to AF. The study was supported by Ghent University (Methusalem Grant BOFMET2015000401).

REFERENCES

- Gut P, Reischauer S, Stainier DYR, Arnaout R. Little fish, big data: zebrafish as a model for cardiovascular and metabolic disease. *Physiol Rev.* (2017) 97:889–938. doi: 10.1152/physrev.00038.2016
- Russel WMS, Burch RL. *The Principles of Humane Experimental Technique*. Wheathampstead: Universities Federation for Animal Welfare (1959).
- Carnovali M, Banfi G, Mariotti M. Zebrafish models of human skeletal disorders: embryo and adult swimming together. *Biomed Res Int.* (2019) 2019:1253710. doi: 10.1155/2019/1253710
- Howe K, Clark MD, Torroja CF, Torrance J, Berthelot C, Muffato M, et al. The zebrafish reference genome sequence and its relationship to the human genome. *Nature.* (2013) 496:498–503. doi: 10.1038/nature12111
- Hamilton F. *An Account of the Fishes Found in the River Ganges and Its Branches*. Edinburgh: Edinburgh Printed for Constable A, and Company (1822).
- Streisinger G, Walker C, Dower N, Knauber D, Singer F. Production of clones of homozygous diploid zebra fish (*Brachydanio rerio*). *Nature.* (1981) 291:293–6. doi: 10.1038/291293a0
- Kimmel CB. Genetics and early development of zebrafish. *Trends Genet.* (1989) 5:283–8. doi: 10.1016/0168-9525(89)90103-0
- Poss KD, Keating MT, Nechiporuk A. Tales of regeneration in zebrafish. *Dev Dyn.* (2003) 226:202–10. doi: 10.1002/dvdy.10220
- Zon LI, Peterson RT. *In vivo* drug discovery in the zebrafish. *Nat Rev Drug Discov.* (2005) 4:35–44. doi: 10.1038/nrd1606
- Parichy DM, Elizondo MR, Mills MG, Gordon TN, Engeszer RE. Normal table of postembryonic zebrafish development: staging by externally visible anatomy of the living fish. *Dev Dyn.* (2009) 238:2975–3015. doi: 10.1002/dvdy.22113
- Harper C, Lawrence C. *The Laboratory Zebrafish*. Notre Dame: CRC Press (2016). 274 p.
- Bergen DJM, Kague E, Hammond CL. Zebrafish as an emerging model for osteoporosis: a primary testing platform for screening new osteo-active compounds. *Front Endocrinol.* (2019) 10:6. doi: 10.3389/fendo.2019.00006
- Besio R, Chow CW, Tonelli F, Marini JC, Forlino A. Bone biology: insights from osteogenesis imperfecta and related rare fragility syndromes. *FEBS J.* (2019) 286:3033–56. doi: 10.1111/febs.14963
- Fiedler IAK, Schmidt FN, Wolfel EM, Plumeyer C, Milovanovic P, Gioia R, et al. Severely impaired bone material quality in chihuahua zebrafish resembles classical dominant human osteogenesis imperfecta. *J Bone Min Res.* (2018) 33:1489–99. doi: 10.1002/jbmr.3445
- Gioia R, Tonelli F, Ceppi I, Biggiogera M, Leikin S, Fisher S, et al. The chaperone activity of 4PBA ameliorates the skeletal phenotype of chihuahua, a zebrafish model for dominant osteogenesis imperfecta. *Hum Mol Genet.* (2017) 26:2897–911. doi: 10.1093/hmg/ddx171
- Gistelink C, Witten PE, Huijsseune A, Symoens S, Malfait F, Larionova D, et al. Loss of type I collagen telopeptide lysyl hydroxylation causes musculoskeletal abnormalities in a zebrafish model of bruck syndrome. *J Bone Min Res.* (2016) 31:1930–42. doi: 10.1002/jbmr.2977
- Tonelli F, Cotti S, Leoni L, Besio R, Gioia R, Marchese L, et al. Crtp and p3h1 knock out zebrafish support defective collagen chaperoning as the cause of their osteogenesis imperfecta phenotype. *Matrix Biol.* (2020) 90:40–60. doi: 10.1016/j.matbio.2020.03.004
- van Dijk FS, Zillikens MC, Micha D, Riessland M, Marcellis CL, de Die-Smulders CE, et al. PLS3 mutations in X-linked osteoporosis with fractures. *N Engl J Med.* (2013) 369:1529–36. doi: 10.1056/NEJMoa1308223
- Willems B, Tao S, Yu T, Huijsseune A, Witten PE, Winkler C. The Wnt co-receptor Lrp5 is required for cranial neural crest cell migration in zebrafish. *PLoS ONE.* (2015) 10:e0131768. doi: 10.1371/journal.pone.0131768
- Zhang Y, Huang H, Zhao G, Yokoyama T, Vega H, Huang Y, et al. ATP6V1H deficiency impairs bone development

- through activation of MMP9 and MMP13. *PLoS Genet.* (2017) 13:e1006481. doi: 10.1371/journal.pgen.1006481
21. Lam PY, Peterson RT. Developing zebrafish disease models for *in vivo* small molecule screens. *Curr Opin Chem Biol.* (2019) 50:37–44. doi: 10.1016/j.cbpa.2019.02.005
 22. Gemberling M, Bailey TJ, Hyde DR, Poss KD. The zebrafish as a model for complex tissue regeneration. *Trends Genet.* (2013) 29:611–20. doi: 10.1016/j.tig.2013.07.003
 23. Lleras-Forero L, Winkler C, Schulte-Merker S. Zebrafish and medaka as models for biomedical research of bone diseases. *Dev Biol.* (2020) 457:191–205. doi: 10.1016/j.ydbio.2019.07.009
 24. Witten PE, Harris MP, Huisseune A, Winkler C. Small teleost fish provide new insights into human skeletal diseases. *Methods Cell Biol.* (2017) 138:321–46. doi: 10.1016/bs.mcb.2016.09.001
 25. Witten PE, Huisseune A, Hall BK. A practical approach for the identification of the many cartilaginous tissues in teleost fish. *J Appl Ichthyol.* (2010) 26:257–62. doi: 10.1111/j.1439-0426.2010.01416.x
 26. Iwasaki M, Kuroda J, Kawakami K, Wada H. Epidermal regulation of bone morphogenesis through the development and regeneration of osteoblasts in the zebrafish scale. *Dev Biol.* (2018) 437:105–19. doi: 10.1016/j.ydbio.2018.03.005
 27. Van der heyden C, Huisseune A. Dynamics of tooth formation and replacement in the zebrafish (*Danio rerio*) (*Teleostei, Cyprinidae*). *Dev Dyn.* (2000) 219:486–96. doi: 10.1002/1097-0177(2000)9999:9999::AID-DVDY1069>3.0.CO;2-Z
 28. Reif WE. *Evolution of Dermal Skeleton and Dentition in Vertebrates: The Odontode Regulation Theory Evolutionary Biology*. Boston, MA: Springer (1982).
 29. Huisseune A, Sire JY. Evolution of patterns and processes in teeth and tooth-related tissues in non-mammalian vertebrates. *Eur J Oral Sci.* (1998) 106(Suppl. 1):437–81. doi: 10.1111/j.1600-0722.1998.tb02211.x
 30. Sire JY, Huisseune A. Formation of dermal skeletal and dental tissues in fish: a comparative and evolutionary approach. *Biol Rev Camb Philos Soc.* (2003) 78:219–49. doi: 10.1017/S1464793102006073
 31. Kague E, Gallagher M, Burke S, Parsons M, Franz-Odenaal T, Fisher S. Skeletogenic fate of zebrafish cranial and trunk neural crest. *PLoS ONE.* (2012) 7:e47394. doi: 10.1371/journal.pone.0047394
 32. Mongera A, Nusslein-Volhard C. Scales of fish arise from mesoderm. *Curr Biol.* (2013) 23:R338–9. doi: 10.1016/j.cub.2013.02.056
 33. Bird NC, Mabee PM. Developmental morphology of the axial skeleton of the zebrafish, *Danio rerio* (*Ostariophysi: Cyprinidae*). *Dev Dyn.* (2003) 228:337–57. doi: 10.1002/dvdy.10387
 34. Fleming A, Kishida MG, Kimmel CB, Keynes RJ. Building the backbone: the development and evolution of vertebral patterning. *Development.* (2015) 142:1733–44. doi: 10.1242/dev.118950
 35. Lleras Forero L, Narayanan R, Huitema LF, VanBergem M, Apschner A, Peterson-Maduro J, et al. Segmentation of the zebrafish axial skeleton relies on notochord sheath cells and not on the segmentation clock. *Elife.* (2018) 7:e33843. doi: 10.7554/eLife.33843.043
 36. Weigele J, Franz-Odenaal TA. Functional bone histology of zebrafish reveals two types of endochondral ossification, different types of osteoblast clusters and a new bone type. *J Anat.* (2016) 229:92–103. doi: 10.1111/joa.12480
 37. Witten PE, Huisseune A. A comparative view on mechanisms and functions of skeletal remodelling in teleost fish, with special emphasis on osteoclasts and their function. *Biol Rev Camb Philos Soc.* (2009) 84:315–46. doi: 10.1111/j.1469-185X.2009.00077.x
 38. Eames BF, Amores A, Yan YL, Postlethwait JH. Evolution of the osteoblast: skeletogenesis in gar and zebrafish. *BMC Evol Biol.* (2012) 12:27. doi: 10.1186/1471-2148-12-27
 39. Schlombs K, Wagner T, Scheel J. Site-1 protease is required for cartilage development in zebrafish. *Proc Natl Acad Sci USA.* (2003) 100:14024–9. doi: 10.1073/pnas.2331794100
 40. Hammond CL, Schulte-Merker S. Two populations of endochondral osteoblasts with differential sensitivity to Hedgehog signalling. *Development.* (2009) 136:3991–4000. doi: 10.1242/dev.042150
 41. Mackie EJ, Ahmed YA, Tatarczuch L, Chen KS, Mirams M. Endochondral ossification: how cartilage is converted into bone in the developing skeleton. *Int J Biochem Cell Biol.* (2008) 40:46–62. doi: 10.1016/j.biocel.2007.06.009
 42. Maes C, Kobayashi T, Selig MK, Torrekens S, Roth SI, Mackem S, et al. Osteoblast precursors, but not mature osteoblasts, move into developing and fractured bones along with invading blood vessels. *Dev Cell.* (2010) 19:329–44. doi: 10.1016/j.devcel.2010.07.010
 43. Horton JM, Summers AP. The material properties of acellular bone in a teleost fish. *J Exp Biol.* (2009) 212(Pt 9):1413–20. doi: 10.1242/jeb.020636
 44. Bar-Shavit Z. The osteoclast: a multinucleated, hematopoietic-origin, bone-resorbing osteoimmune cell. *J Cell Biochem.* (2007) 102:1130–9. doi: 10.1002/jcb.21553
 45. Hall BK. *Bones and Cartilage: Developmental and Evolutionary Skeletal Biology*. 2nd ed. London: Elsevier/Academic Press (2015).
 46. To TT, Witten PE, Renn J, Bhattacharya D, Huisseune A, Winkler C. Rankl-induced osteoclastogenesis leads to loss of mineralization in a medaka osteoporosis model. *Development.* (2012) 139:141–50. doi: 10.1242/dev.071035
 47. Eames BF, Singer A, Smith GA, Wood ZA, Yan YL, He X, et al. UDP xylose synthase 1 is required for morphogenesis and histogenesis of the craniofacial skeleton. *Dev Biol.* (2010) 341:400–15. doi: 10.1016/j.ydbio.2010.02.035
 48. Li N, Felber K, Elks P, Croucher P, Roehl HH. Tracking gene expression during zebrafish osteoblast differentiation. *Dev Dyn.* (2009) 238:459–66. doi: 10.1002/dvdy.21904
 49. Yan YL, Willoughby J, Liu D, Crump JG, Wilson C, Miller CT, et al. A pair of sox: distinct and overlapping functions of zebrafish sox9 co-orthologs in craniofacial and pectoral fin development. *Development.* (2005) 132:1069–83. doi: 10.1242/dev.01674
 50. Gistelinc C, Gioia R, Gagliardi A, Tonelli F, Marchese L, Bianchi L, et al. Zebrafish collagen type I: molecular and biochemical characterization of the major structural protein in bone and skin. *Sci Rep.* (2016) 6:21540. doi: 10.1038/srep21540
 51. Christoffels A, Koh EG, Chia JM, Brenner S, Aparicio S, Venkatesh B. Fugu genome analysis provides evidence for a whole-genome duplication early during the evolution of ray-finned fishes. *Mol Biol Evol.* (2004) 21:1146–51. doi: 10.1093/molbev/msh114
 52. Hirasawa T, Kuratani S. Evolution of the vertebrate skeleton: morphology, embryology, and development. *Zoological Lett.* (2015) 1:2. doi: 10.1186/s40851-014-0007-7
 53. Corallo D, Schiavinato A, Trapani V, Moro E, Argenton F, Bonaldo P. Emilin3 is required for notochord sheath integrity and interacts with Scube2 to regulate notochord-derived Hedgehog signals. *Development.* (2013) 140:4594–601. doi: 10.1242/dev.094078
 54. Stemple DL. Structure and function of the notochord: an essential organ for chordate development. *Development.* (2005) 132:2503–12. doi: 10.1242/dev.01812
 55. Bensimon-Brito A, Cancela ML, Huisseune A, Witten PE. Vestiges, rudiments and fusion events: the zebrafish caudal fin endoskeleton in an evo-devo perspective. *Evol Dev.* (2012) 14:116–27. doi: 10.1111/j.1525-142X.2011.00526.x
 56. Arratia G, Schultze HP. Reevaluation of the caudal skeleton of certain actinopterygian fishes: III. Salmonidae. Homologization of caudal skeletal structures. *J Morphol.* (1992) 214:187–249. doi: 10.1002/jmor.1052140209
 57. Arratia G, Schultze HP, Casciotta J. Vertebral column and associated elements in dipnoans and comparison with other fishes: development and homology. *J Morphol.* (2001) 250:101–72. doi: 10.1002/jmor.1062
 58. Drier W, Solnica-Krezel L, Schier AF, Neuhaus SC, Malicki J, Stemple DL, et al. A genetic screen for mutations affecting embryogenesis in zebrafish. *Development.* (1996) 123:37–46.
 59. Haffter P, Granato M, Brand M, Mullins MC, Hammerschmidt M, Kane DA, et al. The identification of genes with unique and essential functions in the development of the zebrafish, *Danio rerio*. *Development.* (1996) 123:1–36.
 60. Lawson ND, Wolfe SA. Forward and reverse genetic approaches for the analysis of vertebrate development in the zebrafish. *Dev Cell.* (2011) 21:48–64. doi: 10.1016/j.devcel.2011.06.007
 61. Zuniga E, Stellabotte F, Crump JG. Jagged-Notch signaling ensures dorsal skeletal identity in the vertebrate face. *Development.* (2010) 137:1843–52. doi: 10.1242/dev.049056

62. Ashikov A, Abu Bakar N, Wen XY, Niemeijer M, Osorio GRP, Brand-Arzamendi K, et al. Integrating glycomics and genomics uncovers SLC10A7 as essential factor for bone mineralization by regulating post-Golgi protein transport and glycosylation. *Hum Mol Genet.* (2018) 27:3029–45. doi: 10.1093/hmg/ddy213
63. Miller CT, Swartz ME, Khuu PA, Walker MB, Eberhart JK, Kimmel CB. *mef2ca* is required in cranial neural crest to effect endothelin1 signaling in zebrafish. *Dev Biol.* (2007) 308:144–57. doi: 10.1016/j.ydbio.2007.05.018
64. Yan YL, Miller CT, Nissen RM, Singer A, Liu D, Kirn A, et al. A zebrafish *sox9* gene required for cartilage morphogenesis. *Development.* (2002) 129:5065–79.
65. Sun X, Zhang R, Liu M, Chen H, Chen L, Luo F, et al. *Rmrp* mutation disrupts chondrogenesis and bone ossification in zebrafish model of cartilage-hair hypoplasia via enhanced Wnt/beta-catenin signaling. *J Bone Miner Res.* (2019) 34:2101–16. doi: 10.1002/jbmr.3820
66. Tian J, Shao J, Liu C, Hou HY, Chou CW, Shboul M, et al. Deficiency of *lrp4* in zebrafish and human LRP4 mutation induce aberrant activation of jagged-Notch signaling in fin and limb development. *Cell Mol Life Sci.* (2019) 76:163–78. doi: 10.1007/s00018-018-2928-3
67. Burger A, Vasilyev A, Tomar R, Selig MK, Nielsen GP, Peterson RT, et al. A zebrafish model of chordoma initiated by notochord-driven expression of HRASV12. *Dis Models Mech.* (2014) 7:907–13. doi: 10.1242/dmm.013128
68. Flores MV, Lam EY, Crosier P, Crosier K. A hierarchy of Runx transcription factors modulate the onset of chondrogenesis in craniofacial endochondral bones in zebrafish. *Dev Dyn.* (2006) 235:3166–76. doi: 10.1002/dvdy.20957
69. Swartz ME, Sheehan-Rooney K, Dixon MJ, Eberhart JK. Examination of a palatogenic gene program in zebrafish. *Dev Dyn.* (2011) 240:2204–20. doi: 10.1002/dvdy.22713
70. Blumel R, Zink M, Klopocki E, Liedtke D. On the traces of *tcfl2*: investigation of the gene expression pattern during development and cranial suture patterning in zebrafish (*Danio rerio*). *PLoS ONE.* (2019) 14:e0218286. doi: 10.1371/journal.pone.0218286
71. Laue K, Janicke M, Plaster N, Sonntag C, Hammerschmidt M. Restriction of retinoic acid activity by *Cyp26b1* is required for proper timing and patterning of osteogenesis during zebrafish development. *Development.* (2008) 135:3775–87. doi: 10.1242/dev.021238
72. Spoorendonk KM, Peterson-Maduro J, Renn J, Trowe T, Kranenborg S, Winkler C, et al. Retinoic acid and *Cyp26b1* are critical regulators of osteogenesis in the axial skeleton. *Development.* (2008) 135:3765–74. doi: 10.1242/dev.024034
73. Aman AJ, Fulbright AN, Parichy DM. Wnt/beta-catenin regulates an ancient signaling network during zebrafish scale development. *Elife.* (2018) 7:e37001. doi: 10.7554/eLife.37001.020
74. Suarez-Bregua P, Saxena A, Bronner ME, Rotllant J. Targeted Pth4-expressing cell ablation impairs skeletal mineralization in zebrafish. *PLoS ONE.* (2017) 12:e0186444. doi: 10.1371/journal.pone.0186444
75. Franz-Odenaal TA, Edsall SC. Long-term effects of simulated microgravity and vibration exposure on skeletal development in zebrafish. *Stem Cells Dev.* (2018) 27:1278–86. doi: 10.1089/scd.2017.0266
76. Delbaere S, Van Damme T, Sxy D, Symoens S, Coucke P, Willaert A, et al. Hypomorphic zebrafish models mimic the musculoskeletal phenotype of beta4GalT7-deficient ehlers-danlos syndrome. *Matrix Biol.* (2019) 89:59–75. doi: 10.1016/j.matbio.2019.12.002
77. LaBonty M, Pray N, Yelick PC. A zebrafish model of human fibrodysplasia ossificans progressiva. *Zebrafish.* (2017) 14:293–304. doi: 10.1089/zeb.2016.1398
78. Zancan I, Belleso S, Costa R, Salvailo M, Stroppiano M, Hammond C, et al. Glucocerebrosidase deficiency in zebrafish affects primary bone ossification through increased oxidative stress and reduced Wnt/beta-catenin signaling. *Hum Mol Genet.* (2015) 24:1280–94. doi: 10.1093/hmg/ddu538
79. Liang ST, Chen JR, Tsai JJ, Lai YH, Hsiao CD. Overexpression of notch signaling induces hyperosteoegeny in zebrafish. *Int J Mol Sci.* (2019) 20:3613. doi: 10.3390/ijms20153613
80. Hur M, Gistelink CA, Huber P, Lee J, Thompson MH, Monstad-Rios AT, et al. MicroCT-based phenomics in the zebrafish skeleton reveals virtues of deep phenotyping in a distributed organ system. *Zebrafish.* (2018) 15:77–78. doi: 10.1089/zeb.2017.1540
81. Harris MP, Rohner N, Schwarz H, Perathoner S, Konstantinidis P, Nusslein-Volhard C. Zebrafish *eda* and *edar* mutants reveal conserved and ancestral roles of ectodysplasin signaling in vertebrates. *PLoS Genet.* (2008) 4:e1000206. doi: 10.1371/journal.pgen.1000206
82. Kague E, Hughes SM, Lawrence EA, Cross S, Martin-Silverstone E, Hammond CL, et al. Scleraxis genes are required for normal musculoskeletal development and for rib growth and mineralization in zebrafish. *FASEB J.* (2019) 33:9116–30. doi: 10.1096/fj.201802654RR
83. Dauer MVP, Currie PD, Berger J. Skeletal malformations of *Meox1*-deficient zebrafish resemble human Klippel-Feil syndrome. *J Anat.* (2018) 233:687–95. doi: 10.1111/joa.12890
84. Clement A, Wiweger M, von der Hardt S, Rusch MA, Selleck SB, Chien CB, et al. Regulation of zebrafish skeletogenesis by *ext2/dackel* and *papst1/pinscher*. *PLoS Genet.* (2008) 4:e1000136. doi: 10.1371/journal.pgen.1000136
85. Huitema LF, Apschner A, Logister I, Spoorendonk KM, Bussmann J, Hammond CL, et al. *Entpd5* is essential for skeletal mineralization and regulates phosphate homeostasis in zebrafish. *Proc Natl Acad Sci USA.* (2012) 109:21372–7. doi: 10.1073/pnas.1214231110
86. Zhang Y, Cui FZ, Wang XM, Feng QL, Zhu XD. Mechanical properties of skeletal bone in gene-mutated *stoppel(dtl28d)* and wild-type zebrafish (*Danio rerio*) measured by atomic force microscopy-based nanoindentation. *Bone.* (2002) 30:541–6. doi: 10.1016/S8756-3282(02)00676-2
87. Cheah FS, Winkler C, Jabs EW, Chong SS. *Tgfbeta3* regulation of chondrogenesis and osteogenesis in zebrafish is mediated through formation and survival of a subpopulation of the cranial neural crest. *Mech Dev.* (2010) 127:329–44. doi: 10.1016/j.mod.2010.04.003
88. Eberhart JK, He X, Swartz ME, Yan YL, Song H, Boling TC, et al. MicroRNA *Mir140* modulates Pdgfr signaling during palatogenesis. *Nat Genet.* (2008) 40:290–8. doi: 10.1038/ng.82
89. Ghassibe-Sabbagh M, Desmyter L, Langenberg T, Claes F, Boute O, Bayet B, et al. *FAF1*, a gene that is disrupted in cleft palate and has conserved function in zebrafish. *Am J Hum Genet.* (2011) 88:150–61. doi: 10.1016/j.ajhg.2011.01.003
90. Dougherty M, Kamel G, Grimaldi M, Gfrerer L, Shubinets V, Ethier R, et al. Distinct requirements for *wnt9a* and *irf6* in extension and integration mechanisms during zebrafish palate morphogenesis. *Development.* (2013) 140:76–81. doi: 10.1242/dev.080473
91. Lawrence EA, Kague E, Aggleton JA, Harniman RL, Roddy KA, Hammond CL. The mechanical impact of *coll11a2* loss on joints; *coll11a2* mutant zebrafish show changes to joint development and function, which leads to early-onset osteoarthritis. *Philos Trans R Soc Lond B Biol Sci.* (2018) 373:20170335. doi: 10.1098/rstb.2017.0335
92. Askary A, Smeeton J, Paul S, Schindler S, Braasch I, Ellis NA, et al. Ancient origin of lubricated joints in bony vertebrates. *Elife.* (2016) 5:e16415. doi: 10.7554/eLife.16415.016
93. Fisher S, Jagadeeswaran P, Halpern ME. Radiographic analysis of zebrafish skeletal defects. *Dev Biol.* (2003) 264:64–76. doi: 10.1016/S0012-1606(03)00399-3
94. Asharani PV, Keupp K, Semler O, Wang W, Li Y, Thiele H, et al. Attenuated *BMP1* function compromises osteogenesis, leading to bone fragility in humans and zebrafish. *Ame J Hum Genet.* (2012) 90:661–74. doi: 10.1016/j.ajhg.2012.02.026
95. Kague E, Roy P, Asselin G, Hu G, Simonet J, Stanley A, et al. *Osterix/Sp7* limits cranial bone initiation sites and is required for formation of sutures. *Dev Biol.* (2016) 413:160–72. doi: 10.1016/j.ydbio.2016.03.011
96. Henke K, Daane JM, Hawkins MB, Dooley CM, Busch-Nentwich EM, Stemple DL, et al. Genetic screen for postembryonic development in the zebrafish (*Danio rerio*): dominant mutations affecting adult form. *Genetics.* (2017) 207:609–23. doi: 10.1534/genetics.117.300187
97. Chatani M, Takano Y, Kudo A. Osteoclasts in bone modeling, as revealed by *in vivo* imaging, are essential for organogenesis in fish. *Dev Biol.* (2011) 360:96–109. doi: 10.1016/j.ydbio.2011.09.013

98. Chen JR, Lai YH, Tsai JJ, Hsiao CD. Live fluorescent staining platform for drug-screening and mechanism-analysis in zebrafish for bone mineralization. *Molecules*. (2017) 22:2068. doi: 10.3390/molecules22122068
99. Huo L, Wang L, Yang Z, Li P, Geng D, Xu Y. Prednisolone induces osteoporosis-like phenotypes via focal adhesion signaling pathway in zebrafish larvae. *Biol Open*. (2018) 7. doi: 10.1242/bio.029405
100. Urso K, Caetano-Lopes J, Lee PY, Yan J, Henke K, Sury M, et al. A role for G protein-coupled receptor 137b in bone remodeling in mouse and zebrafish. *Bone*. (2019) 127:104–13. doi: 10.1016/j.bone.2019.06.002
101. Monma Y, Shimada Y, Nakayama H, Zhang L, Nishimura N, Tanaka T. Aging-associated microstructural deterioration of vertebra in zebrafish. *Bone Rep*. (2019) 11:100215. doi: 10.1016/j.bonr.2019.100215
102. Zhang W, Xu J, Qiu J, Xing C, Li X, Leng B, et al. Novel and rapid osteoporosis model established in zebrafish using high iron stress. *Biochem Biophys Res Commun*. (2018) 496:654–60. doi: 10.1016/j.bbrc.2017.12.172
103. Jafari A, Qanie D, Andersen TL, Zhang Y, Chen L, Postert B, et al. Legumain regulates differentiation fate of human bone marrow stromal cells and is altered in postmenopausal osteoporosis. *Stem Cell Rep*. (2017) 8:373–86. doi: 10.1016/j.stemcr.2017.01.003
104. Huang HX, Lin H, Lan F, Wu YF, Yang ZG, Zhang JJ. Application of bone transgenic zebrafish in anti-osteoporosis chemical screening. *Anim Models Exp Med*. (2018) 1:53–61. doi: 10.1002/ame2.12000
105. Apschner A, Huitema LF, Ponsioen B, Peterson-Maduro J, Schulte-Merker S. Zebrafish *enpp1* mutants exhibit pathological mineralization, mimicking features of generalized arterial calcification of infancy (GACI) and pseudoxanthoma elasticum (PXE). *Dis Models Mech*. (2014) 7:811–22. doi: 10.1242/dmm.015693
106. Mackay EW, Apschner A, Schulte-Merker S. Vitamin K reduces hypermineralisation in zebrafish models of PXE and GACI. *Development*. (2015) 142:1095–101. doi: 10.1242/dev.113811
107. Teng CS, Ting MC, Farmer DT, Brockop M, Maxson RE, Crump JG. Altered bone growth dynamics prefigure craniostenosis in a zebrafish model of Saethre-Chotzen syndrome. *Elife*. (2018) 7:e37024. doi: 10.7554/eLife.37024.041
108. Ferreira CR, Xia ZJ, Clement A, Parry DA, Davids M, Taylan F, et al. A recurrent *de novo* heterozygous COG4 substitution leads to saul-wilson syndrome, disrupted vesicular trafficking, and altered proteoglycan glycosylation. *Am J Hum Genet*. (2018) 103:553–67. doi: 10.1016/j.ajhg.2018.09.003
109. Buchan JG, Gray RS, Gansner JM, Alvarado DM, Burgert L, Gitlin JD, et al. Kinesin family member 6 (*kif6*) is necessary for spine development in zebrafish. *Dev Dyn*. (2014) 243:1646–57. doi: 10.1002/dvdy.24208
110. Grimes DT, Boswell CW, Morante NF, Henkelman RM, Burdine RD, Ciruna B. Zebrafish models of idiopathic scoliosis link cerebrospinal fluid flow defects to spine curvature. *Science*. (2016) 352:1341–4. doi: 10.1126/science.aaf6419
111. Haller G, McCall K, Jenkitkasemwong S, Sadler B, Antunes L, Nikolov M, et al. A missense variant in *SLC39A8* is associated with severe idiopathic scoliosis. *Nat Commun*. (2018) 9:4171. doi: 10.1038/s41467-018-06705-0
112. Gray RS, Wilm TP, Smith J, Bagnat M, Dale RM, Topczewski J, et al. Loss of *col8a1a* function during zebrafish embryogenesis results in congenital vertebral malformations. *Dev Biol*. (2014) 386:72–85. doi: 10.1016/j.ydbio.2013.11.028
113. Zhang X, Jia S, Chen Z, Chong YL, Xie H, Feng D, et al. Cilia-driven cerebrospinal fluid flow directs expression of urotensin neuropeptides to straighten the vertebrate body axis. *Nat Genet*. (2018) 50:1666–73. doi: 10.1038/s41588-018-0260-3
114. Printzi A, Fragkoulis S, Dimitriadis A, Keklikoglou K, Arvanitidis C, Witten PE, et al. Exercise-induced lordosis in zebrafish *Danio rerio* (Hamilton, 1822). *J Fish Biol*. (2019). doi: 10.1111/jfb.14240
115. Burrage LC, Reynolds JJ, Baratang NV, Phillips JB, Wegner J, McFarquhar A, et al. Bi-allelic variants in *TONSL* Cause SPONASTRIME dysplasia and a spectrum of skeletal dysplasia phenotypes. *Am J Hum Genet*. (2019) 104:422–38. doi: 10.1016/j.ajhg.2019.01.007
116. Baas D, Malbouyres M, Haftek-Terreau Z, Le Guellec D, Ruggiero F. Craniofacial cartilage morphogenesis requires zebrafish *coll11a1* activity. *Matrix Biol*. (2009) 28:490–502. doi: 10.1016/j.matbio.2009.07.004
117. Bergen DJM, Stevenson NL, Skinner REH, Stephens DJ, Hammond CL. The golgi matrix protein giantin is required for normal cilia function in zebrafish. *Biol Open*. (2017) 6:1180–89. doi: 10.1242/bio.025502
118. Newham E, Kague E, Aggleton JA, Fernee C, Brown KR, Hammond CL. Finite element and deformation analyses predict pattern of bone failure in loaded zebrafish spines. *J R Soc Interface*. (2019) 16:20190430. doi: 10.1098/rsif.2019.0430
119. Andreeva V, Connolly MH, Stewart-Swift C, Fraher D, Burt J, Cardarelli J, et al. Identification of adult mineralized tissue zebrafish mutants. *Genesis*. (2011) 49:360–6. doi: 10.1002/dvg.20712
120. Gistelincx C, Kwon RY, Malfait F, Symoens S, Harris MP, Henke K, et al. Zebrafish type I collagen mutants faithfully recapitulate human type I collagenopathies. *Proc Natl Acad Sci USA*. (2018) 115:E8037–46. doi: 10.1073/pnas.1722200115
121. Draper BW, Morcos PA, Kimmel CB. Inhibition of zebrafish *fgfr8* pre-mRNA splicing with morpholino oligos: a quantifiable method for gene knockdown. *Genesis*. (2001) 30:154–6. doi: 10.1002/gene.1053
122. Nasevicius A, Ekker SC. Effective targeted gene 'knockdown' in zebrafish. *Nat Genet*. (2000) 26:216–20. doi: 10.1038/79951
123. Ekker SC, Larson JD. Morphant technology in model developmental systems. *Genesis*. (2001) 30:89–93. doi: 10.1002/gene.1038
124. Pickart MA, Klee EW, Nielsen AL, Sivasubbu S, Mendenhall EM, Bill BR, et al. Genome-wide reverse genetics framework to identify novel functions of the vertebrate secretome. *PLoS ONE*. (2006) 1:e104. doi: 10.1371/journal.pone.0000104
125. Robu ME, Larson JD, Nasevicius A, Beiraghi S, Brenner C, Farber SA, et al. p53 activation by knockdown technologies. *PLoS Genet*. (2007) 3:e78. doi: 10.1371/journal.pgen.0030078
126. Amoyel M, Cheng YC, Jiang YJ, Wilkinson DG. Wnt1 regulates neurogenesis and mediates lateral inhibition of boundary cell specification in the zebrafish hindbrain. *Development*. (2005) 132:775–85. doi: 10.1242/dev.01616
127. Gerety SS, Wilkinson DG. Morpholino artifacts provide pitfalls and reveal a novel role for pro-apoptotic genes in hindbrain boundary development. *Dev Biol*. (2011) 350:279–89. doi: 10.1016/j.ydbio.2010.11.030
128. Kok FO, Shin M, Ni CW, Gupta A, Grosse AS, van Impel A, et al. Reverse genetic screening reveals poor correlation between morpholino-induced and mutant phenotypes in zebrafish. *Dev Cell*. (2015) 32:97–108. doi: 10.1016/j.devcel.2014.11.018
129. El-Brolosy MA, Stainier DYR. Genetic compensation: a phenomenon in search of mechanisms. *PLoS Genet*. (2017) 13:e1006780. doi: 10.1371/journal.pgen.1006780
130. Doyon Y, McCammon JM, Miller JC, Faraji F, Ngo C, Katibah GE, et al. Heritable targeted gene disruption in zebrafish using designed zinc-finger nucleases. *Nat Biotechnol*. (2008) 26:702–8. doi: 10.1038/nbt1409
131. Meng X, Noyes MB, Zhu LJ, Lawson ND, Wolfe SA. Targeted gene inactivation in zebrafish using engineered zinc-finger nucleases. *Nat Biotechnol*. (2008) 26:695–701. doi: 10.1038/nbt1398
132. Cade L, Reyon D, Hwang WY, Tsai SQ, Patel S, Khayter C, et al. Highly efficient generation of heritable zebrafish gene mutations using homo- and heterodimeric TALENs. *Nucleic Acids Res*. (2012) 40:8001–10. doi: 10.1093/nar/gks518
133. Watson CJ, Monstad-Rios AT, Bhimani RM, Gistelincx C, Willaert A, Coucke P, et al. Phenomics-based quantification of CRISPR-induced mosaicism in zebrafish. *Cell Syst*. (2020) 10:275–86.e5. doi: 10.1016/j.cels.2020.02.007
134. Wu RS, Lam II, Clay H, Duong DN, Deo RC, Coughlin SR, et al. A rapid method for directed gene knockout for screening in G0 zebrafish. *Dev Cell*. (2018) 46:112–25.e4. doi: 10.1016/j.devcel.2018.06.003
135. Salsman J, Dellaire G. Precision genome editing in the CRISPR era. *Biochem Cell Biol*. (2017) 95:187–201. doi: 10.1139/bcb-2016-0137
136. Mikuni T, Nishiyama J, Sun Y, Kamasawa N, Yasuda R. High-throughput high-resolution mapping of protein localization in mammalian brain by *in vivo* genome editing. *Cell*. (2016) 165:1803–17. doi: 10.1016/j.cell.2016.04.044
137. Leonetti MD, Sekine S, Kamiyama D, Weissman JS, Huang B. A scalable strategy for high-throughput GFP tagging of endogenous human proteins. *Proc Natl Acad Sci USA*. (2016) 113:E3501–8. doi: 10.1073/pnas.1606731113

138. Forlino A, Marini JC. Osteogenesis imperfecta. *Lancet*. (2016) 387:1657–71. doi: 10.1016/S0140-6736(15)00728-X
139. El-Brolosy MA, Kontarakis Z, Rossi A, Kuenne C, Gunther S, Fukuda N, et al. Genetic compensation triggered by mutant mRNA degradation. *Nature*. (2019) 568:193–7. doi: 10.1038/s41586-019-1064-z
140. Coggins NB, Stultz J, O'Geen H, Carvajal-Carmona LG, Segal DJ. Methods for scarless, selection-free generation of human cells and allele-specific functional analysis of disease-associated SNPs and variants of uncertain significance. *Sci Rep*. (2017) 7:15044. doi: 10.1038/s41598-017-15407-4
141. Renaud JB, Boix C, Charpentier M, De Cian A, Cochenne C, Duvernois-Berthet E, et al. Improved genome editing efficiency and flexibility using modified oligonucleotides with TALEN and CRISPR-Cas9 nucleases. *Cell Rep*. (2016) 14:2263–72. doi: 10.1016/j.celrep.2016.02.018
142. Richardson CD, Kazane KR, Feng SJ, Zelin E, Bray NL, Schafer AJ, et al. CRISPR-Cas9 genome editing in human cells occurs via the fanconi anemia pathway. *Nat Genet*. (2018) 50:1132–9. doi: 10.1038/s41588-018-0174-0
143. Lin S, Staahl BT, Alla RK, Doudna JA. Enhanced homology-directed human genome engineering by controlled timing of CRISPR/Cas9 delivery. *Elife*. (2014) 3:e04766. doi: 10.7554/eLife.04766.010
144. Jayatilaka K, Sheridan SD, Bold TD, Bochenska K, Logan HL, Weichselbaum RR, et al. A chemical compound that stimulates the human homologous recombination protein RAD51. *Proc Natl Acad Sci USA*. (2008) 105:15848–53. doi: 10.1073/pnas.0808046105
145. Maruyama T, Dougan SK, Truttmann MC, Bilate AM, Ingram JR, Ploegh HL. Increasing the efficiency of precise genome editing with CRISPR-Cas9 by inhibition of nonhomologous end joining. *Nat Biotechnol*. (2015) 33:538–42. doi: 10.1038/nbt.3190
146. Paquet D, Kwart D, Chen A, Sproul A, Jacob S, Teo S, et al. Efficient introduction of specific homozygous and heterozygous mutations using CRISPR/Cas9. *Nature*. (2016) 533:125–9. doi: 10.1038/nature17664
147. Singh P, Schimenti JC, Bolcun-Filas E. A mouse geneticist's practical guide to CRISPR applications. *Genetics*. (2015) 199:1–15. doi: 10.1534/genetics.114.169771
148. Song J, Yang D, Xu J, Zhu T, Chen YE, Zhang J. RS-1 enhances CRISPR/Cas9- and TALEN-mediated knock-in efficiency. *Nat Commun*. (2016) 7:10548. doi: 10.1038/ncomms10548
149. Srivastava M, Nambiar M, Sharma S, Karki SS, Goldsmith G, Hegde M, et al. An inhibitor of nonhomologous end-joining abrogates double-strand break repair and impedes cancer progression. *Cell*. (2012) 151:1474–87. doi: 10.1016/j.cell.2012.11.054
150. Xiong X, Chen M, Lim WA, Zhao D, Qi LS. CRISPR/Cas9 for human genome engineering and disease research. *Annu Rev Genomics Hum Genet*. (2016) 17:131–54. doi: 10.1146/annurev-genom-083115-022258
151. Yu C, Liu Y, Ma T, Liu K, Xu S, Zhang Y, et al. Small molecules enhance CRISPR genome editing in pluripotent stem cells. *Cell Stem Cell*. (2015) 16:142–7. doi: 10.1016/j.stem.2015.01.003
152. Boel A, De Saffel H, Steyaert W, Callewaert B, De Paepe A, Coucke PJ, et al. CRISPR/Cas9-mediated homology-directed repair by ssODNs in zebrafish induces complex mutational patterns resulting from genomic integration of repair-template fragments. *Dis Model Mech*. (2018) 11. doi: 10.1242/dmm.035352
153. Boel A, Steyaert W, De Rocker N, Menten B, Callewaert B, De Paepe A, et al. BATCH-GE: batch analysis of next-generation sequencing data for genome editing assessment. *Sci Rep*. (2016) 6:30330. doi: 10.1038/srep30330
154. Armstrong GA, Liao M, You Z, Lissouba A, Chen BE, Drapeau P. Homology directed knockin of point mutations in the zebrafish *tardbp* and *fus* genes in ALS using the CRISPR/Cas9 system. *PLoS ONE*. (2016) 11:e0150188. doi: 10.1371/journal.pone.0150188
155. Farr GH 3rd, Imani K, Povov D, Maves L. Functional testing of a human *PBX3* variant in zebrafish reveals a potential modifier role in congenital heart defects. *Dis Model Mech*. (2018) 11. doi: 10.1242/dmm.035972
156. Tessadori F, Roessler HL, Savelberg SMC, Chocron S, Kamel SM, Duran KJ, et al. Effective CRISPR/Cas9-based nucleotide editing in zebrafish to model human genetic cardiovascular disorders. *Dis Model Mech*. (2018) 11. doi: 10.1242/dmm.035469
157. Gaudelli NM, Komor AC, Rees HA, Packer MS, Badran AH, Bryson DI, et al. Programmable base editing of A*T to G*C in genomic DNA without DNA cleavage. *Nature*. (2017) 551:464–71. doi: 10.1038/nature24644
158. Qin W, Lu X, Lin S. Programmable base editing in zebrafish using a modified CRISPR-Cas9 system. *Methods*. (2018) 150:19–23. doi: 10.1016/j.ymeth.2018.07.010
159. Zhang Y, Qin W, Lu X, Xu J, Huang H, Bai H, et al. Programmable base editing of zebrafish genome using a modified CRISPR-Cas9 system. *Nat Commun*. (2017) 8:118. doi: 10.1038/s41467-017-00175-6
160. Anzalone AV, Randolph PB, Davis JR, Sousa AA, Koblan LW, Levy JM, et al. Search-and-replace genome editing without double-strand breaks or donor DNA. *Nature*. (2019) 576:149–57. doi: 10.1038/s41586-019-1711-4
161. Stuart T, Satija R. Integrative single-cell analysis. *Nat Rev Genet*. (2019) 20:257–72. doi: 10.1038/s41576-019-0093-7
162. Farrell JA, Wang Y, Riesenfeld SJ, Shekhar K, Regev A, Schier AF. Single-cell reconstruction of developmental trajectories during zebrafish embryogenesis. *Science*. (2018) 360. doi: 10.1126/science.aar3131
163. Spanjaard B, Hu B, Mitic N, Olivares-Chauvet P, Janjua S, Ninov N, et al. Simultaneous lineage tracing and cell-type identification using CRISPR-Cas9-induced genetic scars. *Nat Biotechnol*. (2018) 36:469–73. doi: 10.1038/nbt.4124
164. Wagner DE, Weinreb C, Collins ZM, Briggs JA, Megason SG, Klein AM. Single-cell mapping of gene expression landscapes and lineage in the zebrafish embryo. *Science*. (2018) 360:981–7. doi: 10.1126/science.aar4362
165. Long F. Building strong bones: molecular regulation of the osteoblast lineage. *Nat Rev Mol Cell Biol*. (2011) 13:27–38. doi: 10.1038/nrm3254
166. Miller RL. Transgenic mice: beyond the knockout. *Am J Physiol Renal Physiol*. (2011) 300:F291–300. doi: 10.1152/ajprenal.00082.2010
167. Tampieri A, Sprio S, Sandri M, Valentini F. Mimicking natural biomineralization processes: a new tool for osteochondral scaffold development. *Trends Biotechnol*. (2011) 29:526–35. doi: 10.1016/j.tibtech.2011.04.011
168. Gregg CL, Butcher JT. Quantitative *in vivo* imaging of embryonic development: opportunities and challenges. *Differentiation*. (2012) 84:149–62. doi: 10.1016/j.diff.2012.05.003
169. Moro E, Vettori A, Porazzi P, Schiavone M, Rampazzo E, Casari A, et al. Generation and application of signaling pathway reporter lines in zebrafish. *Mol Genet Genomics*. (2013) 288:231–42. doi: 10.1007/s00438-013-0750-z
170. Dutton JR, Antonellis A, Carney TJ, Rodrigues FS, Pavan WJ, Ward A, et al. An evolutionarily conserved intronic region controls the spatiotemporal expression of the transcription factor Sox10. *BMC Dev Biol*. (2008) 8:105. doi: 10.1186/1471-213X-8-105
171. Dougherty M, Kamel G, Shubinets V, Hickey G, Grimaldi M, Liao EC. Embryonic fate map of first pharyngeal arch structures in the *sox10:kaede* zebrafish transgenic model. *J Craniofac Surg*. (2012) 23:1333–7. doi: 10.1097/SCS.0b013e318260f20b
172. Kirby BB, Takada N, Latimer AJ, Shin J, Carney TJ, Kelsh RN, et al. *In vivo* time-lapse imaging shows dynamic oligodendrocyte progenitor behavior during zebrafish development. *Nat Neurosci*. (2006) 9:1506–11. doi: 10.1038/nn1803
173. Rodrigues FS, Doughton G, Yang B, Kelsh RN. A novel transgenic line using the Cre-lox system to allow permanent lineage-labeling of the zebrafish neural crest. *Genesis*. (2012) 50:750–7. doi: 10.1002/dvg.22033
174. Brunt LH, Begg K, Kague E, Cross S, Hammond CL. Wnt signalling controls the response to mechanical loading during zebrafish joint development. *Development*. (2017) 144:2798–09. doi: 10.1242/dev.153528
175. Wada N, Javidan Y, Nelson S, Carney TJ, Kelsh RN, Schilling TF. Hedgehog signaling is required for cranial neural crest morphogenesis and chondrogenesis at the midline in the zebrafish skull. *Development*. (2005) 132:3977–88. doi: 10.1242/dev.01943
176. Hochgreb-Hägelen T, Koo DES, Bronner M. *Znf385C* mediates a novel p53-dependent transcriptional switch to control timing of facial bone formation. *Dev Biol*. (2015) 400:23–32. doi: 10.1016/j.ydbio.2015.01.011
177. Li L, Mao A, Wang P, Ning G, Cao Y, Wang Q. Endodermal pouch-expressed *dmrt2b* is important for pharyngeal cartilage formation. *Biol Open*. (2018) 7. doi: 10.1242/bio.035444
178. Lawson ND, Weinstein BM. *In vivo* imaging of embryonic vascular development using transgenic zebrafish. *Dev Biol*. (2002) 248:307–18. doi: 10.1006/dbio.2002.0711

179. Flanagan-Steele H, Aarnio M, Kwan B, Guihard P, Petrey A, Haskins M, et al. Cathepsin-mediated alterations in TGF β s-related signaling underlie disrupted cartilage and bone maturation associated with impaired lysosomal targeting. *J Bone Miner Res.* (2016) 31:535–48. doi: 10.1002/jbmr.2722
180. Bonkowski JL, Wang X, Fujimoto E, Lee JE, Chien CB, Dorsky RI. Domain-specific regulation of foxP2 CNS expression by lef1. *BMC Dev Biol.* (2008) 8:103. doi: 10.1186/1471-213X-8-103
181. DeLaurier A, Eames BF, Blanco-Sanchez B, Peng G, He X, Swartz ME, et al. Zebrafish sp7:EGFP: a transgenic for studying otic vesicle formation, skeletogenesis, bone regeneration. *Genesis.* (2010) 48:505–11. doi: 10.1002/dvg.20639
182. Kague E, Witten PE, Soenens M, Campos CL, Lubiana T, Fisher S, et al. Zebrafish sp7 mutants show tooth cycling independent of attachment, eruption and poor differentiation of teeth. *Dev Biol.* (2018) 435:176–84. doi: 10.1016/j.ydbio.2018.01.021
183. Dale RM, Topczewski J. Identification of an evolutionarily conserved regulatory element of the zebrafish col2a1a gene. *Dev Biol.* (2011) 357:518–31. doi: 10.1016/j.ydbio.2011.06.020
184. Filipek-Górniok B, Carlsson P, Haitina T, Habicher J, Ledin J, Kjellén L. The NDST gene family in zebrafish: role of NDST1B in pharyngeal arch formation. *PLoS ONE.* (2015) 10:e0119040. doi: 10.1371/journal.pone.0119040
185. Kague E, Bessling SL, Lee J, Hu G, Passos-Bueno MR, Fisher S. Functionally conserved cis-regulatory elements of COL18A1 identified through zebrafish transgenesis. *Dev Biol.* (2010) 337:496–505. doi: 10.1016/j.ydbio.2009.10.028
186. Pogoda HM, Riedel-Quinkertz I, Lohr H, Waxman JS, Dale RM, Topczewski J, et al. Direct activation of chordoblasts by retinoic acid is required for segmented centra mineralization during zebrafish spine development. *Development.* (2018) 145. doi: 10.1242/dev.159418
187. Hu P, Tian M, Bao J, Xing G, Gu X, Gao X, et al. Retinoid regulation of the zebrafish cyp26a1 promoter. *Dev Dyn.* (2008) 237:3798–808. doi: 10.1002/dvdy.21801
188. Li J, Hu P, Li K, Zhao Q. Identification and characterization of a novel retinoic acid response element in zebrafish cyp26a1 promoter. *Anat Rec (Hoboken).* (2012) 295:268–77. doi: 10.1002/ar.21520
189. Haga Y, Dominique VJ 3rd, Du SJ. Analyzing notochord segmentation and intervertebral disc formation using the twhh:gfz transgenic zebrafish model. *Transgenic Res.* (2009) 18:669–83. doi: 10.1007/s11248-009-9259-y
190. Ma RC, Jacobs CT, Sharma P, Kocha KM, Huang P. Stereotypic generation of axial tenocytes from bipartite sclerotome domains in zebrafish. *PLoS Genet.* (2018) 14:e1007775. doi: 10.1371/journal.pgen.1007775
191. DeLaurier A, Huycke TR, Nichols JT, Swartz ME, Larsen A, Walker C, et al. Role of mef2ca in developmental buffering of the zebrafish larval hyoid dermal skeleton. *Dev Biol.* (2014) 385:189–99. doi: 10.1016/j.ydbio.2013.11.016
192. Eames BF, Yan YL, Swartz ME, Levic DS, Knapik EW, Postlethwait JH, et al. Mutations in fam20b and xylt1 reveal that cartilage matrix controls timing of endochondral ossification by inhibiting chondrocyte maturation. *PLoS Genet.* (2011) 7:e1002246. doi: 10.1371/journal.pgen.1002246
193. Stewart S, Gomez AW, Armstrong BE, Henner A, Stankunas K. Sequential and opposing activities of Wnt and BMP coordinate zebrafish bone regeneration. *Cell Rep.* (2014) 6:482–98. doi: 10.1016/j.celrep.2014.01.010
194. Blum N, Begemann G. Osteoblast de- and redifferentiation are controlled by a dynamic response to retinoic acid during zebrafish fin regeneration. *Development.* (2015) 142:2894–903. doi: 10.1242/dev.120204
195. Geurtzen K, Knopf F, Wehner D, Huitema LF, Schulte-Merker S, Weidinger G. Mature osteoblasts differentiate in response to traumatic bone injury in the zebrafish fin and skull. *Development.* (2014) 141:2225–34. doi: 10.1242/dev.105817
196. Bek JW, De Clercq A, De Saffel H, Soenens M, Huisseune A, Witten PE, et al. Photoconvertible fluorescent proteins: a versatile tool in zebrafish skeletal imaging. *J Fish Biol.* (2020) doi: 10.1111/jfb.14335
197. Singh SP, Holdway JE, Poss KD. Regeneration of amputated zebrafish fin rays from de novo osteoblasts. *Dev Cell.* (2012) 22:879–86. doi: 10.1016/j.devcel.2012.03.006
198. Cox BD, De Simone A, Tornini VA, Singh SP, Di Talia S, Poss KD. In toto imaging of dynamic osteoblast behaviors in regenerating skeletal bone. *Curr Biol.* (2018) 28:3937–47.e4. doi: 10.1016/j.cub.2018.10.052
199. Oralova V, Rosa JT, Soenens M, Bek JW, Willaert A, Witten PE, et al. Beyond the whole-mount phenotype: high-resolution imaging in fluorescence-based applications on zebrafish. *Biol Open.* (2019) 8. doi: 10.1242/bio.042374
200. Willems B, Buttner A, Huisseune A, Renn J, Witten PE, Winkler C. Conditional ablation of osteoblasts in medaka. *Dev Biol.* (2012) 364:128–37. doi: 10.1016/j.ydbio.2012.01.023
201. Kobayashi-Sun J, Yamamori S, Kondo M, Kuroda J, Ikegami M, Suzuki N, et al. Uptake of osteoblast-derived extracellular vesicles promotes the differentiation of osteoclasts in the zebrafish scale. *Commun Biol.* (2020) 3:190. doi: 10.1038/s42003-020-0925-1
202. Mitchell RE, Huitema LF, Skinner RE, Brunt LH, Severn C, Schulte-Merker S, et al. New tools for studying osteoarthritis genetics in zebrafish. *Osteoarthritis Cartilage.* (2013) 21:269–78. doi: 10.1016/j.joca.2012.11.004
203. Kim YI, Lee S, Jung SH, Kim HT, Choi JH, Lee MS, et al. Establishment of a bone-specific col10a1:GFP transgenic zebrafish. *Mol Cells.* (2013) 36:145–50. doi: 10.1007/s10059-013-0117-7
204. Hu Z, Chen B, Zhao Q. Hedgehog signaling regulates osteoblast differentiation in zebrafish larvae through modulation of autophagy. *Biol Open.* (2019) 8. doi: 10.1242/bio.040840
205. Knopf F, Hammond C, Chekuru A, Kurth T, Hans S, Weber CW, et al. Bone regenerates via dedifferentiation of osteoblasts in the zebrafish fin. *Dev Cell.* (2011) 20:713–24. doi: 10.1016/j.devcel.2011.04.014
206. Bussmann J, Schulte-Merker S. Rapid BAC selection for tol2-mediated transgenesis in zebrafish. *Development.* (2011) 138:4327–32. doi: 10.1242/dev.068080
207. Caetano-Lopes J, Henke K, Urso K, Duryea J, Charles JF, Warman ML, et al. Correction: unique and non-redundant function of csflr paralogs in regulation and evolution of post-embryonic development of the zebrafish. *Development.* (2020) 147. doi: 10.1242/dev.192211
208. To TT, Witten PE, Huisseune A, Winkler C. An adult osteopetrosis model in medaka reveals the importance of osteoclast function for bone remodeling in teleost fish. *Comp Biochem Physiol C Toxicol Pharmacol.* (2015) 178:68–75. doi: 10.1016/j.cbpc.2015.08.007
209. Alexander C, Zuniga E, Blitz IL, Wada N, Le Pabic P, Javidan Y, et al. Combinatorial roles for BMPs and Endothelin 1 in patterning the dorsal-ventral axis of the craniofacial skeleton. *Development.* (2011) 138:5135–46. doi: 10.1242/dev.067801
210. Laux DW, Febbo JA, Roman BL. Dynamic analysis of BMP-responsive smad activity in live zebrafish embryos. *Dev Dyn.* (2011) 240:682–94. doi: 10.1002/dvdy.22558
211. Moro E, Ozhan-Kizil G, Mongera A, Beis D, Wierzbicki C, Young RM, et al. In vivo Wnt signaling tracing through a transgenic biosensor fish reveals novel activity domains. *Dev Biol.* (2012) 366:327–40. doi: 10.1016/j.ydbio.2012.03.023
212. Weidinger G, Thorpe CJ, Wuennenberg-Stapleton K, Ngai J, Moon RT. The Sp1-related transcription factors sp5 and sp5-like act downstream of Wnt/beta-catenin signaling in mesoderm and neuroectoderm patterning. *Curr Biol.* (2005) 15:489–500. doi: 10.1016/j.cub.2005.01.041
213. Felber K, Elks PM, Lecca M, Roehl HH. Expression of osterix is regulated by FGF and Wnt/beta-catenin signalling during osteoblast differentiation. *PLoS ONE.* (2015) 10:e0144982. doi: 10.1371/journal.pone.0144982
214. Stoick-Cooper CL, Weidinger G, Riehle KJ, Hubbert C, Major MB, Fausto N, et al. Distinct Wnt signaling pathways have opposing roles in appendage regeneration. *Development.* (2007) 134:479–89. doi: 10.1242/dev.011123
215. Huang CJ, Tu CT, Hsiao CD, Hsieh FJ, Tsai HJ. Germ-line transmission of a myocardium-specific GFP transgene reveals critical regulatory elements in the cardiac myosin light chain 2 promoter of zebrafish. *Dev Dyn.* (2003) 228:30–40. doi: 10.1002/dvdy.10356
216. Li J, Chen Z, Gao LY, Colomi A, Ucko M, Fang S, et al. A transgenic zebrafish model for monitoring xbp1 splicing and endoplasmic reticulum stress in vivo. *Mech Dev.* (2015) 137:33–44. doi: 10.1016/j.mod.2015.04.001
217. Clark EM, Nonarath HJT, Bostrom JR, Link BA. Establishment and validation of an endoplasmic reticulum stress reporter to monitor zebrafish ATF6 activity in development and disease. *Dis Model Mech.* (2020) 13. doi: 10.1242/dmm.041426

218. Ding Y, Lee J, Hsu JJ, Chang CC, Baek KI, Ranjbarvaziri S, et al. Light-sheet imaging to elucidate cardiovascular injury and repair. *Curr Cardiol Rep.* (2018) 20:35. doi: 10.1007/s11886-018-0979-6
219. Coltery RF, Link BA. Dynamic smad-mediated BMP signaling revealed through transgenic zebrafish. *Dev Dyn.* (2011) 240:712–22. doi: 10.1002/dvdy.22567
220. Dorsky RI, Itoh M, Moon RT, Chitnis A. Two tcf3 genes cooperate to pattern the zebrafish brain. *Development.* (2003) 130:1937–47. doi: 10.1242/dev.00402
221. Schwend T, Loucks EJ, Ahlgren SC. Visualization of gli activity in craniofacial tissues of hedgehog-pathway reporter transgenic zebrafish. *PLoS ONE.* (2010) 5:e14396. doi: 10.1371/journal.pone.0014396
222. Blair H, Schlesinger P, Huang C, Zaidi M. Calcium signalling and calcium transport in bone disease. *Subcell Biochem.* (2007) 45:539–62. doi: 10.1007/978-1-4020-6191-2_21
223. Cao X, Chen D. The BMP signaling and *in vivo* bone formation. *Gene.* (2005) 357:1–8. doi: 10.1016/j.gene.2005.06.017
224. Houschyar KS, Tapking C, Borrelli MR, Popp D, Duscher D, Maan ZN, et al. Wnt pathway in bone repair and regeneration - what do we know so far. *Front Cell Dev Biol.* (2019) 6:170. doi: 10.3389/fcell.2018.00170
225. Huang S, Wang Y, Luo L, Li X, Jin X, Li S, et al. BMP2 is related to hirschsprung's disease and required for enteric nervous system development. *Front Cell Neurosci.* (2019) 13:523. doi: 10.3389/fncel.2019.00523
226. Besio R, Garibaldi N, Leoni L, Cipolla L, Sabbioneda S, Biggiogera M, et al. Cellular stress due to impairment of collagen prolyl hydroxylation complex is rescued by the chaperone 4-phenylbutyrate. *Dis Model Mech.* (2019) 12. doi: 10.1242/dmm.038521
227. Besio R, Iula G, Garibaldi N, Cipolla L, Sabbioneda S, Biggiogera M, et al. 4-PBA ameliorates cellular homeostasis in fibroblasts from osteogenesis imperfecta patients by enhancing autophagy and stimulating protein secretion. *Biochim Biophys Acta Mol Basis Dis.* (2018) 1864(5 Pt A):1642–52. doi: 10.1016/j.bbdis.2018.02.002
228. Howarth DL, Lindtner C, Vacaru AM, Sachidanandam R, Tsedensodnom O, Vasilkova T, et al. Activating transcription factor 6 is necessary and sufficient for alcoholic fatty liver disease in zebrafish. *PLoS Genet.* (2014) 10:e1004335. doi: 10.1371/journal.pgen.1004335
229. Yeh KY, Lai CY, Lin CY, Hsu CC, Lo CP, Her GM. ATF4 overexpression induces early onset of hyperlipidaemia and hepatic steatosis and enhances adipogenesis in zebrafish. *Sci Rep.* (2017) 7:16362. doi: 10.1038/s41598-017-16587-9
230. Cardeira J, Gavaia PJ, Fernandez I, Cengiz IF, Moreira-Silva J, Oliveira JM, et al. Quantitative assessment of the regenerative and mineralogenic performances of the zebrafish caudal fin. *Sci Rep.* (2016) 6:39191. doi: 10.1038/srep39191
231. Chen CH, Puliafito A, Cox BD, Primo L, Fang Y, Di Talia S, et al. Multicolor cell barcoding technology for long-term surveillance of epithelial regeneration in zebrafish. *Dev Cell.* (2016) 36:668–80. doi: 10.1016/j.devcel.2016.02.017
232. Park S, Greco V, Cockburn K. Live imaging of stem cells: answering old questions and raising new ones. *Curr Opin Cell Biol.* (2016) 43:30–37. doi: 10.1016/j.ccb.2016.07.004
233. Mishra R, Sehring I, Cederlund M, Mulaw M, Weidinger G. NF-kappaB signaling negatively regulates osteoblast dedifferentiation during zebrafish bone regeneration. *Dev Cell.* (2020) 52:167–82.e7. doi: 10.1016/j.devcel.2019.11.016
234. Bruneel B, Witten PE. Power and challenges of using zebrafish as a model for skeletal tissue imaging. *Connect Tissue Res.* (2015) 56:161–73. doi: 10.3109/03008207.2015.1013193
235. Witten PE, Gil Martens L, Huysseune A, Takle H, Hjelde K. Towards a classification and an understanding of developmental relationships of vertebral body malformations in Atlantic salmon (*Salmo salar* Aquaculture L). *Aquaculture.* 295:6–14. doi: 10.1016/j.aquaculture.2009.06.037
236. Witten PE, Obach A, Huysseune A, Baeverfjord G. Vertebrae fusion in Atlantic salmon (*Salmo salar*): development, aggravation and pathways of containment. *Aquaculture.* (2006) 258:164–72. doi: 10.1016/j.aquaculture.2006.05.005
237. du Plessis A, Broeckhoven C, Guelpa A, le Roux SG. Laboratory x-ray micro-computed tomography: a user guideline for biological samples. *Gigascience.* (2017) 6:1–11. doi: 10.1093/gigascience/gix027
238. Rawson SD, Maksimcuka J, Withers PJ, Cartmell SH. X-ray computed tomography in life sciences. *BMC Biol.* (2020) 18:21. doi: 10.1186/s12915-020-0753-2
239. Babaei F, Hong TL, Yeung K, Cheng SH, Lam YW. Contrast-enhanced X-ray micro-computed tomography as a versatile method for anatomical studies of adult zebrafish. *Zebrafish.* (2016) 13:310–6. doi: 10.1089/zeb.2016.1245
240. Descamps E, Sochacka A, De Kegel B, Van Loo D, Van Hoorebeke L, Adriaens D. Soft tissue discrimination with contrast agents using micro-CT scanning. *Belgian J Zool.* (2014) 144:20–40. doi: 10.26496/bjz.2014.63
241. Charles JF, Sury M, Tsang K, Urso K, Henke K, Huang Y, et al. Utility of quantitative micro-computed tomographic analysis in zebrafish to define gene function during skeletogenesis. *Bone.* (2017) 101:162–71. doi: 10.1016/j.bone.2017.05.001
242. Suniaga S, Rolvien T, Vom Scheidt A, Fiedler IAK, Bale HA, Huysseune A, et al. Increased mechanical loading through controlled swimming exercise induces bone formation and mineralization in adult zebrafish. *Sci Rep.* (2018) 8:3646. doi: 10.1038/s41598-018-21776-1
243. Gadow H, Abbott EC. On the evolution of the vertebral column of fishes. *Philos Trans R Soc Lond.* (1985) 186:163–221. doi: 10.1098/rstb.1895.0004
244. Sakata-Haga H, Uchishiba M, Shimada H, Tsukada T, Mitani M, Arikawa T, et al. A rapid and nondestructive protocol for whole-mount bone staining of small fish and *Xenopus*. *Sci Rep.* (2018) 8:7453–60. doi: 10.1038/s41598-018-25836-4
245. Moriguchi T, Yano K, Nakagawa S, Kaji F. Elucidation of adsorption mechanism of bone-staining agent alizarin red S on hydroxyapatite by FT-IR microspectroscopy. *J Colloid Interface Sci.* (2003) 260:19–25. doi: 10.1016/S0021-9797(02)00157-1
246. Fraser TWK, Witten PE, Albrektzen S, Breck O, Fontanillas R, Nankervis L, et al. Phosphorus nutrition in farmed Atlantic salmon (*Salmo salar*): life stage and temperature effects on bone pathologies. *Aquaculture.* (2019) 511:1–12. doi: 10.1016/j.aquaculture.2019.734246
247. Witten PE, Fjelldal PG, Huysseune A, McGurk C, Obach A, Owen MAG. Bone without minerals and its secondary mineralization in Atlantic salmon (*Salmo salar*): the recovery from phosphorus deficiency. *J Exp Biol.* (2019) 222:1–15. doi: 10.1242/jeb.188763
248. Vandenplas S, De Clercq A, Huysseune A. Tooth replacement without a dental lamina: the search for epithelial stem cells in *Polypterus senegalus*. *J Exp Zool B Mol Dev Evol.* (2014) 322:281–93. doi: 10.1002/jez.b.22577
249. Woltmann I, Shkil FN, De Clercq A, Huysseune A, Witten PE. Supernumerary teeth in the pharyngeal dentition of slow developing zebrafish. *J Appl Ichthyol.* (2018) 34:455–64. doi: 10.1111/jai.13668
250. Bensimon-Brito A, Cardeira J, Dionísio G, Huysseune A, Cancela ML, Witten PE. Revisiting *in vivo* staining with alizarin red S - a valuable approach to analyse zebrafish skeletal mineralization during development and regeneration. *BMC Dev Biol.* (2016) 16:1–9. doi: 10.1186/s12861-016-0102-4
251. Kiernan JA. *Histological and Histochemical Methods: Theory and Practice.* 5th ed. Banbury: Scion Publishing. (2015)
252. Cabbage CC, Mabee PM. Development of the cranium and paired fins in the zebrafish *Danio rerio* (*Ostariophysi, Cyprinidae*). *J Morphol.* (1996) 229:121–60. doi: 10.1002/(SICI)1097-4687(199608)229:2<121::AID-JMORI>3.0.CO;2-4
253. Kimmel CB, Miller CT, Moens CB. Specification and morphogenesis of the zebrafish larval head skeleton. *Dev Biol.* (2001) 233:239–57. doi: 10.1006/dbio.2001.0201
254. Kimmel CB, Walker MB, Miller CT. Morphing the hyomandibular skeleton in development and evolution. *J Exp Zool B Mol Dev Evol.* (2007) 308:609–24. doi: 10.1002/jez.b.21155
255. Walker M, Kimmel C. A two-color acid-free cartilage and bone stain for zebrafish larvae. *Biotech Histochem.* (2007) 82:23–28. doi: 10.1080/10520290701333558
256. Philip NS, Green DM. Recovery and enhancement of faded cleared and double stained specimens. *Biotech Histochem.* (2000) 75:193–6. doi: 10.3109/10520290009066500
257. Copper JE, Budgeon LR, Foutz CA, van Rossum DB, Vanselow DJ, Hubley MJ, et al. Comparative analysis of fixation and embedding techniques for

- optimized histological preparation of zebrafish. *Comp Biochem Physiol C Toxicol Pharmacol.* (2018) 208:38–46. doi: 10.1016/j.cbpc.2017.11.003
258. Witten PE. Enzyme histochemical characteristics of osteoblasts and mononucleated osteoclasts in a teleost fish with acellular bone (*Oreochromis niloticus*, *Cichlidae*). *Cell Tissue Res.* (1997) 287:591–9. doi: 10.1007/s004410050782
259. Sarmah S, Barrallo-Gimeno A, Melville DB, Topczewski J, Solnica-Krezel L, Knapik EW. Sec24D-dependent transport of extracellular matrix proteins is required for zebrafish skeletal morphogenesis. *PLoS ONE.* (2010) 5:e10367. doi: 10.1371/journal.pone.0010367
260. Pasqualetti S, Banfi G, Mariotti M. The zebrafish scale as model to study the bone mineralization process. *J Mol Histol.* (2012) 43:589–95. doi: 10.1007/s10735-012-9425-z
261. Duran I, Mari-Beffa M, Santamaria JA, Becerra J, Santos-Ruiz L. Actinotrichia collagens and their role in fin formation. *Dev Biol.* (2011) 354:160–72. doi: 10.1016/j.ydbio.2011.03.014
262. Liedtke D, Orth M, Meissler M, Geuer S, Knaup S, Koblitz I, et al. ECM alterations in FnDC3a (fibronectin domain containing protein 3A) deficient zebrafish cause temporal fin development and regeneration defects. *Sci Rep.* (2019) 9:13383. doi: 10.1038/s41598-019-50055-w
263. Schring IM, Weidinger G. Recent advancements in understanding fin regeneration in zebrafish. *Wiley Interdiscip Rev Dev Biol.* (2019) 9:e367. doi: 10.1002/wdev.367
264. Stewart S, Stankunas K. Limited dedifferentiation provides replacement tissue during zebrafish fin regeneration. *Dev Biol.* (2012) 365:339–49. doi: 10.1016/j.ydbio.2012.02.031
265. Paul S, Schindler S, Giovannone D, de Millo Terrazzani A, Mariani FV, Crump JG. Ihha induces hybrid cartilage-bone cells during zebrafish jawbone regeneration. *Development.* (2016) 143:2066–76. doi: 10.1242/dev.131292
266. Azevedo AS, Grotek B, Jacinto A, Weidinger G, Saude L. The regenerative capacity of the zebrafish caudal fin is not affected by repeated amputations. *PLoS ONE.* (2011) 6:e22820. doi: 10.1371/journal.pone.0022820
267. Kinoshita M, Murata K, Naruse K, Tanaka M, Kamei Y. *Medaka: Biology, Management, Experimental Protocols.* Vol. 2. Wiley-Blackwell (2019).
268. Furutani-Seiki M, Wittbrodt J. Medaka and zebrafish, an evolutionary twin study. *Mech Dev.* (2004) 121:629–37. doi: 10.1016/j.mod.2004.05.010
269. Wittbrodt J, Shima A, Scharlt M. Medaka—a model organism from the far East. *Nat Rev Genet.* (2002) 3:53–64. doi: 10.1038/nrg704
270. Azetsu Y, Inohaya K, Takano Y, Kinoshita M, Tasaki M, Kudo A. The sp7 gene is required for maturation of osteoblast-lineage cells in medaka (*Oryzias latipes*) vertebral column development. *Dev Biol.* (2017) 431:252–62. doi: 10.1016/j.ydbio.2017.09.010
271. Irie K, Kuroda Y, Mimori N, Hayashi S, Abe M, Tsuji N, et al. Histopathology of a wavy medaka. *J Toxicol Pathol.* (2016) 29:115–8. doi: 10.1293/tox.2015-0070
272. Mantoku A, Chatani M, Aono K, Inohaya K, Kudo A. Osteoblast and osteoclast behaviors in the turnover of attachment bones during medaka tooth replacement. *Dev Biol.* (2016) 409:370–81. doi: 10.1016/j.ydbio.2015.12.002
273. Yu T, Witten PE, Huysseune A, Buettner A, To TT, Winkler C. Live imaging of osteoclast inhibition by bisphosphonates in a medaka osteoporosis model. *Dis Model Mech.* (2016) 9:155–63. doi: 10.1242/dmm.019091
274. Meyer A, Van de Peer Y. From 2R to 3R: evidence for a fish-specific genome duplication (FSGD). *Bioessays.* (2005) 27:937–45. doi: 10.1002/bies.20293
275. Hadjantonakis AK, Pirity M, Nagy A. Cre recombinase mediated alterations of the mouse genome using embryonic stem cells. *Methods Mol Biol.* (2008) 461:111–32. doi: 10.1007/978-1-60327-483-8_8
276. Utomo AR, Nikitin AY, Lee WH. Temporal, spatial, and cell type-specific control of Cre-mediated DNA recombination in transgenic mice. *Nat Biotechnol.* (1999) 17:1091–6. doi: 10.1038/15073

Conflict of Interest: PS is a Bruker employee.

The remaining authors declare that the research was conducted in the absence of any commercial or financial relationships that could be construed as a potential conflict of interest.

Copyright © 2020 Tonelli, Bek, Besio, De Clercq, Leoni, Salmon, Coucke, Willaert and Forlino. This is an open-access article distributed under the terms of the Creative Commons Attribution License (CC BY). The use, distribution or reproduction in other forums is permitted, provided the original author(s) and the copyright owner(s) are credited and that the original publication in this journal is cited, in accordance with accepted academic practice. No use, distribution or reproduction is permitted which does not comply with these terms.

Bibliography

- Apschner, A., S. Schulte-Merker, and P. E. Witten. 2011. "Not all bones are created equal - using zebrafish and other teleost species in osteogenesis research." *Methods Cell Biol* 105:239-55. doi: 10.1016/B978-0-12-381320-6.00010-2.
- Arratia, G., and H. P. Schultze. 1992. "Reevaluation of the caudal skeleton of certain actinopterygian fishes: III. Salmonidae. Homologization of caudal skeletal structures." *J Morphol* 214 (2):187-249. doi: 10.1002/jmor.1052140209.
- Asharani, P. V., K. Keupp, O. Semler, W. Wang, Y. Li, H. Thiele, G. Yigit, E. Pohl, J. Becker, P. Frommolt, C. Sonntag, J. Altmüller, K. Zimmermann, D. S. Greenspan, N. A. Akarsu, C. Netzer, E. Schönau, R. Wirth, M. Hammerschmidt, P. Nürnberg, B. Wollnik, and T. J. Carney. 2012. "Attenuated BMP1 function compromises osteogenesis, leading to bone fragility in humans and zebrafish." *Am J Hum Genet* 90 (4):661-74. doi: 10.1016/j.ajhg.2012.02.026.
- Balasubramanian, M., N. Fratzl-Zelman, R. O'Sullivan, M. Bull, N. Fa Peel, R. C. Pollitt, R. Jones, E. Milne, K. Smith, P. Roschger, K. Klaushofer, and N. J. Bishop. 2018. "Novel PLS3 variants in X-linked osteoporosis: Exploring bone material properties." *Am J Med Genet A* 176 (7):1578-1586. doi: 10.1002/ajmg.a.38830.
- Baldrige, D., U. Schwarze, R. Morello, J. Lenington, T. K. Bertin, J. M. Pace, M. G. Pepin, M. Weis, D. R. Eyre, J. Walsh, D. Lambert, A. Green, H. Robinson, M. Michelson, G. Houge, C. Lindman, J. Martin, J. Ward, E. Lemyre, J. J. Mitchell, D. Krakow, D. L. Rimoim, D. H. Cohn, P. H. Byers, and B. Lee. 2008. "CRTAP and LEPRE1 mutations in recessive osteogenesis imperfecta." *Hum Mutat* 29 (12):1435-42. doi: 10.1002/humu.20799.
- Bargman, R., A. Huang, A. L. Boskey, C. Raggio, and N. Pleshko. 2010. "RANKL inhibition improves bone properties in a mouse model of osteogenesis imperfecta." *Connect Tissue Res* 51 (2):123-31. doi: 10.3109/03008200903108472.
- Barnes, A. M., W. Chang, R. Morello, W. A. Cabral, M. Weis, D. R. Eyre, S. Leikin, E. Makareeva, N. Kuznetsova, T. E. Uveges, A. Ashok, A. W. Flor, J. J. Mulvihill, P. L. Wilson, U. T. Sundaram, B. Lee, and J. C. Marini. 2006. "Deficiency of cartilage-associated protein in recessive lethal osteogenesis imperfecta." *N Engl J Med* 355 (26):2757-64. doi: 10.1056/NEJMoa063804.
- Barnes, A. M., G. Duncan, M. Weis, W. Paton, W. A. Cabral, E. L. Mertz, E. Makareeva, M. J. Gambello, F. L. Lacbawan, S. Leikin, A. Fertala, D. R. Eyre, S. J. Bale, and J. C. Marini. 2013. "Kuskokwim syndrome, a recessive congenital contracture disorder, extends the phenotype of FKBP10 mutations." *Hum Mutat* 34 (9):1279-88. doi: 10.1002/humu.22362.
- Baron, R., and M. Kneissel. 2013. "WNT signaling in bone homeostasis and disease: from human mutations to treatments." *Nat Med* 19 (2):179-92. doi: 10.1038/nm.3074.
- Barrangou, R., C. Fremaux, H. Deveau, M. Richards, P. Boyaval, S. Moineau, D. A. Romero, and P. Horvath. 2007. "CRISPR provides acquired resistance against viruses in prokaryotes." *Science* 315 (5819):1709-12. doi: 10.1126/science.1138140.
- Becker, J., O. Semler, C. Gilissen, Y. Li, H. J. Bolz, C. Giunta, C. Bergmann, M. Rohrbach, F. Koerber, K. Zimmermann, P. de Vries, B. Wirth, E. Schoenau, B. Wollnik, J. A. Veltman, A. Hoischen, and C. Netzer. 2011. "Exome sequencing identifies truncating mutations in human SERPINF1 in autosomal-recessive osteogenesis imperfecta." *Am J Hum Genet* 88 (3):362-71. doi: 10.1016/j.ajhg.2011.01.015.
- Bella, J., and D. J. Hulmes. 2017. "Fibrillar Collagens." *Subcell Biochem* 82:457-490. doi: 10.1007/978-3-319-49674-0_14.
- Bensimon-Brito, A., M. L. Cancela, A. Huysseune, and P. E. Witten. 2012. "Vestiges, rudiments and fusion events: the zebrafish caudal fin endoskeleton in an evo-devo perspective." *Evol Dev* 14 (1):116-27. doi: 10.1111/j.1525-142X.2011.00526.x.

- Berg, R. A., and D. J. Prockop. 1973. "The thermal transition of a non-hydroxylated form of collagen. Evidence for a role for hydroxyproline in stabilizing the triple-helix of collagen." *Biochem Biophys Res Commun* 52 (1):115-20. doi: 10.1016/0006-291x(73)90961-3.
- Berridge, M. J., M. D. Bootman, and H. L. Roderick. 2003. "Calcium signalling: dynamics, homeostasis and remodelling." *Nat Rev Mol Cell Biol* 4 (7):517-29. doi: 10.1038/nrm1155.
- Besio, R., N. Garibaldi, L. Leoni, L. Cipolla, S. Sabbioneda, M. Biggiogera, M. Mottes, M. Aglan, G. A. Otaify, S. A. Temtamy, A. Rossi, and A. Forlino. 2019. "Cellular stress due to impairment of collagen prolyl hydroxylation complex is rescued by the chaperone 4-phenylbutyrate." *Dis Model Mech* 12 (6). doi: 10.1242/dmm.038521.
- Besio, R., G. Iula, N. Garibaldi, L. Cipolla, S. Sabbioneda, M. Biggiogera, J. C. Marini, A. Rossi, and A. Forlino. 2018. "4-PBA ameliorates cellular homeostasis in fibroblasts from osteogenesis imperfecta patients by enhancing autophagy and stimulating protein secretion." *Biochim Biophys Acta Mol Basis Dis* 1864 (5 Pt A):1642-1652. doi: 10.1016/j.bbadis.2018.02.002.
- Bhaya, D., M. Davison, and R. Barrangou. 2011. "CRISPR-Cas systems in bacteria and archaea: versatile small RNAs for adaptive defense and regulation." *Annu Rev Genet* 45:273-97. doi: 10.1146/annurev-genet-110410-132430.
- Biggin, A., and C. F. Munns. 2017. "Long-Term Bisphosphonate Therapy in Osteogenesis Imperfecta." *Curr Osteoporos Rep* 15 (5):412-418. doi: 10.1007/s11914-017-0401-0.
- Bird, N. C., and P. M. Mabee. 2003. "Developmental morphology of the axial skeleton of the zebrafish, *Danio rerio* (Ostariophysi: Cyprinidae)." *Dev Dyn* 228 (3):337-57. doi: 10.1002/dvdy.10387.
- Bogan, R., R. C. Riddle, Z. Li, S. Kumar, A. Nandal, M. C. Faugere, A. Boskey, S. E. Crawford, and T. L. Clemens. 2013. "A mouse model for human osteogenesis imperfecta type VI." *J Bone Miner Res* 28 (7):1531-6. doi: 10.1002/jbmr.1892.
- Bone, H. G., R. B. Wagman, M. L. Brandi, J. P. Brown, R. Chapurlat, S. R. Cummings, E. Czerwiński, A. Fahrleitner-Pammer, D. L. Kendler, K. Lippuner, J. Y. Reginster, C. Roux, J. Malouf, M. N. Bradley, N. S. Daizadeh, A. Wang, P. Dakin, N. Pannaciuoli, D. W. Dempster, and S. Papapoulos. 2017. "10 years of denosumab treatment in postmenopausal women with osteoporosis: results from the phase 3 randomised FREEDOM trial and open-label extension." *Lancet Diabetes Endocrinol* 5 (7):513-523. doi: 10.1016/S2213-8587(17)30138-9.
- Boot-Handford, R. P., and M. D. Briggs. 2010. "The unfolded protein response and its relevance to connective tissue diseases." *Cell Tissue Res* 339 (1):197-211. doi: 10.1007/s00441-009-0877-8.
- Bourhis, J. M., N. Mariano, Y. Zhao, K. Harlos, J. Y. Exposito, E. Y. Jones, C. Moali, N. Aghajari, and D. J. Hulmes. 2012. "Structural basis of fibrillar collagen trimerization and related genetic disorders." *Nat Struct Mol Biol* 19 (10):1031-6. doi: 10.1038/nsmb.2389.
- Brouns, S. J., M. M. Jore, M. Lundgren, E. R. Westra, R. J. Slijkhuis, A. P. Snijders, M. J. Dickman, K. S. Makarova, E. V. Koonin, and J. van der Oost. 2008. "Small CRISPR RNAs guide antiviral defense in prokaryotes." *Science* 321 (5891):960-4. doi: 10.1126/science.1159689.
- Bulleid, Neil J, Jane A Dalley, and Janice F Lees. 1997. "The C-propeptide domain of procollagen can be replaced with a transmembrane domain without affecting trimer formation or collagen triple helix folding during biosynthesis." *The EMBO Journal* 16 (22):6694-6701.
- Burmistrz, M., and K. Pyré. 2015. "CRISPR-Cas Systems in Prokaryotes." *Pol J Microbiol* 64 (3):193-202.
- Bächinger, H. P., P. Bruckner, R. Timpl, D. J. Prockop, and J. Engel. 1980. "Folding mechanism of the triple helix in type-III collagen and type-III pN-collagen. Role of disulfide bridges and peptide bond isomerization." *Eur J Biochem* 106 (2):619-32. doi: 10.1111/j.1432-1033.1980.tb04610.x.

- Bächinger, Hans Peter, Kazunori Mizuno, Janice A. Vranka, and Sergei P. Boudko. 2010. "5.16 - Collagen Formation and Structure." In *Comprehensive Natural Products II*, edited by Hung-Wen Liu and Lew Mander, 469-530. Oxford: Elsevier.
- Cabral, W. A., M. Ishikawa, M. Garten, E. N. Makareeva, B. M. Sargent, M. Weis, A. M. Barnes, E. A. Webb, N. J. Shaw, L. Ala-Kokko, F. L. Lacbawan, W. Högler, S. Leikin, P. S. Blank, J. Zimmerberg, D. R. Eyre, Y. Yamada, and J. C. Marini. 2016. "Absence of the ER Cation Channel TMEM38B/TRIC-B Disrupts Intracellular Calcium Homeostasis and Dysregulates Collagen Synthesis in Recessive Osteogenesis Imperfecta." *PLoS Genet* 12 (7):e1006156. doi: 10.1371/journal.pgen.1006156.
- Cabral, W. A., S. Milgrom, A. D. Letocha, E. Moriarty, and J. C. Marini. 2006. "Biochemical screening of type I collagen in osteogenesis imperfecta: detection of glycine substitutions in the amino end of the alpha chains requires supplementation by molecular analysis." *J Med Genet* 43 (8):685-90. doi: 10.1136/jmg.2005.040493.
- Cabral, W. A., I. Perdivara, M. Weis, M. Terajima, A. R. Blissett, W. Chang, J. E. Perosky, E. N. Makareeva, E. L. Mertz, S. Leikin, K. B. Tomer, K. M. Kozloff, D. R. Eyre, M. Yamauchi, and J. C. Marini. 2014. "Abnormal type I collagen post-translational modification and crosslinking in a cyclophilin B KO mouse model of recessive osteogenesis imperfecta." *PLoS Genet* 10 (6):e1004465. doi: 10.1371/journal.pgen.1004465.
- Canty, E. G., and K. E. Kadler. 2005. "Procollagen trafficking, processing and fibrillogenesis." *J Cell Sci* 118 (Pt 7):1341-53. doi: 10.1242/jcs.01731.
- Caparros-Martin, J. A., M. S. Aglan, S. Temtamy, G. A. Otaify, M. Valencia, J. Nevado, E. Vallespin, A. Del Pozo, C. Prior de Castro, L. Calatrava-Ferreras, P. Gutierrez, A. M. Bueno, B. Sagastizabal, E. Guillen-Navarro, M. Ballesta-Martinez, V. Gonzalez, S. Y. Basaran, R. Buyukoglan, B. Sarikepe, C. Espinoza-Valdez, F. Cammarata-Scalisi, V. Martinez-Glez, K. E. Heath, P. Lapunzina, and V. L. Ruiz-Perez. 2017. "Molecular spectrum and differential diagnosis in patients referred with sporadic or autosomal recessive osteogenesis imperfecta." *Mol Genet Genomic Med* 5 (1):28-39. doi: 10.1002/mgg3.257.
- Castagnola, P., M. Gennari, R. Morello, L. Tonachini, O. Marin, A. Gaggero, and R. Cancedda. 1997. "Cartilage associated protein (CASP) is a novel developmentally regulated chick embryo protein." *J Cell Sci* 110 (Pt 12):1351-9.
- Catterall, W. A. 2010. "Ion channel voltage sensors: structure, function, and pathophysiology." *Neuron* 67 (6):915-28. doi: 10.1016/j.neuron.2010.08.021.
- Chang, W., A. M. Barnes, W. A. Cabral, J. N. Bodurtha, and J. C. Marini. 2010. "Prolyl 3-hydroxylase 1 and CRTAP are mutually stabilizing in the endoplasmic reticulum collagen prolyl 3-hydroxylation complex." *Hum Mol Genet* 19 (2):223-34. doi: 10.1093/hmg/ddp481.
- Chen, J., L. Xia, M. R. Bruchas, and L. Solnica-Krezel. 2017. "Imaging early embryonic calcium activity with GCaMP6s transgenic zebrafish." *Dev Biol* 430 (2):385-396. doi: 10.1016/j.ydbio.2017.03.010.
- Chou, J. Y. 1989. "Differentiated mammalian cell lines immortalized by temperature-sensitive tumor viruses." *Mol Endocrinol* 3 (10):1511-4. doi: 10.1210/mend-3-10-1511.
- Christiansen, H. E., U. Schwarze, S. M. Pyott, A. AlSwaid, M. Al Balwi, S. Alrasheed, M. G. Pepin, M. A. Weis, D. R. Eyre, and P. H. Byers. 2010. "Homozygosity for a missense mutation in SERPINH1, which encodes the collagen chaperone protein HSP47, results in severe recessive osteogenesis imperfecta." *Am J Hum Genet* 86 (3):389-98. doi: 10.1016/j.ajhg.2010.01.034.
- Christoffels, A., E. G. L. Koh, J. Chia, S. Brenner, S. Aparicio, and B. Venkatesh. 2004. "Fugu Genome Analysis Provides Evidence for a Whole-Genome Duplication Early During the Evolution of Ray-Finned Fishes." *Molecular Biology and Evolution*.
- Clark, C. C. 1979. "The distribution and initial characterization of oligosaccharide units on the COOH-terminal propeptide extensions of the pro-alpha 1 and pro-alpha 2 chains of type I procollagen." *J Biol Chem* 254 (21):10798-802.

- Colland, F., X. Jacq, V. Trouplin, C. Mouglin, C. Groizeleau, A. Hamburger, A. Meil, J. Wojcik, P. Legrain, and J. M. Gauthier. 2004. "Functional proteomics mapping of a human signaling pathway." *Genome Res* 14 (7):1324-32. doi: 10.1101/gr.2334104.
- Corbett, E. F., and M. Michalak. 2000. "Calcium, a signaling molecule in the endoplasmic reticulum?" *Trends Biochem Sci* 25 (7):307-11. doi: 10.1016/s0968-0004(00)01588-7.
- Cosman, F., D. B. Crittenden, J. D. Adachi, N. Binkley, E. Czerwinski, S. Ferrari, L. C. Hofbauer, E. Lau, E. M. Lewiecki, A. Miyauchi, C. A. Zerbin, C. E. Milmont, L. Chen, J. Maddox, P. D. Meisner, C. Libanati, and A. Grauer. 2016. "Romosozumab Treatment in Postmenopausal Women with Osteoporosis." *N Engl J Med* 375 (16):1532-1543. doi: 10.1056/NEJMoal607948.
- Costantini, A., P. Krallis, A. Kämpe, E. M. Karavitakis, F. Taylan, O. Mäkitie, and A. Doulgeraki. 2018. "A novel frameshift deletion in PLS3 causing severe primary osteoporosis." *J Hum Genet* 63 (8):923-926. doi: 10.1038/s10038-018-0472-5.
- Crane, J. L., L. Xian, and X. Cao. 2016. "Role of TGF- β Signaling in Coupling Bone Remodeling." *Methods Mol Biol* 1344:287-300. doi: 10.1007/978-1-4939-2966-5_18.
- Czekanska, E. M., M. J. Stoddart, R. G. Richards, and J. S. Hayes. 2012. "In search of an osteoblast cell model for in vitro research." *Eur Cell Mater* 24:1-17. doi: 10.22203/ecm.v024a01.
- Daley, E., E. A. Streeten, J. D. Sorkin, N. Kuznetsova, S. A. Shapses, S. M. Carleton, A. R. Shuldiner, J. C. Marini, C. L. Phillips, S. A. Goldstein, S. Leikin, and D. J. McBride. 2010. "Variable bone fragility associated with an Amish COL1A2 variant and a knock-in mouse model." *J Bone Miner Res* 25 (2):247-61. doi: 10.1359/jbmr.090720.
- de Bruyn, J. R., M. Goiko, M. Mozaffari, D. Bator, R. L. Dauphinee, Y. Liao, R. L. Flemming, M. S. Bramble, G. K. Hunter, and H. A. Goldberg. 2013. "Dynamic light scattering study of inhibition of nucleation and growth of hydroxyapatite crystals by osteopontin." *PLoS One* 8 (2):e56764. doi: 10.1371/journal.pone.0056764.
- Deveau, H., R. Barrangou, J. E. Garneau, J. Labonté, C. Fremaux, P. Boyaval, D. A. Romero, P. Horvath, and S. Moineau. 2008. "Phage response to CRISPR-encoded resistance in *Streptococcus thermophilus*." *J Bacteriol* 190 (4):1390-400. doi: 10.1128/JB.01412-07.
- Dewit, J., P. E. Witten, and A. Huisseune. 2011. "The mechanism of cartilage subdivision in the reorganization of the zebrafish pectoral fin endoskeleton." *J Exp Zool B Mol Dev Evol* 316 (8):584-97. doi: 10.1002/jez.b.21433.
- Diener, S., S. Bayer, S. Sabrautzki, T. Wieland, B. Mentrup, G. K. Przemec, B. Rathkolb, E. Graf, W. Hans, H. Fuchs, M. Horsch, T. Schwarzmayr, E. Wolf, E. Klopocki, F. Jakob, T. M. Strom, M. Hrabě de Angelis, and B. Lorenz-Depiereux. 2016. "Exome sequencing identifies a nonsense mutation in *Fam46a* associated with bone abnormalities in a new mouse model for skeletal dysplasia." *Mamm Genome* 27 (3-4):111-21. doi: 10.1007/s00335-016-9619-x.
- Doyard, M., S. Bacrot, C. Huber, M. Di Rocco, A. Goldenberg, M. S. Aglan, P. Brunelle, S. Temtamy, C. Michot, G. A. Otaify, C. Haudry, M. Castanet, J. Leroux, J. P. Bonnefont, A. Munnich, G. Baujat, P. Lapunzina, S. Monnot, V. L. Ruiz-Perez, and V. Cormier-Daire. 2018. "mutations are responsible for autosomal recessive osteogenesis imperfecta." *J Med Genet* 55 (4):278-284. doi: 10.1136/jmedgenet-2017-104999.
- Drake, M. T., B. L. Clarke, and S. Khosla. 2008. "Bisphosphonates: mechanism of action and role in clinical practice." *Mayo Clin Proc* 83 (9):1032-45. doi: 10.4065/83.9.1032.
- Dubail, J., P. Brunelle, G. Baujat, C. Huber, M. Doyard, C. Michot, P. Chavassieux, A. Khairouni, V. Topouchian, S. Monnot, E. Koumakis, and V. Cormier-Daire. 2020. "Homozygous Loss-of-Function Mutations in *CCDC134* Are Responsible for a Severe Form of Osteogenesis Imperfecta." *J Bone Miner Res*. doi: 10.1002/jbmr.4011.
- Eames, B. F., A. Singer, G. A. Smith, Z. A. Wood, Y. L. Yan, X. He, S. J. Polizzi, J. M. Catchen, A. Rodriguez-Mari, T. Linbo, D. W. Raible, and J. H. Postlethwait. 2010. "UDP xylose synthase 1 is required for morphogenesis and histogenesis of the craniofacial skeleton." *Dev Biol* 341 (2):400-15. doi: 10.1016/j.ydbio.2010.02.035.

- Eyre, D. R., M. A. Paz, and P. M. Gallop. 1984. "Cross-linking in collagen and elastin." *Annu Rev Biochem* 53:717-48. doi: 10.1146/annurev.bi.53.070184.003441.
- Fahiminiya, S., J. Majewski, H. Al-Jallad, P. Moffatt, J. Mort, F. H. Glorieux, P. Roschger, K. Klaushofer, and F. Rauch. 2014. "Osteoporosis caused by mutations in PLS3: clinical and bone tissue characteristics." *J Bone Miner Res* 29 (8):1805-14. doi: 10.1002/jbmr.2208.
- Faqeih, E., R. Shaheen, and F. S. Alkuraya. 2013. "WNT1 mutation with recessive osteogenesis imperfecta and profound neurological phenotype." *J Med Genet* 50 (7):491-2. doi: 10.1136/jmedgenet-2013-101750.
- Farber, C. R., A. Reich, A. M. Barnes, P. Becerra, F. Rauch, W. A. Cabral, A. Bae, A. Quinlan, F. H. Glorieux, T. L. Clemens, and J. C. Marini. 2014. "A novel *IFITM5* mutation in severe atypical osteogenesis imperfecta type VI impairs osteoblast production of pigment epithelium-derived factor." *J Bone Miner Res* 29 (6):1402-11. doi: 10.1002/jbmr.2173.
- Ferrari, S., E. M. Lewiecki, P. W. Butler, D. L. Kendler, N. Napoli, S. Huang, D. B. Crittenden, N. Pannacciulli, E. Siris, and N. Binkley. 2020. "Favorable skeletal benefit/risk of long-term denosumab therapy: A virtual-twin analysis of fractures prevented relative to skeletal safety events observed." *Bone* 134:115287. doi: 10.1016/j.bone.2020.115287.
- Fiscaletti, M., A. Biggin, B. Bennetts, K. Wong, J. Briody, V. Pacey, C. Birman, and C. F. Munns. 2018. "Novel variant in *Sp7/Osx* associated with recessive osteogenesis imperfecta with bone fragility and hearing impairment." *Bone* 110:66-75. doi: 10.1016/j.bone.2018.01.031.
- Fisher, S., P. Jagadeeswaran, and M. E. Halpern. 2003. "Radiographic analysis of zebrafish skeletal defects." *Dev Biol* 264 (1):64-76. doi: 10.1016/s0012-1606(03)00399-3.
- Fitzgerald, J., S. R. Lamandé, and J. F. Bateman. 1999. "Proteasomal degradation of unassembled mutant type I collagen pro- α 1(I) chains." *J Biol Chem* 274 (39):27392-8. doi: 10.1074/jbc.274.39.27392.
- Fontani, F., G. Marcucci, T. Iantomasi, M. L. Brandi, and M. T. Vincenzini. 2015. "Glutathione, N-acetylcysteine and lipoic acid down-regulate starvation-induced apoptosis, RANKL/OPG ratio and sclerostin in osteocytes: involvement of JNK and ERK1/2 signalling." *Calcif Tissue Int* 96 (4):335-46. doi: 10.1007/s00223-015-9961-0.
- Forlino, A., W. A. Cabral, A. M. Barnes, and J. C. Marini. 2011. "New perspectives on osteogenesis imperfecta." *Nat Rev Endocrinol* 7 (9):540-57. doi: 10.1038/nrendo.2011.81.
- Forlino, A., N. V. Kuznetsova, J. C. Marini, and S. Leikin. 2007. "Selective retention and degradation of molecules with a single mutant α 1(I) chain in the *Brtl* IV mouse model of OI." *Matrix Biol* 26 (8):604-14. doi: 10.1016/j.matbio.2007.06.005.
- Forlino, A., and J. C. Marini. 2016. "Osteogenesis imperfecta." *Lancet* 387 (10028):1657-71. doi: 10.1016/S0140-6736(15)00728-X.
- Fratzl-Zelman, N., I. Schmidt, P. Roschger, A. Roschger, F. H. Glorieux, K. Klaushofer, W. Wagermaier, F. Rauch, and P. Fratzl. 2015. "Unique micro- and nano-scale mineralization pattern of human osteogenesis imperfecta type VI bone." *Bone* 73:233-41. doi: 10.1016/j.bone.2014.12.023.
- Fujisawa, R., and M. Tamura. 2012. "Acidic bone matrix proteins and their roles in calcification." *Front Biosci (Landmark Ed)* 17:1891-903. doi: 10.2741/4026.
- Fukao, Y. 2015. "Discordance between protein and transcript levels detected by selected reaction monitoring." *Plant Signal Behav* 10 (5):e1017697. doi: 10.1080/15592324.2015.1017697.
- Gagnon, J. A., E. Valen, S. B. Thyme, P. Huang, L. Akhmetova, L. Akhmetova, A. Pauli, T. G. Montague, S. Zimmerman, C. Richter, and A. F. Schier. 2014. "Efficient mutagenesis by Cas9 protein-mediated oligonucleotide insertion and large-scale assessment of single-guide RNAs." *PLoS One* 9 (5):e98186. doi: 10.1371/journal.pone.0098186.
- Garneau, J. E., M. Dupuis, M. Villion, D. A. Romero, R. Barrangou, P. Boyaval, C. Fremaux, P. Horvath, A. H. Magadán, and S. Moineau. 2010. "The CRISPR/Cas bacterial immune system cleaves bacteriophage and plasmid DNA." *Nature* 468 (7320):67-71. doi: 10.1038/nature09523.

- Gatti, D., M. Rossini, O. Viapiana, M. R. Povino, S. Liuzza, E. Fracassi, L. Idolazzi, and S. Adami. 2013. "Teriparatide treatment in adult patients with osteogenesis imperfecta type I." *Calcif Tissue Int* 93 (5):448-52. doi: 10.1007/s00223-013-9770-2.
- Gawron, K. 2016. "Endoplasmic reticulum stress in chondrodysplasias caused by mutations in collagen types II and X." *Cell Stress Chaperones* 21 (6):943-958. doi: 10.1007/s12192-016-0719-z.
- Gelse, K., E. Poschl, and T. Aigner. 2003. "Collagens--structure, function, and biosynthesis." *Advanced Drug Delivery Reviews* 55 (12):1531-46.
- Gioia, R., C. Panaroni, R. Besio, G. Palladini, G. Merlini, V. Giansanti, I. A. Scovassi, S. Villani, I. Villa, A. Villa, P. Vezzoni, R. Tenni, A. Rossi, J. C. Marini, and A. Forlino. 2012. "Impaired osteoblastogenesis in a murine model of dominant osteogenesis imperfecta: a new target for osteogenesis imperfecta pharmacological therapy." *Stem Cells* 30 (7):1465-76. doi: 10.1002/stem.1107.
- Gioia, R., F. Tonelli, I. Ceppi, M. Biggiogera, S. Leikin, S. Fisher, E. Tenedini, T. A. Yorgan, T. Schinke, K. Tian, J. M. Schwartz, F. Forte, R. Wagener, S. Villani, A. Rossi, and A. Forlino. 2017. "The chaperone activity of 4PBA ameliorates the skeletal phenotype of Chihuahua, a zebrafish model for dominant osteogenesis imperfecta." *Hum Mol Genet* 26 (15):2897-2911. doi: 10.1093/hmg/ddx171.
- Gistelincq, C., R. Gioia, A. Gagliardi, F. Tonelli, L. Marchese, L. Bianchi, C. Landi, L. Bini, A. Huisseune, P. E. Witten, A. Staes, K. Gevaert, N. De Rocker, B. Menten, F. Malfait, S. Leikin, S. Carra, R. Tenni, A. Rossi, A. De Paepe, P. Coucke, A. Willaert, and A. Forlino. 2016. "Zebrafish Collagen Type I: Molecular and Biochemical Characterization of the Major Structural Protein in Bone and Skin." *Sci Rep* 6:21540. doi: 10.1038/srep21540.
- Gistelincq, C., R. Y. Kwon, F. Malfait, S. Symoens, M. P. Harris, K. Henke, M. B. Hawkins, S. Fisher, P. Sips, B. Guillemy, J. W. Bek, P. Vermassen, H. De Saffel, P. E. Witten, M. Weis, A. De Paepe, D. R. Eyre, A. Willaert, and P. J. Coucke. 2018. "Zebrafish type I collagen mutants faithfully recapitulate human type I collagenopathies." *Proc Natl Acad Sci U S A* 115 (34):E8037-E8046. doi: 10.1073/pnas.1722200115.
- Gistelincq, C., P. E. Witten, A. Huisseune, S. Symoens, F. Malfait, D. Larionova, P. Simoens, M. Dierick, L. Van Hoorebeke, A. De Paepe, R. Y. Kwon, M. Weis, D. R. Eyre, A. Willaert, and P. J. Coucke. 2016. "Loss of Type I Collagen Telopeptide Lysyl Hydroxylation Causes Musculoskeletal Abnormalities in a Zebrafish Model of Bruck Syndrome." *J Bone Miner Res* 31 (11):1930-1942. doi: 10.1002/jbmr.2977.
- Gjaltema, R. A., and R. A. Bank. 2017. "Molecular insights into prolyl and lysyl hydroxylation of fibrillar collagens in health and disease." *Crit Rev Biochem Mol Biol* 52 (1):74-95. doi: 10.1080/10409238.2016.1269716.
- Glorieux, F. H., J. P. Devogelaer, M. Durigova, S. Goemaere, S. Hemsley, F. Jakob, U. Junker, J. Ruckle, L. Seefried, and P. J. Winkle. 2017. "BPS804 Anti-Sclerostin Antibody in Adults With Moderate Osteogenesis Imperfecta: Results of a Randomized Phase 2a Trial." *J Bone Miner Res* 32 (7):1496-1504. doi: 10.1002/jbmr.3143.
- Godde, J. S., and A. Bickerton. 2006. "The repetitive DNA elements called CRISPRs and their associated genes: evidence of horizontal transfer among prokaryotes." *J Mol Evol* 62 (6):718-29. doi: 10.1007/s00239-005-0223-z.
- Gong, Y., R. B. Slee, N. Fukai, G. Rawadi, S. Roman-Roman, A. M. Reginato, H. Wang, T. Cundy, F. H. Glorieux, D. Lev, M. Zacharin, K. Oexle, J. Marcelino, W. Suwairi, S. Heeger, G. Sabatakos, S. Apte, W. N. Adkins, J. Allgrove, M. Arslan-Kirchner, J. A. Batch, P. Beighton, G. C. Black, R. G. Boles, L. M. Boon, C. Borrone, H. G. Brunner, G. F. Carle, B. Dallapiccola, A. De Paepe, B. Floege, M. L. Halfhide, B. Hall, R. C. Hennekam, T. Hirose, A. Jans, H. Jüppner, C. A. Kim, K. Kepler-Noreuil, A. Kohlschuetter, D. LaCombe, M. Lambert, E. Lemyre, T. Letteboer, L. Peltonen, R. S. Ramesar, M. Romanengo, H. Somer, E. Steichen-Gersdorf, B. Steinmann, B. Sullivan, A. Superti-Furga, W. Swoboda, M. J. van

- den Boogaard, W. Van Hul, M. Vikkula, M. Votruba, B. Zabel, T. Garcia, R. Baron, B. R. Olsen, M. L. Warman, and Osteoporosis-Pseudoglioma Syndrome Collaborative Group. 2001. "LDL receptor-related protein 5 (LRP5) affects bone accrual and eye development." *Cell* 107 (4):513-23. doi: 10.1016/s0092-8674(01)00571-2.
- Grafe, I., S. Alexander, T. Yang, C. Lietman, E. P. Homan, E. Munivez, Y. Chen, M. M. Jiang, T. Bertin, B. Dawson, F. Asuncion, H. Z. Ke, M. S. Ominsky, and B. Lee. 2016. "Sclerostin Antibody Treatment Improves the Bone Phenotype of Crtap(-/-) Mice, a Model of Recessive Osteogenesis Imperfecta." *J Bone Miner Res* 31 (5):1030-40. doi: 10.1002/jbmr.2776.
- Grafe, I., T. Yang, S. Alexander, E. P. Homan, C. Lietman, M. M. Jiang, T. Bertin, E. Munivez, Y. Chen, B. Dawson, Y. Ishikawa, M. A. Weis, T. K. Sampath, C. Ambrose, D. Eyre, H. P. Bächinger, and B. Lee. 2014. "Excessive transforming growth factor- β signaling is a common mechanism in osteogenesis imperfecta." *Nat Med* 20 (6):670-5. doi: 10.1038/nm.3544.
- Graham, Jeffrey B. 1997b. *Air-breathing fishes: evolution, diversity, and adaptation*: Elsevier.
- Gresch, O., and L. Altrogge. 2012. "Transfection of difficult-to-transfect primary mammalian cells." *Methods Mol Biol* 801:65-74. doi: 10.1007/978-1-61779-352-3_5.
- Grigoriadis, A. E., P. M. Petkovich, R. Ber, J. E. Aubin, and J. N. Heersche. 1985. "Subclone heterogeneity in a clonally-derived osteoblast-like cell line." *Bone* 6 (4):249-56. doi:10.1016/8756-3282(85)90008-0.
- Grynkiewicz, G., M. Poenie, and R. Y. Tsien. 1985. "A new generation of Ca²⁺ indicators with greatly improved fluorescence properties." *J Biol Chem* 260 (6):3440-50.
- Guillemyn, B., H. Kayserili, L. Demuynck, P. Sips, A. De Paepe, D. Syx, P. J. Coucke, F. Malfait, and S. Symoens. 2019. "A homozygous pathogenic missense variant broadens the phenotypic and mutational spectrum of CREB3L1-related osteogenesis imperfecta." *Hum Mol Genet* 28 (11):1801-1809. doi: 10.1093/hmg/ddz017.
- Gupta, S. K., and P. Shukla. 2017. "Gene editing for cell engineering: trends and applications." *Crit Rev Biotechnol* 37 (5):672-684. doi: 10.1080/07388551.2016.1214557.
- Hall, B.K. 2015. *Bones & Cartilage: Developmental and Evolutionary Skeletal Biology*. 2nd ed. London: Elsevier/Academic Press .
- Halling Linder, C., B. Ek-Rylander, M. Krumpel, M. Norgård, S. Narisawa, J. L. Millán, G. Andersson, and P. Magnusson. 2017. "Bone Alkaline Phosphatase and Tartrate-Resistant Acid Phosphatase: Potential Co-regulators of Bone Mineralization." *Calcif Tissue Int* 101 (1):92-101. doi: 10.1007/s00223-017-0259-2.
- Hanagata, N., X. Li, H. Morita, T. Takemura, J. Li, and T. Minowa. 2011. "Characterization of the osteoblast-specific transmembrane protein IFITM5 and analysis of IFITM5-deficient mice." *J Bone Miner Metab* 29 (3):279-90. doi: 10.1007/s00774-010-0221-0.
- Harris, S. A., R. J. Enger, B. L. Riggs, and T. C. Spelsberg. 1995. "Development and characterization of a conditionally immortalized human fetal osteoblastic cell line." *J Bone Miner Res* 10 (2):178-86. doi: 10.1002/jbmr.5650100203.
- Henke, K., J. M. Daane, M. B. Hawkins, C. M. Dooley, E. M. Busch-Nentwich, D. L. Stemple, and M. P. Harris. 2017. "Genetic Screen for Postembryonic Development in the Zebrafish (" *Genetics* 207 (2):609-623. doi: 10.1534/genetics.117.300187.
- Hennet, T. 2019. "Collagen glycosylation." *Curr Opin Struct Biol* 56:131-138. doi: 10.1016/j.sbi.2019.01.015.
- Hicok, K. C., T. Thomas, F. Gori, D. J. Rickard, T. C. Spelsberg, and B. L. Riggs. 1998. "Development and characterization of conditionally immortalized osteoblast precursor cell lines from human bone marrow stroma." *J Bone Miner Res* 13 (2):205-17. doi: 10.1359/jbmr.1998.13.2.205.
- Hill, T. P., D. Später, M. M. Taketo, W. Birchmeier, and C. Hartmann. 2005. "Canonical Wnt/beta-catenin signaling prevents osteoblasts from differentiating into chondrocytes." *Dev Cell* 8 (5):727-38. doi: 10.1016/j.devcel.2005.02.013.

- Hirasawa, T., and S. Kuratani. 2015. "Evolution of the vertebrate skeleton: morphology, embryology, and development." *Zoological Lett* 1:2. doi: 10.1186/s40851-014-0007-7.
- Howe, K., M. D. Clark, C. F. Torroja, J. Torrance, C. Berthelot, M. Muffato, J. E. Collins, S. Humphray, K. McLaren, L. Matthews, S. McLaren, I. Sealy, M. Caccamo, C. Churcher, C. Scott, J. C. Barrett, R. Koch, G. J. Rauch, S. White, W. Chow, B. Kilian, L. T. Quintais, J. A. Guerra-Assunção, Y. Zhou, Y. Gu, J. Yen, J. H. Vogel, T. Eyre, S. Redmond, R. Banerjee, J. Chi, B. Fu, E. Langley, S. F. Maguire, G. K. Laird, D. Lloyd, E. Kenyon, S. Donaldson, H. Sehra, J. Almeida-King, J. Loveland, S. Trevanion, M. Jones, M. Quail, D. Willey, A. Hunt, J. Burton, S. Sims, K. McLay, B. Plumb, J. Davis, C. Clee, K. Oliver, R. Clark, C. Riddle, D. Elliot, D. Elliott, G. Threadgold, G. Harden, D. Ware, S. Begum, B. Mortimore, B. Mortimer, G. Kerry, P. Heath, B. Phillimore, A. Tracey, N. Corby, M. Dunn, C. Johnson, J. Wood, S. Clark, S. Pelan, G. Griffiths, M. Smith, R. Glithero, P. Howden, N. Barker, C. Lloyd, C. Stevens, J. Harley, K. Holt, G. Panagiotidis, J. Lovell, H. Beasley, C. Henderson, D. Gordon, K. Auger, D. Wright, J. Collins, C. Raisen, L. Dyer, K. Leung, L. Robertson, K. Ambridge, D. Leongamornlert, S. McGuire, R. Gilderthorp, C. Griffiths, D. Manthravadi, S. Nichol, G. Barker, S. Whitehead, M. Kay, J. Brown, C. Murnane, E. Gray, M. Humphries, N. Sycamore, D. Barker, D. Saunders, J. Wallis, A. Babbage, S. Hammond, M. Mashreghi-Mohammadi, L. Barr, S. Martin, P. Wray, A. Ellington, N. Matthews, M. Ellwood, R. Woodmansey, G. Clark, J. Cooper, A. Tromans, D. Grafham, C. Skuce, R. Pandian, R. Andrews, E. Harrison, A. Kimberley, J. Garnett, N. Fosker, R. Hall, P. Garner, D. Kelly, C. Bird, S. Palmer, I. Gehring, A. Berger, C. M. Dooley, Z. Ersan-Ürün, C. Eser, H. Geiger, M. Geisler, L. Karotki, A. Kirn, J. Konantz, M. Konantz, M. Oberländer, S. Rudolph-Geiger, M. Teucke, C. Lanz, G. Raddatz, K. Osoegawa, B. Zhu, A. Rapp, S. Widaa, C. Langford, F. Yang, S. C. Schuster, N. P. Carter, J. Harrow, Z. Ning, J. Herrero, S. M. Searle, A. Enright, R. Geisler, R. H. Plasterk, C. Lee, M. Westerfield, P. J. de Jong, L. I. Zon, J. H. Postlethwait, C. Nüsslein-Volhard, T. J. Hubbard, H. Roest Crolius, J. Rogers, and D. L. Stemple. 2013. "The zebrafish reference genome sequence and its relationship to the human genome." *Nature* 496 (7446):498-503. doi: 10.1038/nature12111.
- Hoyer-Kuhn, H., J. Franklin, G. Allo, M. Kron, C. Netzer, P. Eysel, B. Hero, E. Schoenau, and O. Semler. 2016. "Safety and efficacy of denosumab in children with osteogenesis imperfecta—a first prospective trial." *J Musculoskelet Neuronal Interact* 16 (1):24-32.
- Hsieh, J. C., L. Lee, L. Zhang, S. Wefer, K. Brown, C. DeRossi, M. E. Wines, T. Rosenquist, and B. C. Holdener. 2003. "Mesd encodes an LRP5/6 chaperone essential for specification of mouse embryonic polarity." *Cell* 112 (3):355-67. doi: 10.1016/s0092-8674(03)00045-x.
- Hsu, P. D., E. S. Lander, and F. Zhang. 2014. "Development and applications of CRISPR-Cas9 for genome engineering." *Cell* 157 (6):1262-78. doi: 10.1016/j.cell.2014.05.010.
- Huang, J., T. Shi, T. Ma, Y. Zhang, X. Ma, Y. Lu, Q. Song, W. Liu, D. Ma, and X. Qiu. 2008. "CCDC134, a novel secretory protein, inhibits activation of ERK and JNK, but not p38 MAPK." *Cell Mol Life Sci* 65 (2):338-49. doi: 10.1007/s00018-007-7448-5.
- Hudson, D. M., R. Werther, M. Weis, J. J. Wu, and D. R. Eyre. 2014. "Evolutionary origins of C-terminal (GPP)n 3-hydroxyproline formation in vertebrate tendon collagen." *PLoS One* 9 (4):e93467. doi: 10.1371/journal.pone.0093467.
- Iannitti, T., and B. Palmieri. 2011. "Clinical and experimental applications of sodium phenylbutyrate." *Drugs R D* 11 (3):227-49. doi: 10.2165/11591280-000000000-00000.
- Inohaya, K., Y. Takano, and A. Kudo. 2007. "The teleost intervertebral region acts as a growth center of the centrum: in vivo visualization of osteoblasts and their progenitors in transgenic fish." *Dev Dyn* 236 (11):3031-46. doi: 10.1002/dvdy.21329.
- Ishida, Y., and K. Nagata. 2011. "Hsp47 as a collagen-specific molecular chaperone." *Methods Enzymol* 499:167-82. doi: 10.1016/B978-0-12-386471-0.00009-2.

- Ishikawa, Y., S. Ito, K. Nagata, L. Y. Sakai, and H. P. Bächinger. 2016. "Intracellular mechanisms of molecular recognition and sorting for transport of large extracellular matrix molecules." *Proc Natl Acad Sci U S A* 113 (41):E6036-E6044. doi: 10.1073/pnas.1609571113.
- Ishikawa, Y., J. A. Vranka, S. P. Boudko, E. Pokidysheva, K. Mizuno, K. Zientek, D. R. Keene, A. M. Rashmir-Raven, K. Nagata, N. J. Winand, and H. P. Bächinger. 2012. "Mutation in cyclophilin B that causes hyperelastosis cutis in American Quarter Horse does not affect peptidylprolyl cis-trans isomerase activity but shows altered cyclophilin B-protein interactions and affects collagen folding." *J Biol Chem* 287 (26):22253-65. doi: 10.1074/jbc.M111.333336.
- Ishikawa, Y., J. Vranka, J. Wirz, K. Nagata, and H. P. Bächinger. 2008. "The rough endoplasmic reticulum-resident FK506-binding protein FKBP65 is a molecular chaperone that interacts with collagens." *J Biol Chem* 283 (46):31584-90. doi: 10.1074/jbc.M802535200.
- Ishikawa, Y., J. Wirz, J. A. Vranka, K. Nagata, and H. P. Bächinger. 2009. "Biochemical characterization of the prolyl 3-hydroxylase 1.cartilage-associated protein.cyclophilin B complex." *J Biol Chem* 284 (26):17641-7. doi: 10.1074/jbc.M109.007070.
- Jao, L. E., S. R. Wentz, and W. Chen. 2013. "Efficient multiplex biallelic zebrafish genome editing using a CRISPR nuclease system." *Proc Natl Acad Sci U S A* 110 (34):13904-9. doi: 10.1073/pnas.1308335110.
- Jenkins, C. L., L. E. Bretscher, I. A. Guzei, and R. T. Raines. 2003. "Effect of 3-hydroxyproline residues on collagen stability." *J Am Chem Soc* 125 (21):6422-7. doi: 10.1021/ja034015j.
- Jilka, R. L., C. A. O'Brien, A. A. Ali, P. K. Roberson, R. S. Weinstein, and S. C. Manolagas. 2009. "Intermittent PTH stimulates periosteal bone formation by actions on post-mitotic preosteoblasts." *Bone* 44 (2):275-86. doi: 10.1016/j.bone.2008.10.037.
- Jilka, R. L., R. S. Weinstein, T. Bellido, P. Roberson, A. M. Parfitt, and S. C. Manolagas. 1999. "Increased bone formation by prevention of osteoblast apoptosis with parathyroid hormone." *J Clin Invest* 104 (4):439-46. doi: 10.1172/JCI6610.
- Jinek, M., K. Chylinski, I. Fonfara, M. Hauer, J. A. Doudna, and E. Charpentier. 2012. "A programmable dual-RNA-guided DNA endonuclease in adaptive bacterial immunity." *Science* 337 (6096):816-21. doi: 10.1126/science.1225829.
- Kague, E., P. Roy, G. Asselin, G. Hu, J. Simonet, A. Stanley, C. Albertson, and S. Fisher. 2016. "Osterix/Sp7 limits cranial bone initiation sites and is required for formation of sutures." *Dev Biol* 413 (2):160-72. doi: 10.1016/j.ydbio.2016.03.011.
- Kang, H., A. C. S. Aryal, and J. C. Marini. 2017. "Osteogenesis imperfecta: new genes reveal novel mechanisms in bone dysplasia." *Transl Res* 181:27-48. doi: 10.1016/j.trsl.2016.11.005.
- Kartsogiannis, V., and K. W. Ng. 2004. "Cell lines and primary cell cultures in the study of bone cell biology." *Mol Cell Endocrinol* 228 (1-2):79-102. doi: 10.1016/j.mce.2003.06.002.
- Kasperk, C., J. Wergedal, D. Strong, J. Farley, K. Wangerin, H. Gropp, R. Ziegler, and D. J. Baylink. 1995. "Human bone cell phenotypes differ depending on their skeletal site of origin." *J Clin Endocrinol Metab* 80 (8):2511-7. doi: 10.1210/jcem.80.8.7629252.
- Katz, S., R. Boland, and G. Santillán. 2006. "Modulation of ERK 1/2 and p38 MAPK signaling pathways by ATP in osteoblasts: involvement of mechanical stress-activated calcium influx, PKC and Src activation." *Int J Biochem Cell Biol* 38 (12):2082-91. doi: 10.1016/j.biocel.2006.05.018.
- Keupp, K., F. Beleggia, H. Kayserili, A. M. Barnes, M. Steiner, O. Semler, B. Fischer, G. Yigit, C. Y. Janda, J. Becker, S. Breer, U. Altunoglu, J. Grünhagen, P. Krawitz, J. Hecht, T. Schinke, E. Makareeva, E. Lausch, T. Cankaya, J. A. Caparrós-Martín, P. Lapunzina, S. Temtamy, M. Aglan, B. Zabel, P. Eysel, F. Koerber, S. Leikin, K. C. Garcia, C. Netzer, E. Schönau, V. L. Ruiz-Perez, S. Mundlos, M. Amling, U. Kornak, J. Marini, and B. Wollnik. 2013. "Mutations in WNT1 cause different forms of bone fragility." *Am J Hum Genet* 92 (4):565-74. doi: 10.1016/j.ajhg.2013.02.010.

- Khadempar, S., S. Familghadakchi, R. A. Motlagh, N. Farahani, M. Dashtiahangar, H. Rezaei, and S. M. Gheibi Hayat. 2019. "CRISPR-Cas9 in genome editing: Its function and medical applications." *J Cell Physiol* 234 (5):5751-5761. doi: 10.1002/jcp.27476.
- Khan, F. R., and S. S. Alhewairini. 2018. "Zebrafish (*Danio rerio*) as a Model Organism." *Chapter in Current Trends in Cancer Management*.
- Kleinstiver, B. P., M. S. Prew, S. Q. Tsai, V. V. Topkar, N. T. Nguyen, Z. Zheng, A. P. Gonzales, Z. Li, R. T. Peterson, J. R. Yeh, M. J. Aryee, and J. K. Joung. 2015. "Engineered CRISPR-Cas9 nucleases with altered PAM specificities." *Nature* 523 (7561):481-5. doi: 10.1038/nature14592.
- Koivu, J. 1987. "Identification of disulfide bonds in carboxy-terminal propeptides of human type I procollagen." *FEBS Lett* 212 (2):229-32. doi: 10.1016/0014-5793(87)81350-9.
- Komori, T. 2010. "Regulation of bone development and extracellular matrix protein genes by RUNX2." *Cell Tissue Res* 339 (1):189-95. doi: 10.1007/s00441-009-0832-8.
- Kostenuik, P. J., H. Q. Nguyen, J. McCabe, K. S. Warmington, C. Kurahara, N. Sun, C. Chen, L. Li, R. C. Cattley, G. Van, S. Scully, R. Elliott, M. Grisanti, S. Morony, H. L. Tan, F. Asuncion, X. Li, M. S. Ominsky, M. Stolina, D. Dwyer, W. C. Dougall, N. Hawkins, W. J. Boyle, W. S. Simonet, and J. K. Sullivan. 2009. "Denosumab, a fully human monoclonal antibody to RANKL, inhibits bone resorption and increases BMD in knock-in mice that express chimeric (murine/human) RANKL." *J Bone Miner Res* 24 (2):182-95. doi: 10.1359/jbmr.081112.
- Kozloff, K. M., A. Carden, C. Bergwitz, A. Forlino, T. E. Uveges, M. D. Morris, J. C. Marini, and S. A. Goldstein. 2004. "Brittle IV mouse model for osteogenesis imperfecta IV demonstrates postpubertal adaptations to improve whole bone strength." *J Bone Miner Res* 19 (4):614-22. doi: 10.1359/JBMR.040111.
- Kuchta, K., A. Muszewska, L. Knizewski, K. Steczkiewicz, L. S. Wyrwicz, K. Pawlowski, L. Rychlewski, and K. Ginalski. 2016. "FAM46 proteins are novel eukaryotic non-canonical poly(A) polymerases." *Nucleic Acids Res* 44 (8):3534-48. doi: 10.1093/nar/gkw222.
- Kulmala, K. A., R. K. Korhonen, P. Julkunen, J. S. Jurvelin, T. M. Quinn, H. Kröger, and J. Töyräs. 2010. "Diffusion coefficients of articular cartilage for different CT and MRI contrast agents." *Med Eng Phys* 32 (8):878-82. doi: 10.1016/j.medengphy.2010.06.002.
- Lagali, P. S., L. E. Kakuk, I. B. Griesinger, P. W. Wong, and R. Ayyagari. 2002. "Identification and characterization of C6orf37, a novel candidate human retinal disease gene on chromosome 6q14." *Biochem Biophys Res Commun* 293 (1):356-65. doi: 10.1016/S0006-291X(02)00228-0.
- Laine, C. M., K. S. Joeng, P. M. Campeau, R. Kiviranta, K. Tarkkonen, M. Grover, J. T. Lu, M. Pekkinen, M. Wessman, T. J. Heino, V. Nieminen-Pihala, M. Aronen, T. Laine, H. Kröger, W. G. Cole, A. E. Lehesjoki, L. Nevarez, D. Krakow, C. J. Curry, D. H. Cohn, R. A. Gibbs, B. H. Lee, and O. Mäkitie. 2013. "WNT1 mutations in early-onset osteoporosis and osteogenesis imperfecta." *N Engl J Med* 368 (19):1809-16. doi: 10.1056/NEJMoa1215458.
- Laize, V., P. J. Gavaia, and M.L. Cancela. 2014. "Fish: a suitable system to model human bone disorders and discover drugs with osteogenic or osteotoxic activities." *Drug Discovery Today: Disease Models*.
- Lapunzina, P., M. Aglan, S. Temtamy, J. A. Caparrós-Martín, M. Valencia, R. Letón, V. Martínez-Glez, R. Elhossini, K. Amr, N. Vilaboa, and V. L. Ruiz-Perez. 2010. "Identification of a frameshift mutation in Osterix in a patient with recessive osteogenesis imperfecta." *Am J Hum Genet* 87 (1):110-4. doi: 10.1016/j.ajhg.2010.05.016.
- Lawson, N. D., and S. A. Wolfe. 2011. "Forward and reverse genetic approaches for the analysis of vertebrate development in the zebrafish." *Dev Cell* 21 (1):48-64. doi: 10.1016/j.devcel.2011.06.007.
- Lees, J. F., M. Tasab, and N. J. Bulleid. 1997. "Identification of the molecular recognition sequence which determines the type-specific assembly of procollagen." *The EMBO Journal* 16 (5):908-16. doi: 10.1093/emboj/16.5.908.

- Leis, H. J., W. Hulla, R. Gruber, E. Huber, D. Zach, H. Gleispach, and W. Windischhofer. 1997. "Phenotypic heterogeneity of osteoblast-like MC3T3-E1 cells: changes of bradykinin-induced prostaglandin E2 production during osteoblast maturation." *J Bone Miner Res* 12 (4):541-51. doi: 10.1359/jbmr.1997.12.4.541.
- Levin, L. S., C. F. Salinas, and R. J. Jorgenson. 1978. "Classification of osteogenesis imperfecta by dental characteristics." *Lancet* 1 (8059):332-3. doi: 10.1016/s0140-6736(78)90108-3.
- Lewiecki, E. M. 2014. "Role of sclerostin in bone and cartilage and its potential as a therapeutic target in bone diseases." *Ther Adv Musculoskelet Dis* 6 (2):48-57. doi: 10.1177/1759720X13510479.
- Lewiecki, E. M. 2018. "New and emerging concepts in the use of denosumab for the treatment of osteoporosis." *Ther Adv Musculoskelet Dis* 10 (11):209-223. doi: 10.1177/1759720X18805759.
- Li, H., X. Jiang, J. Delaney, T. Franceschetti, I. Bilic-Curcic, J. Kalinovsky, J. A. Lorenzo, D. Grcevic, D. W. Rowe, and I. Kalajzic. 2010. "Immature osteoblast lineage cells increase osteoclastogenesis in osteogenesis imperfecta murine." *Am J Pathol* 176 (5):2405-13. doi: 10.2353/ajpath.2010.090704.
- Li, N., K. Felber, P. Elks, P. Croucher, and H. H. Roehl. 2009. "Tracking gene expression during zebrafish osteoblast differentiation." *Dev Dyn* 238 (2):459-66. doi: 10.1002/dvdy.21838.
- Li, X., Y. Zhang, H. Kang, W. Liu, P. Liu, J. Zhang, S. E. Harris, and D. Wu. 2005. "Sclerostin binds to LRP5/6 and antagonizes canonical Wnt signaling." *J Biol Chem* 280 (20):19883-7. doi: 10.1074/jbc.M413274200.
- Liang, S. H., W. Zhang, B. C. McGrath, P. Zhang, and D. R. Cavener. 2006. "PERK (eIF2alpha kinase) is required to activate the stress-activated MAPKs and induce the expression of immediate-early genes upon disruption of ER calcium homeostasis." *Biochem J* 393 (Pt 1):201-9. doi: 10.1042/BJ20050374.
- Lindert, U., W. A. Cabral, S. Ausavarat, S. Tongkobpetch, K. Ludin, A. M. Barnes, P. Yeetong, M. Weis, B. Krabichler, C. Srichomthong, E. N. Makareeva, A. R. Janecke, S. Leikin, B. Röthlisberger, M. Rohrbach, I. Kennerknecht, D. R. Eyre, K. Suphapeetiporn, C. Giunta, J. C. Marini, and V. Shotelersuk. 2016. "MBTPS2 mutations cause defective regulated intramembrane proteolysis in X-linked osteogenesis imperfecta." *Nat Commun* 7:11920. doi: 10.1038/ncomms11920.
- Liu, M., Z. Feng, H. Ke, Y. Liu, T. Sun, J. Dai, W. Cui, and J. C. Pastor-Pareja. 2017. "Tango1 spatially organizes ER exit sites to control ER export." *The Journal of Cell Biology* 216 (4):1035-1049. doi: 10.1083/jcb.201611088.
- Lodola, F., U. Laforenza, F. Cattaneo, F. A. Ruffinatti, V. Poletto, M. Massa, R. Tancredi, E. Zuccolo, D. A. Khdar, A. Riccardi, M. Biggiogera, V. Rosti, G. Guerra, and F. Moccia. 2017. "VEGF-induced intracellular Ca." *Oncotarget* 8 (56):95223-95246. doi: 10.18632/oncotarget.20255.
- Ludlow, J. W., J. A. DeCaprio, C. M. Huang, W. H. Lee, E. Paucha, and D. M. Livingston. 1989. "SV40 Large T Antigen Binds Preferentially to an Underphosphorylated Member of the Retinoblastoma Susceptibility Gene Product Family." *Cell*. doi: 10.1016/0092-8674(89)90983-5.
- Lv, F., X. J. Xu, J. Y. Wang, Y. Liu, Asan, J. W. Wang, L. J. Song, Y. W. Song, Y. Jiang, O. Wang, W. B. Xia, X. P. Xing, and M. Li. 2016. "Two novel mutations in TMEM38B result in rare autosomal recessive osteogenesis imperfecta." *J Hum Genet* 61 (6):539-45. doi: 10.1038/jhg.2016.11.
- Makareeva, E., and S. Leikin. 2014. "Chapter 7 - Collagen Structure, Folding and Function." *Osteogenesis Imperfecta A Translational Approach to Brittle Bone Disease*.
- Makarova, K. S., D. H. Haft, R. Barrangou, S. J. Brouns, E. Charpentier, P. Horvath, S. Moineau, F. J. Mojica, Y. I. Wolf, A. F. Yakunin, J. van der Oost, and E. V. Koonin. 2011. "Evolution

- and classification of the CRISPR-Cas systems." *Nat Rev Microbiol* 9 (6):467-77. doi: 10.1038/nrmicro2577.
- Malhotra, V., and P. Erlmann. 2015. "The pathway of collagen secretion." *Annual Review of Cell and Developmental Biology* 31:109-24. doi: 10.1146/annurev-cellbio-100913-013002.
- Maqsood, M. I., M. M. Matin, A. R. Bahrami, and M. M. Ghasroldasht. 2013. "Immortality of cell lines: challenges and advantages of establishment." *Cell Biol Int* 37 (10):1038-45. doi: 10.1002/cbin.10137.
- Marini, J. C., W. A. Cabral, and A. M. Barnes. 2010. "Null mutations in *LEPRE1* and *CRTAP* cause severe recessive osteogenesis imperfecta." *Cell Tissue Res* 339 (1):59-70. doi: 10.1007/s00441-009-0872-0.
- Marini, J. C., W. A. Cabral, A. M. Barnes, and W. Chang. 2007. "Components of the collagen prolyl 3-hydroxylation complex are crucial for normal bone development." *Cell Cycle* 6 (14):1675-81. doi: 10.4161/cc.6.14.4474.
- Marini, J. C., A. Forlino, H. P. Bächinger, N. J. Bishop, P. H. Byers, A. Paepe, F. Fassier, N. Fratzl-Zelman, K. M. Kozloff, D. Krakow, K. Montpetit, and O. Semler. 2017. "Osteogenesis imperfecta." *Nat Rev Dis Primers* 3:17052. doi: 10.1038/nrdp.2017.52.
- Marini, J. C., A. Forlino, W. A. Cabral, A. M. Barnes, J. D. San Antonio, S. Milgrom, J. C. Hyland, J. Körkkö, D. J. Prockop, A. De Paepe, P. Coucke, S. Symoens, F. H. Glorieux, P. J. Roughley, A. M. Lund, K. Kuurila-Svahn, H. Hartikka, D. H. Cohn, D. Krakow, M. Mottes, U. Schwarze, D. Chen, K. Yang, C. Kuslich, J. Troendle, R. Dagleish, and P. H. Byers. 2007. "Consortium for osteogenesis imperfecta mutations in the helical domain of type I collagen: regions rich in lethal mutations align with collagen binding sites for integrins and proteoglycans." *Hum Mutat* 28 (3):209-21. doi: 10.1002/humu.20429.
- Marini, J., and S. M. Smith. 2015. *Osteogenesis Imperfecta*: Endotext.
- Martínez, M. E., M. T. del Campo, S. Medina, M. Sánchez, M. J. Sánchez-Cabezudo, P. Esbrit, P. Martínez, I. Moreno, A. Rodrigo, M. V. Garcés, and L. Munuera. 1999. "Influence of skeletal site of origin and donor age on osteoblastic cell growth and differentiation." *Calcif Tissue Int* 64 (4):280-6. doi: 10.1007/s002239900619.
- Martínez-Glez, V., M. Valencia, J. A. Caparrós-Martín, M. Aglan, S. Temtamy, J. Tenorio, V. Pulido, U. Lindert, M. Rohrbach, D. Eyre, C. Giunta, P. Lapunzina, and V. L. Ruiz-Perez. 2012. "Identification of a mutation causing deficient BMP1/mTLD proteolytic activity in autosomal recessive osteogenesis imperfecta." *Hum Mutat* 33 (2):343-50. doi: 10.1002/humu.21647.
- Masci, M., M. Wang, L. Imbert, A. M. Barnes, L. Spevak, L. Lukashova, Y. Huang, Y. Ma, J. C. Marini, C. M. Jacobsen, M. L. Warman, and A. L. Boskey. 2016. "Bone mineral properties in growing *Coll1a2(+)/G610C* mice, an animal model of osteogenesis imperfecta." *Bone* 87:120-9. doi: 10.1016/j.bone.2016.04.011.
- Matoori, S., and J. C. Leroux. 2015. "Recent advances in the treatment of hyperammonemia." *Adv Drug Deliv Rev* 90:55-68. doi: 10.1016/j.addr.2015.04.009.
- Mendoza-Londono, R., S. Fahiminiya, J. Majewski, M. Tétreault, J. Nadaf, P. Kannu, E. Sochett, A. Howard, J. Stimec, L. Dupuis, P. Roschger, K. Klaushofer, T. Palomo, J. Ouellet, H. Al-Jallad, J. S. Mort, P. Moffatt, S. Boudko, H. P. Bächinger, F. Rauch, and Care4Rare Canada Consortium. 2015. "Recessive osteogenesis imperfecta caused by missense mutations in SPARC." *Am J Hum Genet* 96 (6):979-85. doi: 10.1016/j.ajhg.2015.04.021.
- Meyer, A., and M. Schartl. 1999. "Gene and genome duplications in vertebrates: the one-to-four (-to-eight in fish) rule and the evolution of novel gene functions." *Curr Opin Cell Biol* 11 (6):699-704. doi: 10.1016/s0955-0674(99)00039-3.
- Michalak, M., J. Groenendyk, E. Szabo, L. I. Gold, and M. Opas. 2009. "Calreticulin, a multi-process calcium-buffering chaperone of the endoplasmic reticulum." *Biochem J* 417 (3):651-66. doi: 10.1042/BJ20081847.

- Mienaltowski, M. J., and D. E. Birk. 2014. "Structure, physiology, and biochemistry of collagens." *Advances in Experimental Medicine and Biology* 802:5-29. doi: 10.1007/978-94-007-7893-1_2.
- Moosa, S., G. L. Yamamoto, L. Garbes, K. Keupp, A. Beleza-Meireles, C. A. Moreno, E. R. Valadares, S. B. de Sousa, S. Maia, J. Saraiva, R. S. Honjo, C. A. Kim, H. Cabral de Menezes, E. Lausch, P. V. Lorini, A. Lamounier, T. C. B. Carniero, C. Giunta, M. Rohrbach, M. Janner, O. Semler, F. Beleggia, Y. Li, G. Yigit, N. Reintjes, J. Altmüller, P. Nürnberg, D. P. Cavalcanti, B. Zabel, M. L. Warman, D. R. Bertola, B. Wollnik, and C. Netzer. 2019. "Autosomal-Recessive Mutations in MESD Cause Osteogenesis Imperfecta." *Am J Hum Genet* 105 (4):836-843. doi: 10.1016/j.ajhg.2019.08.008.
- Morello, R., T. K. Bertin, Y. Chen, J. Hicks, L. Tonachini, M. Monticone, P. Castagnola, F. Rauch, F. H. Glorieux, J. Vranka, H. P. Bächinger, J. M. Pace, U. Schwarze, P. H. Byers, M. Weis, R. J. Fernandes, D. R. Eyre, Z. Yao, B. F. Boyce, and B. Lee. 2006. "CRTAP is required for prolyl 3- hydroxylation and mutations cause recessive osteogenesis imperfecta." *Cell* 127 (2):291-304. doi: 10.1016/j.cell.2006.08.039.
- Morello, R., L. Tonachini, M. Monticone, L. Viggiano, M. Rocchi, R. Cancedda, and P. Castagnola. 1999. "cDNA cloning, characterization and chromosome mapping of Crtap encoding the mouse cartilage associated protein." *Matrix Biol* 18 (3):319-24. doi: 10.1016/s0945-053x(99)00002-5.
- Morgan, E. F., A. De Giacomo, and L. C. Gerstenfeld. 2014. "Overview of skeletal repair (fracture healing and its assessment)." *Methods Mol Biol* 1130:13-31. doi: 10.1007/978-1-62703-989-5_2.
- Morvan-Dubois, G., D. Le Guellec, R. Garrone, L. Zylberberg, and L. Bonnaud. 2003. "Phylogenetic analysis of vertebrate fibrillar collagen locates the position of zebrafish alpha3(I) and suggests an evolutionary link between collagen alpha chains and hox clusters." *J Mol Evol* 57 (5):501-14. doi: 10.1007/s00239-003-2502-x.
- Murray, L. S., Y. Lu, A. Taggart, N. Van Regemorter, C. Vilain, M. Abramowicz, K. E. Kadler, and T. Van Aghtmael. 2014. "Chemical chaperone treatment reduces intracellular accumulation of mutant collagen IV and ameliorates the cellular phenotype of a COL4A2 mutation that causes haemorrhagic stroke." *Hum Mol Genet* 23 (2):283-92. doi: 10.1093/hmg/ddt418.
- Murtha, J. M., and E. T. Keller. 2003. "Characterization of the heat shock response in mature zebrafish (Danio rerio)." *Exp Gerontol* 38 (6):683-91. doi: 10.1016/s0531-5565(03)00067-6.
- Muto, A., M. Ohkura, T. Kotani, S. Higashijima, J. Nakai, and K. Kawakami. 2011. "Genetic visualization with an improved GCaMP calcium indicator reveals spatiotemporal activation of the spinal motor neurons in zebrafish." *Proc Natl Acad Sci U S A* 108 (13):5425-30. doi: 10.1073/pnas.1000887108.
- Nagata, K. 2003. "HSP47 as a collagen-specific molecular chaperone: function and expression in normal mouse development." *Semin Cell Dev Biol* 14 (5):275-82. doi: 10.1016/j.semcdb.2003.09.020.
- Nakai, A., M. Satoh, K. Hirayoshi, and K. Nagata. 1992. "Involvement of the stress protein HSP47 in procollagen processing in the endoplasmic reticulum." *J Cell Biol* 117 (4):903-14. doi: 10.1083/jcb.117.4.903.
- Neer, R. M., C. D. Arnaud, J. R. Zanchetta, R. Prince, G. A. Gaich, J. Y. Reginster, A. B. Hodsmann, E. F. Eriksen, S. Ish-Shalom, H. K. Genant, O. Wang, and B. H. Mitlak. 2001. "Effect of parathyroid hormone (1-34) on fractures and bone mineral density in postmenopausal women with osteoporosis." *N Engl J Med* 344 (19):1434-41. doi: 10.1056/NEJM200105103441904.
- Nelson, David L., Albert L. Lehninger, and Michael M. Cox. 2008. *Lehninger principles of biochemistry*: Macmillan.

- Nishimasu, H., F. A. Ran, P. D. Hsu, S. Konermann, S. I. Shehata, N. Dohmae, R. Ishitani, F. Zhang, and O. Nureki. 2014. "Crystal structure of Cas9 in complex with guide RNA and target DNA." *Cell* 156 (5):935-49. doi: 10.1016/j.cell.2014.02.001.
- Orwoll, E. S., J. Shapiro, S. Veith, Y. Wang, J. Lapidus, C. Vanek, J. L. Reeder, T. M. Keaveny, D. C. Lee, M. A. Mullins, S. C. Nagamani, and B. Lee. 2014. "Evaluation of teriparatide treatment in adults with osteogenesis imperfecta." *J Clin Invest* 124 (2):491-8. doi: 10.1172/JCI11101.
- Parichy, D. M., M. R. Elizondo, M. G. Mills, T. N. Gordon, and R. E. Engeszer. 2009. "Normal table of postembryonic zebrafish development: staging by externally visible anatomy of the living fish." *Dev Dyn* 238 (12):2975-3015. doi: 10.1002/dvdy.22113.
- Patoine, A., M. H. Gaumont, P. K. Jaiswal, F. Fassier, F. Rauch, and P. Moffatt. 2014. "Topological mapping of BRIL reveals a type II orientation and effects of osteogenesis imperfecta mutations on its cellular destination." *J Bone Miner Res* 29 (9):2004-16. doi: 10.1002/jbmr.2243.
- Piersma, B., and R. A. Bank. 2019. "Collagen cross-linking mediated by lysyl hydroxylase 2: an enzymatic battlefield to combat fibrosis." *Essays Biochem* 63 (3):377-387. doi: 10.1042/EBC20180051.
- Pitt, S. J., K. H. Park, M. Nishi, T. Urashima, S. Aoki, D. Yamazaki, J. Ma, H. Takeshima, and R. Sitsapesan. 2010. "Charade of the SR K⁺-channel: two ion-channels, TRIC-A and TRIC-B, masquerade as a single K⁺-channel." *Biophys J* 99 (2):417-26. doi: 10.1016/j.bpj.2010.04.051.
- Rauch, F., P. Moffatt, M. Cheung, P. Roughley, L. Lalic, A. M. Lund, N. Ramirez, S. Fahiminiya, J. Majewski, and F. H. Glorieux. 2013. "Osteogenesis imperfecta type V: marked phenotypic variability despite the presence of the IFITM5 c.-14C>T mutation in all patients." *J Med Genet* 50 (1):21-4. doi: 10.1136/jmedgenet-2012-101307.
- Rauch, F., R. Travers, A. M. Parfitt, and F. H. Glorieux. 2000. "Static and dynamic bone histomorphometry in children with osteogenesis imperfecta." *Bone* 26 (6):581-9. doi: 10.1016/s8756-3282(00)00269-6.
- Recker, R. R., C. T. Benson, T. Matsumoto, M. A. Bolognese, D. A. Robins, J. Alam, A. Y. Chiang, L. Hu, J. H. Krege, H. Sowa, B. H. Mitlak, and S. L. Myers. 2015. "A randomized, double-blind phase 2 clinical trial of bloszumab, a sclerostin antibody, in postmenopausal women with low bone mineral density." *J Bone Miner Res* 30 (2):216-24. doi: 10.1002/jbmr.2351.
- Ricard-Blum, S. 2011. "The collagen family." *Cold Spring Harb Perspect Biol* 3 (1):a004978. doi: 10.1101/cshperspect.a004978.
- Rob, Willemsen, van't Padje Sandra, Van Swieten John C., and Oostra Ben A. 2010. "Zebrafish (*Danio Rerio*) as a model organism for demetia." *Animal Models of Dementia*.
- Roschger, A., P. Roschger, P. Keplinger, K. Klaushofer, S. Abdullah, M. Kneissel, and F. Rauch. 2014. "Effect of sclerostin antibody treatment in a mouse model of severe osteogenesis imperfecta." *Bone* 66:182-8. doi: 10.1016/j.bone.2014.06.015.
- Rosset, Jerome, and Benoit de Crombrughe. 2002. "Type I collagen: structure, synthesis, and regulation." In *Principles of bone biology*, 189-XVIII. Elsevier.
- Rosset, E. M., and A. D. Bradshaw. 2016. "SPARC/osteonectin in mineralized tissue." *Matrix Biol* 52-54:78-87. doi: 10.1016/j.matbio.2016.02.001.
- Rubinato, E., A. Morgan, A. D'Eustacchio, V. Pecile, G. Gortani, P. Gasparini, and F. Faletta. 2014. "A novel deletion mutation involving TMEM38B in a patient with autosomal recessive osteogenesis imperfecta." *Gene* 545 (2):290-2. doi: 10.1016/j.gene.2014.05.028.
- Saeidnia, S., A. Manayi, and M. Abdollahi. 2015. "From in vitro Experiments to in vivo and Clinical Studies; Pros and Cons." *Curr Drug Discov Technol* 12 (4):218-24. doi: 10.2174/1570163813666160114093140.

- Saita, Y., M. Ishijima, and K. Kaneko. 2015. "Atypical femoral fractures and bisphosphonate use: current evidence and clinical implications." *Ther Adv Chronic Dis* 6 (4):185-93. doi: 10.1177/2040622315584114.
- Saito, K., M. Chen, F. Bard, S. Chen, H. Zhou, D. Woodley, R. Polischuk, R. Schekman, and V. Malhotra. 2009. "TANGO1 facilitates cargo loading at endoplasmic reticulum exit sites." *Cell* 136 (5):891-902. doi: 10.1016/j.cell.2008.12.025.
- Satoh, M., K. Hirayoshi, S. Yokota, N. Hosokawa, and K. Nagata. 1996. "Intracellular interaction of collagen-specific stress protein HSP47 with newly synthesized procollagen." *J Cell Biol* 133 (2):469-83. doi: 10.1083/jcb.133.2.469.
- Schneider, V. A., and M. Granato. 2007. "Genomic structure and embryonic expression of zebrafish lysyl hydroxylase 1 and lysyl hydroxylase 2." *Matrix Biol* 26 (1):12-9. doi: 10.1016/j.matbio.2006.09.007.
- Schwarze, U., T. Cundy, S. M. Pyott, H. E. Christiansen, M. R. Hegde, R. A. Bank, G. Pals, A. Ankala, K. Conneely, L. Seaver, S. M. Yandow, E. Raney, D. Babovic-Vuksanovic, J. Stoler, Z. Ben-Neriah, R. Segel, S. Lieberman, L. Siderius, A. Al-Aqeel, M. Hannibal, L. Hudgins, E. McPherson, M. Clemens, M. D. Sussman, R. D. Steiner, J. Mahan, R. Smith, K. Anyane-Yeboa, J. Wynn, K. Chong, T. Uster, S. Aftimos, V. R. Sutton, E. C. Davis, L. S. Kim, M. A. Weis, D. Eyre, and P. H. Byers. 2013. "Mutations in FKBP10, which result in Bruck syndrome and recessive forms of osteogenesis imperfecta, inhibit the hydroxylation of telopeptide lysines in bone collagen." *Hum Mol Genet* 22 (1):1-17. doi: 10.1093/hmg/dd371.
- Semler, O., L. Garbes, K. Keupp, D. Swan, K. Zimmermann, J. Becker, S. Iden, B. Wirth, P. Eysel, F. Koerber, E. Schoenau, S. K. Bohlander, B. Wollnik, and C. Netzer. 2012. "A mutation in the 5'-UTR of IFITM5 creates an in-frame start codon and causes autosomal-dominant osteogenesis imperfecta type V with hyperplastic callus." *Am J Hum Genet* 91 (2):349-57. doi: 10.1016/j.ajhg.2012.06.011.
- Shaheen, R., A. M. Alazami, M. J. Alshammari, E. Fageih, N. Alhashmi, N. Mousa, A. Alsinani, S. Ansari, F. Alzahrani, M. Al-Owain, Z. S. Alzayed, and F. S. Alkuraya. 2012. "Study of autosomal recessive osteogenesis imperfecta in Arabia reveals a novel locus defined by TMEM38B mutation." *J Med Genet* 49 (10):630-5. doi: 10.1136/jmedgenet-2012-101142.
- Shoulders, M. D., and R. T. Raines. 2009. "Collagen structure and stability." *Annual Review of Biochemistry* 78:929-58. doi: 10.1146/annurev.biochem.77.032207.120833.
- Sillence, D. O., D. L. Rimoin, and D. M. Danks. 1979. "Clinical variability in osteogenesis imperfecta-variable expressivity or genetic heterogeneity." *Birth Defects Orig Artic Ser* 15 (5B):113-29.
- Sillence, D. O., A. Senn, and D. M. Danks. 1979. "Genetic heterogeneity in osteogenesis imperfecta." *J Med Genet* 16 (2):101-16. doi: 10.1136/jmg.16.2.101.
- Sinder, B. P., J. D. Salemi, M. S. Ominsky, M. S. Caird, J. C. Marini, and K. M. Kozloff. 2015. "Rapidly growing Brl/+ mouse model of osteogenesis imperfecta improves bone mass and strength with sclerostin antibody treatment." *Bone* 71:115-23. doi: 10.1016/j.bone.2014.10.012.
- Sinder, B. P., L. E. White, J. D. Salemi, M. S. Ominsky, M. S. Caird, J. C. Marini, and K. M. Kozloff. 2014. "Adult Brl/+ mouse model of osteogenesis imperfecta demonstrates anabolic response to sclerostin antibody treatment with increased bone mass and strength." *Osteoporos Int* 25 (8):2097-107. doi: 10.1007/s00198-014-2737-y.
- Sinikumpu, J. J., M. Ojaniemi, P. Lehenkari, and W. Serlo. 2015. "Severe osteogenesis imperfecta Type-III and its challenging treatment in newborn and preschool children. A systematic review." *Injury* 46 (8):1440-6. doi: 10.1016/j.injury.2015.04.021.
- Sinkunas, T., G. Gasiunas, C. Fremaux, R. Barrangou, P. Horvath, and V. Siksnys. 2011. "Cas3 is a single-stranded DNA nuclease and ATP-dependent helicase in the CRISPR/Cas immune system." *EMBO J* 30 (7):1335-42. doi: 10.1038/emboj.2011.41.

- Soares, A. P., R. F. do Espírito Santo, S. R. Line, M. Pinto, P.e M Santos, M. B. Toralles, and A. R. do Espírito Santo. 2016. "Bisphosphonates: Pharmacokinetics, bioavailability, mechanisms of action, clinical applications in children, and effects on tooth development." *Environ Toxicol Pharmacol* 42:212-7. doi: 10.1016/j.etap.2016.01.015.
- Sorushanova, A., L. M. Delgado, Z. Wu, N. Shologu, A. Kshirsagar, R. Raghunath, A. M. Mullen, Y. Bayon, A. Pandit, M. Raghunath, and D. I. Zeugolis. 2019. "The Collagen Suprafamily: From Biosynthesis to Advanced Biomaterial Development." *Adv Mater* 31 (1):e1801651. doi: 10.1002/adma.201801651.
- Spurr, A. R. 1969. "A low-viscosity epoxy resin embedding medium for electron microscopy." *J Ultrastruct Res* 26 (1):31-43. doi: 10.1016/s0022-5320(69)90033-1.
- Steinmann, B., P. Bruckner, and A. Superti-Furga. 1991. "Cyclosporin A slows collagen triple-helix formation in vivo: indirect evidence for a physiologic role of peptidyl-prolyl cis-trans-isomerase." *J Biol Chem* 266 (2):1299-303.
- Stemple, D. L. 2005. "Structure and function of the notochord: an essential organ for chordate development." *Development* 132 (11):2503-12. doi: 10.1242/dev.01812.
- Sweeney, S. M., J. P. Orgel, A. Fertala, J. D. McAuliffe, K. R. Turner, G. A. Di Lullo, S. Chen, O. Antipova, S. Perumal, L. Ala-Kokko, A. Forlino, W. A. Cabral, A. M. Barnes, J. C. Marini, and J. D. San Antonio. 2008. "Candidate cell and matrix interaction domains on the collagen fibril, the predominant protein of vertebrates." *J Biol Chem* 283 (30):21187-97. doi: 10.1074/jbc.M709319200.
- Symoens, S., F. Malfait, S. D'hondt, B. Callewaert, A. Dheedene, W. Steyaert, H. P. Bächinger, A. De Paepe, H. Kayserili, and P. J. Coucke. 2013. "Deficiency for the ER-stress transducer OASIS causes severe recessive osteogenesis imperfecta in humans." *Orphanet J Rare Dis* 8:154. doi: 10.1186/1750-1172-8-154.
- Tao, S., D. Yamazaki, S. Komazaki, C. Zhao, T. Iida, S. Kakizawa, Y. Imaizumi, and H. Takeshima. 2013. "Facilitated hyperpolarization signaling in vascular smooth muscle-overexpressing TRIC-A channels." *J Biol Chem* 288 (22):15581-9. doi: 10.1074/jbc.M112.435396.
- Tonelli, F., J. W. Bek, R. Besio, A. De Clercq, L. Leoni, P. Salmon, P. J. Coucke, A. Willaert, and A. Forlino. 2020. "Zebrafish: A Resourceful Vertebrate Model to Investigate Skeletal Disorders." *Front Endocrinol* 11:489. doi: 10.3389/fendo.2020.00489.
- Tonelli, F., S. Cotti, L. Leoni, R. Besio, R. Gioia, L. Marchese, S. Giorgetti, S. Villani, C. Gistelink, R. Wagener, B. Kobbe, D. Larionova, I. A. K. Fiedler, B. Busse, D. Eyre, A. Rossi, P. E. Witten, and A. Forlino. 2020. "Crtap and p3h1 knock out zebrafish support defective collagen chaperoning as the cause of their osteogenesis imperfecta phenotype." *Matrix Biol*. doi: 10.1016/j.matbio.2020.03.004.
- Trejo, P., T. Palomo, K. Montpetit, F. Fassier, A. Sato, F. H. Glorieux, and F. Rauch. 2017. "Long-term follow-up in osteogenesis imperfecta type VI." *Osteoporos Int* 28 (10):2975-2983. doi: 10.1007/s00198-017-4141-x.
- Uitto, J. 1979. "Collagen polymorphism: isolation and partial characterization of alpha 1(I)-trimer molecules in normal human skin." *Arch Biochem Biophys* 192 (2):371-9. doi: 10.1016/0003-9861(79)90105-x.
- Uveges, T. E., P. Collin-Osdoby, W. A. Cabral, F. Ledgard, L. Goldberg, C. Bergwitz, A. Forlino, P. Osdoby, G. A. Gronowicz, and J. C. Marini. 2008. "Cellular mechanism of decreased bone in Brl mouse model of OI: imbalance of decreased osteoblast function and increased osteoclasts and their precursors." *J Bone Miner Res* 23 (12):1983-94. doi: 10.1359/jbmr.080804.
- Valadares, E. R., T. B. Carneiro, P. M. Santos, A. C. Oliveira, and B. Zabel. 2014. "What is new in genetics and osteogenesis imperfecta classification?" *J Pediatr (Rio J)* 90 (6):536-41. doi: 10.1016/j.jpmed.2014.05.003.

- van der Ploeg, J. R. 2009. "Analysis of CRISPR in *Streptococcus mutans* suggests frequent occurrence of acquired immunity against infection by M102-like bacteriophages." *Microbiology* 155 (Pt 6):1966-1976. doi: 10.1099/mic.0.027508-0.
- Van Dijk, F. S., and D. O. Sillence. 2014. "Osteogenesis imperfecta: clinical diagnosis, nomenclature and severity assessment." *Am J Med Genet A* 164A (6):1470-81. doi: 10.1002/ajmg.a.36545.
- van Dijk, F. S., M. C. Zillikens, D. Micha, M. Riessland, C. L. Marcelis, C. E. de Die-Smulders, J. Milbradt, A. A. Franken, A. J. Harsevoort, K. D. Lichtenbelt, H. E. Pruijs, M. E. Rubio-Gozalbo, R. Zwertbroek, Y. Moutaouakil, J. Egthuijsen, M. Hammerschmidt, R. Bijman, C. M. Semeins, A. D. Bakker, V. Everts, J. Klein-Nulend, N. Campos-Obando, A. Hofman, G. J. te Meerman, A. J. Verkerk, A. G. Uitterlinden, A. Mageri, E. A. Sijtermans, Q. Waisfisz, H. Meijers-Heijboer, B. Wirth, M. E. Simon, and G. Pals. 2013. "PLS3 mutations in X-linked osteoporosis with fractures." *N Engl J Med* 369 (16):1529-36. doi: 10.1056/NEJMoa1308223.
- Venturi, E., A. Matyjaszkiewicz, S. J. Pitt, K. Tsaneva-Atanasova, M. Nishi, D. Yamazaki, H. Takeshima, and R. Sitsapesan. 2013. "TRIC-B channels display labile gating: evidence from the TRIC-A knockout mouse model." *Pflugers Arch* 465 (8):1135-48. doi: 10.1007/s00424-013-1251-y.
- Volodarsky, M., B. Markus, I. Cohen, O. Staretz-Chacham, H. Flusser, D. Landau, I. Shelef, Y. Langer, and O. S. Birk. 2013. "A deletion mutation in TMEM38B associated with autosomal recessive osteogenesis imperfecta." *Hum Mutat* 34 (4):582-6. doi: 10.1002/humu.22274.
- Vranka, J. A., L. Y. Sakai, and H. P. Bächinger. 2004. "Prolyl 3-hydroxylase 1, enzyme characterization and identification of a novel family of enzymes." *J Biol Chem* 279 (22):23615-21. doi: 10.1074/jbc.M312807200.
- Wang, D. C., and X. Wang. 2019. "Off-target genome editing: A new discipline of gene science and a new class of medicine." *Cell Biol Toxicol* 35 (3):179-183. doi: 10.1007/s10565-019-09475-7.
- Wang, X. H., M. Su, F. Gao, W. Xie, Y. Zeng, D. L. Li, X. L. Liu, H. Zhao, L. Qin, F. Li, Q. Liu, O. B. Clarke, S. M. Lam, G. H. Shui, W. A. Hendrickson, and Y. H. Chen. 2019. "Structural basis for activity of TRIC counter-ion channels in calcium release." *Proc Natl Acad Sci U S A* 116 (10):4238-4243. doi: 10.1073/pnas.1817271116.
- Wang, X., H. He, W. Tang, X. A. Zhang, X. Hua, and J. Yan. 2012. "Two origins of blastemal progenitors define blastemal regeneration of zebrafish lower jaw." *PLoS One* 7 (9):e45380. doi: 10.1371/journal.pone.0045380.
- Webb, E. A., M. Balasubramanian, N. Fratzl-Zelman, W. A. Cabral, H. Titheradge, A. Alsaedi, V. Saraff, J. Vogt, T. Cole, S. Stewart, N. J. Crabtree, B. M. Sargent, S. Gamsjaeger, E. P. Paschalis, P. Roschger, K. Klaushofer, N. J. Shaw, J. C. Marini, and W. Högl. 2017. "Phenotypic Spectrum in Osteogenesis Imperfecta Due to Mutations in *TMEM38B*: Unraveling a Complex Cellular Defect." *J Clin Endocrinol Metab* 102 (6):2019-2028. doi: 10.1210/jc.2016-3766.
- Weigle, J., and T. A. Franz-Odenaal. 2016. "Functional bone histology of zebrafish reveals two types of endochondral ossification, different types of osteoblast clusters and a new bone type." *J Anat* 229 (1):92-103. doi: 10.1111/joa.12480.
- Winata, C. L., S. Korzh, I. Kondrychyn, W. Zheng, V. Korzh, and Z. Gong. 2009. "Development of zebrafish swimbladder: The requirement of Hedgehog signaling in specification and organization of the three tissue layers." *Dev Biol* 331 (2):222-36. doi: 10.1016/j.ydbio.2009.04.035.
- Witten, P. E., M. P. Harris, A. Huysseune, and C. Winkler. 2017. "Small teleost fish provide new insights into human skeletal diseases." *Methods Cell Biol* 138:321-346. doi: 10.1016/bs.mcb.2016.09.001.

- Wopat, S., J. Bagwell, K. D. Sumigray, A. L. Dickson, L. F. A. Huitema, K. D. Poss, S. Schulte-Merker, and M. Bagnat. 2018. "Spine Patterning Is Guided by Segmentation of the Notochord Sheath." *Cell Rep* 22 (8):2026-2038. doi: 10.1016/j.celrep.2018.01.084.
- Wu, M., G. Chen, and Y. P. Li. 2016. "TGF- β and BMP signaling in osteoblast, skeletal development, and bone formation, homeostasis and disease." *Bone Res* 4:16009. doi: 10.1038/boneres.2016.9.
- Yamauchi, Mitsuo, and Marnisa Sricholpech. 2012. "Lysine post-translational modifications of collagen." *Essays in Biochemistry* 52:113. doi: 10.1042/bse0520113.
- Yamazaki, D., S. Komazaki, H. Nakanishi, A. Mishima, M. Nishi, M. Yazawa, T. Yamazaki, R. Taguchi, and H. Takeshima. 2009. "Essential role of the TRIC-B channel in Ca²⁺ handling of alveolar epithelial cells and in perinatal lung maturation." *Development* 136 (14):2355-61. doi: 10.1242/dev.036798.
- Yamazaki, D., Y. Tabara, S. Kita, H. Hanada, S. Komazaki, D. Naitou, A. Mishima, M. Nishi, H. Yamamura, S. Yamamoto, S. Kakizawa, H. Miyachi, T. Miyata, Y. Kawano, K. Kamide, T. Ogihara, A. Hata, S. Umemura, M. Soma, N. Takahashi, Y. Imaizumi, T. Miki, T. Iwamoto, and H. Takeshima. 2011. "TRIC-A channels in vascular smooth muscle contribute to blood pressure maintenance." *Cell Metab* 14 (2):231-41. doi: 10.1016/j.cmet.2011.05.011.
- Yan, Y. L., J. Willoughby, D. Liu, J. G. Crump, C. Wilson, C. T. Miller, A. Singer, C. Kimmel, M. Westerfield, and J. H. Postlethwait. 2005. "A pair of Sox: distinct and overlapping functions of zebrafish sox9 co-orthologs in craniofacial and pectoral fin development." *Development* 132 (5):1069-83. doi: 10.1242/dev.01674.
- Yazawa, M., C. Ferrante, J. Feng, K. Mio, T. Ogura, M. Zhang, P. H. Lin, Z. Pan, S. Komazaki, K. Kato, M. Nishi, X. Zhao, N. Weisleder, C. Sato, J. Ma, and H. Takeshima. 2007. "TRIC channels are essential for Ca²⁺ handling in intracellular stores." *Nature* 448 (7149):78-82. doi: 10.1038/nature05928.
- Zeng, B., J. R. MacDonald, J. G. Bann, K. Beck, J. E. Gambee, B. A. Boswell, and H. P. Bächinger. 1998. "Chicken FK506-binding protein, FKBP65, a member of the FKBP family of peptidylprolyl cis-trans isomerases, is only partially inhibited by FK506." *Biochem J* 330 (Pt 1):109-14. doi: 10.1042/bj3300109.
- Zhao, C., A. Ichimura, N. Qian, T. Iida, D. Yamazaki, N. Noma, M. Asagiri, K. Yamamoto, S. Komazaki, C. Sato, F. Aoyama, A. Sawaguchi, S. Kakizawa, M. Nishi, and H. Takeshima. 2016b. "Mice lacking the intracellular cation channel TRIC-B have compromised collagen production and impaired bone mineralization." *Sci Signal* 9 (428):ra49. doi: 10.1126/scisignal.aad9055.
- Zhao, X., D. Yamazaki, K. H. Park, S. Komazaki, A. Tjondrokoesoemo, M. Nishi, P. Lin, Y. Hirata, M. Brotto, H. Takeshima, and J. Ma. 2010. "Ca²⁺ overload and sarcoplasmic reticulum instability in tric-a null skeletal muscle." *J Biol Chem* 285 (48):37370-6. doi: 10.1074/jbc.M110.170084.
- Zhou, X., P. Lin, D. Yamazaki, K. H. Park, S. Komazaki, S. R. Chen, H. Takeshima, and J. Ma. 2014. "Trimeric intracellular cation channels and sarcoplasmic/endoplasmic reticulum calcium homeostasis." *Circ Res* 114 (4):706-16. doi: 10.1161/CIRCRESAHA.114.301816.